LA-UR-16-23500
Approved for public release; distribution is unlimited.

Title:	Modeling of a Compact Terahertz Source based on the Two-Stream Instability
Author(s):	Svimonishvili, Tengiz Bishofberger, Kip A.
Intended for:	Doctoral Dissertation for University of New Mexico
Issued:	2016-05-17

Tengiz Svimonishvili

Candidate

Electrical and Computer Engineering

Department

This dissertation is approved, and it is acceptable in quality and form for publication:

Approved by the Dissertation Committee:

_____, Chairperson

_____

_____

_____

_____

_____

_____

_____

MODELING OF A COMPACT TERAHERTZ SOURCE BASED ON THE TWO-STREAM INSTABILITY

by

Tengiz Svimonishvili

B.S., Physics, Tbilisi State University, 1994
M.S., Electrical Engineering, University of New Mexico, 2002

DISSERTATION

Submitted in Partial Fulfillment of the
Requirements for the Degree of

Doctor of Philosophy
Engineering

The University of New Mexico

Albuquerque, New Mexico

July, 2011

Acknowledgments

First and foremost, I would like to thank my advisor, Professor Edl Schamiloglu, for his mentoring, continued encouragement, patience, and support (both moral and financial) throughout my Ph.D. work, which was full of ups and downs.

My dissertation work was a collaborative effort between the UNM and the High-Power Electrodynamics Group (ISR-6) at the Los Alamos National Laboratory, where I was supervised by Dr. Kip Bishofberger. I was hired by Kip to assist him with his LDRD project, which also became my Ph.D. topic. I would like to express my gratitude to Kip for always trying to get the best out of me. My almost daily interactions with Kip helped me deepen my understating of the subject and improved my analysis skills considerably.

I would like to acknowledge Dr. Rickey Faehl for informative and exciting discussions of various topics relevant to my dissertation. In addition, I would like to thank Dr. Bruce Carlsten, the group leader of ISR-6, and everyone else in the group for allowing me to pursue my Ph.D. work at LANL. It was a wonderful experience. Last but not least, I would like to thank Dr. Christos Christodoulou and Dr. Bernd Bassalleck for their words of encouragement and for being on my dissertation committee.

I will always be indebted to my childhood friend, Ika Tsitsishvili, who made it possible for me to come to the United States. I owe a special and personal thanks to my parents, my brother and his family, my relatives, and my friends for believing in me and for being there for me. This dissertation is dedicated to all of them.

MODELING OF A COMPACT TERAHERTZ SOURCE BASED ON THE TWO-STREAM INSTABILITY

by

Tengiz Svimonishvili

ABSTRACT OF DISSERTATION

Submitted in Partial Fulfillment of the
Requirements for the Degree of

Doctor of Philosophy
Engineering

The University of New Mexico

Albuquerque, New Mexico

July, 2011

MODELING OF A COMPACT TERAHERTZ SOURCE BASED ON THE TWO-STREAM INSTABILITY

by

Tengiz Svimonishvili

B.S., Physics, Tbilisi State University, 1994
M.S., Electrical Engineering, University of New Mexico, 2002

Ph.D., Engineering, University of New Mexico, 2011

Abstract

THz radiation straddles the microwave and infrared bands of the electromagnetic spectrum, thus combining the penetrating power of lower-frequency waves and imaging capabilities of higher-energy infrared radiation. THz radiation is employed in various fields such as cancer research, biology, agriculture, homeland security, and environmental monitoring. Conventional vacuum electronic sources of THz radiation (e.g., fast- and slow-wave devices) either require very small structures or are bulky and expensive to operate. Optical sources necessitate cryogenic cooling and are presently capable of producing milliwatt levels of power at THz frequencies.

We propose a millimeter and sub-millimeter wave source based on a well-known phenomenon called the two-stream instability. The two-beam source relies on low-energy and low-current electron beams for operation. Also, it is compact, simple in

design, and does not contain expensive parts that require complex machining and precise alignment.

In this dissertation, we perform 2-D particle-in-cell (PIC) simulations of the interaction region of the two-beam source. The interaction region consists of a beam pipe of radius r_a and two electron beams of radius r_b co-propagating and interacting inside the pipe. The simulations involve the interaction of unmodulated (no initial energy modulation) and modulated (energy-modulated, seeded at a given frequency) electron beams. In addition, both cold (monoenergetic) and warm (Gaussian) beams are treated.

Using PIC simulations electromagnetic radiation is demonstrated over the frequency range $0.03 \leq f \leq 1$ THz. The two-beam source is found to possess an extremely wide gain bandwidth (over a decade in frequency) from the microwave to the far infrared region of the electromagnetic spectrum. Moreover, the gain obtained is impressive. For example, the interaction of two 0.7-mm and 0.5-A electron beams with energies 20 keV and 16.95 keV (typical in this dissertation) yields the value of gain of 0.35 dB/mm, which is over a factor of 10 greater than that reported in the literature for a proposed two-stream relativistic klystron amplifier involving 1.0- and 5.0-kA annular relativistic electron beams. Hence, the two-beam amplifier promises to be a reliable and inexpensive source of millimeter and sub-millimeter wave radiation and has the potential to generate watts of power at THz frequencies.

Contents

List of Figures

List of Tables

Chapter 1

Introduction

The purpose of this dissertation is to perform 2-D particle-in-cell (PIC) simulations to study a potential millimeter and sub-millimeter radiation source based on a phenomenon known as the two-stream instability. More specifically, PIC simulations are performed of the interaction region of the source (discussed in Section 1.2). The interaction region consists of a beam pipe of radius r_a and two electron beams of radius r_b co-propagating and interacting inside the pipe. A detailed discussion of the simulation structure and parameters is given in Chapter 5.

Simulations are performed on a single personal computer using a software package called MAGIC, a PIC code developed by ATK/Mission Research [13]. The simulations presented in Chapters 6 and 7 involve the interaction of unmodulated (no initial energy modulation) and modulated (energy-modulated, seeded at a given frequency) electron beams. In addition, both cold (monoenergetic) and warm (having a Gaussian energy profile) beams are treated. Moreover, the interaction frequencies considered range from 30 GHz up to and including 1 THz. The interaction of two co-propagating electron beams gives rise to exponentially growing waves and the emphasis in this dissertation is placed on the variation of the gain of exponentially

growing modes as a function of total beam current (sum of the currents of two interacting beams), beam radius, percent energy spread, and interaction frequency. Gain obtained from simulations is compared with theoretical gain to validate the 1-D theory presented in Chapter 4.

1.1 Millimeter and sub-millimeter radiation, its applications, and conventional sources

The region of the electromagnetic spectrum that lies between 50 GHz and 10 THz ($\lambda = 6 - 0.03$ mm) is called millimeter and sub-millimeter radiation [4]. This is a rough designation since some authors refer to the sub-millimeter region as extending from 300 GHz to 3 THz or 30 THz. Hence, the border between far-infrared and sub-millimeter regions is somewhat arbitrary. The scientific community has shown much interest in the terahertz region since as early as the 1920s. Still, this part of the spectrum remains one of the least used [2]. Terahertz radiation is not absorbed by most dry, non-polar materials (e.g., plastic, paper, fat) and it does not transmit through water. Moreover, waves at terahertz frequency are reflected by metals because of free electrons [4]. An increased interest in terahertz technology and recent advances have led to a multitude of applications in such research fields as biology, pharmacy, medical science, imaging, security, environmental protection, communications, etc. The following is a list of some of the existing and potential applications of terahertz radiation:

- **Space and Earth applications**

  Astronomy. Terahertz technology should help to resolve and identify spectral lines coming from interstellar dust clouds (likely emitting 40,000 individual spectral lines) and observable galaxies. This is important since 98% of photons

emitted by observable galaxies fall in the sub-millimeter and far-IR range [2].

Radar and satellite communications. Although opacity of water to terahertz waves limits radar and communications applications in the atmosphere, operation in the stratosphere should be very effective because of low scattering compared to IR and optical wavelengths and enhanced penetration through aerosols and clouds [2].

Environmental protection. Terahertz radiation makes it possible to monitor various chemical species (H_2O, O_3, etc.), which allows scientists to obtain information on ozone chemistry, structure and, thus, gain a better understanding of global warming [3].

- **Biological, medical, industrial applications**

  Terahertz spectroscopy. This technique, among other things, allows one to observe inter-molecular vibrations in chemicals and organic molecules.

  Cancer research. Opacity of water and other polar molecules to terahertz waves may enable cancer researchers to identify tumors by distinguishing between reflections from cancerous tissues and those from healthy ones [3].

  Terahertz imaging. This technique has been used to detect defects, such as voids, in foam insulation used for the space shuttle [3].

  Quality control. Sensitivity to water could be used to control food and agricultural products for damage, water content, etc. [3].

- **Security**

  Detection of explosives, harmful substances. Every explosive, hazardous substance has a distinct signature in its terahertz spectra. This fact can be exploited to identify and separate them from harmless substances [3].

  Penetrability. A combination of non-ionizing photon energy (1.2 meV at 300 GHz) and the ability of terahertz radiation to detect through smoke, opaque

containers, even concrete walls, makes them ideal for imaging of hazardous chemicals/agents through opaque containers and factories [3, 4].

Emerging applications in imaging, medicine, biology, space exploration, homeland security, etc., necessitate reliable, compact, and high-power terahertz sources. Table 1.1 compares several commercially available optical techniques for generating terahertz radiation.

Table 1.1: Optical techniques for terahertz generation [2, 6].

Technique	Frequency (THz)	Regime	Power
Optically pumped THz lasers	0.3 – 10	CW or pulsed	$>$ 100 mW
Time domain spectroscopy	0.1 – 0.2	Pulsed	$>$ 1 μW
Multipliers	0.1 – 1	CW	μW-mW
Photomixing	0.1 – 10	CW	μW
Ultrashort pulse lasers	0.2 – 2	Pulsed	nW, μW

Two common, currently available optical sources are solid-state and optically pumped lasers. Quantum-cascade lasers are capable of producing pulses with peak power of 2 mW at up to 4 THz [5]. Although compact, their room-temperature operation is virtually impossible without cryogenic cooling. This is due to the fact that the photon energy at 1 THz is about 4 meV, as compared to thermal energy of 26 meV at room temperature [6]. Optically pumped lasers are usually based on a grating tuned CO_2 pump laser injected into gas cells that lase to emit terahertz radiation. Power levels of 1 – 20 mW are attainable depending on the selected spectral line, one of the most pronounced being that of methanol at 2522.78 GHz [2].

Tube-based sources of terahertz radiation offer the most power and frequency tunning range at sub-millimeter frequencies [6]. They use electrons to generate coherent electromagnetic radiation and can be classified into two groups: slow- and fast-wave devices. In slow-wave devices, an electron beam drives a wave whose phase velocity

is less than the speed of light in vacuum. By contrast, waves in fast-wave devices (for example, FEL) travel at the speed of light. The shortcoming of slow-wave devices (Smith-Purcell FEL, TWT, BWO) is that they require structures comparable in size to the wavelength at terahertz frequencies. This leads to low currents, fabrication issues and output powers on the order of milliwatts or less [1]. Fast-wave devices (FEL, gyrotron) have no fabrication problems (the physical size is much larger than than the radiation wavelength), but require large facilities. For instance, although an ultrarelativistic FEL is capable of producing kW levels of terahertz radiation, it requires room-size accelerators and extremely large magnetic fields for its operation [6, 8]. Gyrotrons utilize lower energy beams (10 – 100 keV) and, therefore, have smaller dimensions. However, they are far from being compact. A good example is a gyrotron developed by GYCOM [7]. This device, operating at 110 GHz and producing kW of power in the range 350 – 850 kW, is 3 meters long and weighs as much as 250 kg without the superconducting magnet. It is interesting to note that Siegel reports tube-based benchtop units that are commercially available and produce milliwatt levels of power at up to 1200 GHz [2].

1.2 Two-stream instability as a better mm and sub-mm radiation generation technique

From the brief review of conventional sources in Section 1.1 it is clear that conventional tube-based sources are bulky, expensive to operate, and have physical scaling problems. Optical sources, such as various optically pumped and solid-state lasers, are either low-power devices ($\approx$ milliwatt) or they must operate at very low energy levels ($\approx$ millielectronvolt) unless cryogenic cooling is used [2].

We propose a millimeter and sub-millimeter wave source based on a phenomenon

known as the two-stream instability [1]. The proposed source, shown in Figure 1.1, comprises two electron guns in the kiloelectronvolt range, two sector magnets with

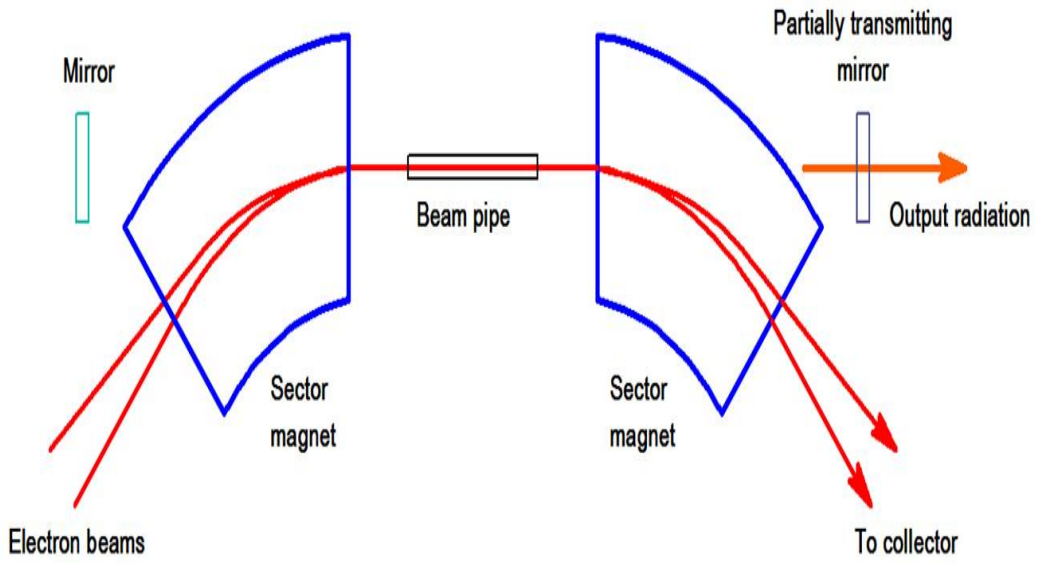

Figure 1.1: Potential two-beam source of millimeter and sub-millimeter wave radiation [1].

a field gradient n, a beam pipe in which co-propagating electron beams are merged and interact unstably, a partially transmitting mirror and another mirror with a frequency-selective grating. As two electron beams with slightly different energies enter the sector magnet, they merge in the beam pipe, where natural current fluctuations seed the two-stream instability. The generated wave, originally a non-radiative Coulomb field, is stripped off, reflected back to the front by the mirrors, and interacts with the beams again. The desired frequency of oscillation is selected using the mirror with the frequency-selective grating and a portion of the saturated wave exits through the partially transmitting mirror [1].

The merging of the beams can be accomplished by properly choosing the bend radius, which is a function of beam energy, and the field gradient n. It can be

shown (to first order) that when $0 < n < 1$, the equations of motion in the sector magnet (Kerst-Serber equations) have sinusoidal functions as their solutions, which means that the magnet can act as a focusing lens [11]. Moreover, when $n = 0.5$, the focal planes in radial and axial directions coincide and the magnet produces a 2-D image [11].

The source in Figure 1.1 is superior to conventional tube-based and optical sources in that it is compact, simple in design, and only requires low-energy and low-current electron beams. This table-top source, which is free from problems associated with complex machining, precise alignment, expensive parts, and catastrophic failures, promises to be a reliable and inexpensive source of millimeter and sub-millimeter wave radiation [1]. Moreover, it has the potential to generate watts of power at terahertz frequencies.

1.3 Background

The idea to use two streams of electrons in a tube to obtain an increasing wave dates back to two papers published in 1949 and entitled "A New Type of High-Frequency Amplifier" and "The Electron-Wave Tube - A Novel Method of Generation and Amplification of Microwave Energy". The former [20], by J. Pierce and W. Hebenstreit, treats the case of two solid cylindrical beams propagating in a very remote tube, thus disregarding space-charge depression and electron plasma frequency reduction. The beams have slightly different average velocities and are subjected to an infinitely strong, longitudinal dc magnetic field. The authors evaluate conditions for an increasing wave and derive an expression for the gain of the growing wave. They find the broadness of gain curves to be comparable to that of curves for helix-type traveling-wave tubes [20]. The latter paper [21], by A. Haeff, has an analysis similar to that in [20] and also gives expressions and curves for the propagation constant,

gain, and bandwidth of the so-called "electron-wave tube". In addition to theory, however, Haeff's paper also reports on the design and performance of the "two-beam"- and "single-beam"-type tubes. In the "two-beam" tube, electron streams are generated by two separate cathodes. By means of accelerating and focusing electrodes the streams are accelerated into a very long drift tube, where the unstable interaction takes place. An rf perturbation imposed on one of the streams via an input helix is amplified along the length of the tube and then extracted at the end of the tube through an output circuit. Haeff reports electronic bandwidths of over 30% and gains of the order of 80 dB at a frequency of 3 GHz [21].

In 1949 an experimental paper written by A. Hollenberg discusses the construction and performance of a two-stream amplifier [22]. The two-stream amplifier consists of two cathodes, input and output helices, and a drift tube. Again, an rf signal imposed on one of the beams by the input helix is amplified in the drift tube and extracted by the output helix. The electron streams are hollow annular beams that are separated in space and not intermixed. Space-charge spreading is countered by an axial magnetic field of approximately 700 gauss. Hollenberg reports gains of 33 dB at 255 MHz, and a bandwidth of 110 MHz between 3dB points [22].

More recently, Chen et al. proposed a two-stream relativistic klystron amplifier (RKA) and carried out analytical and numerical studies of the proposed device [23]. Amplification of stimulated beam modulation in the RKA is achieved by means of the unstable interaction of two concentric annular relativistic electron beams. The beams propagate and interact in a drift tube that is free from passive circuits, which eliminates the possibility of rf breakdown at the passive elements. Through particle-in-cell simulations using MAGIC [13], the intensity growth rate is found to be 30 dB/m and in good agreement with the theoretical analysis presented. It is also determined that a substantial difference in beam energies is required to bring about large instability growth [23].

1.4 Road map of dissertation

This dissertation is organized as follows. Chapter 2 is a review of single particle dynamics. Chapter 3 is devoted to space-charge effects such as potential depression, space-charge waves on unfocused beams, plasma frequency reduction, and space-charge spreading and focusing. In Chapter 4, we present a small-signal theory of the two-stream instability and derive a theoretical expression for the gain of exponentially growing modes. In Chapter 5, the simulation setup and parameters are discussed and the calculation of numerical gain is presented. Chapters 6 and 7 present simulation results. Specifically, Chapter 6 discusses the interaction of unmodulated electron beams, while Chapter 7 is devoted to the interaction of modulated electron beams. In Chapter 8, conclusions are presented and future work is discussed.

Chapter 2

Single particle dynamics

In Chapter 2, we ignore the interaction between electrons and review single particle dynamics. In Section 2.1, the components of the equation of motion are derived and expressed in terms of the cylindrical coordinates $(r,\ \varphi,\ z)$. In Section 2.2, the Lagrangian and Hamiltonian formalisms are used to rewrite the components of the equation of motion in a coordinate-free from. The radial equation of motion from Section 2.1 is combined with an expression for the conservation of generalized momenta (derived in Section 2.2) to find analytic and numerical solutions to the beam envelope equation in Chapter 3.

2.1 The Lorentz force and the equations of motion

The charged particle dynamics is concerned with the motion of charged particles in the presence of electromagnetic fields. Denoting the force acting on a point charge q by $\vec{F}$, the Lorentz force equation reads:

$$\vec{F} \ = \ q(\vec{E} + \vec{v} \times \vec{B}), \tag{2.1}$$

where $\vec{v}$ is the particle's velocity, $\vec{E}$ is the electric field intensity and $\vec{B}$ is the magnetic flux density. $\vec{E}$ and $\vec{B}$ in Equation 2.1 satisfy Maxwell's equations, which in vacuum have the form

$$\vec{\nabla} \times \vec{E} = -\frac{\partial \vec{B}}{\partial t}, \tag{2.2}$$

$$\vec{\nabla} \times \vec{B} = \mu_0 \vec{J} + \frac{1}{c^2}\frac{\partial \vec{E}}{\partial t}, \tag{2.3}$$

$$\vec{\nabla} \cdot \vec{E} = \frac{\varrho}{\epsilon_0}, \tag{2.4}$$

$$\vec{\nabla} \cdot \vec{B} = 0, \tag{2.5}$$

where ϵ_0 and μ_0 are the permittivity and permeability of free space, $\vec{J}$ is the current density, ϱ is the volume charge density, and c is the speed of light in vacuum.

Before deriving the equations of motion due to the force in Equation 2.1, we need to determine a charged particle's position in space and its velocity as a function of time. To describe the motion of a particle, we define a position vector, $\vec{r}$, whose tale is fixed at the origin of a given coordinate system as the head follows the particle. Of primary interest to us is the cylindrical coordinate system, in which the position vector is given as follows

$$\vec{r} = r\hat{r} + z\hat{k}, \tag{2.6}$$

where $\hat{r}$ and $\hat{k}$ are unit vectors in the radial and axial directions, respectively. Having defined the position vector, velocity, $\vec{v}$, and acceleration, $\vec{a}$, vectors and their radial, azimuthal, and axial components can now be obtained by differentiating Equation 2.6 with respect to time to yield

$$\vec{v} = \dot{r}\hat{r} + r\dot{\varphi}\hat{\varphi} + \dot{z}\hat{k}, \tag{2.7}$$

$$\vec{a} = (\ddot{r} - r\dot{\varphi}^2)\hat{r} + (2\dot{r}\dot{\varphi} + r\ddot{\varphi})\hat{\varphi} + \ddot{z}\hat{k}, \tag{2.8}$$

where "˙" and "¨" stand for the first and second derivatives with respect to time, respectively.

Newton's equation of motion due to the force in Equation 2.1 reads

$$\frac{d\vec{P}}{dt} = q(\vec{E} + \vec{v} \times \vec{B}), \tag{2.9}$$

where $\vec{P}$, the mechanical momentum, is equal to

$$\vec{P} = \gamma m\vec{v} = \frac{m\vec{v}}{\sqrt{1-\beta^2}}. \tag{2.10}$$

In Equation 2.10, γ is the Lorentz factor, while β is the ratio of the particle's velocity to the speed of light in vacuum. Equation 2.10 is suitable for relativistic mechanics and reduces to $\vec{P} = m\vec{v}$ in the case of nonrelativistic particles ($\gamma = 1$, $\beta \ll 1$). Substituting Equation 2.10 into 2.9, expanding out the LHS and solving for $\vec{F}$, we have

$$\vec{F} = \gamma m\frac{d\vec{v}}{dt} + m\vec{v}\frac{d\gamma}{dt}. \tag{2.11}$$

With

$$\frac{d\gamma}{dt} = \gamma^3\beta\frac{d\beta}{dt}, \tag{2.12}$$

Equation 2.11 becomes

$$\vec{F} = \gamma m(\frac{d\vec{v}}{dt} + \gamma^2\frac{\beta}{c}\frac{dv}{dt}\vec{v}). \tag{2.13}$$

Thus, the force and acceleration are not necessarily unidirectional for relativistic particles. Writing Equation 2.9 in terms of cylindrical coordinates and substituting

Equations 2.7 and 2.8, we have

$$\frac{d}{dt}[\gamma m\dot{r}] - \gamma m r\dot{\varphi}^2 = q(E_r + r\dot{\varphi}B_z - \dot{z}B_\varphi), \tag{2.14}$$

$$\frac{1}{r}\frac{d}{dt}[\gamma m r^2\dot{\varphi}] = q(E_\varphi + \dot{z}B_r - \dot{r}B_z), \tag{2.15}$$

$$\frac{d}{dt}[\gamma m\dot{z}] = q(E_z + \dot{r}B_\varphi - r\dot{\varphi}B_r). \tag{2.16}$$

Equations (2.14 – 2.16) are coupled, second-order, inhomogeneous differential equations. In general, they do not admit solutions in closed form and must be solved numerically, unless certain simplifying assumptions are made. Moreover, the mathematical form of the above equations depends on a selected frame of reference. In the following section, we will rewrite the equations of motion in a frame-independent form via a Lagrange's function $L = L(q_i, \dot{q}_i, t)$ and a Hamilton's function $H = H(q_i, p_i, t)$, where q_i, $\dot{q}_i$, p_i represent generalized coordinates, associated velocities, and generalized momenta, respectively.

2.2 The Lagrangian and Hamiltonian formalisms

2.2.1 The Lagrangian and Lagrange's equation of motion

In order to rewrite the equations of motion in a coordinate-independent form, we make use of generalized coordinates, q_i, and define a function, $L = L(q_i, \dot{q}_i, t)$, called the Lagrangian. Assuming a Lagrangian exists for a given system, Hamilton's variational principle states that the motion of the system between two fixed points, one at time t_1 and the other at t_2, is such that the variation of the integral $\int_{t_1}^{t_2} L\,dt$ along the actual path taken vanishes [9]

$$\delta\int_{t_1}^{t_2} L\,dt = \int_{t_1}^{t_2} \delta L\,dt = 0. \tag{2.17}$$

For a conservative system, $\partial L/\partial t = 0$, and δL can be written as

$$\delta L = \frac{\partial L}{\partial q_i}\delta q_i + \frac{\partial L}{\partial \dot{q}_i}\delta \dot{q}_i, \tag{2.18}$$

where a summation is implied over the repeated index ($i = 1, 2, 3$). Substituting Equation 2.18 into Equation 2.17 and integrating by parts with $\delta q_i|_{t_1} = \delta q_i|_{t_2} = 0$, we get

$$\int_{t_1}^{t_2} \left(\frac{\partial L}{\partial q_i}\delta q_i + \frac{\partial L}{\partial \dot{q}_i}\delta \dot{q}_i \right) dt = 0 \Rightarrow$$

$$\int_{t_1}^{t_2} \frac{\partial L}{\partial q_i}\delta q_i \, dt + \overbrace{\delta q_i \left.\frac{\partial L}{\partial q_i}\right|_{t_1}^{t_2}}^{=0} - \int_{t_1}^{t_2} \delta q_i \frac{d}{dt}\left(\frac{\partial L}{\partial \dot{q}_i}\right) dt = 0 \Rightarrow$$

$$\int_{t_1}^{t_2} \left(\frac{\partial L}{\partial q_i} - \frac{d}{dt}\left(\frac{\partial L}{\partial \dot{q}_i}\right) \right) \delta q_i \, dt = 0. \tag{2.19}$$

Since δq_i are arbitrary, Equation 2.19 is satisfied if and only if the integrand is zero

$$\frac{\partial L}{\partial q_i} - \frac{d}{dt}\left(\frac{\partial L}{\partial \dot{q}_i}\right) = 0. \tag{2.20}$$

Equation 2.20, for a given value of i, is called the Lagrange equation of motion. It is invariant regardless of the coordinate system chosen. Let us consider a conservative system ($\vec{E} = -\vec{\nabla}\phi$) for which $\gamma = 1$ and $\vec{B} = \vec{0}$. The Lagrangian in this case is defined by the difference between kinetic and potential energy and in cylindrical coordinates reads [9]

$$L = T - U = \frac{1}{2}m(\dot{r}^2 + r^2\dot{\varphi}^2 + \dot{z}^2) - q\phi(r, \varphi, z). \tag{2.21}$$

Setting $q_i = q_1 = r$ and substituting Equation 2.21 into 2.20, we have

$$m\ddot{r} - mr\dot{\varphi}^2 = qE_r. \tag{2.22}$$

Equation 2.22 is seen to be identical to 2.14 when $\gamma = 1$ and $\vec{B} = \vec{0}$. The Lagrangian for a system in which forces are derivable from generalized or velocity-dependent potentials is given as [9]

$$L = T - q\phi + q\vec{v} \cdot \vec{A}, \tag{2.23}$$

$$L = -mc^2\sqrt{(1-\beta^2)} - q\phi + q\vec{v} \cdot \vec{A}, \tag{2.24}$$

where the vector potential, $\vec{A}$, and scalar potential, ϕ, are related through the Lorentz gauge condition

$$\vec{\nabla} \cdot \vec{A} + \frac{1}{c^2}\frac{\partial \phi}{\partial t} = 0. \tag{2.25}$$

Equations 2.23 and 2.24 are suitable for nonrelativistic and relativistic particles, respectively. Expressed in cylindrical coordinates, they become

$$L = \frac{1}{2}m(\dot{r}^2 + r^2\dot{\varphi}^2 + \dot{z}^2) - q\phi(r,\varphi,z) + q(\dot{r}A_r + r\dot{\varphi}A_\varphi + \dot{z}A_z), \tag{2.26}$$

$$L = -mc^2\sqrt{1 - \frac{\dot{r}^2 + r^2\dot{\varphi}^2 + \dot{z}^2}{c^2}} - q\phi(r,\varphi,z) + q(\dot{r}A_r + r\dot{\varphi}A_\varphi + \dot{z}A_z). \tag{2.27}$$

2.2.2 The Hamiltonian and Hamilton's equations of motion

In the preceding section we successfully expressed the equations of motion in a frame-independent form by introducing the Lagrangian, $L = L(q_i, \dot{q}_i, t)$, which is a function of generalized coordinates and velocities. An alternative approach to defining the Lagrangian is to introduce a different function, the Hamiltonian, via the following transformation [9]

$$H(q_i, p_i, t) = p_j\dot{q}_j - L(q_i, \dot{q}_i, t). \tag{2.28}$$

The Hamiltonian is a function of generalized coordinates, q_i, and momenta, p_i, which are given by

$$p_i = \frac{\partial L}{\partial \dot{q}_i}. \tag{2.29}$$

Substituting Equation 2.27 into 2.29, we can obtain the three generalized momentum components in cylindrical coordinates

$$p_r = \gamma m \dot{r} + q A_r, \tag{2.30}$$
$$p_\varphi = \gamma m r^2 \dot{\varphi} + q r A_\varphi, \tag{2.31}$$
$$p_z = \gamma m \dot{z} + q A_z. \tag{2.32}$$

Comparing Equations (2.30 – 2.32) and Equation 2.10, the components of the mechanical momentum can be related to those of the generalized momentum as

$$P_r = p_r - q A_r, \tag{2.33}$$
$$P_\varphi = \frac{p_\varphi - q r A_\varphi}{r}, \tag{2.34}$$
$$P_z = p_z - q A_z. \tag{2.35}$$

In order to derive an alternative form of the equations of motion using the Hamiltonian, let us write down the total differential of $H = H(q_i, p_i, t)$

$$dH = \frac{\partial H}{\partial q_i} dq_i + \frac{\partial H}{\partial p_i} dp_i + \frac{\partial H}{\partial t} dt. \tag{2.36}$$

According to Equation 2.28, dH may also be written as

$$dH = p_i d\dot{q}_i + \dot{q}_i dp_i - \frac{\partial L}{\partial q_i} dq_i - \frac{\partial L}{\partial \dot{q}_i} d\dot{q}_i - \frac{\partial L}{\partial t} dt. \tag{2.37}$$

Substituting Equation 2.29 and $\partial L / \partial q_i = \dot{p}_i$ (from Equation 2.20) into 2.37, we get

$$dH = -\dot{p}_i dq_i + \dot{q}_i dp_i - \frac{\partial L}{\partial t} dt. \tag{2.38}$$

Finally, equating the coefficients of dq_i, dp_i and dt in Equations 2.36 and 2.38, we arrive at the following formulas

$$\dot{q}_i = \frac{\partial H}{\partial p_i}, \tag{2.39}$$

$$\dot{p}_i = -\frac{\partial H}{\partial q_i}, \tag{2.40}$$

$$\frac{\partial L}{\partial t} = -\frac{\partial H}{\partial t}. \tag{2.41}$$

Equations 2.39 and 2.40 are Hamilton's equations of motion. As i takes on values from 1 to 3, each of the equations represents three differential equations and, therefore, there are twice as many equations to solve in Hamiltonian dynamics as there are in Lagrangian dynamics. However, Equations 2.39 and 2.40 are first-order differential equations and easier to solve, which makes them particularly useful in numerical codes for calculating particle motion [9]. In general, to solve a problem using Hamiltonian dynamics, one must first construct the Hamiltonian as a function of generalized coordinates and momenta. While this might be possible in some cases, we may still end up setting up the Lagrangian first to calculate the generalized momenta given by Equation 2.29. Having determined the generalized momenta, the equations of motion are then derived from Equations 2.39 and 2.40.

Let us calculate the Hamiltonian for a conservative system ($\vec{F} = -\vec{\nabla}U$, $\partial L/\partial t = 0$) in the nonrelativistic approximation ($\gamma = 1$). Substituting Equations (2.30 – 2.32) into Equation 2.28, we have

$$H = (m\dot{r} + qA_r)\dot{r} + (mr^2\dot{\varphi} + qrA_\varphi)\dot{\varphi} + (m\dot{z} + qA_z)\dot{z} - L.$$

In view of Equation 2.26, the above expression becomes

$$H = \frac{1}{2}m(\dot{r}^2 + r^2\dot{\varphi}^2 + \dot{z}^2) + q\phi(r, \varphi, z) = T + U. \tag{2.42}$$

Therefore, for a conservative system, the Hamiltonian is equal to the total energy (kinetic plus potential).

2.2.3 Conservation of energy and generalized angular momentum

The equations of motion given in terms of the Hamiltonian are very useful for deriving various conservation laws. Here we will derive the conservation of total energy and that of generalized momenta. The latter is very important for charged particle motion in axisymmetric fields. Again considering a conservative system ($\vec{F} = -\vec{\nabla}U$, $\partial L/\partial t = 0$), we can write [9]

$$\frac{dL}{dt} = \frac{\partial L}{\partial q_i}\frac{dq_i}{dt} + \frac{\partial L}{\partial \dot{q}_i}\frac{d\dot{q}_i}{dt}. \tag{2.43}$$

Putting Equation 2.20 into 2.43 and rearranging terms

$$\frac{dL}{dt} = \frac{d}{dt}\left(\frac{\partial L}{\partial \dot{q}_i}\right)\frac{dq_i}{dt} + \frac{\partial L}{\partial \dot{q}_i}\frac{d\dot{q}_i}{dt} = \frac{d}{dt}\left(p_i\dot{q}_i\right) \Rightarrow$$

$$\frac{d}{dt}(p_i\dot{q}_i - L) = 0. \tag{2.44}$$

Combined with Equation 2.28, Equation 2.44 becomes

$$\frac{dH}{dt} = 0 \Rightarrow H = \text{const.} \tag{2.45}$$

According to Equation 2.42, H represents the total energy for a conservative system. Thus, the total energy is a constant of the motion.

When H does not depend on q_i explicitly, from Equation 2.40 it follows that the generalized momenta are invariant quantities

$$\dot{p}_i = 0 \Rightarrow p_i = \text{const.}$$

In axisymmetric systems, H is not a function of $q_2 = \varphi$, and p_φ (Equation 2.31) is conserved

$$p_\varphi \;=\; \gamma m r^2 \dot{\varphi} + qrA_\varphi \;=\; \text{const.} \tag{2.46}$$

Equation 2.46 can be rewritten as

$$\gamma m r^2 \dot{\varphi} + \frac{q}{2\pi}\psi \;=\; \text{const,} \tag{2.47}$$

where ψ is the magnetic flux flowing through an open surface S enclosed by a charged particle trajectory and

$$\psi \;=\; \int_S \vec{B}\cdot d\vec{S} \;=\; \int_S \vec{\nabla}\times\vec{A}\cdot d\vec{S}. \tag{2.48}$$

Using Stokes's theorem, the above surface integral may be transformed into a line integral along the particle trajectory to give

$$\psi \;=\; \oint \vec{A}\cdot d\vec{l} \;=\; \oint A_\varphi r d\varphi \;=\; 2\pi r A_\varphi \Rightarrow rA_\varphi \;=\; \frac{\psi}{2\pi}. \tag{2.49}$$

Upon substitution of Equation 2.49 into 2.47, the latter reduces to Equation 2.46. In some applications, the initial angular velocity, $\dot{\varphi}_0$, is zero (for example, at the surface of a cathode). If the angular velocity and flux away from the cathode (at some point downstream) are denoted by $\dot{\varphi}$ and ψ, then from Equation 2.47 we have

$$\frac{q}{2\pi}\psi_0 \;=\; \gamma m r^2 \dot{\varphi} + \frac{q}{2\pi}\psi \Longrightarrow$$

$$\dot{\varphi} \;=\; \frac{q}{2\pi m \gamma r^2}(\psi_0 - \psi), \tag{2.50}$$

where ψ_0 is the flux at the cathode. Equation 2.50 represents Busch's theorem [16]. According to Equation 2.50, the angular velocity of a given electron is proportional

to the difference between the amount of flux it crosses at the cathode and at some point downstream. Moreover, the angular velocity does not depend on the path between those two points [12, 16]. Busch's theorem will be used in Chapter 3 to solve the radial equation of motion in the presence of a focusing solenoid.

Let us conclude this chapter by considering the motion of an electron in a uniform magnetic field $\vec{B} = (0, 0, B)$. The vector equation of motion (Equation 2.9) reads

$$\frac{d}{dt}(\gamma m \vec{v}) \;=\; -e\,\vec{v} \times \vec{B}. \tag{2.51}$$

The magnetic force is always perpendicular to $\vec{v}$ and does not change the particle's kinetic energy. Therefore, the electron will move in the z direction with uniform velocity. In addition, the total velocity is conserved and γ in Equation 2.51 can be taken out of the time derivative. Rewriting Equation 2.51 in cylindrical coordinates with the help of Equation 2.8, the radial force equation takes the form

$$\ddot{r} - r\dot{\varphi}^2 \;=\; -\frac{e}{\gamma m} v_\varphi B \Longrightarrow$$

$$\ddot{r} \;=\; \frac{v_\varphi^2}{r} - \frac{eB}{\gamma m} v_\varphi. \tag{2.52}$$

In the $z = 0$ plane, the magnetic field is directed radially inward and is again normal to the electron motion: the particle moves in a circle of constant radius. This means that $\dot{r} = \ddot{r} = 0$ and, according to Equation 2.52, the outward centrifugal force is exactly balanced by the focusing force

$$\frac{v_\varphi^2}{r_g} \;=\; \frac{eB}{\gamma m} v_\varphi \Longrightarrow$$

$$r_g \;=\; \frac{\gamma m}{eB} v_\varphi \;=\; \frac{v_\varphi}{\omega_g}, \tag{2.53}$$

and

$$\omega_g = \frac{eB}{\gamma m}. \tag{2.54}$$

r_g is known as the cyclotron radius or gyroradius and ω_g is the angular frequency of rotation of the electron, called the cyclotron frequency or gyrofrequency. By combining the electron motion in the z direction with that in the x-y plane, we see that the particle orbit in a uniform magnetic field is a helix.

Chapter 3

Space-charge effects

In Chapter 2, we presented a review of single particle dynamics relevant to the two-stream instability problem. In this chapter, we cover space-charge effects due to the interaction between electrons. Section 3.1 discusses potential depression of an electron beam in a beam pipe. In Section 3.2, we give a quantitative analysis of space-charge waves supported by a focused electron beam. In addition, we introduce the plasma frequency reduction factor, F, which is used in Chapters 4, 6, and 7 to determine the theoretical gain of exponentially growing modes resulting from the interaction of two co-propagating electron beams. Finally, in Section 3.3, space-charge spreading and focusing are discussed.

3.1 Potential depression

The space charge of a charged particle beam propagating in a drift tube causes a potential distribution inside the tube. As a result, according to energy conservation, the kinetic energy of the beam will be reduced [9]. This is called potential or space-charge depression. In this section, we present a quantitative treatment of space-

charge depression for an electron beam of radius r_b inside a beam pipe of radius r_a and derive analytic expressions for the variation of the kinetic energy of the beam as a function of radial distance.

Consider a cylindrical electron beam of radius r_b propagating in a beam pipe of radius r_a. Let us determine the electric potential, Φ, both outside and inside the beam in the static case ($\partial/\partial t = 0$). Assuming that Φ is only a function of r, Poisson's equation in cylindrical coordinates becomes

$$\frac{1}{r}\frac{d}{dr}\left(r\frac{d\Phi}{dr}\right) = -\frac{\varrho}{\epsilon_0}, \tag{3.1}$$

where ϱ is the uniform volume charge density and ϵ_0 is the permittivity of free space. Outside the beam, $r > r_b$, the right-hand side of Equation 3.1 vanishes and we have

$$\frac{1}{r}\frac{d}{dr}\left(r\frac{d\Phi_{\rm out}}{dr}\right) = 0 \Longrightarrow$$

$$\Phi_{\rm out}(r) = C_1 \ln r + C_2, \tag{3.2}$$

where the integration constants C_1 and C_2 are determined by appropriate boundary conditions. Inside the beam, $r < r_b$ and $\varrho \neq 0$, Equation 3.1 may be simplified to give

$$\frac{d^2\Phi_{\rm in}}{dr^2} + \frac{1}{r}\frac{d\Phi_{\rm in}}{dr} = -\frac{\varrho}{\epsilon_0}. \tag{3.3}$$

Since Equation 3.3 does not contain the dependent variable explicitly, we can define a new variable Y such that

$$Y = \frac{d\Phi_{\rm in}}{dr} \Longrightarrow \frac{dY}{dr} = \frac{d^2\Phi_{\rm in}}{dr^2}. \tag{3.4}$$

Substituting Equation 3.4 into Equation 3.3, the latter becomes

$$\frac{dY}{dr} + \frac{1}{r}Y = -\frac{\varrho}{\epsilon_0}. \tag{3.5}$$

Equation 3.5 is a linear first-order ODE, whose solution is given by

$$Y(r) = -\frac{\varrho}{2\epsilon_0} r + \frac{D_1}{r}. \tag{3.6}$$

The solution to Equation 3.3 can now be found by integrating Equation 3.6 and reads

$$\Phi_{\text{in}}(r) = -\frac{\varrho}{4\epsilon_0} r^2 + D_1 \ln r + D_2, \tag{3.7}$$

where D_1 and D_2 are integration constants. At the center of the beam, where $r = 0$, the second term in Equation 3.7 becomes undefined, which means that D_1 needs to be set to zero and the electric potential inside the beam takes the form

$$\Phi_{\text{in}}(r) = -\frac{\varrho}{4\epsilon_0} r^2 + D_2. \tag{3.8}$$

To determine the rest of the integration constants, C_1, C_2, and D_2, three equations are necessary. We can obtain two of the required three equations by demanding that $\Phi_{\text{out}}(r)$ vanish on the beam pipe wall ($r = r_a$) and that $\Phi(r)$ must be continuous at the beam edge ($r = r_b$). Imposing the said boundary conditions at $r = r_a$ and $r = r_b$, we get

$$C_1 \ln r_a + C_2 = 0, \tag{3.9}$$

$$C_1 \ln r_b + C_2 = -\frac{\varrho}{4\epsilon_0} r_b^2 + D_2. \tag{3.10}$$

According to Gauss' law, the radial electric field outside the beam of length L is given by

$$\oint \vec{E} \cdot \vec{ds} = \frac{Q}{\epsilon_0} = \frac{\varrho}{\epsilon_0} \int dV \Longrightarrow$$

$$E_r = \frac{\varrho}{2\epsilon_0}\frac{r_b^2}{r}. \tag{3.11}$$

Expressing the volume charge density, ϱ, in terms of the beam current, I, and velocity, $v = \beta c$, Equation 3.11 becomes

$$E_r = \frac{I}{2\pi\epsilon_0\beta c r}. \tag{3.12}$$

Having determined the radial electric field, the remaining third equation may be written as

$$E_r = -\frac{d\Phi_{\text{out}}}{dr}. \tag{3.13}$$

Substituting Equations 3.12 and 3.2 into Equation 3.13 yields

$$C_1 = -\frac{I}{2\pi\epsilon_0\beta c}, \tag{3.14}$$

and, from Equation 3.9,

$$C_2 = \frac{I}{2\pi\epsilon_0\beta c}\ln r_a. \tag{3.15}$$

In view of Equations 3.14 and 3.15, the electric potential outside the beam is

$$\Phi_{\text{out}}(r) = \frac{I}{2\pi\epsilon_0\beta c}\ln\frac{r_a}{r}. \tag{3.16}$$

Solving Equation 3.10 for D_2 and using Equations 3.14 and 3.15, we have

$$D_2 = \frac{\varrho}{4\epsilon_0}r_b^2 + \frac{I}{2\pi\epsilon_0\beta c}\ln\frac{r_a}{r_b}. \tag{3.17}$$

With D_2 thus given, the electric potential inside the beam, Equation 3.8, becomes

$$\Phi_{\text{in}}(r) = \frac{I}{4\pi\epsilon_0 r_b^2\beta c}(r_b^2 - r^2) + \frac{I}{2\pi\epsilon_0\beta c}\ln\frac{r_a}{r_b}. \tag{3.18}$$

Equations 3.16 and 3.18, $\Phi_{\text{out}}(r)$ and $\Phi_{\text{in}}(r)$, are plotted in Figure 3.1 for a 0.7-mm and 0.3-A electron beam with the energy of 20 keV propagating in a 2-mm beam pipe. The potential variation from the vertical axis ($r = 0$) to the edge of the beam and from there to the beam pipe wall is shown by the solid ($\Phi_{\text{in}}(r)$) and dashed ($\Phi_{\text{in}}(r)$) curves, respectively. As required by the boundary conditions, $\Phi(r)$ is continuous at the beam edge and tends to zero on the beam pipe wall. From

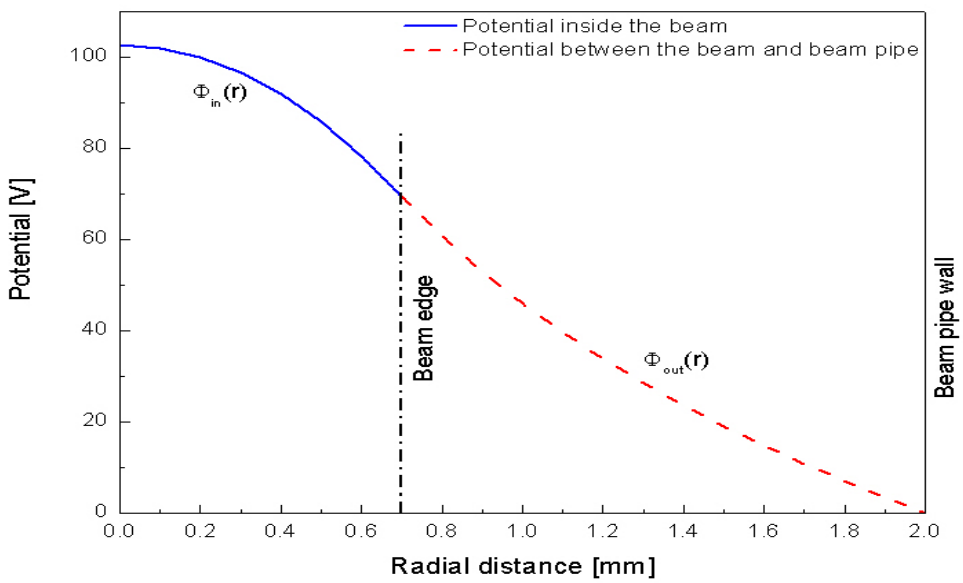

Figure 3.1: Variation of electric potential inside and outside of a 0.7-mm and 0.3-A electron beam propagating in a 2-mm beam pipe. The beam energy is 20 keV. $\Phi_{\text{in}}(r)$ is given by the solid line, whereas $\Phi_{\text{out}}(r)$ is represented by the dashed line.

energy conservation, the kinetic energy of the particles inside the pipe is

$$T(r) = T_0 - q\Phi(r), \tag{3.19}$$

where T_0 is the initial kinetic energy of the particles, at the entrance to the beam pipe, and $\Phi(r)$ is the electric potential. With the help of Equations 3.18 and 3.16,

the kinetic energy distribution within the beam ($T_{\text{in}}(r)$) and between the beam and the pipe ($T_{\text{out}}(r)$), respectively, has the form

$$T_{\text{in}}(r) = T_0 - \frac{qI}{2\pi\epsilon_0\beta c}\left\{\frac{r_b^2 - r^2}{2r_b^2} + \ln\frac{r_a}{r_b}\right\}, \tag{3.20}$$

$$T_{\text{out}}(r) = T_0 - \frac{qI}{2\pi\epsilon_0\beta c}\ln\frac{r_a}{r}. \tag{3.21}$$

Therefore, according to Equations 3.20 and 3.21, a potential distribution inside the beam pipe will reduce the kinetic energy. Equations 3.20 and 3.21 are plotted in Figure 3.2 for the same beam parameters as in Figure 3.1. As in the case of the

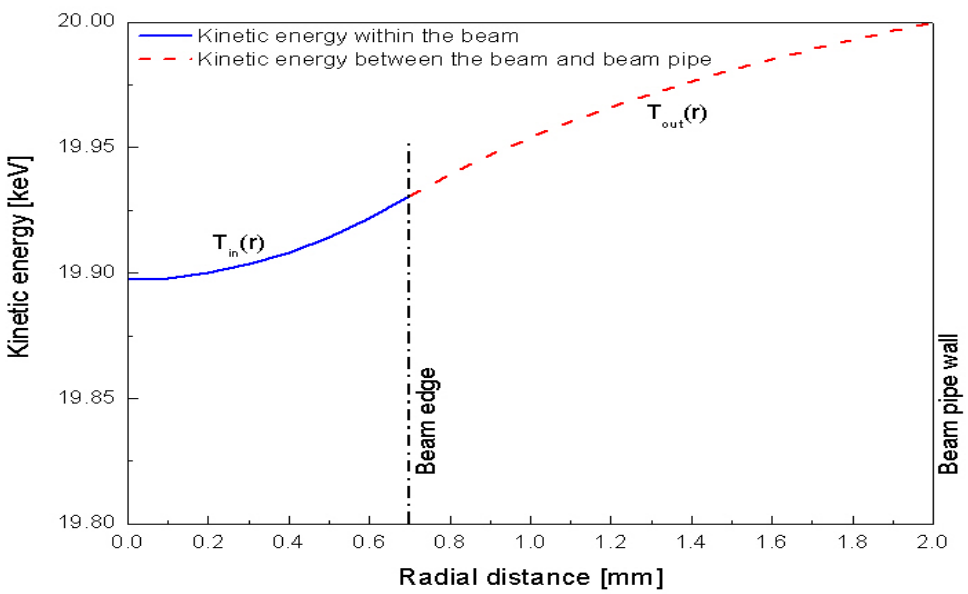

Figure 3.2: Kinetic energy distribution versus radial distance for the same beam as in Figure 3.1. $T_{\text{in}}(r)$ corresponds to the solid line, while $T_{\text{out}}(r)$ is represented by the dashed line.

electric potential in Figure 3.1, the variation of kinetic energy within the beam and between the beam and the beam pipe is shown by the solid and dashed lines,

respectively. The kinetic energy is continuous at the edge of the beam and tends to T_0 on the beam pipe wall.

In this dissertation, we study the interaction of two electron beams of radius r_b and energies E_1 and E_2 co-propagating in a beam pipe of radius r_a. In Chapter 4, a theoretical formula for the interaction frequency, f_{bunching}, of two electron beams is derived and it is shown that f_{bunching} is a function E_1 and E_2. According to Figure 3.2, space-charge depression will modify E_1 and E_2, which means that the interaction frequency of two beams will also be affected. A discussion of this issue is presented at the beginning of Chapter 6.

3.2 Space-charge waves on focused electron beams

In this section, we present a quantitative analysis of space-charge waves that can be supported by a focused (axially confined) electron beam of radius r_b propagating in a beam pipe of radius r_a. Space-charge waves are mainly longitudinal oscillations of the electrons and they interact with electromagnetic fields to produce amplification [15]. We examine two cases: 1) r_b and r_a are infinite, and 2) r_b and r_a are finite. It will be shown that in both cases we obtain slow and fast space-charge waves, whose velocities are slightly greater and less than the dc velocity of the beam. However, in the second case, the electron plasma frequency is reduced by a factor of F, where F is the space-charge reduction factor.

Consider a cylindrical electron beam of radius r_b propagating in a beam pipe of radius r_a. The uniform charge density and dc velocity are given by $-\varrho_0$ and $\vec{v_0} = v_0\hat{k}$. The dc current density, $J_0 = -\varrho_0 v_0$, is in the z direction and all dc quantities are independent of time and spatial coordinates. Their ac counterparts, ϱ, v_z, and J_z, are functions of spatial coordinates and time and have $e^{j(\omega t - kz)}$ dependences, where k is a yet-to-be-determined propagation constant. For our analysis, in addition to

Maxwell's equations (Equations 2.2 – 2.5), we will need the following set of equations:

$$\vec{\nabla} \cdot \vec{J} = -\frac{\partial \varrho}{\partial t}, \tag{3.22}$$

$$\frac{d\vec{v}}{dt} = -\eta\vec{E} - \eta\vec{v} \times \vec{B}_0, \tag{3.23}$$

$$\vec{J}_0 + \vec{J} = (\varrho - \varrho_0)(\vec{v_0} + \vec{v}), \tag{3.24}$$

where Equations 3.22 and 3.23 are the continuity and Lorentz force equations, while Equation 3.24 is the total current density and $\eta = q/m$ in Equation 3.23. The left-hand side of Equation 3.23 can be expanded as [15]

$$\frac{d\vec{v}}{dt} = \frac{\partial\vec{v}}{\partial t} + \frac{\partial\vec{v}}{\partial x}\frac{dx}{dt} + \frac{\partial\vec{v}}{\partial y}\frac{dy}{dt} + \frac{\partial\vec{v}}{\partial z}\frac{dz}{dt} = \frac{\partial\vec{v}}{\partial t} + [(\vec{v_0} + \vec{v}) \cdot \vec{\nabla}](\vec{v_0} + \vec{v}),$$

which, on neglecting the second-order term, $(\vec{v} \cdot \vec{\nabla})\vec{v}$, becomes

$$\frac{d\vec{v}}{dt} = \frac{\partial\vec{v}}{\partial t} + [\vec{v_0} \cdot \vec{\nabla}]\vec{v}. \tag{3.25}$$

Substituting Equation 3.25 into Equation 3.23 and assuming a large $\vec{B_0}$ (no transverse velocity components), the axial component of Equation 3.23 yields

$$\frac{\partial v_z}{\partial t} + v_0\frac{\partial v_z}{\partial z} = -\eta E_z - \eta\overbrace{(\vec{v} \times \vec{B_0})_z}^{=0}.$$

Differentiating v_z with respect to time and z (recalling that v_z is proportional to $e^{j(\omega t - kz)}$)

$$v_z = -\frac{\eta E_z}{j(\omega - kv_0)}. \tag{3.26}$$

Writing Equations 3.22 and 3.24 in component form, we get

$$J_z = \frac{\omega}{k}\varrho, \tag{3.27}$$

$$J_0 = -\varrho_0 v_0, \tag{3.28}$$

and

$$J_z = \varrho v_0 - \varrho_0 v_z, \tag{3.29}$$

where the second-order term, ϱv_z, has been neglected. With the help of Equations 3.26, 3.27 and 3.29, ϱ can be written in terms of E_z as

$$\varrho = \frac{\varrho_0 k\eta}{j(\omega - kv_0)^2} E_z. \tag{3.30}$$

Substituting Equation 3.30 into Equation 3.27, J_z can likewise be expressed as a function of E_z

$$J_z = \frac{\varrho_0 \omega\eta}{j(\omega - kv_0)^2} E_z. \tag{3.31}$$

Having derived Equations 3.30 and 3.31, we could combine them with Maxwell's equations and seek wave solutions. However, we will take a different approach [15] and use the vector potential, $\vec{A}$, which satisfies the inhomogeneous Helmholtz equation [15]

$$\nabla^2 \vec{A} + k_0^2 \vec{A} = -\mu_0 \vec{J}, \tag{3.32}$$

and is related to $\vec{E}$ and $\vec{H}$ as follows

$$\vec{H} = \frac{1}{\mu_0} \vec{\nabla} \times \vec{A}, \tag{3.33}$$

$$\vec{E} = -j\omega \vec{A} + \frac{\vec{\nabla}(\vec{\nabla} \cdot \vec{A})}{j\omega\mu_0\epsilon_0}, \tag{3.34}$$

where k_0 in Equation 3.32 is the free-space wavenumber and $k_0 = \omega\sqrt{\mu_0\epsilon_0}$. Assuming azimuthal symmetry, all boundary conditions can be satisfied by the z component of $\vec{A}$, where [15]

$$A_z(r,z) \;=\; \xi(r)e^{-jkz}. \tag{3.35}$$

Taking the z component of Equation 3.34

$$E_z \;=\; -\frac{j}{\omega\mu_0\epsilon_0}(k_0^2 - k^2)A_z. \tag{3.36}$$

Solving Equation 3.31 for E_z, putting the result in Equation 3.36 and multiplying both sides by μ_0, we get

$$\mu_0 J_z \;=\; -\left(\frac{\omega_p}{\omega}\right)^2 k_0^2 \left\{\frac{k_0^2 - k^2}{(k_0 - k)^2}\right\} A_z, \tag{3.37}$$

where $\omega_p^2 = \eta\varrho/\epsilon_0$ is the electron plasma frequency and $k_0 = \omega/v_0$. Writing the z component of the Helmholtz equation in cylindrical coordinates and substituting Equation 3.37 yields

$$\frac{1}{r}\frac{\partial}{\partial r}\left(r\frac{\partial A_z}{\partial r}\right) + \overbrace{\frac{\partial^2 A_z}{\partial z^2}}^{=\,-k^2 A_z} + k_0^2 A_z \;=\; \left(\frac{\omega_p}{\omega}\right)^2 k_0^2 \left\{\frac{k_0^2 - k^2}{(k_0 - k)^2}\right\} A_z \Longrightarrow$$

$$\frac{1}{r}\frac{\partial}{\partial r}\left(r\frac{\partial \xi(r)}{\partial r}\right) - (k^2 - k_0^2)\left\{1 - \left(\frac{\omega_p}{\omega}\right)^2 \frac{k_0^2}{(k_0 - k)^2}\right\}\xi(r) \;=\; 0. \tag{3.38}$$

Inside the beam, $0 \le r \le r_b$, Equation 3.38 takes the form

$$\frac{1}{r}\frac{\partial}{\partial r}\left(r\frac{\partial \xi(r)}{\partial r}\right) + p^2\xi(r) \;=\; 0, \tag{3.39}$$

where

$$p^2 \;=\; -(k^2 - k_0^2)\left\{1 - \left(\frac{\omega_p}{\omega}\right)^2 \frac{k_0^2}{(k_0 - k)^2}\right\}, \tag{3.40}$$

while in the region between the beam and beam pipe, $r_b \leq r \leq r_a$, it reduces to

$$\frac{1}{r}\frac{\partial}{\partial r}\left(r\frac{\partial \xi(r)}{\partial r}\right) - h^2\xi(r) \;=\; 0, \tag{3.41}$$

where

$$h^2 \;=\; k^2 - k_0^2. \tag{3.42}$$

Our next task is to solve Equations 3.39 and 3.41 subject to the appropriate boundary conditions. First consider the case of an infinitely large beam and beam pipe. When r_a and r_b tend to infinity, A_z is no longer a function of the transverse coordinate, r, and Equations 3.39 and 3.41 become (assuming a nontrivial solution, $A_z \neq 0$)

$$p^2 \;=\; 0 \quad \text{and} \quad h^2 \;=\; 0.$$

According to Equations 3.40 and 3.42, the above expressions yield the following four roots

$$k \;=\; \pm k_0, \tag{3.43}$$

$$k \;=\; k_0\left(1 \pm \frac{\omega_p}{\omega}\right). \tag{3.44}$$

Equation 3.43 represents traveling wave solutions, whereas Equation 3.44 corresponds to space-charge waves. As will be shown in Chapters 6 and 7, the interaction frequencies considered are in the range from 30 GHz to 1 THz. Taking a typical 0.7-mm and 20-keV beam, the ratio of ω_p to ω (for 30 GHz) is about 0.04 and 0.05 for 0.3 A and 0.5 A, respectively. This enables us to expand Equation 3.44 in a binomial series

$$v \;=\; \frac{\omega}{k} \;=\; \frac{\omega}{k_0}\left(1 \pm \frac{\omega_p}{\omega}\right)^{-1} \approx v_0\left(1 \mp \frac{\omega_p}{\omega}\right). \tag{3.45}$$

To estimate the error incurred in approximating v by Equation 3.45, we need to consider the next term, $(\omega_p/\omega)^2$, in the series. Using the same beam parameters as above, it can be shown that the error is about 0.1% and 0.2% for 0.3 A and 0.5 A, respectively. According to Equation 3.45, the wave velocities are slightly greater and less than the dc velocity of the beam. Hence, the solutions given by Equation 3.44 are referred to as fast and slow space-charge waves.

In the case of finite r_b and r_a, Equation 3.39 may be rewritten to read

$$r^2\frac{\partial^2\xi}{\partial r^2} + r\frac{\partial\xi}{\partial r} + p^2r^2\xi \;=\; 0. \tag{3.46}$$

Equation 3.46 is Bessel's equation of order zero and has the solution [17]

$$\xi(r) \;=\; A_1J_0(pr) + A_2Y_0(pr), \tag{3.47}$$

where $J_0(pr)$ and $Y_0(pr)$ represent the Bessel functions of the first and second kind, respectively. Since the region of interest ($0 \le r \le r_b$) contains the origin, where $Y_0(pr)$ becomes undefined, the constant A_2 in Equation 3.47 needs to be set to zero and

$$\xi(r) \;=\; A_1J_0(pr), \quad 0 \le r \le r_b. \tag{3.48}$$

Equation 3.41, which looks identical to Equation 3.46 except for the minus sign, is easily reduced to the modified Bessel equation of order zero and admits the solution [17]

$$\xi(r) \;=\; B_1I_0(hr) + B_2K_0(hr), \quad r_b \le r \le r_a, \tag{3.49}$$

where $I_0(hr)$ and $K_0(hr)$ are the modified Bessel functions of the first and second kind, respectively. To determine the arbitrary constants A_1, B_1, and B_2, three equations are required and we can generate those by imposing the appropriate boundary

conditions on the longitudinal and transverse filed components. Expressing Equations 3.33 and 3.34 in component form, we have

$$H_\phi = \frac{1}{\mu_0}\left(\frac{\partial A_r}{\partial z} - \frac{\partial A_z}{\partial r}\right) = -\frac{1}{\mu_0}\frac{\partial A_z}{\partial r}, \tag{3.50}$$

and

$$E_r = -j\omega A_r + \frac{1}{j\omega\mu_0\epsilon_0}\frac{\partial}{\partial r}\left(\frac{\partial A_z}{\partial z}\right) = -\frac{k}{\omega\mu_0\epsilon_0}\frac{\partial A_z}{\partial r}. \tag{3.51}$$

Thus, H_ϕ and E_r are the nonzero field components that are present in addition to E_z. We are now in a position to determine A_1, B_1, and B_2 by requiring that: a) E_z vanish on the beam pipe wall ($r = r_a$), and b) E_z and E_r (or H_ϕ) be continuous at the edge of the beam ($r = r_b$). After some algebraic manipulations, we arrive at the following set of linear equations involving A_1, B_1, and B_2:

$$\begin{aligned} J_0(pr_b)A_1 - I_0(hr_b)B_1 - K_0(hr_b)B_2 &= 0 \\ 0A_1 - I_0(hr_a)B_1 - K_0(hr_a)B_2 &= 0. \\ pJ_0'(pr_b)A_1 - hI_0'(hr_b)B_1 - hK_0'(hr_b)B_2 &= 0 \end{aligned} \tag{3.52}$$

This system will admit a nontrivial solution if and only if the determinant of the coefficient matrix vanishes. Setting the determinant of the coefficient matrix equal to zero and performing some algebraic manipulations, we have

$$p\frac{J_0'(pr_b)}{J_0(pr_b)} = h\frac{K_0(hr_a)I_0'(hr_b) - K_0'(hr_b)I_0(hr_a)}{K_0(hr_a)I_0(hr_b) - K_0(hr_b)I_0(hr_a)}. \tag{3.53}$$

Equation 3.53 is transcendental and in general needs to be solved numerically. Nevertheless, we will first attempt to solve Equation 3.53 for a special case of the beam filling the beam pipe ($r_b = r_a$). Having accomplished that, Equation 3.53 will be solved for an arbitrary ratio of r_a to r_b.

Inverting Equation 3.53 and taking the limit as r_b tends to r_a, we get $J_0(pr_a) = 0$ and

$$p = \frac{p_{0m}}{r_a}, \tag{3.54}$$

where p_{0m} is the mth zero of J_0. Substituting Equation 3.54 into Equation 3.40, we have

$$\left(\frac{p_{0m}}{r_a}\right)^2 = (k_0^2 - k^2)\left\{1 - \left(\frac{\omega_p}{\omega}\right)^2 \frac{k_0^2}{(k_0 - k)^2}\right\}. \tag{3.55}$$

As was discussed above, ω_p is over a factor of 20 less than ω. Hence, $k \approx k_0$ and from Equation 3.44

$$k = k_0(1 + \delta), \tag{3.56}$$

where $\delta \ll 1$. Substituting Equation 3.56 into Equation 3.55 and solving for δ yields [15]

$$\delta = \pm \frac{\frac{\omega_p}{\omega}}{\sqrt{1 + \left(\frac{p_{0m}}{k_0 r_a}\right)^2}}. \tag{3.57}$$

With δ thus given, Equation 3.56 becomes [15]

$$k = k_0 \left\{1 \pm \frac{\frac{\omega_p}{\omega}}{\sqrt{1 + \left(\frac{p_{0m}}{k_0 r_a}\right)^2}}\right\} = k_0 \left\{1 \pm F\frac{\omega_p}{\omega}\right\}, \tag{3.58}$$

where F is called the space-charge reduction or plasma frequency reduction factor. Equation 3.58 looks almost identical to Equation 3.44 (infinitely large r_b and r_a), except that the electron plasma frequency is reduced by a factor of F. For the infinitely large r_b and r_a discussed earlier, F is unity and both E_r (Equation 3.51) and H_ϕ

(Equation 3.50) are zero. By contrast, due to the presence of the beam pipe and a new set of imposed boundary conditions, E_r and H_ϕ are no longer zero when r_b and r_a are both finite. This leads us to conclude that the reduction in plasma frequency for the beam of finite radius r_b results from transverse variations in the field (nonzero E_r and H_ϕ components).

When the beam radius r_b is different from the beam pipe radius r_a, the solution of Equation 3.53 is no longer trivial. Nevertheless, the propagation constant k can be expressed in terms of the plasma frequency reduction factor similar to Equation 3.58 and reads [15]

$$F = \frac{1}{\sqrt{1+\left(\frac{pr_b}{hr_b}\right)^2}}, \tag{3.59}$$

where h and p are determined by numerically solving Equation 3.53 for a given pipe-to-beam ratio. In this dissertation, we only treat nonrelativistic beams. Hence, $k^2 \gg k_0^2$ and $h^2 \approx k^2 \approx (\omega/v_0)^2$ (Equation 3.42). Equation 3.59 represents a plasma frequency reduction factor for finite r_b and r_a. The plot of F as a function of hr_b ($hr_b \approx \frac{\omega r_b}{v_0}$) is shown in Figure 3.3 for 5 different ratios of the beam pipe radius, r_a, to beam radius, r_b.

According to Figure 3.3, the smaller the ratio of r_a to r_b, the smaller the magnitude of F. For $hr_b = 0.1$, the reduction factor for the open squares ($r_a/r_b = 1$) is approximately 54% less than that for the stars ($r_a/r_b = 4$). The percent difference between the former and the latter decreases to about 33% for $hr_b = 1.0$. For values of hr_b greater than or equal to 6.0, as can be seen in Figure 3.3, the curves become indistinguishable and asymptotically approach unity, which is the same value as that for the ratio of r_a to r_b when both tend to infinity.

The plasma reduction factor plotted in Figure 3.3 is used in Chapter 4 to calculate the theoretical gain (Equation 4.38) of exponentially growing modes resulting from

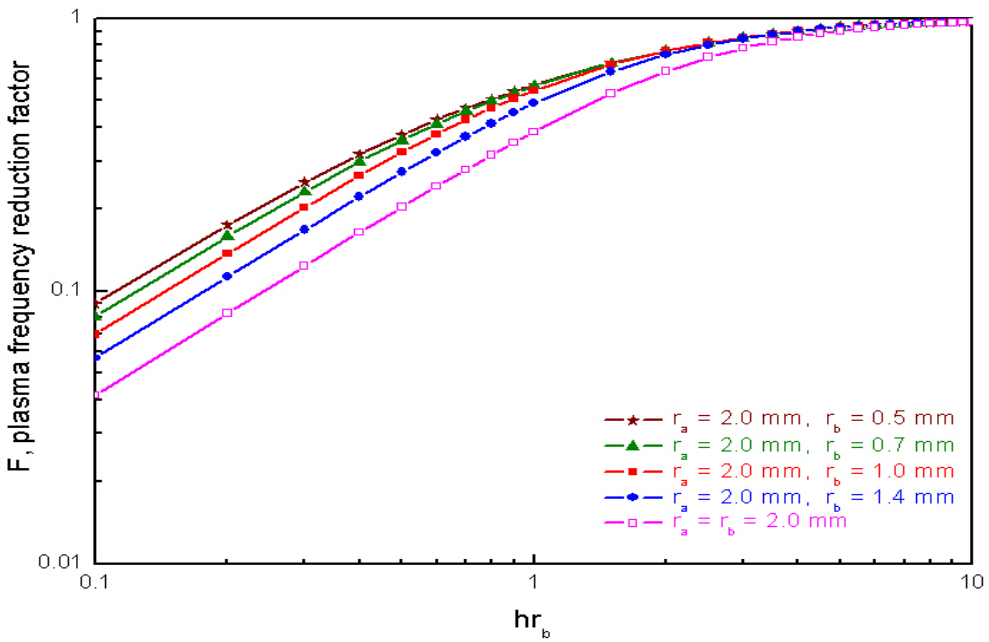

Figure 3.3: Plasma frequency reduction factor versus hr_b for 5 different pipe-to-beam ratios. r_a is kept fixed at 2 mm, while r_b is 0.5 mm (stars), 0.7 mm (triangles), 1.0 mm (solid squares), 1.4 mm (circles), and 2.0 mm (open squares).

the interaction of two electron beams of radius r_b. Moreover, Equation 4.38 is used extensively in Chapters 6 and 7 to make a comparison between theory and simulations involving the interaction of two beams at frequencies ranging from 30 GHz up to and including 1 THz. It should be noted that in the case of two co-propagating and interacting beams of radius r_b, v_0 in hr_b (the abscissa of Figure 3.3) becomes $\bar{v}$, where $\bar{v}$ is the average velocity of two beams.

3.3 Space-charge spreading and beam focusing

Typical microwave sources use high-density electron beams and space-charge spreading due to mutual repulsion of individual electrons is always a concern [16]. A com-

mon way to prevent space-charge spreading and to confine beams is to use a magnetic field parallel to the direction of motion. This can be accomplished with the help of a solenoid. Two well-known focusing techniques that use axial magnetic fields for radial confinement are called immersed flow and Brillouin flow. In the former, the solenoid surrounds both the source of electrons and the tube. Electrons start to traverse helical paths as they intersect magnetic flux lines, the deviations from the equilibrium radius being inversely proportional to the applied magnetic field. The disadvantage of the this technique is that in theory an infinite magnetic field is required to eliminate radial excursions [16].

As opposed to immersed flow focusing, in Brillouin flow focusing the source is

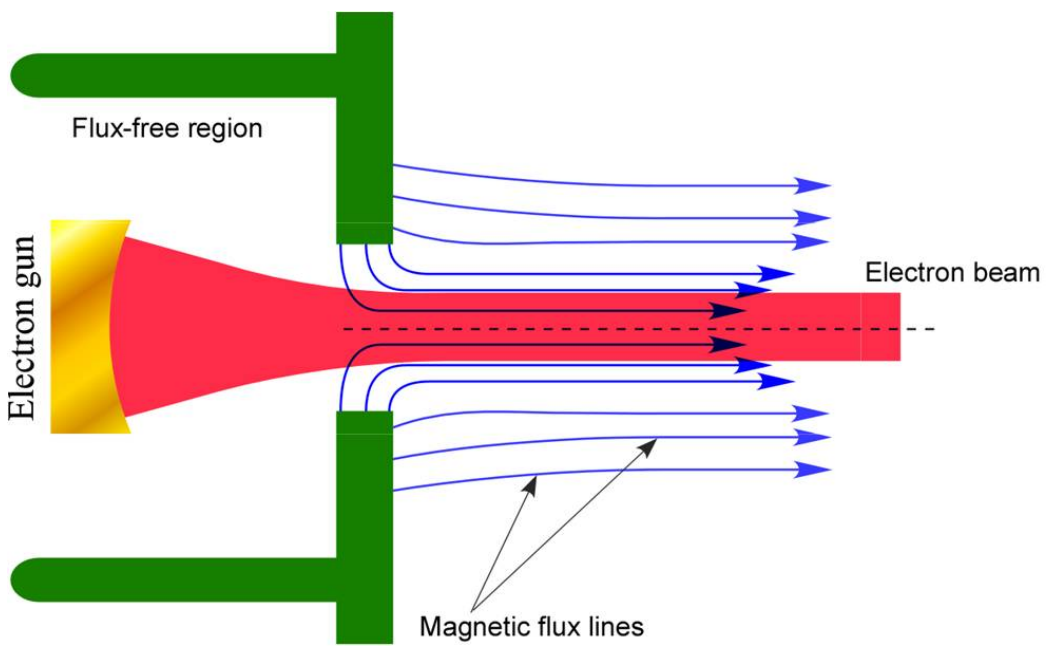

Figure 3.4: Setup for Brillouin flow focusing [12].

shielded from the external magnetic field as shown in Figure 3.4. The beam here first interacts with the predominantly radial component of the field at the entrance to the focusing structure. Having acquired an angular velocity, the electrons start to follow helical trajectories about the axis of the solenoid. As the rotating beam

interacts with the predominantly axial component of the focusing field, each of the electrons in the beam begins to experience an inward radial focusing force in addition to a centrifugal one. If the magnitude of the external magnetic field and the beam radius are adjusted such that there is a balance between the focusing and defocusing forces, then the beam will maintain constant radius as it propagates. Brillouin flow focusing is discussed in the next two subsections.

In the next subsection, we explore Equation 2.14, the radial equation of motion, in the presence of an axial focusing filed. In Subsection 3.3.2, we write an approximate solution to a beam envelope equation, which is the same as the radial equation of motion at the edge of an electron beam. In Subsection 3.3.3, approximate and numerical solutions to the beam envelope equation are compared with simulations.

3.3.1 Radial equation of motion in the presence of a focusing solenoid

Consider a nonrelativistic electron beam of radius r_b moving in the z direction with uniform velocity βc. Space-charge spreading is counteracted by an axial magnetic field whose magnitude is B_z. The radial component of the equation of motion, Equation 2.14, is modified as

$$m\ddot{r} = qE_r + qv_\varphi B_z - qv_z B_\varphi + \frac{mv_\varphi^2}{r} + F_{\text{dia}}, \tag{3.60}$$

where F_{dia} is due to the rotation of the beam and is given by [24]

$$F_{\text{dia}} = \frac{q^3 \mu_0 B_z^2 \varrho}{8m^2}(r_b^2 r - r^3), \tag{3.61}$$

where ϱ is the volume charge density and μ_0 is the permeability of free space. In Equation 3.60, the first and third terms are directed radially outward and cause

the beam to spread. By contrast, the second and fourth terms are directed radially inward, towards the axis of the beam, and keep the beam from spreading. By combining the first and third terms, we have

$$F_{\text{sc}} = qE_r - qv_z B_\varphi. \tag{3.62}$$

The sum of the second and fourth terms yields

$$F_{\text{focusing}} = qv_\varphi B_z + \frac{mv_\varphi^2}{r}. \tag{3.63}$$

In Equations 3.62 and 3.63, F_{sc} and F_{focusing} are the space-charge and focusing forces, respectively [24]. To solve Equation 3.60, we make the following simplifying assumptions:

1. Paraxial approximation: v_r, $v_\varphi \ll v_z = \beta c$.
2. Charge density, ϱ, is uniform over the beam cross-section. J, ϱ, and v_z are independent of r.
3. External magnetic field is uniform inside the tube: $B_z(r, z) = B_z(0, z) = B$.
4. The cathode is shielded from the external magnetic field. Electrons are born with zero initial transverse velocity components (in other words, zero canonical angular momentum).

Combining Assumption 2 with Ampere's law and Poisson's equation, it is straightforward to show that B_φ and E_r are given as

$$B_\varphi = \frac{\mu_0 I}{2\pi r}\frac{r^2}{r_b^2}, \tag{3.64}$$

$$E_r = \frac{I}{2\pi\epsilon_0 r_b^2 \beta c} r, \tag{3.65}$$

where I is the total beam current and ϵ_0 is the permittivity of free space. From Busch's theorem, Equation 2.50, and Assumptions 3 and 4 it follows that ψ_0 (magnetic flux at the emitter) is zero and $\psi = \pi r^2 B$, where ψ is the magnetic flux away from the emitter. As a result, v_φ away from the emitter has the form

$$v_\varphi = -\frac{qB}{2m}r. \tag{3.66}$$

On substituting Equations 3.64 through 3.66 into Equations 3.62 and 3.63, F_{sc} and F_{focusing} become

$$F_{\text{sc}} = \frac{qI}{2\pi\epsilon_0 r_b^2 \beta c}r, \tag{3.67}$$

$$F_{\text{focusing}} = -\frac{q^2B^2}{4m}r. \tag{3.68}$$

With the expressions for F_{sc}, F_{focusing}, and F_{dia} determined, we are in a position to solve the radial equation of motion (Equation 3.60), which is nonlinear because F_{dia} is proportional to r^3. To simplify Equation 3.60 further, we will now compare the three forces for an equilibrium flow of a 1.0-mm and 1.0-A beam with a beam energy of 20 keV (typical parameters in dissertation). Plotted in Figure 3.5 are Equations 3.67, 3.68, and 3.61 as functions of radial distance, r, for the above beam parameters and an axial magnetic field of 0.065 T.

According to Figure 3.5, F_{dia} is about four orders of magnitude smaller than F_{sc} and F_{focusing} over the entire range shown. This means that the F_{dia} term is negligible and can be dropped from Equation 3.60. Hence, the radial equation of motion (Equation 3.60) may be rewritten as

$$\ddot{r} + \frac{q^2B^2}{4m^2}r - \frac{qI}{2\pi\epsilon_0 r_b^2 \beta c m}r = 0. \tag{3.69}$$

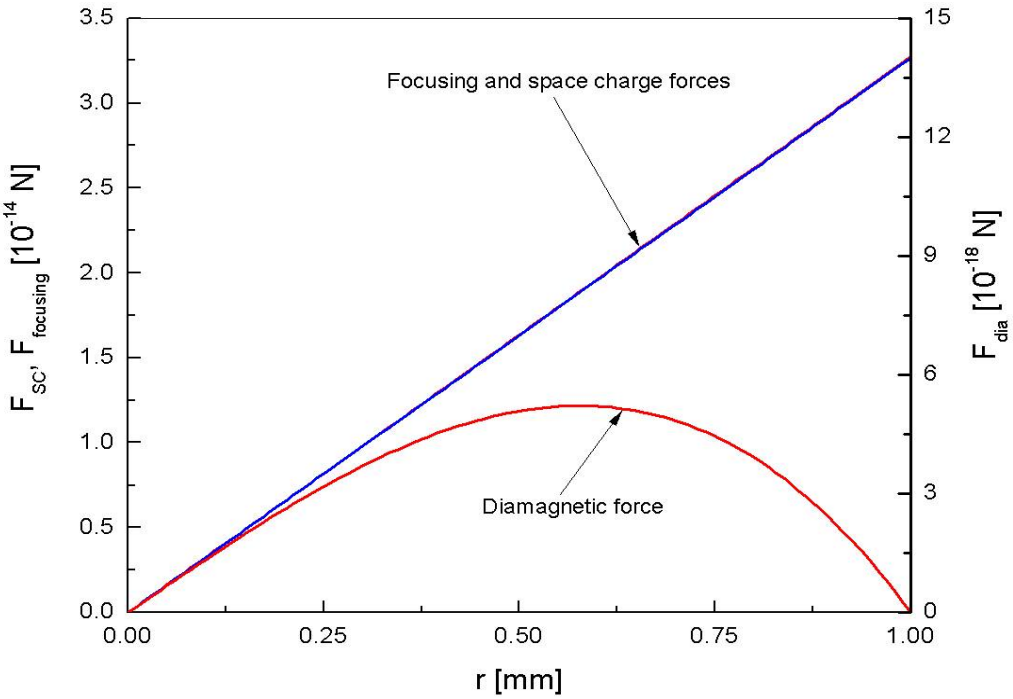

Figure 3.5: The variation of F_{sc}, F_{focusing}, and F_{dia} with radial distance, r.

In the next subsection, Equation 3.69 is solved for electrons on the outer edge of a beam and the beam envelope expression is derived for small deviations from its equilibrium radius.

3.3.2 Beam envelope equation for Brillouin flow

According to Equations 3.67 and 3.68, both F_{sc} and F_{focusing} are proportional to radial position. Consequently, the radial acceleration is proportional to radial position and the beam is laminar, which means that electron trajectories do not intersect [12]. Hence, the analysis to follow will apply equally well to electrons within the beam and at the edge of the beam. Let us examine and solve Equation 3.69 at the beam boundary, where $r = r_b$. If we replace r with r_b and define a new quantity r_{eq} such

that

$$r_{eq}^2\omega_L^2 \;=\; \frac{qI}{2\pi\epsilon_0\beta cm}, \tag{3.70}$$

where ω_L is equal to half the cyclotron frequency (qB/m) and is called the Larmor frequency, then Equation 3.69 can be rearranged to read [12]

$$\ddot{r_b} \;=\; -\omega_L^2\left(r_b - \frac{r_{eq}^2}{r_b}\right). \tag{3.71}$$

According to Equation 3.71, the right-hand side vanishes when $r_{eq} = r_b$. This situation represents a balance between the focusing and defocusing forces: electrons make no radial excursions and the beam maintains its shape as it travels downstream. Because of the nonlinear nature of Equation 3.71, we will now look for a solution that is slightly deviated from r_{eq}, the equilibrium radius, and has the form [12]

$$r_b \;=\; r_{eq}(1+\delta), \tag{3.72}$$

where $\delta \ll 1$. Substituting Equation 3.72 into Equation 3.71 and expanding the right-hand side in a binomial series, we get

$$\ddot{\delta} + 2r_{eq}\omega_L^2\delta \;=\; 0. \tag{3.73}$$

The general solution to Equation 3.73 is

$$\delta(t) \;=\; C_1\cos(\sqrt{2r_{eq}}\omega_L t) + C_2\sin(\sqrt{2r_{eq}}\omega_L t), \tag{3.74}$$

where C_1 and C_2 are constants. Substitution of Equation 3.74 into Equation 3.72 and some algebraic manipulations yield

$$r_b \;=\; r_{eq} + A\sin(\sqrt{2r_{eq}}\frac{\omega_L}{v_z}z + \psi), \tag{3.75}$$

where $A = r_{eq}\sqrt{C_1^2 + C_2^2}$ and $\psi = \tan^{-1}(C_1/C_2)$. Assuming that the beam enters the magnetic field at $z = 0$, where $r_b = r_{b0}$ and $dr_{b0}/dz = \tan(\vartheta)$, Equation 3.75 may be transformed as

$$r_b = r_{eq} + r_c \sin\left(\sqrt{2r_{eq}}\frac{\omega_L}{v_z}z + \tan^{-1}\left\{\frac{r_{b0} - r_{eq}}{\tan(\vartheta)/(\sqrt{2r_{eq}}\frac{\omega_L}{v_z})}\right\}\right), \tag{3.76}$$

where $r_c = \sqrt{(r_{b0} - r_{eq})^2 + ((\tan(\vartheta)v_z)/(\sqrt{2r_{eq}}\omega_L))^2}$.

According to Equation 3.76, for small deviations from the equilibrium radius r_{eq} (Equation 3.72), the beam envelope is a sinusoidal function. Therefore, its magnitude, phase, and shape are functions of initial conditions. If the beam's initial radius is $r_b(z = 0) = r_{eq}$ and it enters the magnetic field parallel to the z axis ($\tan(\vartheta) = 0$), then from Equation 3.76 it follows that the beam will maintain constant radius ($r_b = r_{eq}$) as it propagates. A beam emitted from a field-free cathode and undergoing this type of motion is called a Brillouin beam. The magnitude of the Brillouin magnetic field, B_{eq}, may be determined from Equation 3.70 and reads

$$B_{eq} = \sqrt{\frac{2mI}{\pi\epsilon_0\beta c q r_{eq}^2}}. \tag{3.77}$$

Increasing the current and decreasing the radius and velocity lead to more space charge. Hence, we require larger B_{eq} to keep the beam focused.

Equation 3.77 is used in all simulations presented in this dissertation with minor modifications. Specifically, I is replaced by the sum of the currents of two interacting electron beams. In addition, βc is replaced by the average velocity of two electron streams, $\bar{\beta}c$.

According to Equation 3.76, when the electron beam enters a focusing structure at a radius that is either greater or less than the equilibrium radius, the balance between focusing and defocusing forces no longer exists and the beam radius starts

to oscillate about the equilibrium value. This periodic variation of beam radius is called scalloping. It should be noted that, despite our efforts, we were unable to eliminate scalloping in simulations involving the interaction of two electron beams. However, the scalloping amplitude never exceeded 6% of the beams radius and, as shown in Appendix C, the gain was virtually unaffected.

3.3.3 Beam envelope equation versus simulations

In this subsection, we compare Equation 3.76 and a numerical solutions to the beam envelope equation (Equation 3.71) with simulations for a 1-A and 20-keV electron beam entering a focusing structure parallel to its axis. Recall that Equation 3.76 is also a solution to the beam envelope equation, but it is valid provided deviations from the equilibrium radius are small.

Shown in Figure 3.6 are Equation 3.76 (green triangles), a numerical solution to Equation 3.71 (red squares), and a 1-A and 20-keV electron beam from simulations (blue particles). The focusing magnetic field, B_{eq}, and the corresponding equilibrium beam radius, r_{eq}, from Equation 3.77 were 0.0695 T and 1 mm. In Figure 3.6, the initial radius, r_{b0}, was 0.8 mm and 1.1 mm for the top and bottom plots, respectively.

In the top plot, the initial beam radius, 0.8 mm, is less than the equilibrium radius, which is equal to 1.0 mm. Since there is more space charge than necessary for equilibrium flow, the magnitude of B_{eq} (0.0695 T) is not large enough to focus the beam. As a result, the beam scallops outward and begins to oscillate about the equilibrium radius in a sinusoidal fashion. In the bottom plot, the initial radius, 1.1 mm, is greater than the equilibrium radius, 1.0 mm, which means that the amount of space charge is less than that required for equilibrium flow. Consequently, the beam starts to scallop inward and then oscillates about the equilibrium radius, the shape of the beam envelope again being a sinusoid.

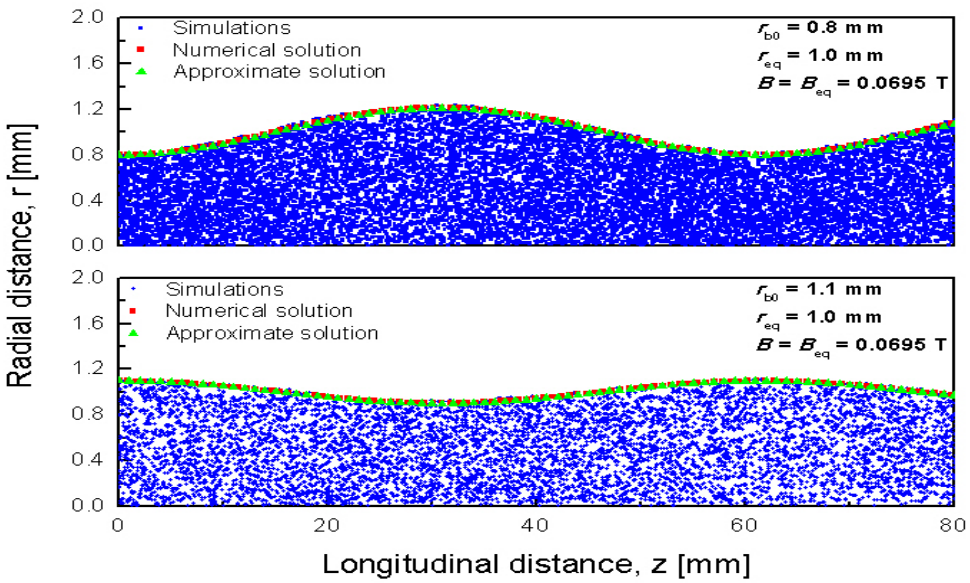

Figure 3.6: Comparison of approximate (triangles, Equation 3.76) and numerical (squares) solutions to Equation 3.71 with simulations (particles) for a 1-A and 20-keV electron beam. r_{b0} is 0.8 mm and 1.1 mm for the top and bottom plots. Also, $r_{eq} = 1.0$ mm and $B_{eq} = 0.0695$ T.

In Figure 3.6, r_{b0} and r_{eq} differ by 9.1% and by as much as 20% in the bottom and top plots, respectively. Nevertheless, the approximate (triangles) and numerical (squares) solutions in Figure 3.6 differ by less than 1%. Moreover, the former and the latter are within 2% of the edge of the beam (particles) from simulations. Hence, the agreement between theory and simulations is excellent. Note that if r_{eq} is kept at 1.0 mm and r_{b0} is chosen to be 1.4 mm ($\approx$ 28.6% difference), the largest percent deviation between the approximate (triangles) and numerical (squares) solutions in Figure 3.6 increases from less than 1% to about 8.9%. Hence, the larger the deviation between r_{eq} and r_{b0}, the poorer the agreement between the approximate and numerical solutions to the beam envelope equation (Equation 3.71).

Chapter 4

A small-signal derivation of the two-stream instability

The two-stream instability is a well-known phenomenon and it falls into the category of longitudinal instabilities, which cause randomization of the axial velocity distribution of a charged particle beam [25]. This phenomenon may be caused, for instance, by counter-propagating or co-propagating electron beams. As the beams flow through each other, free energy is available to cause axial bunching of the beams. This leads to a growing wave amplitude at the expense of the kinetic energy of the electrons. In this and subsequent sections we will show that, under the right conditions, the two-stream instability can be used to generate radiation in the millimeter and sub-millimeter range of the electromagnetic spectrum [1].

In Section 4.1, we use a small-signal theory to derive and solve a dispersion relation for a single electron beam of infinite cross section. The expressions for current density and volume charge density derived in Section 4.1 are used in Section 4.2 to solve a dispersion relation for the case of two co-propagating electron beams of infinite cross section. The focus is on complex conjugate roots that yield exponentially

growing and decaying solutions. The results obtained in Section 4.2 are employed in Section 4.3 for two co-propagating electron beams of finite cross section. Namely, we derive expressions for a velocity separation condition for maximum gain and the gain per unit length.

4.1 Dispersion relation for a single electron beam of infinite cross section

Let us consider a nonrelativistic electron beam of infinite cross section and use a small-signal analysis to derive linearized expressions for current and charge density. We start with the following equations

$$\vec{\nabla} \times \vec{E} = -\mu_0 \frac{\partial \vec{H}}{\partial t}, \tag{4.1}$$

$$\vec{\nabla} \times \vec{H} = -\vec{J} + \epsilon_0 \frac{\partial \vec{E}}{\partial t}, \tag{4.2}$$

$$\vec{\nabla} \cdot \vec{E} = -\frac{\varrho}{\epsilon_0}, \tag{4.3}$$

$$\vec{\nabla} \cdot \vec{J} = -\frac{\partial \varrho}{\partial t}, \tag{4.4}$$

$$\frac{d}{dt}(m\vec{v}) = -q\vec{E} - q\vec{v} \times \vec{B}, \tag{4.5}$$

$$\vec{J} = \varrho \vec{v}, \tag{4.6}$$

where Equations (4.1 – 4.3) represent Maxwell's equations, whereas Equations 4.4 and 4.5 are the continuity and Lorentz force equations. Also, ϵ_0 and μ_0 are the permittivity and permeability of free space, while ϱ is the volume charge density. In order to simplify the mathematics, we now make the following assumptions: a) Quantities can be written in terms of dc and ac parts, where dc components are denoted by the subscript 0 and ac components by the subscript z. b) There are no transverse variations and ac components are much smaller than dc components. c)

All ac quantities vary as $e^{j(\omega t - kz)}$. In view of the assumptions, Equations 4.4 and 4.6 become

$$\varrho_z = \frac{k}{\omega} J_z, \tag{4.7}$$

and

$$J_0 + J_z = (\varrho_0 + \varrho_z)(v_0 + v_z) = \varrho_0 v_0 + \varrho_0 v_z + \varrho_z v_0 + \varrho_z v_z \Rightarrow$$

$$J_0 = \varrho_0 v_0, \tag{4.8}$$

$$J_z = \varrho_0 v_z + \varrho_z v_0, \tag{4.9}$$

where we have neglected a second-order term $\varrho_z v_z$. Substituting Equation 4.7 into Equation 4.9, we have

$$J_z = \left\{ \frac{\omega \varrho_0}{\omega - k v_0} \right\} v_z. \tag{4.10}$$

Transforming Equation 4.5 and solving for v_z, we get

$$\frac{dv_z}{dt} = \frac{\partial v_z}{\partial t} + \frac{\partial v_z}{\partial z}\frac{dz}{dt} = -\frac{q}{m} E_z \Rightarrow$$

$$v_z = -\frac{\eta}{j(\omega - k v_0)} E_z, \tag{4.11}$$

where $\eta = q/m$. Let us now express J_z and ϱ_z in terms of E_z by first putting Equation 4.11 into Equation 4.10 and then substituting Equation 4.10 into Equation 4.7, to yield

$$J_z = j\omega\epsilon_0 \frac{\omega_p^2}{(\omega - k v_0)^2} E_z, \tag{4.12}$$

$$\varrho_z = jk\epsilon_0 \frac{\omega_p^2}{(\omega - k v_0)^2} E_z, \tag{4.13}$$

where $\omega_p^2 = \eta\varrho_0/\epsilon_0$ is the electron plasma frequency. Taking the curl of Equation 4.1 and substituting Equations 4.2 and 4.3, the linearized wave equation takes the form

$$\begin{aligned} \frac{\partial^2 E_z}{\partial z^2} - \epsilon_0\mu_0\frac{\partial^2 E_z}{\partial t^2} &= -\mu_0\frac{\partial J_z}{\partial t} - \frac{1}{\epsilon_0}\frac{\partial \varrho_z}{\partial z} \Rightarrow \\ (k^2 - k_0^2)E_z &= j\omega\mu_0 J_z - j\frac{k}{\epsilon_0}\varrho_z, \end{aligned} \tag{4.14}$$

where $k_0 = \omega/c$ is the free-space wavenumber. Combining Equations 4.12, 4.13, and 4.14, we obtain

$$(k^2 - k_0^2)\left\{1 - \frac{\omega_p^2}{(\omega - kv_0)^2}\right\}E_z = 0, \tag{4.15}$$

which has the following four solutions (assuming $E_z \neq 0$)

$$k = \pm\, k_0, \tag{4.16}$$

$$k = \frac{\omega}{v_0} \pm \frac{\omega_p}{v_0}. \tag{4.17}$$

Equation 4.16 corresponds to waves traveling in free space, while Equation 4.17 represents fast and slow space-charge waves.

4.2 Dispersion relation for two electron beams of infinite cross section

In this section, we are going to apply the results of Section 4.1 to derive a dispersion relation for the case of two co-propagating electron beams of infinite cross section and different velocity. By analyzing the solutions of the dispersion relation, we will identify a range of values for the velocity difference, plasma frequency, and wave number that yields growing waves.

In the case of two nonrelativistic electron beams of infinite cross section, J_z and ϱ_z are identical to those in Equations 4.12 and 4.13. This can be verified by writing Equations 4.7, 4.9, and the equation motion for each beam separately. Hence, for two electron beams of infinite cross section, the total ac current density and ac charge density read

$$J_z = j\omega\epsilon_0 \left(\frac{\omega_{1p}^2}{(\omega - kv_{10})^2} + \frac{\omega_{2p}^2}{(\omega - kv_{20})^2} \right) E_z, \tag{4.18}$$

$$\varrho_z = jk\epsilon_0 \left(\frac{\omega_{1p}^2}{(\omega - kv_{10})^2} + \frac{\omega_{2p}^2}{(\omega - kv_{20})^2} \right) E_z, \tag{4.19}$$

where ω_{1p} and ω_{2p} are plasma frequencies for the two beams and v_{10} and v_{20} are their dc velocities. Substituting Equations 4.18 and 4.19 into Equation 4.14, we obtain

$$(k^2 - k_0^2) \left\{ 1 - \frac{\omega_{1p}^2}{(\omega - kv_{10})^2} - \frac{\omega_{2p}^2}{(\omega - kv_{20})^2} \right\} E_z = 0. \tag{4.20}$$

Two solutions to Equation 4.20 can be written be inspection and they are $\pm k_0$. These are purely traveling waves and are the same as those in Equation 4.16. Setting the expression in curly braces to zero (assuming $E_z \neq 0$)

$$\omega_{1p}^2(\omega - kv_{20})^2 + \omega_{2p}^2(\omega - kv_{10})^2 = (\omega - kv_{10})^2(\omega - kv_{20})^2. \tag{4.21}$$

Equation 4.21 is extremely tedious to solve for an arbitrary set of beam parameters. Hence, we will limit our analysis to a special case when $\omega_{1p} = \omega_{2p} = \omega_p$. This will enable us to relate the beams' velocities and currents. To simplify Equation 4.21 more, let us define the following average and difference quantities

$$\bar{v} = \frac{v_{10} + v_{20}}{2}, \tag{4.22}$$

$$\Delta = \frac{v_{10} - v_{20}}{2}, \tag{4.23}$$

$$\Omega = \omega - k\bar{v}. \tag{4.24}$$

With the above definitions and some algebra, Equation 4.21 reduces to a quadratic equation with respect to Ω^2

$$\Omega^4 - 2\Omega^2(\omega_p^2 + k^2\Delta^2) + k^4\Delta^4 - 2k^2\Delta^2\omega_p^2 \;=\; 0, \tag{4.25}$$

which has the following roots

$$\Omega_1^2 \;=\; (\omega_p^2 + k^2\Delta^2)\left\{1 - \sqrt{1 + \frac{2k^2\Delta^2\omega_p^2 - k^4\Delta^4}{(\omega_p^2 + k^2\Delta^2)^2}}\right\}, \tag{4.26}$$

$$\Omega_2^2 \;=\; (\omega_p^2 + k^2\Delta^2)\left\{1 + \sqrt{1 + \frac{2k^2\Delta^2\omega_p^2 - k^4\Delta^4}{(\omega_p^2 + k^2\Delta^2)^2}}\right\}. \tag{4.27}$$

Letting $x = k\Delta/\omega_p$ and dividing Equations 4.26 and 4.27 through by ω_p

$$\frac{\Omega_1^2}{\omega_p^2} \;=\; (1 + x^2)\left\{1 - \sqrt{1 + \frac{2x^2 - x^4}{(1 + x^2)^2}}\right\}, \tag{4.28}$$

$$\frac{\Omega_2^2}{\omega_p^2} \;=\; (1 + x^2)\left\{1 + \sqrt{1 + \frac{2x^2 - x^4}{(1 + x^2)^2}}\right\}. \tag{4.29}$$

Equations 4.28 and 4.29 are plotted in Figure 4.1. Ω_1^2/ω_p^2 and Ω_2^2/ω_p^2 in Figure 4.1 are shown by the red and green curves. Equations 4.28 and 4.29 are solutions for an absolute instability (temporal growth): k is assumed to be fixed and real as we solve for an imaginary part of ω. In the present analysis, however, we are interested in a convective instability (spatial growth), which means that ω will be assumed to be fixed and real as we solve for an imaginary part of k [26].

In order to have a growing instability (exponentially growing solution), the wave number, k, in Equation 4.24 must have an imaginary part. Since ω and $\bar{v}$ in Equation 4.24 are assumed to be real quantities, k will be a complex number provided either Ω_1 or Ω_2 is imaginary. Ω_1 and Ω_2 will become complex if the right-hand sides of Equations 4.28 and 4.29 are negative for some values of $x = k\Delta/\omega_p$. According to

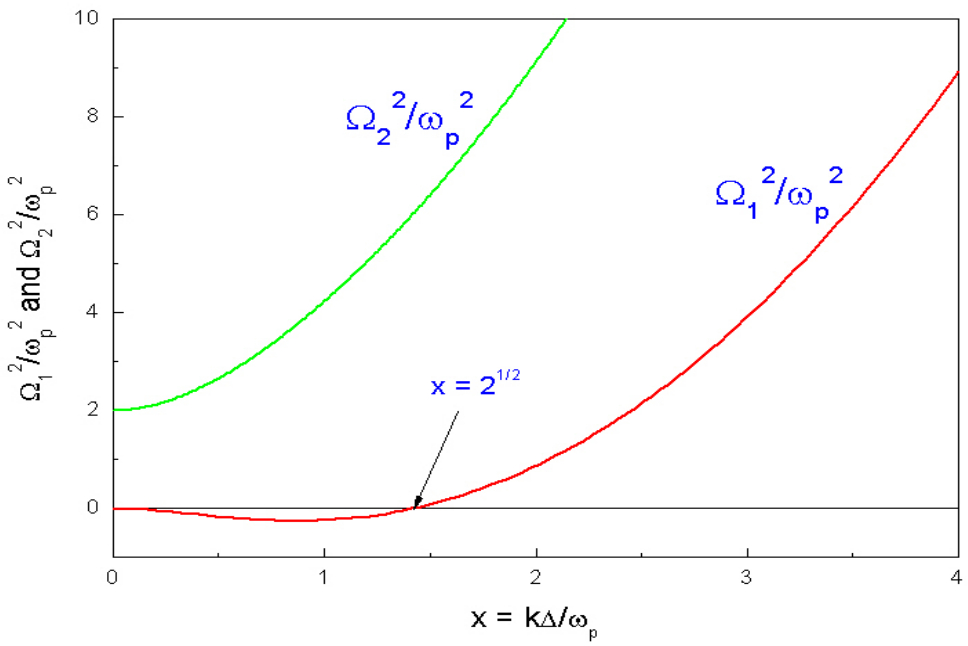

Figure 4.1: Roots of Equation 4.25 as a function of $x = k\Delta/\omega_p$. Ω_1^2/ω_p^2 is represented by the red curve, while Ω_2^2/ω_p^2 is given by the green curve.

Figure 4.1, Ω_2^2 is positive for all values of x. By contrast, as can be shown, Ω_1^2 can be negative when $0 < x < \sqrt{2}$. Hence, this condition on x determines whether or not there will be growing waves. Within the range $0 < x < \sqrt{2}$, Ω_1/ω_p becomes purely imaginary and reads

$$\mathrm{Im}\left(\frac{\Omega_1}{\omega_p}\right) = \pm\sqrt{(1+x^2)\left\{\sqrt{1+\frac{2x^2-x^4}{(1+x^2)^2}}-1\right\}}. \tag{4.30}$$

The plot of the absolute value of $\mathrm{Im}(\Omega_1/\omega_p)$ as a function of $x = k\Delta/\omega_p$ is shown in Figure 4.2. The dashed vertical line represents the value of x that maximizes $\mathrm{Im}(\Omega_1/\omega_p)$. In Figure 4.2, growing solutions can only be obtained for values of x lying within the endpoints of the curve. Outside the range shown in Figure 4.2, the only possible solutions are ordinary traveling waves that lead to zero growth.

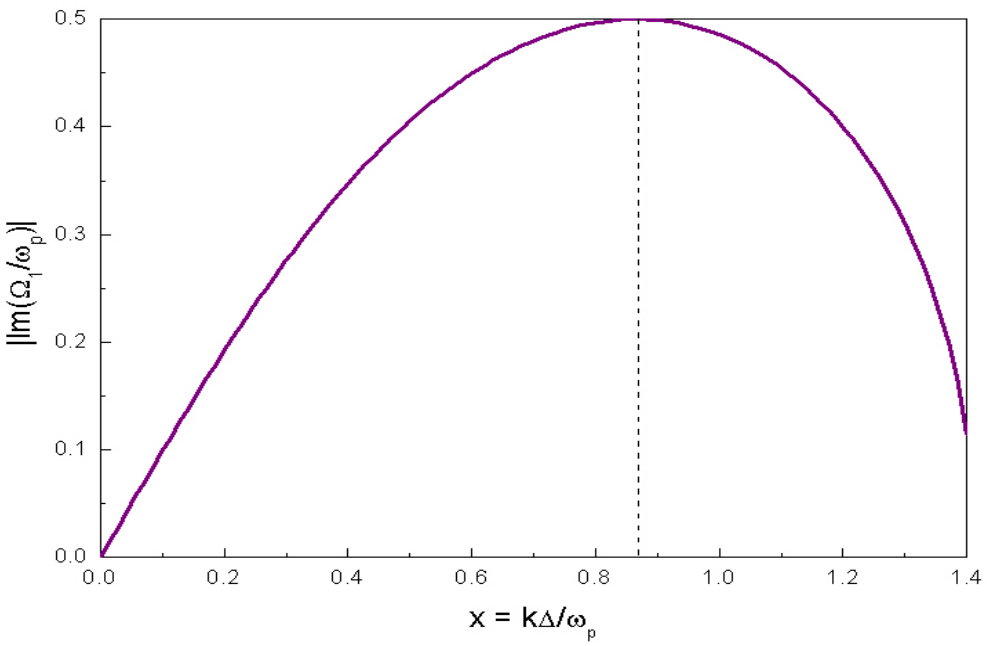

Figure 4.2: The variation of $|\mathrm{Im}(\Omega_1/\omega_p)|$ with $x = k\Delta/\omega_p$ over the range $0 < x < 1.4$.

According to Figure 4.2, growing solutions with the largest gain will be obtained when $\mathrm{Im}(\Omega_1/\omega_p)$ is equal to 0.5. Differentiating Equation 4.30 with respect to x and setting it equal to zero, we can determine the value of $x = k\Delta/\omega_p$ that maximizes $\mathrm{Im}(\Omega_1/\omega_p)$ and, therefore, yields the largest growth

$$\frac{d}{dx}\left(\mathrm{Im}\frac{\Omega_1}{\omega_p}\right) = 0 \Rightarrow$$

$$x_{\max} = \left(\frac{k\Delta}{\omega_p}\right)_{\max} = \frac{\sqrt{3}}{2}. \tag{4.31}$$

From the foregoing discussion, within the range $0 < x < \sqrt{2}$ and with $\mathrm{Im}(\Omega_1/\omega_p) = 0.5$, the wave number, k, from Equation 4.24 can be expressed as follows

$$k = \frac{\omega}{\bar{v}} \mp j\frac{\omega_p}{2\bar{v}}. \tag{4.32}$$

Earlier we assumed that all ac quantities vary with distance as e^{-jkz}. Hence, it is straightforward to show that the negative and positive imaginary parts in Equation 4.32 lead to decaying and growing waves, respectively.

4.3 Gain for two electron beams of finite cross section

In this section, our goal is to derive a theoretical formula for the gain of two co-propagating and interacting electron beams of radius of r_b. To do that, we will first use Equation 4.31 to determine a velocity separation, $\Delta_{\max}$, corresponding to maximum growth (gain).

In Chapters 6 and 7, we will be looking at the interaction of two electron beams at frequencies ranging from 30 GHz to 1 THz. It can be shown that ω is over an order of magnitude or more greater than ω_p for typical beam parameters used in this dissertation (Section 3.2). Hence, we can assume that the imaginary part of k in Equation 4.32 is much smaller than the real part. With this assumption, Equation 4.31 may be rewritten to give

$$\frac{\Delta_{\max}}{\bar{v}} = \frac{\sqrt{3}}{2}\frac{F\omega_p}{\omega} = \frac{\sqrt{3}}{2}\frac{F}{\omega}\sqrt{\frac{e\varrho_0}{m\epsilon_0}}, \tag{4.33}$$

where F is the plasma reduction factor given in Equation 3.58 and plotted in Figure 3.3. Equation 4.31 was derived for electron beams with infinite cross section. Therefore, the inclusion of F in Equation 4.33 is necessary to account for the fact that the beams under consideration are no longer infinitely wide. Figure 3.3, the plot of F, displayed in Section 3.2 will be used extensively in Chapters 6 and 7 to compare the theoretical gain derived in this section with that from simulations for different ratios of beam pipe radius, r_a, to beam radius, r_b.

The dc charge density, ϱ_0, in Equation 4.33 may be expressed in terms of the total beam current, I (the sum of the currents of two interacting beams), beam radius, r_b, and average velocity of two beams, $\bar{v} = \bar{\beta}c$, as

$$\varrho_0 = \frac{I}{2\pi r_b^2 \bar{\beta} c}, \tag{4.34}$$

where a factor of two in the denominator is introduced because of our assumption that $\omega_{1p} = \omega_{2p} = \omega_p$. Putting Equation 4.34 into Equation 4.33 and performing some algebraic manipulations, the expression for $\Delta_{\max}$ takes the form

$$\frac{\Delta_{max}}{\bar{v}} = F\sqrt{\frac{3I}{2\bar{\beta}I_A}}\frac{c}{\omega r_b}, \tag{4.35}$$

where $I_A = 4\pi\epsilon_0 mc^3/e \approx 17$ kA is the Alfvén current. Solving Equation 4.31 for ω_p and substituting Equation 4.35, we get

$$\frac{\omega_p}{\bar{v}} = F\sqrt{\frac{I}{2\bar{\beta}^3 I_A}}\frac{2}{r_b}. \tag{4.36}$$

With $\omega_p/\bar{v}$ given by Equation 4.36, the wave number, k, from Equation 4.32 becomes

$$k = \frac{\omega}{\bar{v}} \mp jF\sqrt{\frac{I}{2\bar{\beta}^3 I_A}}\frac{1}{r_b}. \tag{4.37}$$

Taking the imaginary part of k from Equation 4.37, the gain, G, over a distance L may be written as follows

$$G = 20\log e^{L\mathrm{Im}k} = 20F\frac{L}{r_b}\sqrt{\frac{I}{2\bar{\beta}^3 I_A}}\log e. \tag{4.38}$$

Equation 4.38 represents the theoretical gain of an exponentially growing mode resulting from the interaction of two electron beams of radius r_b, average velocity $\bar{\beta}c$, and total beam current I. According to Equation 4.38, the larger the beam current

and smaller the radius and average velocity, the higher the gain. To check the validity of Equation 4.38, in Chapters 5, 6, and 7 the theoretical gain will be compared with that obtained from simulations involving the interaction of monoenergetic electron beams of radius r_b.

If we consider the interaction of two 0.7-mm and 0.5-A beams with energies 20 keV and 16.95 keV (typical in this dissertation), it can be shown that G is given by 0.35 dB/mm. This value is over 10 times greater than that (0.03 dB/mm) reported by Chen et al. for a proposed two-stream relativistic klystron amplifier involving 1.0- and 5.0-kA annular relativistic electron beams [23]. Hence, the proposed source, shown in Figure 1.1, can indeed be a compact and inexpensive source of sub-mm and mm radiation.

In Chapters 6 and 7, we will be studying and analyzing two electron beams of radius r_b and energies E_1 and E_2 (velocities $\beta_1\, c$ and $\beta_2\, c$) co-propagating and interacting inside a beam pipe of radius r_a. The interaction frequency of the beams, their bunching frequency, is a crucial parameter along with the gain and may be derived from Equations 4.35 and 4.36 to yield

$$f_{\text{bunching}} \;=\; \frac{\sqrt{3}}{4\,\pi} F \left\{ \frac{0.5\, e\, I}{m\, \epsilon_0\, \pi\, r_b^2\, \bar{\beta}\, c} \right\}^{1/2} \left(\frac{\beta_1 + \beta_2}{\beta_1 - \beta_2} \right). \tag{4.39}$$

Hence, f_{bunching} depends on the total beam current, beam energies and their radii, and the plasma frequency reduction factor. Figure 4.3 shows f_{bunching} as a function of E_2 (energy of the second beam) for four different total beam currents, namely, 0.6 A (black curve), 1.0 A (blue curve), 1.5 A (red curve), and 2.0 A (green curve). The values of E_1, r_b, β_1 and β_2 used to plot Figure 4.3 were 20 kV, 0.7 mm, 0.27, and 0.265, respectively.

According to Figure 4.3, the larger the beam current and more energetic the beams are, the higher the interaction frequency. In addition, f_{bunching} increases

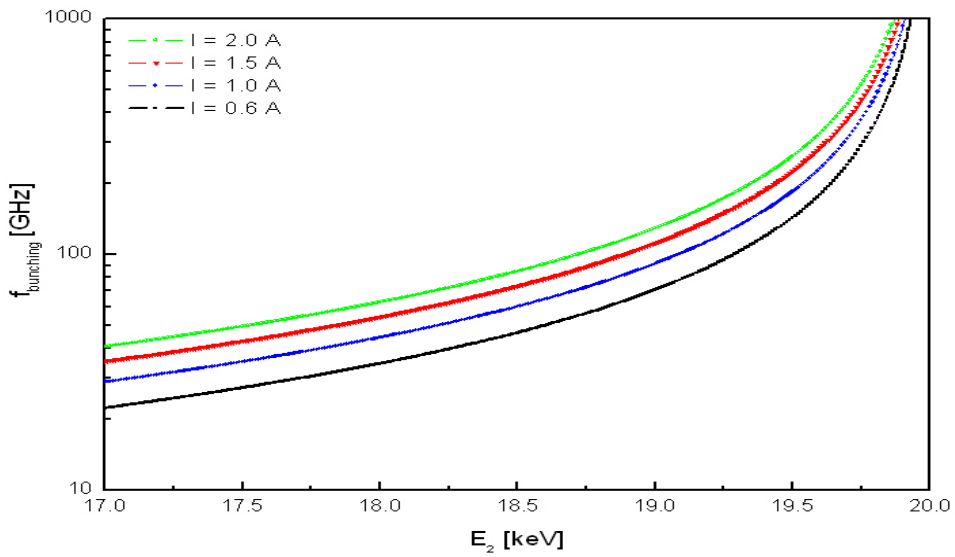

Figure 4.3: Bunching frequency as a function of E_2 (energy of the second beam). The total beam current, I, is 0.6 A (black curve), 1.0 A (blue curve), 1.5 A (red curve), and 2.0 A (green curve). Also, $E_1 = 20$ keV, $r_b = 0.7$ mm, $\beta_1 = 0.27$, and $\beta_2 = 0.265$.

with decreasing beam radius (more space charge). For all currents in Figure 4.3, the separation between the beam energies is largest at low interaction frequencies. Moreover, the higher the current, the larger ΔE is, where $\Delta E = E_1$ - E_2. Note that when the beam energies are equal, the denominator in Equation 4.39 is zero and the interaction frequency becomes undefined, but G tends to zero.

Equations 4.38 and 4.39 are the key analytic formulas in this dissertation. Even though Equation 4.38 does not contain frequency as a variable, G is an implicit function of frequency via the plasma frequency reduction factor. Throughout Chapters 6 and 7, the theoretical gain will be compared with numerical gain from simulations at different interaction frequencies to validate the 1-D theory presented in this chapter. The calculation of numerical gain is discussed in the next chapter.

Equation 4.39 will also be used extensively in Chapters 6 and 7 to predict the

bunching frequency at which two electron beams of given energies, currents, and radii will interact. Theoretical predictions will be compared with those from simulations to again check the validity of the small-signal theory in this chapter.

Chapter 5

Simulation setup

The focus of this dissertation is 2-D particle-in-cell (PIC) simulations of the interaction region of the potential two-beam source depicted in Figure 1.1. Section 5.1 discusses the simulation geometry in detail. In Section 5.2, we look at the propagation and interaction of two electron beams in the simulation structure and discuss some limitations imposed by the PIC code MAGIC. In addition, we present a brief quantitative treatment of various stability and accuracy criteria, such as the Courant stability, particle dynamics, spatial resolution, and aspect ratio requirements. Finally, Section 5.3 discusses the calculation of numerical gain.

5.1 Simulation geometry

The simulation setup, which was mentioned in Section 1.3, is shown in Figure 5.1. This particular setup is used for the majority of simulations involving the interaction of two electron beams. The geometry is described in terms of a cylindrical coordinate system. Since all simulations presented in this dissertation are in two dimensions, only the axial, z, and radial, r, coordinates are used. The 200-mm-long and 2.0-mm-

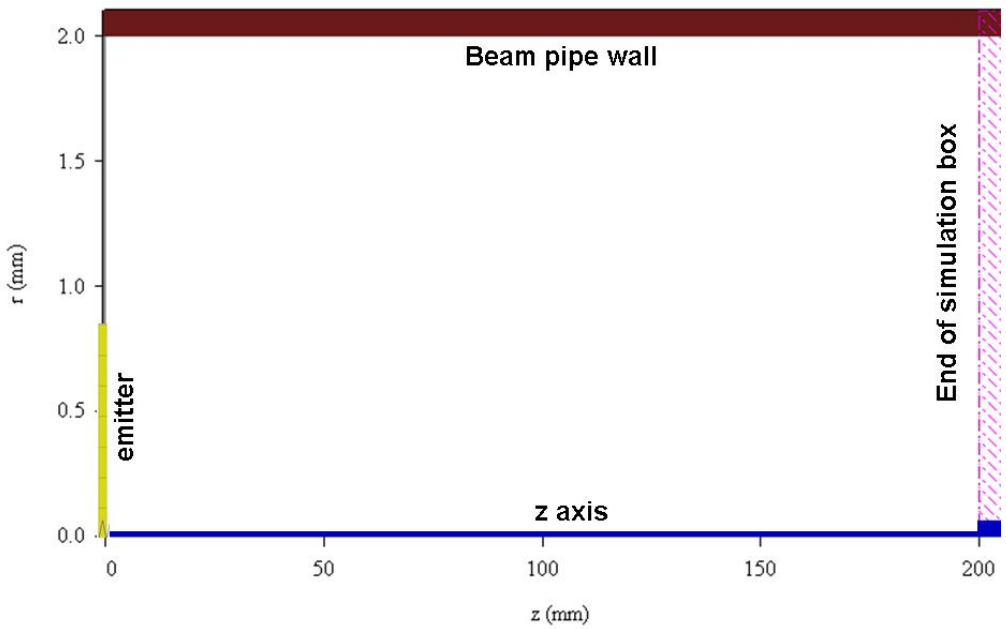

Figure 5.1: Side view of the simulation geometry.

radius structure is a circular beam pipe (perfect conductor) whose thickness is equal to dr, a cell size in the radial direction. Electron beams produced by the emitter travel downstream, from left to right. According to Appendix A, convergence with regard to dr requires that the number of emission cells be greater than or equal to four. Hence, the emitter always consists of four emission cells or more. The right end of the simulation geometry, labeled "end of simulation box", provides an outlet through which outgoing waves and particles exit the simulation box. To prevent space-charge spreading of emitted electron beams, the structure is surrounded by a solenoid (not shown). The magnetic field profile, plotted in Figure 5.2, is mathematically given by

$$B_z = B_0 \left\{ \frac{\pi}{2} \sin \left[\text{ramp} \left(\frac{z}{z_0} \right) \right] \right\}^2, \tag{5.1}$$

where $\text{ramp}\,(z/z_0) = \text{Max}\,[0, \text{Min}(1, z/z_0)]$, z_0 is the ramp length, and B_0 is the magnitude of the desired magnetic field given by Equation 3.77. Also, the function $\text{Max}\,[0, \text{Min}(1, z/z_0)]$ is the largest value of 0 or $\text{Min}(1, z/z_0)$, where $\text{Min}(1, z/z_0)$ is

the smallest value of 1 or z/z_0. In addition to B_z, the radial component of the mag-

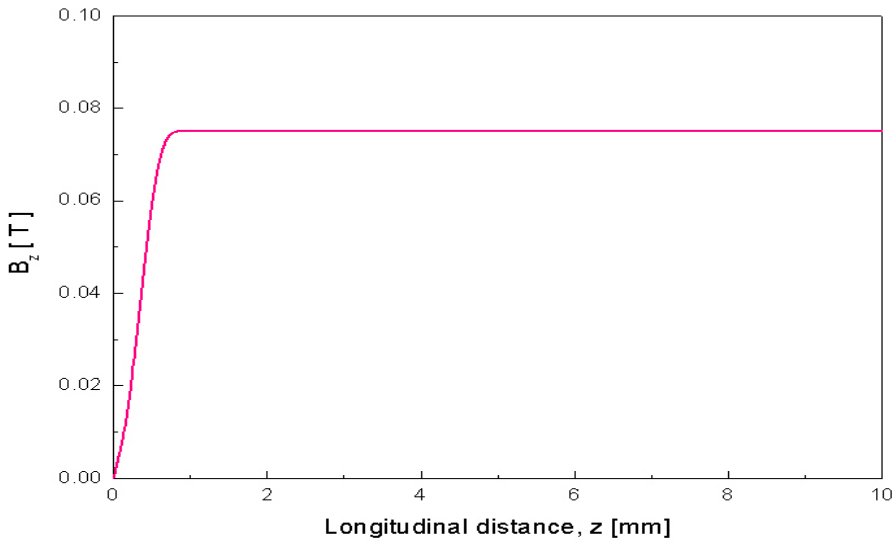

Figure 5.2: B_z component of the applied dc magnetic field, given by Equation 5.1, for $z_0 = 0.7\,\text{mm}$.

netic field, B_r, is defined to satisfy $\vec{\nabla} \cdot \vec{B} = 0$. The shape of the applied dc magnetic field in Figure 5.2 is identical to that for Brillouin flow focusing (Section 3.3): the emitter is shielded from the external field and electrons are born in a field-free region. The ramp length, z_0, in Equation 5.1 is set to 0.7 mm to minimize beam divergence before the electrons start to cross the magnetic flux lines.

Figure 5.3 displays a snapshot of two 0.7-mm and 0.3-A beams (the total beam current is 0.6 A) with energies 20 keV and 17.6 keV co-propagating and interacting in the simulation structure in Figure 5.1. The 20-keV beam is represented by the blue dots, while the 17.6 keV is shown by the red dots.

The length of the beams in Figure 5.3 is about half the size of the simulation geometry in Figure 5.1. This is due to a limitation of the present version of MAGIC used in this dissertation and will be explained in the next section. Also analyzed

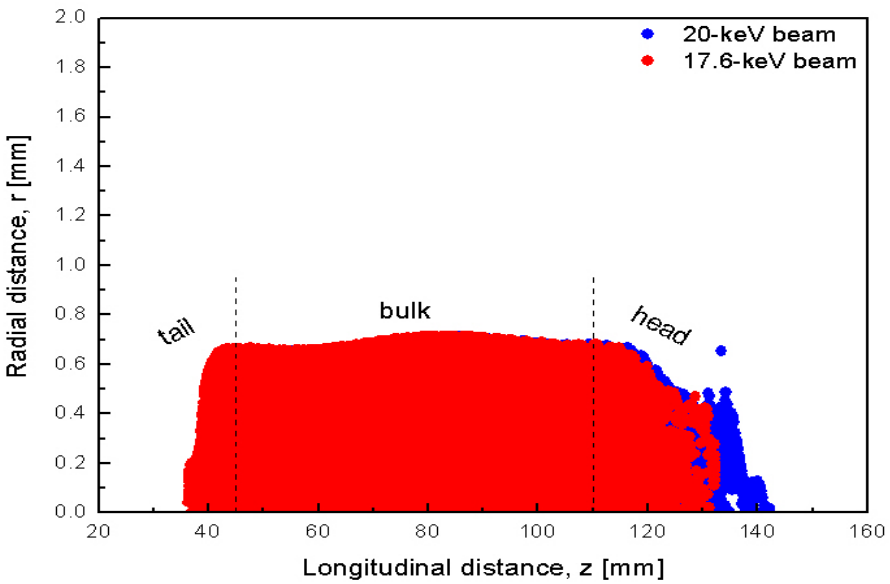

Figure 5.3: Radial distance, r, versus longitudinal distance, z, for two 0.7-mm and 0.3-A beams with energies 20 keV (blue dots) and 17.6 keV (red dots) propagating and interacting in the simulation structure in Figure 5.1.

in the next section will be the three distinct portions labeled "tail," "bulk," and "head." Namely, it will be shown that of the three portions only the one labeled "bulk" is used throughout the dissertation to study the interaction of two electron streams.

Note the variation of the beam envelope for the "bulk" portion in Figure 5.3. The magnetic field profile used to focus the beams in Figure 5.3 had the same shape as that in Figure 5.2 (Brillouin flow focusing) and the magnitude was 0.0747 T (Equation 3.77). As was discussed in Section 3.3, a Brillouin beam will maintain a constant radius as it propagates. In contrast to this, as we can see in Figure 5.3, both beams exhibit scalloping, the periodic variation of the beam envelope. It should be said that scalloping was present in every single simulation in this dissertation. Although we were unable to eliminate it, the scalloping amplitude never exceeded

6% of the beam radius. As a consequence, according to Appendix C, the gain of exponentially growing modes was virtually unaffected.

5.2 Propagation and interaction of two beams in simulation geometry

For both beams shown in Figure 5.3, the beam emission duration, t_{emission}, is the same and is less than half the simulation runtime, t_{run}, the typical values of which range from 2.4 ns to 2.8 ns in the dissertation. The reason we chose t_{emission} less than half t_{run} will be clarified shortly and is particularly relevant to high-frequency simulations ($f \geq 400$ GHz). The present version of MAGIC (version 2008.0818.1808) used in this dissertation can support up to 5×10^6 particles (approximately 5×10^{11} electrons). On the other hand, according to Appendix A, convergence with respect to PPC (particles emitted per cell/per time step) requires that there be 1200 particles/bunch. Let us thus estimate the total number of particles, corresponding to 1200 particles/bunch, for two modulated beams interacting at 30 GHz and 400 GHz.

According to Equation 4.39, two 0.7-mm and 0.3-A beams will interact at 30 GHz when $E_1 = 20$ keV and $E_2 = 17.6$ keV. Using $dz = 0.17$ mm and $dr = 0.1$ mm (from actual simulations at 30 GHz), the electromagnetic time step, δt, from Equation F.15 is

$$\delta t = \frac{\chi}{c} \frac{dz \times dr}{\sqrt{dz^2 + dr^2}} \approx 2.30 \times 10^{-13}\,\text{sec}, \tag{5.2}$$

where $\chi = 0.8$ is the Courant ratio (discussed at the end of the section) and c is the speed of light. Substituting δt from Equation 5.2 into Equation A.2, we can estimate

PPC that will produce 1200 particles/bunch

$$\text{PPC} = 1200 \times \frac{2.30 \times 10^{-13}}{(30 \times 10^{9})^{-1}} \approx 9. \tag{5.3}$$

The total number of particles, N, can be estimated by

$$N = \frac{r_b}{dr} \times \frac{t_{\text{emission}}}{\delta t} \times 2 \times \text{PPC}, \tag{5.4}$$

where r_b is the beam radius. Substituting Equations 5.2 and 5.3 into Equation 5.4 and using $t_{\text{emission}} = 1.1$ ns (the value used in simulations at 30 GHz), N becomes

$$N = \frac{0.7}{0.1} \times \frac{1.1 \times 10^{-9}}{2.3 \times 10^{-13}} \times 2 \times 9 \approx 603,000 \,\text{particles}, \tag{5.5}$$

which is well below 5×10^6 particles. Hence, the imposed particle limit will not be exceeded for the unstable interaction at 30 GHz. In addition, this will hold true even if t_{emission} is as big as t_{run} (2.4 - 2.8 ns).

The situation is markedly different for the interaction at 400 GHz. If we perform calculations similar to those at 30 GHz above, it can be shown that the total number of particles required exceeds 10 million, which is greater than the maximum number of particles allowed (5×10^6). Hence, to stop the simulation at 400 GHz from aborting, we must make t_{emission} smaller. It is straightforward to show that reducing t_{emission} from 1.1 ns to 0.51 ns (the value used in simulations at 400 GHz) will bring the total number of particles just under 5×10^6.

The foregoing quantitative analysis illustrates why the beams displayed in Figure 5.3 have t_{emission} less than half as big as t_{run}. This restriction is imposed by the present version of MAGIC (version 2008.0818.1808), which is capable of producing merely five million particles. Hence, from now on, when we speak of simulations involving cold (monoenergetic) and warm (nonzero energy spread) beams, it will be

implied that the beam emission duration, t_{emission}, is always less than the corresponding simulation runtime, t_{run}. Although the above limitation does not apply to interactions at 30 GHz, t_{emission} is still chosen to be less than t_{run}, namely, 1.1 ns, to make the simulations run twice as fast.

Having discussed the length of the beams in Figure 5.3, we will now talk about the three portions labeled "tail," "bulk," and "head." The emphasis in this dissertation is placed on calculating gain, which will be discussed in the next section at length. To calculate gain, as will be seen, we need to record the magnitude of the ac component of axial electric field as two beams, like those displayed in Figure 5.3, co-propagate and interact in the simulation structure in Figure 5.1. What we want to determine here is whether all three portions, namely, "tail," "bulk," and "head," should be used to analyze and record the magnitude of the ac component of axial electric field.

Plotted in Figure 5.4 is the variation of kinetic energy with longitudinal distance,

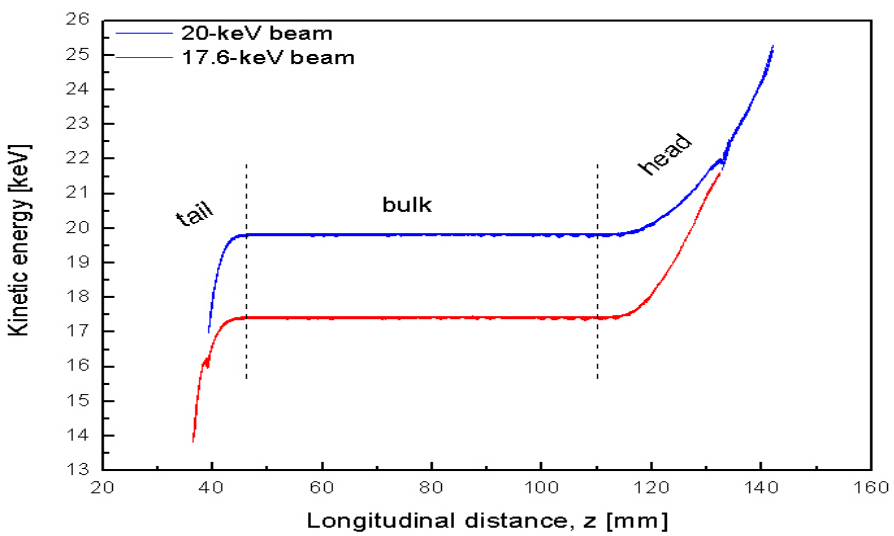

Figure 5.4: Kinetic energy as a function of longitudinal distance, z, for the beams shown in Figure 5.3.

z, for the beams in Figure 5.3. The correspondence between the "tail," "bulk," and "head" portions in Figure 5.4 and those in Figure 5.3 is one-to-one. Based on the curves in Figure 5.4, we can make the following observations:

1. The energies of blue and red electrons in the 'bulk" region are approximately 19.8 keV and 17.4 keV and thus less than the original energies of 20 keV and 17.6 keV. This is normal and is due to space-charge depression, which is discussed in Section 3.1.

2. Electrons in the "tail" portion decelerate due to repulsion by their counterparts in the "bulk" portion of the beams. As a result, the energies of some of the electrons in the former are as many as 3 keV less than those in the latter.

3. As opposed to the "tail" portion, electrons in the "head" of the beam accelerate away from the rest of the beam owing to repulsion by the "bulk" slice and due to proximity of the right wall of the simulation structure. Hence, the energies of some of the electrons are as many as 5 keV more than those in the "bulk" portion of the beams.

As the beams continue to travel downstream, the difference in kinetic energy between the particles in the "tail"/"head" portions and those in the "bulk" becomes even more pronounced. Therefore, of the three regions identified in Figures 5.3 and 5.4, the "bulk" portion is the only one truly representing the original 20-keV and 17.6-keV beams, the energies of which, owing to potential depression, reduce to 19.8 keV and 17.4 keV inside the beam pipe. The preceding discussion leads us to conclude that the analysis of ac electric field (calculation of gain) must be restricted to the "bulk" portion. As a consequence, the "tail" and "head" portions shown in Figure 5.3 are excluded from all analyses in this dissertation.

Before concluding this section, we will present a simple quantitative discussion of stability and accuracy requirements [13] necessary for the PIC simulations in this

dissertation. Consider 20- and 19-keV electron beams (0.7-mm and 0.3-A each) propagating and interacting in the simulation box in Figure 5.1. According to Equation 4.39, the beams will bunch at 70.1 GHz. Using the average beam velocity, $\bar{v} = 0.8 \times 10^8$ m/s, the wavelength corresponding to this interaction is

$$\lambda = \frac{\bar{v}}{f} \approx 1.13\,\text{mm}. \tag{5.6}$$

According to Appendix A, convergence with regard to dz (cell size in axial direction) is achieved (put differently, the spatial resolution requirement is met) if $\lambda \geq 6 \times dz$. Using the value of λ from Equation 5.6, we see that dz must not exceed $1.13/6 \approx 0.18$ mm. To determine dr (cell size in radial direction), we need to take into account the aspect ratio requirement, which states that the ratio of dz to dr (or vice versa) must not exceed 5, and convergence with regard to dr (Appendix A), which requires the number of emission cells be at least four. Since the emitter radius is 0.7 mm, the largest value of dr that will satisfy both requirements is $0.7/4 = 0.175$ mm. Substituting $\chi = 0.8$ (the value used in this dissertation), $dz = 0.18$ mm, and $dr = 0.175$ mm into Equation F.15 and solving it for the time step, we have

$$\delta t \approx 3.35 \times 10^{-13}\,\text{sec}. \tag{5.7}$$

The Courant ratio, χ, which must be less than one, has a default value of 0.8 in MAGIC to satisfy the Courant stability requirement (Appendix F). Using Equation 5.7 and $\bar{v} = 0.8 \times 10^8$ m/s, in a single time step every particle will travel a distance equal to

$$d = \delta t \times \bar{v} \approx 0.027\,\text{mm}, \tag{5.8}$$

which is less than both dz and dr and, therefore, does not violate the particle dynamics requirement (Appendix F). The foregoing simple calculations will not be

repeated elsewhere as the requirements mentioned are automatically met for every single simulation considered in this dissertation.

5.3 Calculation of numerical gain

Over the next two chapters, we will be comparing theoretical gain (Equation 4.38) with that obtained from simulations (numerical gain). Hence, the calculation of numerical gain is central to this dissertation and it is our intention here to illustrate how this important quantity is determined. Figure 5.5 shows the setup in Figure 5.1 with parallel line segments placed throughout the beam pipe. The line segments

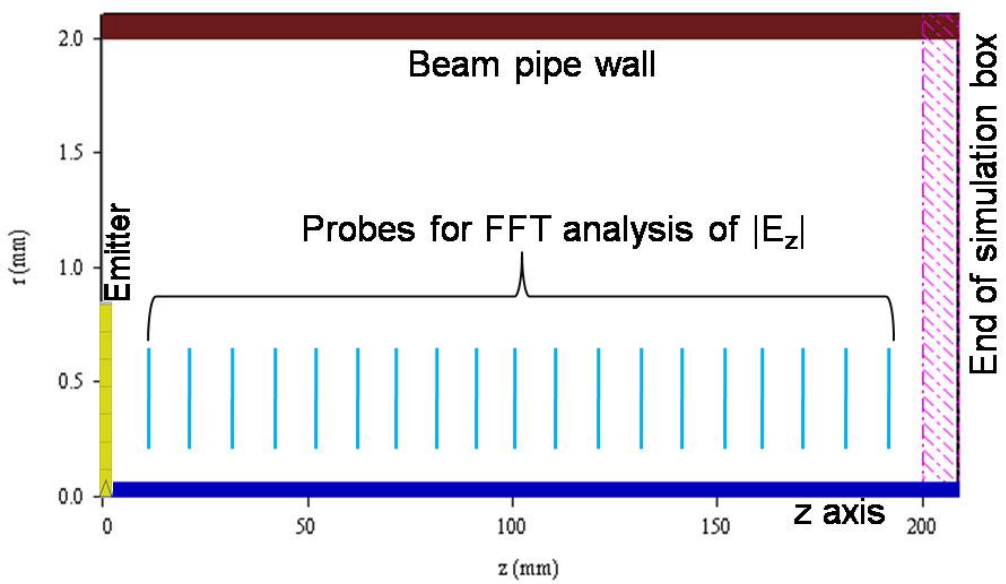

Figure 5.5: The simulation geometry from Figure 5.1 shown with FFT probes.

represent probes for recording the magnitude of the ac component of axial electric field, $|E_z(z,t)|$, as two electron beams interact and propagate in the structure. There are 19 probes in total. The horizontal spacing is uniform and equal to 9.5 mm, the first and last probes being located at $z = 2.5$ mm and $z = 173.5$ mm, respectively.

Note that the smallest beam radius considered in this dissertation equals 0.7 mm. Hence, the probes extend from 0.3 to 0.6 mm in the radial direction. $|E_z(z,t)|$ is recorded by performing a fast Fourier transform (FFT) on it at every single probe. The FFT depends on a time window for the Fourier integration and a frequency window for the frequency boundaries. The former is chosen such that the width of the window is at least 10 times the period at the anticipated interaction frequency of the beams. In addition, as explained in Section 5.2, the time window must be short enough to exclude the "head" and "tail" sections from the FFT analysis. $|E_z(z,t)|$ data thus recorded can be retrieved and plotted versus either frequency at a given axial position or as a function of longitudinal distance, z. To calculate gain, we need to do the latter and the plot of $|E_z(z,t)|$ versus z is shown in Figure 5.6.

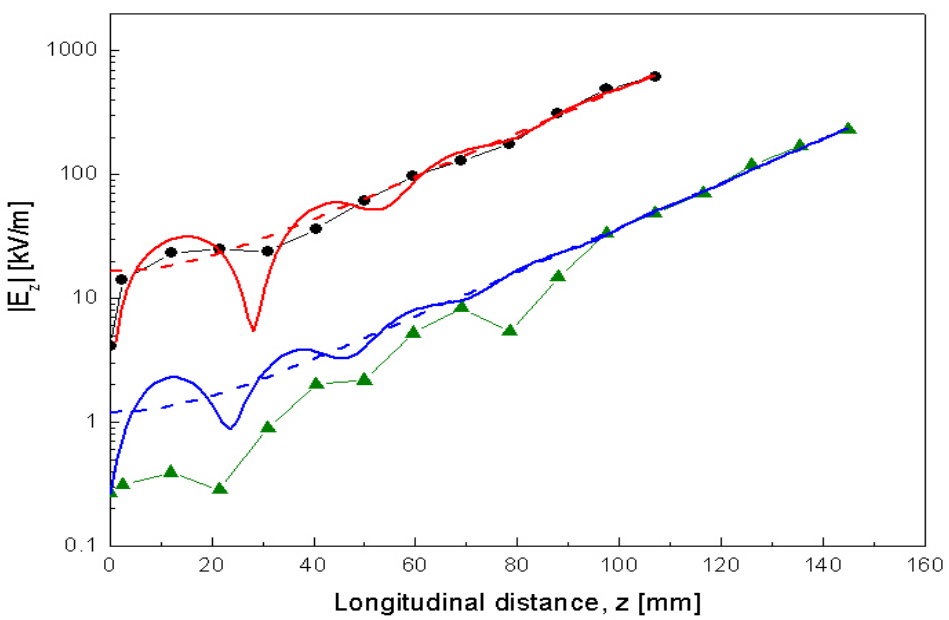

Figure 5.6: The variation of $|E_z(z,t)|$ with z for the interaction of two 0.7-mm and 0.5-A modulated (black curve) and unmodulated (green curve) electron beams. The solid red and blue curves are given by Equations B.19 and B.22. The dashed red and blue curves are given by Equation 5.9.

The green curve in Figure 5.6 was generated from a simulation involving the interaction of two 0.7-mm and 0.5-A unmodulated (with no initial energy modulation) beams with energies 20 keV and 16.95 keV. The black curve was obtained from a simulation involving the interaction of two modulated (energy-modulated at a given frequency) beams with exactly the same beam parameters as the unmodulated beams. The modulation amplitude (Appendix D) was 1% at 30 GHz. The solid red and blue curves are curve fits given by Equations B.19 and B.22 (Appendix B). The dashed red and blue curves represent curve fits to the linear regions of the two data sets and are given by the following function

$$y = A(e^{Rz} + e^{-Rz}), \tag{5.9}$$

where A and R are fitting parameters. The form of Equation 5.9 is dictated by Equation 4.32, the complex conjugate roots of the dispersion relation for two electron beams (Equation 4.25). As was discussed in Chapter 4, the complex conjugate roots yield exponentially growing and decaying solutions. Since the data in Figure 5.6 are plotted on a log-linear scale, the linear regions correspond to exponential growth.

According to Appendix B, $|E_z(z,t)|$ is a function of the modulation amplitude. As a result, the initial slope for the black curve is positive and large. By contrast, the initial slope for the green curve is approximately zero. The initial slope of the solid red curve (Equation B.19) is equal to 706403.3 ± 637444.9 V/m^2 and is within 5% of that for the black curve in Figure 5.6. However, note that the error is as large as 90%. Both the black and solid red curves exhibit an oscillatory behavior and the oscillation amplitude of the latter is much more pronounced than that of the former. Consequently, as can be seen in Figure 5.6, the agreement between the black and solid red curves is poor for values of z less than or equal to 60 mm.

The solid blue curve (Equation B.22) was obtained from Equation B.19 by setting the modulation amplitude and initial slope of $|E_z(z,t)|$ equal to zero. Nevertheless,

as we can see in Figure 5.6, the solid blue curve has a slope that is comparable to that of the solid red curve and is much larger than that of the green curve. Similar to the modulated case, both the green and solid blue curves oscillate. Although the solid blue curve models the shape of the data (green curve) fairly well within the range $0 < z < 69$ mm, the discrepancy between the former and the latter is significant for values of z less than 97.5 mm.

Our task in this section is to determine the gain of exponentially growing modes from simulations. To calculate numerical gain (as opposed to the theoretical gain in Equation 4.38), we determine the slopes of the linear regions in Figure 5.6 and the values thus calculated are substituted into the following expression

$$G = 20 \log\{e^{RL}\} = 20RL \log e, \tag{5.10}$$

where G, the power gain, has units of decibels, R has units of inverse length, and L has units of length. According to Figure 5.6, the solid red and black curves agree poorly within the range $0 < z < 60$ mm. In addition, the agreement between the solid blue and green curves is poor over the range $0 < z < 97.5$ mm. However, as can be seen in Figure 5.6, the solid red, black, and dashed red curves converge in the linear portion of the data. Likewise, the solid blue, green, and dashes blue curves converge in the linear region, which corresponds to exponential growth. The values of G, over a length of one millimeter, obtained from the solid and dashed red curves are given by 0.349 ± 0.018 dB/mm and 0.353 ± 0.016 dB/mm, while those extracted from the solid and dashed blue curves equal 0.359 ± 0.013 dB/mm and 0.358 ± 0.012 dB/mm. Hence, the largest percent difference (ignoring error bars) between the values of G is 2.6% and the agreement is very good.

On the basis of the foregoing discussion, Equation 5.9 will be used in place of Equations B.19 and B.22 (theoretical curve-fit formulas from Appendix B) throughout the rest of the dissertation to curve fit $|E_z(z,t)|$-versus-z data obtained from

simulations involving the interaction of both unmodulated and modulated beams. Also, the values of R determined from Equation 5.9 will be used in Equation 5.10 to calculate numerical gain. Moreover, Equation 5.10 will be compared with Equation 4.38 (theoretical gain formula) in Chapters 6 and 7 in order to validate the small-signal analysis presented in Chapter 4.

Chapter 6

Interaction of unmodulated electron beams

In this chapter, we present simulation results for the interaction of unmodulated electron beams at low-to-medium frequencies (less than 400 GHz). In this dissertation, unmodulated beams refer to unseeded beams or beams with no initial energy modulation. Modulated beams refer to beams seeded (energy-modulated) at a given frequency. Results for simulations involving the interaction of modulated beams are deferred to the next chapter. The primary emphasis in Chapters 6 and 7 is on the variation of the gain of exponentially growing modes with total beam current, beam radius, and percent energy spread. In addition, we look at the saturation length of a growing mode as a function of total beam current. Both cold (monoenergetic) beams and warm (Gaussian) beams are treated. Sections 6.1 through 6.2 are devoted to cold beams, while Section 6.3 discusses the interaction of warm beams.

6.1 Studies at low interaction frequency

In this dissertation, we treat both cold and warm beams. Hence, we open this section by briefly introducing the interaction of cold beams, which are the subject of Sections 6.1 through 6.2. Warm (Gaussian) beams will be discussed in Section 6.3.

Figure 6.1 depicts energy profiles from a simulation involving the interaction of two 0.7-mm and 0.3-A cold electron beams with energies 20 keV and 17.6 keV. The profiles in Figure 6.1 were recorded immediately after the emitter shown in Figure 5.5. According to Figure 6.1, the profiles are sharply defined and each has a

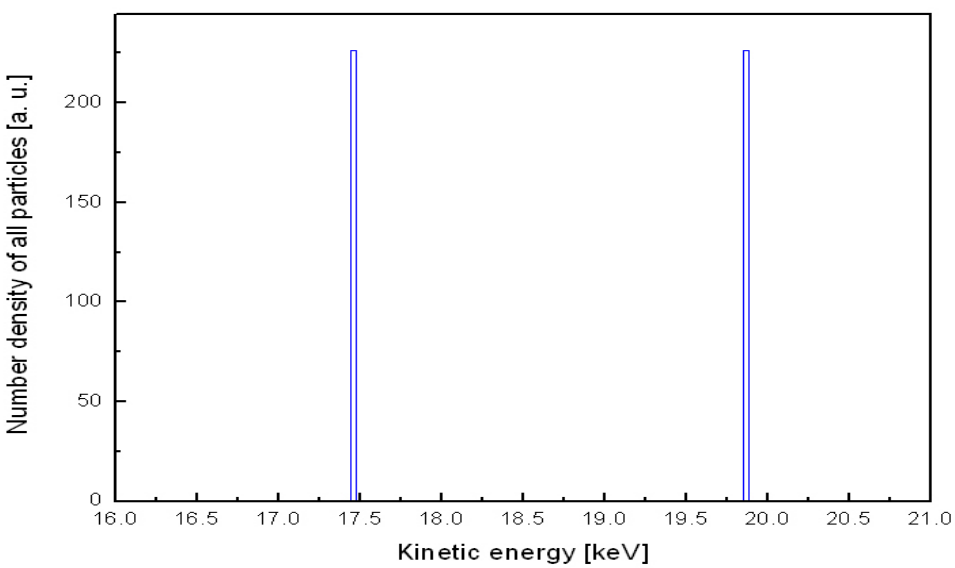

Figure 6.1: Kinetic energy distribution for the interaction of two cold beams with energies 20 keV and 17.6 keV.

width of approximately 100 eV. As the cold beams travel downstream and interact, the profile width increases. Nevertheless, the energy spread remains much less than the beam energy difference and the beams can be considered to be monoenergetic. Note that the beams may no longer be monoenergetic during the latter stages of their

interaction due to nonlinear effects. However, since we are interested in the linear region of the instability growth, cold beams in this dissertation will be referred to as beams with 0% energy spread.

In Figure 6.1, the initial energies of the two beams are centered at 19.868 keV and 17.465 keV. Section 3.1 predicts that due to space-charge depression 20 keV and 17.6 keV will shift to 19.909 keV and 17.503 keV. Hence, the values from theory are approximately 0.2% less than those from simulations. However, if we take into account the finite profile width in Figure 6.1, the discrepancy between theory and simulations is negligible.

Equation 4.39 predicts that the cold beams in Figure 6.1 will interact at 30 GHz. Even though space-charge depression causes the beam energies to shift, it can be shown (Equation 4.39) that the change in bunching frequency (30 GHz) is negligible ($\approx 0.1\%$). As will be seen later, the largest frequency component does occur at 30 GHz for the interaction of both unmodulated and modulated cold beams in Figure 6.1. Despite the fact that space-charge depression was present in every single simulation in this dissertation, the influence on the interaction frequency (given by Equation 4.39) of two co-propagating cold beams was found to be negligible for all interaction frequencies considered (30 GHz to 1 THz). Specifically, it was determined that the variation of interaction frequency approximately equals 0.1%.

According to Equation 4.38, space-charge depression will affect the theoretical gain, henceforth denoted by G_{th}, of an exponentially growing mode. Considering the interaction of two 0.3-A electron beams at 30 GHz, it can be shown that the value of G_{th} (if space-charge depression is included) varies by around 0.3%. The variation in G_{th} increases to about 1.2% for the interaction of two 1.1-A beams at 30 GHz. At higher interaction frequencies, according to Equation 4.39, the energies of two interacting beams are much closer. As a result, e.g., at 1 THz, the variation in G_{th} decreases to about 0.2% and 1.1% for the interaction of two 0.3-A and 1.1-A

electron beams, respectively. It should be noted that the variation of G_{th} due to space-charge depression does not alter the results presented markedly and, thus, is not discussed in this dissertation.

Figure 6.2 shows the interaction of two 1.0-mm and 0.5-A cold beams with energies 20 keV and 18 keV. The 20- and 18-keV beams in Figure 6.2 are shown by the

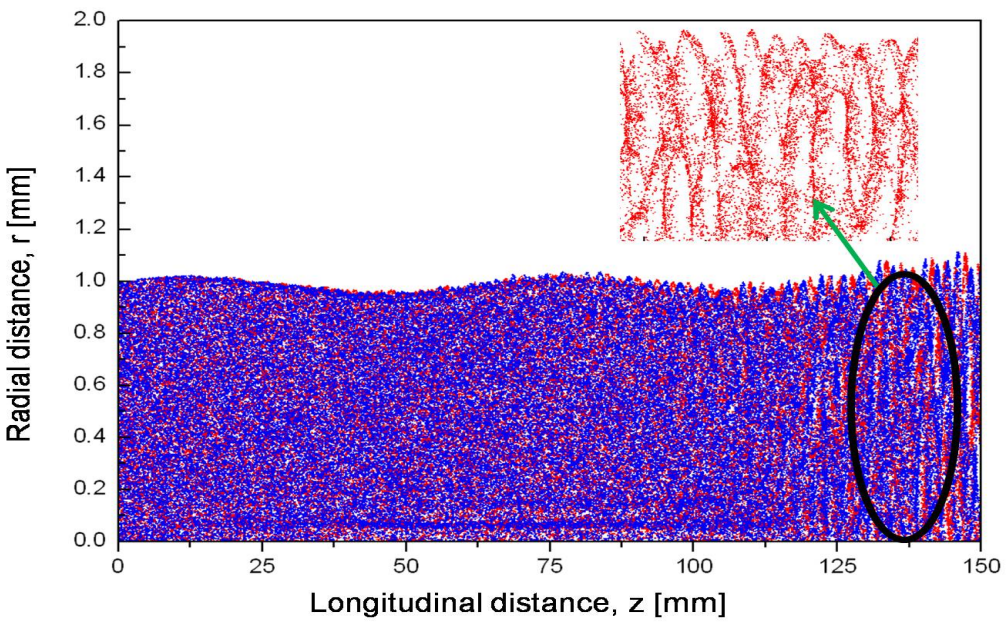

Figure 6.2: Radial distance versus longitudinal distance for the interaction of 1.0-mm and 0.5-A cold beams with energies 20 keV and 18 keV.

red and blue dots, respectively. The inset shows an enlarged portion of the 20-keV beam towards the end of the simulation.

In Figure 6.2, the beam emission duration, t_{emission}, for each beam was 2 ns, while the simulation runtime, t_{run}, equaled 2.8 ns. Also, the grid sizes in longitudinal and radial directions were 0.17 mm and 0.1 mm. Moreover, the electromagnetic time step, δt, was as small as 1.93×10^{-13} sec. With 1200 particles/bunch (as explained in Appendix A), the total number of particles (Equation 5.4) used in the simulation was approximately 1.4 million (half as many per beam). It should be

noted that the particles shown in Figure 6.2 represent macro particles, each of which on average contains 10^5 electrons. Hence, 1.4 million macro particles correspond to about 1.4×10^{11} electrons.

According to Figure 6.2, the two beams are uniform up to about $z = 100$ mm. For greater values of z we start to observe variations in density, commonly known as bunching [16]. As a result, over the range $100 \leq z \leq 150$ mm, the electrons are no longer uniformly distributed and they are arranged in bunches. This is shown in the inset, which represents a portion of the 20-keV beam within the range $135 \leq z \leq 145$ mm. In the inset, we can see several bunches that overlap and are not clearly defined. This is a characteristic feature of all particle plots involving unmodulated beams in this dissertation. By contrast, as will be seen in the next chapter, bunches formed by modulated beams are sharply defined, evenly spaced, and possess a comb-like structure.

As can be seen in Figure 6.2, both beams exhibit scalloping (Chapter 3), the periodic variation of beam radius, r_b. Scalloping was present in all simulations in this dissertation. Even though we were unable to eliminate it, its amplitude was kept to about 6% of r_b. According to Appendix C, gain obtained from simulations is virtually unaffected as long as the scalloping amplitude is less than 13% of r_b. Hence, as far as this dissertation is concerned, the effect of scalloping on numerical gain is negligible at best and this topic will not be discussed further in Chapters 6 and 7.

6.1.1 Axial electric field analysis

Our primary goal in this dissertation is to compare numerical gain, henceforth denoted by G_{sim}, obtained from simulations with that, G_{th}, given by the 1-D theory (Equation 4.38). To calculate numerical gain, according to Chapter 5, we need to extract and analyze the magnitude of the ac component of axial electric field,

$|E_z(z,t)|$. Hence, Subsection 6.1.1 studies $|E_z(z,t)|$ in detail at a low interaction frequency, specifically, 30 GHz. The analysis of $|E_z(z,t)|$ at higher frequencies is presented in Section 6.2.

Figure 6.3 shows an FFT of the magnitude of axial ac electric field, $|E_z|$, for the interaction of two 0.7-mm cold electron beams. For the red curve, the beam currents were 0.5 A. For the blue curve, the beams were 0.3 A each. In both cases, the energy of one of the beams was 20 keV. The energies of the other two beams were determined from Equation 4.39 with $f_{\text{bunching}} = 30$ GHz. Note that the legend in Figure 6.3 (or any other plot in this dissertation) gives the total current, I, of two interacting beams.

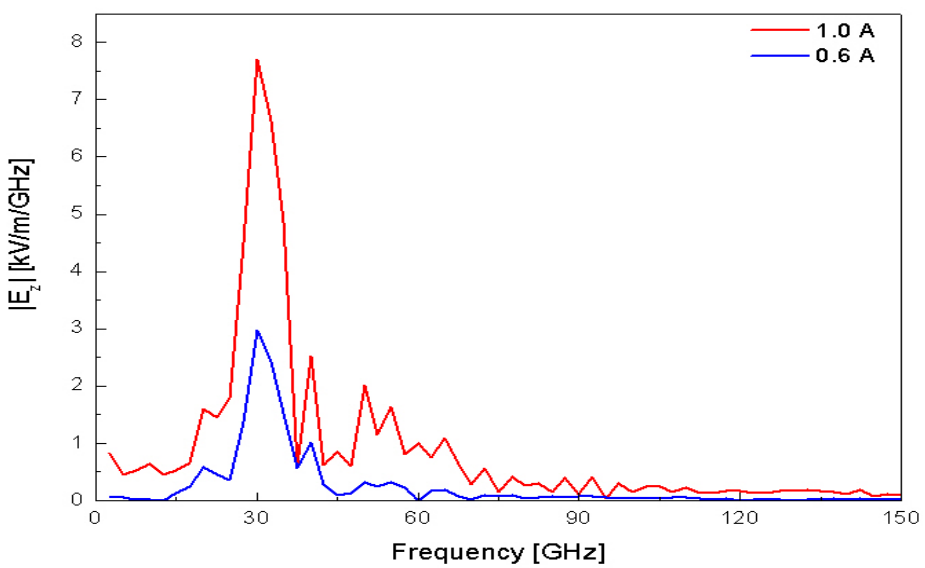

Figure 6.3: FFT of $|E_z|$ for the interaction of two 0.7-mm cold beams at 30 GHz. The blue and red curves correspond to $I = 0.6$ A and $I = 1.0$ A.

No saturation was observed for the interaction of 0.3-A beams. As a result, the blue curve was recorded at $z = 173.5$ mm, the location of the last FFT probe. $|E_z|$ did reach saturation for the 0.5-A beams. Hence, the red curve was recorded

at $z = 145$ mm, right before the onset of nonlinearities. To resolve $|E_z|$ properly (Section 5.3), the FFT curves were recorded using a 0.4-ns time window, which equaled 12 periods at 30 GHz, the frequency component of interest. The frequency window selected ranged from 2 GHz to 150 GHz, while the frequency resolution, corresponding to the 0.4-ns time window, was 2.5 GHz.

As predicted by Equation 4.39, for both 0.6 A and 1.0 A the largest frequency component occurs at 30 GHz, which at first sight appears to be dominant. However, note that the curves have a finite full width at half maximum (FWHM). For the red curve, the FWHM frequency approximately equals 8.8 GHz and is slightly larger than that for the blue curve (≈ 7.3 GHz). Recalling that the frequency resolution is equal to 2.5 GHz, it can be shown that the magnitude of a frequency component at 32.5 GHz is comparable to that of the 30-GHz mode. To quantify, the ratio of $|E_z|$ for 30 GHz to that for 32.5 GHz is approximately 1.16 and 2.18 for 1.0 A and 0.6 A, respectively. Hence, the larger the total beam current, the smaller the ratio.

As we can see in Figure 6.3, the larger the total beam current, the more competing modes there are ($2.5 \leq f \leq 25$ GHz and $f \geq 37.5$ GHz). In addition, the larger the total beam current, the larger their magnitudes are relative to $|E_z|$ of the 30-GHz mode. Note that with the exception of the fundamental mode, all modes (including harmonics) in this dissertation are referred to as competing modes. By dividing $|E_z|$ at 30-GHz by the average value of $|E_z|$ for the rest of the frequencies shown in Figure 6.3, the average signal-to-noise ratios for 0.6 A and 1.0 A yield 13.8 and 9.5, respectively. As will be seen in Section 6.2, the number of competing modes increases for higher interaction frequencies. By contrast, modulated beams, discussed in Chapter 7, can interact at a single frequency given a sufficiently high modulation amplitude.

The blue curve in Figure 6.3 shows a snapshot of a 30-GHz mode. In Figure 6.4, we can see how the 30-GHz mode (black curve) varies with longitudinal distance.

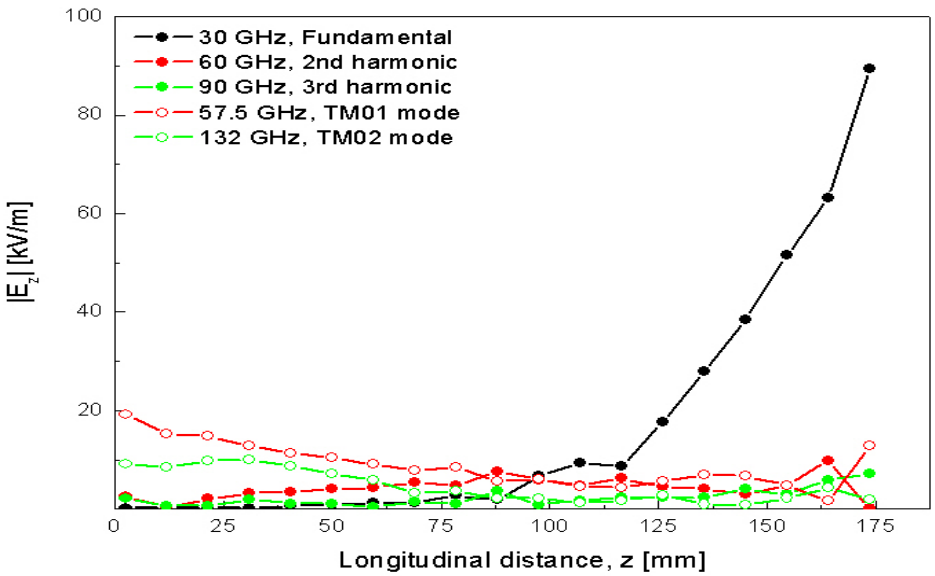

Figure 6.4: $|E_z|$ versus z for the interaction of two 0.7-mm and 0.3-A cold electron beams at 30 GHz. The solid black, red, and green circles represent 30-, 60-, and 90-GHz modes. The open red and green circles are TM_{01} and TM_{02} waveguide modes.

According to Figure 6.4, the fundamental mode (30 GHz) starts out as the smallest of all modes and its magnitude is a factor of 10 less than that of the 2nd and 3rd harmonics. As we can see in Figure 6.4, it is only around $z = 100$ mm that the 30-GHz mode becomes the largest mode. For values of z greater than 100 mm, the 30-GHz mode continues to grow exponentially all the way to $z = 173.5$ mm without saturating over the length of the beam pipe. Note that at $z = 173.5$ mm the magnitude of the fundamental is at least an order of magnitude greater than that of the rest of the modes in Figure 6.4. Hence, the gain of the 30-GHz mode, which is equal to 0.29 dB/mm (this will be shown later in the section), is much greater than that of the two harmonics and TM_{01} and TM_{02} waveguide modes depicted in Figure 6.4.

The open red and green circles in Figure 6.4 represent TM_{01} and TM_{02} waveguide modes at 57.5 GHz and 132 GHz for a 2.0-mm circular waveguide (recall that the

simulation structure in Figure 5.5 has an inner radius of 2 mm). Although the TM_{01} and TM_{02} waveguide modes have the largest initial magnitudes, $|E_z|$ of the former being a factor of two greater than that of the latter, they exhibit no growth over the range of z values shown. As we can see in Figure 6.4, the 2nd and 3rd harmonics (solid red and green circles) increase towards the end of the simulation. However, their magnitudes are over a factor of 10 less than that of the fundamental mode. The foregoing discussion leads us to conclude that the 30-GHz mode is clearly the most dominant mode in Figure 6.4.

Figure 6.5 is similar to Figure 6.4, except that it shows the variation of $|E_z|$ with longitudinal distance, z, for the 1.0-A case in Figure 6.3. As in Figure 6.4, the solid

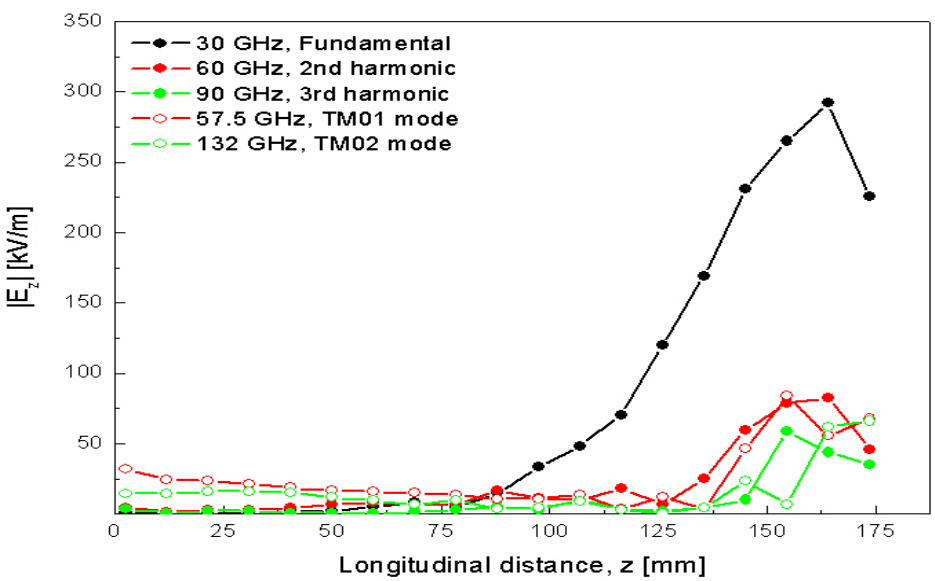

Figure 6.5: $|E_z|$ versus z for the interaction of two 0.7-mm and 0.5-A electron beams. The solid black, red, and green circles represent 30-, 60-, and 90-GHz modes. The open red and green circles are TM_{01} and TM_{02} waveguide modes.

black, red, and green circles represent 30-, 60-, and 90-GHz modes. The open red and green circles display the variation of TM_{01} and TM_{02} waveguide modes.

As we can see in Figure 6.5, for a total beam current of 1.0 A the 30-GHz mode starts to grow exponentially a bit sooner and saturates. Its gain (discussed later in this section) is 0.358 dB/mm. As was the case for the interaction of 0.3-A beams in Figure 6.4, the 30-GHz mode has the smallest magnitude at $z = 2.5$ mm, where its $|E_z|$ is over an order of magnitude less than that of the 60- and 90-GHz modes and over two orders of magnitude less than that of the TM_{01} waveguide mode. Even though the 30-GHz mode in Figure 6.5 starts to grow earlier, it overtakes the rest of the modes at about $z = 100$ mm, which is the same longitudinal location as that for the 30-GHz mode in Figure 6.4. Comparing the fundamental mode in Figure 6.5 with that in Figure 6.4, we see that the former saturates at $z = 164$ mm, while the latter fails to do so over the same range of z values shown. According to Figure 6.5, the gain of the 30-GHz mode is much greater than that of the rest of the modes in the linear region, which extends to approximately $z = 145$ mm.

The variation of the TM_{01} and TM_{02} waveguide modes in Figure 6.5 is very similar to that in Figure 6.4 up to about $z = 125$ mm, where the waveguide modes in Figure 6.5 start to grow. The same is true of the 2nd and 3rd harmonics, which begin to grow and saturate at about the same location as the fundamental mode. The growth of the 60- and 90-GHz modes is clearly indicative of the onset of a nonlinear regime when $|E_z|$ becomes rich in harmonics. At the point of saturation, the magnitude of the 30-GHz mode is approximately a factor of 3.5 and 6.7 greater than that of the 2nd and 3rd harmonics. For the interaction of two 0.7-mm and 0.5-A modulated beams, as it will be shown in Chapter 7, the 60- and 90-GHz modes become comparable in magnitude to the 30-GHz mode. Note that nonlinear effects are outside the scope of this dissertation. Hence, we can conclude, as we did for Figure 6.4, that the 30-GHz mode is again the most dominant mode in the linear regime.

Figure 6.5 showed the variation of $|E_z|$ for 5 different modes. Figure 6.6 dis-

plays the evolution of $|E_z|$ for all possible modes, within a frequency range of

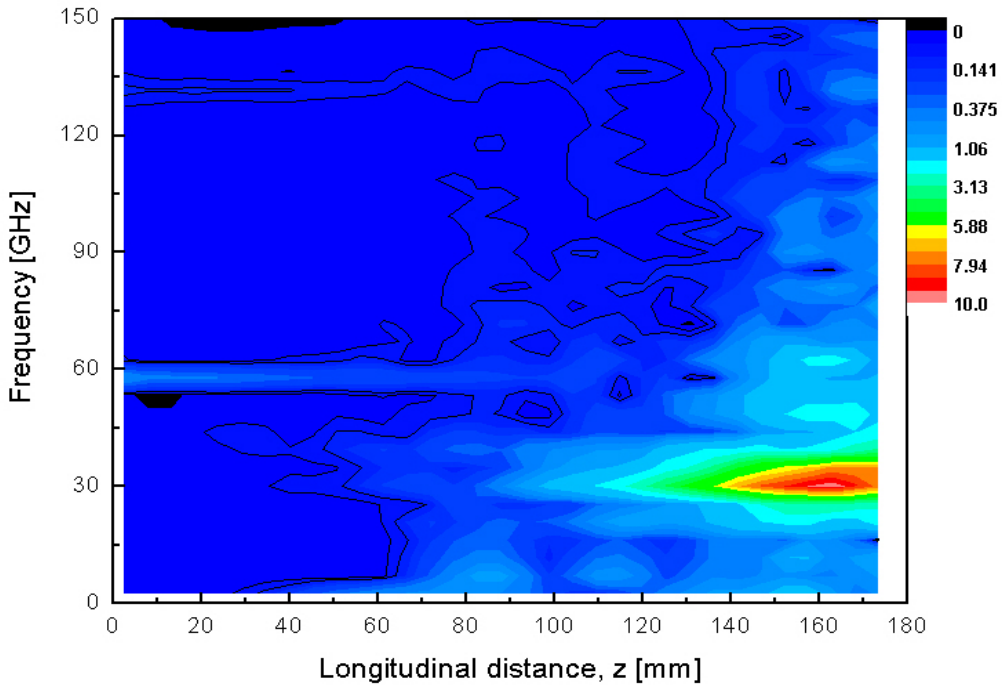

Figure 6.6: Contour plot of $|E_z|$ for two 0.7-mm and 0.5-A electron beams interacting at 30 GHz.

$2 \leq f \leq 150$ GHz, for the interaction of two 0.7-mm and 0.5-A electron beams discussed in Figures 6.3 and 6.5. In Figure 6.6 and other contour plots in this chapter, the left-hand vertical axis is frequency in units of GHz. The horizontal axis is longitudinal distance, z, in units of mm. A color scale legend next to the right-hand vertical axis gives numerical values of $|E_z|$ in units of (kV/m)/GHz.

In Figure 6.6, only two modes stand out at the start of the interaction, namely, those at 57.5 GHz and 132 GHz. These are the same TM_{01} and TM_{02} waveguide modes as in Figure 6.5 (open red and green circles). As we can see in Figure 6.5, the TM_{02} mode maintains approximately the same magnitude throughout most of the interaction and starts to grow well into the nonlinear region. By contrast, the

TM_{01} waveguide mode first decreases and then begins to grow shortly before the fundamental mode reaches saturation. At about the same longitudinal distance we can also observe the 60- and 90-GHz modes appearing, the former being more pronounced than the latter. According to Figure 6.6, 5 modes shown in Figure 6.5 appear to be the most important modes for the interaction of two 0.7-mm and 0.5-A electron beams at 30-GHz, the 30-GHz mode being the most dominant.

From Equation 4.39 (theory), two 0.7-mm and 0.5-A electron beams with energies 20 keV and 16.95 keV (Figure 6.5 and the red curve in Figure 6.3) will interact at 30 GHz. Note that the largest mode in Figure 6.6 has a finite FWHM frequency, which is about 8.8 GHz (also shown in Figure 6.3). However, both theory and simulations agree in that the peak frequency clearly occurs at 30 GHz. The same holds true for the case of two 0.7-mm and 0.3-A electron beams interacting at 30 GHz (Figure 6.4 and the blue curve in Figure 6.3).

6.1.2 Gain and space-charge effects

Having analyzed $|E_z|$ for the interaction of two electron beams at 30 GHz, we will now examine the gain of a 30-GHz mode for different beam currents and beam radii.

Shown in Figure 6.7 is $|E_z|$ as a function of longitudinal distance, z, from 9 different simulations involving the interaction of two 0.7-mm electron beams. In all simulations, the energy of the faster beam was fixed at 20 keV. The energies of slower beams were determined from Equation 4.39, where $f_{\text{bunching}} = 30$ GHz, $F = 0.8$ (average value), and $\bar{\beta} = 0.26$ (average value). Note that the values of current displayed in Figure 6.7 represent the total current of two interacting beams. For instance, the green curve (0.8 A) was generated by the interaction of two 0.4-A beams.

The curves in Figure 6.7 are plotted on a log-linear scale so we can focus on

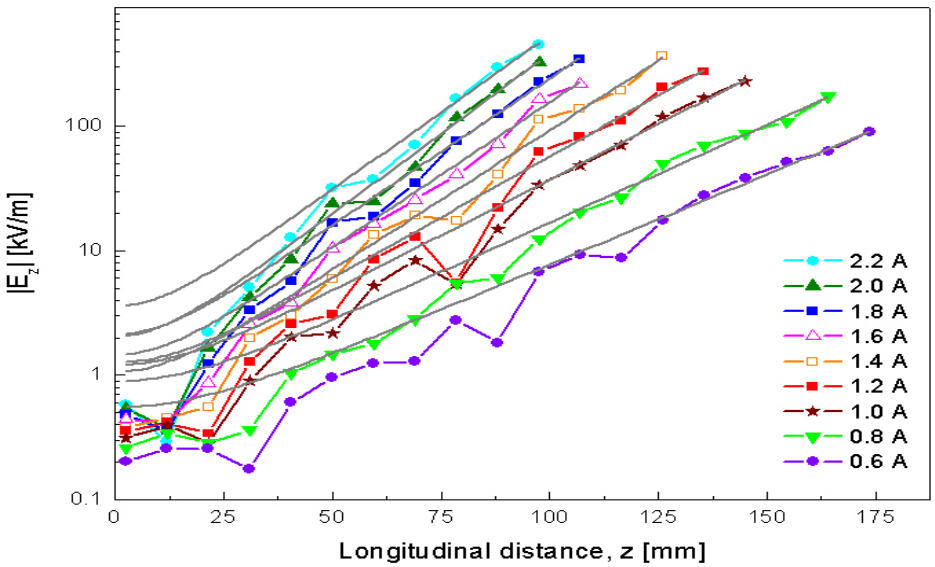

Figure 6.7: The variation of $|E_z|$ of a 30-GHz mode for 9 different values of the total beam current. Solid gray lines are curve fits given by Equation 5.9.

the linear portions of the data. As was explained in Chapter 5, the linear regions correspond to exponential growth and they are used to determine numerical gain, G_{sim}. The solid gray lines on top of the data sets represent curve fits given by Equation 5.9,

$$y = A(e^{Rz} + e^{-Rz}),$$

where z is longitudinal distance and R is proportional to G_{sim} via Equation 5.10.

Figure 6.7 does not show any data points past saturation to exclude nonlinear regions from the analysis. Since the modes corresponding to large currents in Figure 6.7 saturate faster, they are plotted with fewer data points. The variation of the saturation length for the modes in Figure 6.7 is explored at the end of this section.

According to Figure 6.7, the initial value of $|E_z|$ increases with increasing total beam current, I. Also, its initial angle is positive for the values of I less than or

equal to 1.4 A and negative for larger values. We will see in the next chapter that the initial angle of $|E_z|$ for modulated beams is always positive. Note in Figure 6.7 that two pronounced dips in $|E_z|$ move towards lower values of z with increasing total beam current. All curves in Figure 6.7 exhibit strong exponential growth. In addition, as I ranges from 0.6 A to 2.2 A, the slope of the linear region increases and will yield larger G_{sim}. Extracting the values of R from Figure 6.7 and substituting them into Equation 5.10, we will now compare G_{sim} and G_{th} (Equation 4.38).

Figure 6.8 displays G_{sim} (red curve) determined from Figure 6.7 as a function of total beam current, I. Also Plotted in Figure 6.8 is G_{th} (red curve). The red curve

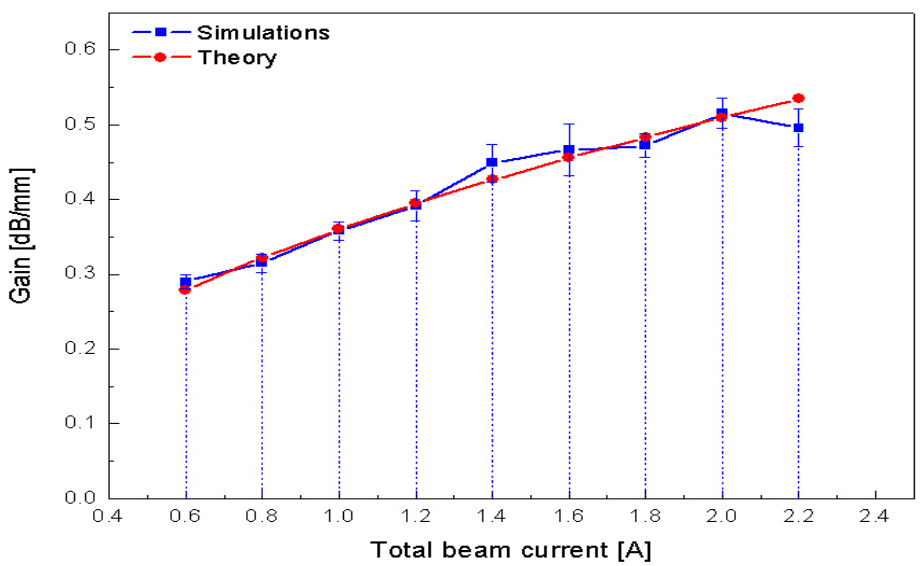

Figure 6.8: The variation of gain of a 30-GHz mode with total beam current. The blue curve represents G_{sim} and the red curve is theoretical gain.

was generated by substituting $r_b = 0.7$ mm, $\bar{\beta} = 0.26$, and $F = 0.712$ (the plasma frequency reduction factor from Figure 3.3) into Equation 4.38.

Over most of the range shown in Figure 6.8, simulations and theory agree in that larger interaction current results in higher gain. The only exception is the data point

for 2.2 A. Note that for the values of I greater than or equal to 1.2 A, the error bars in Figure 6.8 are markedly larger. This is due to the curves (for $I \geq 1.2$ A) in Figure 6.7 having fewer data points.

The average deviation (excluding error bars) between G_{sim} and G_{th} in Figure 6.7 is approximately equal to 2.9%. If we take the error bars into account and consider the fact that we are comparing one-dimensional theory and two-dimensional simulations, then the agreement between G_{sim} and G_{th} is very good. Hence, based on Figure 6.8, we may conclude that for the interaction of 0.7-mm beams at 30 GHz G_{sim} varies in accordance with the 1-D theory. Namely, G_{sim} varies as the square root of total beam current, $\sqrt{I}$.

Our next task is to examine the variation of the gain of a 30-GHz mode with beam radius, r_b. We will do this by looking at three simulations involving the interaction of 0.5-A beams with three different beam radii, specifically, 0.7 mm, 1.0 mm, and 1.4 mm.

Figure 6.9 is similar to Figure 6.7 and displays $|E_z|$ as a function of longitudinal distance, z, from three different simulations. For each of the simulations, the total beam current, I, was kept at 1.0 A, while the beam radii were 0.7 mm (blue curve), 1.0 mm (green curve), and 1.4 mm (burgundy curve). As in Figure 6.7, the energy of the faster beam in each case was fixed at 20 keV. The energies of slower beams were determined from Equation 4.39, where $f_{\text{bunching}} = 30$ GHz. The solid gray lines shown in Figure 6.9 are given by Equation 5.9 and represent curve fits to the linear portions of the data.

What we first notice in Figure 6.9 is that the initial slope of $|E_z|$ is nearly zero for the 0.7-mm and 1.4-mm cases. However, the initial slope is negative and large for the 1.0-mm case. When examining Figure 6.7, we identified two pronounced dips in the data for every single current. Although the same holds true for the blue

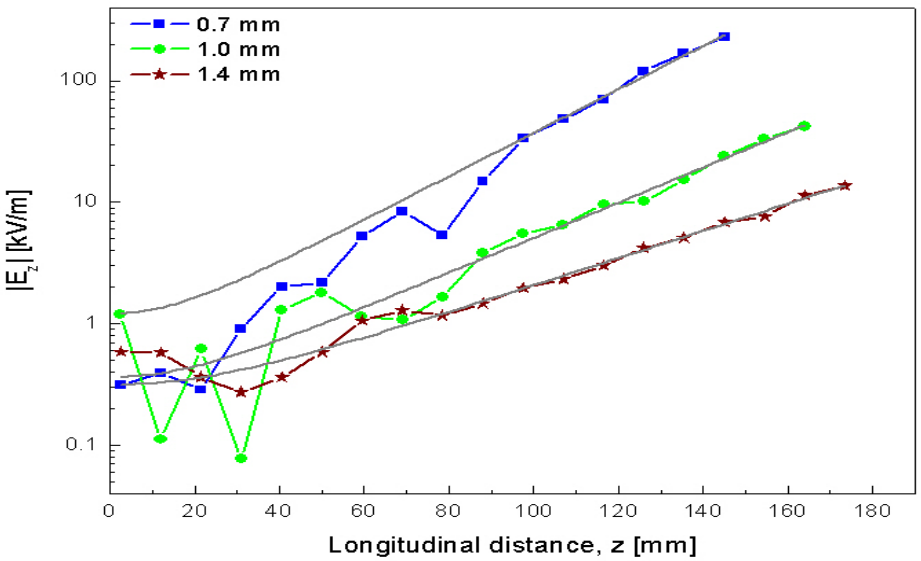

Figure 6.9: The variation of $|E_z|$ of a 30-GHz mode for three different beam radii. Total Beam current is 1.0 A. Solid gray curves are curve fits from Equation 5.9.

and burgundy curves in Figure 6.9, the green curve clearly shows three dips and is markedly different from the other two cases for values of z less than or equal to 40 mm. Note that the initial value of $|E_z|$ in Figure 6.7 increases with increasing space charge. By contrast, the initial values of $|E_z|$ in Figure 6.9 are in random order.

According to Figure 6.9, the smaller the beams radius (more space charge), the larger the slope of the linear portion is and, thus, the higher the gain. This is consistent with the 1-D theory discussed in Chapter 4. Determining the values of R from the curve fits and substituting them into Equation 5.10, we will again make a comparison between simulations and theory, G_{sim} and G_{th}.

In Figure 6.10, G_{sim} (blue curve) of the three 30-GHz modes in Figure 6.9 is plotted as a function of beam radius, r_b. To generate G_{th} (red curve), $\bar{\beta}$ was set equal to 0.26 and the plasma frequency reduction factors used were 0.712, 0.80, and

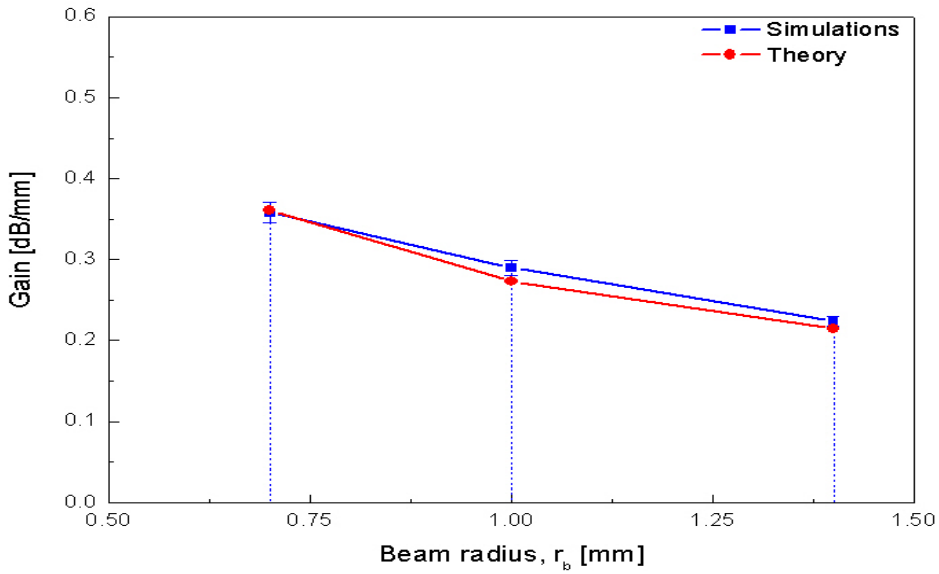

Figure 6.10: The variation of gain of a 30-GHz mode with beam radius. The blue and red curves represent simulations and theory.

0.86, respectively.

According to Figure 6.10, as the beam radius varies from 1.4 mm to 0.7 mm, both $G_{\rm sim}$ and $G_{\rm th}$ increase by approximately 40%. This means that, in comparison with 1.0- and 1.4-mm beams, the interaction of two 0.7-mm beams provides a larger amplification over the same interaction distance. Hence, the proposed radiation source (Figure 1.1) based on the interaction of two 0.7-mm beams would be superior to that involving the interaction of either two 1.0- or 1.4-mm electron beams.

A significantly larger error bar for $r_b = 0.7$ mm in Figure 6.10 is due to the fact that the blue curve in Figure 6.9 has fewer data points. As we can see in Figure 6.10, the agreement between $G_{\rm sim}$ and $G_{\rm th}$ is very good even if the error bars are ignored (the average deviation between the two is less than 4%). This enables us to conclude that, for the interaction of 0.5-A beams at 30 GHz, $G_{\rm sim}$ and $G_{\rm th}$ vary in the same fashion, namely, they vary as $\sqrt{I/r_b^2}$.

Figures 6.8 and 6.10 explore the variation of the gain of a 30-GHz mode with total beam current, I, and beam radius, r_b, separately. Figure 6.11 combines the two plots and displays the gain of a 30-GHz mode as a function of space charge density in units of A/mm^2.

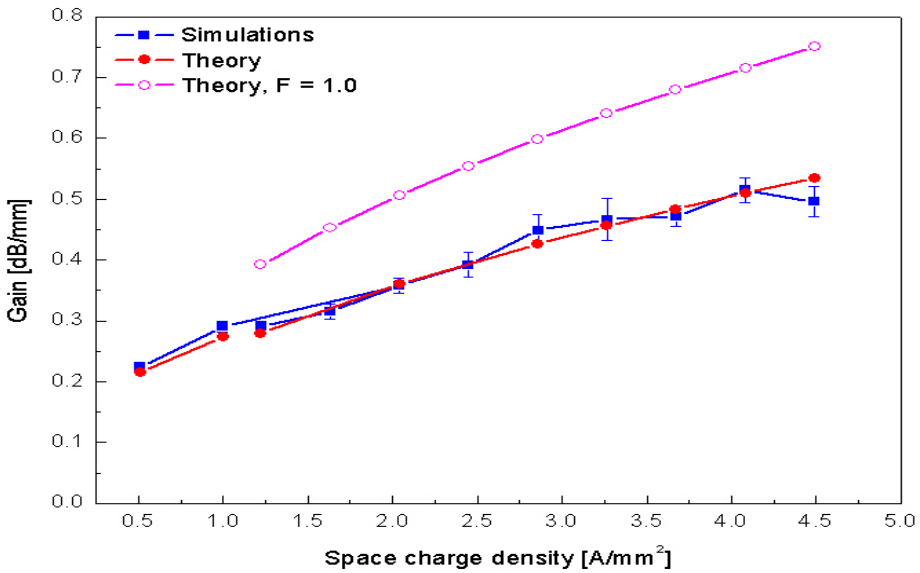

Figure 6.11: The variation of gain of a 30-GHz mode with space charge density. The blue curve corresponds to simulations. The red and magenta curves represent theory.

The magenta curve in Figure 6.11 is G_{th} and was generated by setting the plasma frequency reduction factor, F, equal to unity in Equation 4.38. Recall from Chapter 3 that $F = 1$ always holds for infinitely large r_b and r_a. The reason the magenta curve is plotted in Figure 6.11 is to stress the importance of estimating the value F correctly (Figure 3.3). As we can see in Figure 6.11, the values of G_{th} from the magenta and red curves differ by as much as 29%.

When exploring Figures 6.8 and 6.10, we pointed out how good the agreement was between simulations and theory. The shape of the blue and red curves in Figure 6.11 reinforces our previous observation. Hence, for the interaction of two electron beams

at 30 GHz, we can state that the variation of both G_{sim} and G_{th} with total beam current, I, and beam radius, r_b, has a functional dependence given by $\sqrt{I/r_b^2}$.

When discussing the proposed source of mm and sub-mm wave radiation in Chapter 1, one of the important features we stressed was its compactness. This dissertation is concerned with simulating the proposed source, namely, its interaction region, which certainly affects the overall size of the device. Hence, it would be interesting to determine whether or not the length of the interaction region can vary with total beam current. To that end, we will present a brief quantitative discussion of the saturation length of a growing 30-GHz mode for several values of the total beam current, I.

Shown in Figure 6.12 is $|E_z|$ of a 30-GHz mode for 9 different total beam currents. The curves displayed are exactly the same as those in Figure 6.7. Note, however,

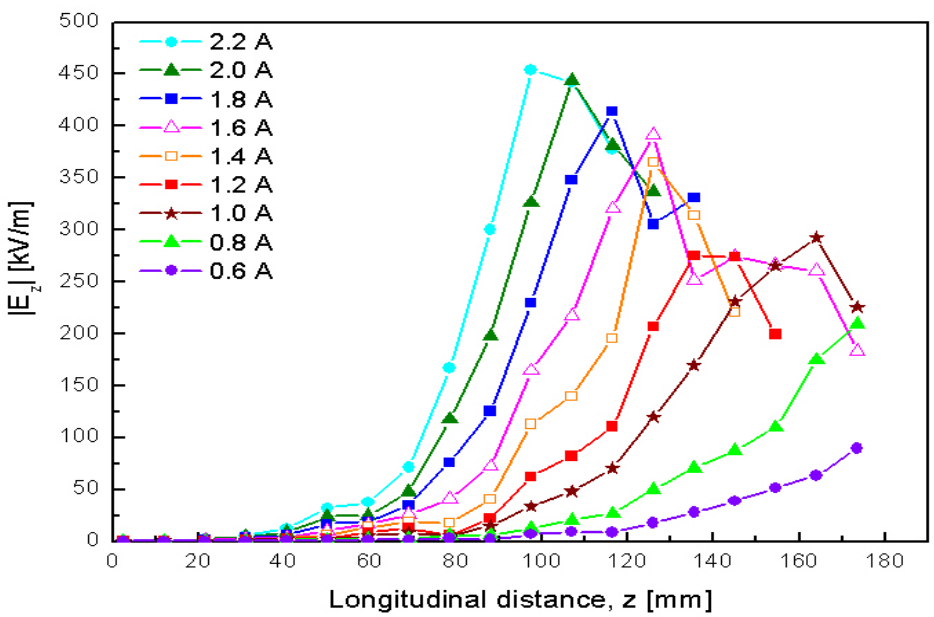

Figure 6.12: The variation of $|E_z|$ of a 30-GHz mode for I ranging from 0.6 A to 2.2 A.

that Figure 6.12 depicts the curves both before and after saturation (for currents $\geq$ 1 A).

Over the range of z values shown in Figure 6.12, no saturation is observed for I less than or equal to 0.8 A. The 30-GHz mode begins to saturate for values of I greater than or equal to 1.0 A. According to Figure 6.12, the larger the total beam current, the faster the corresponding mode grows. In addition, the larger the total beam current, the shorter the longitudinal distance required for the 30-GHz mode to reach saturation. Hence, the interaction region and, thus, the proposed radiation source can indeed be made more compact by increasing the currents of two interacting electron beams.

The effect of the total beam current on the saturation length of the 30-GHz mode shown in Figure 6.12 is explored in Figure 6.13. The green curve depicted in

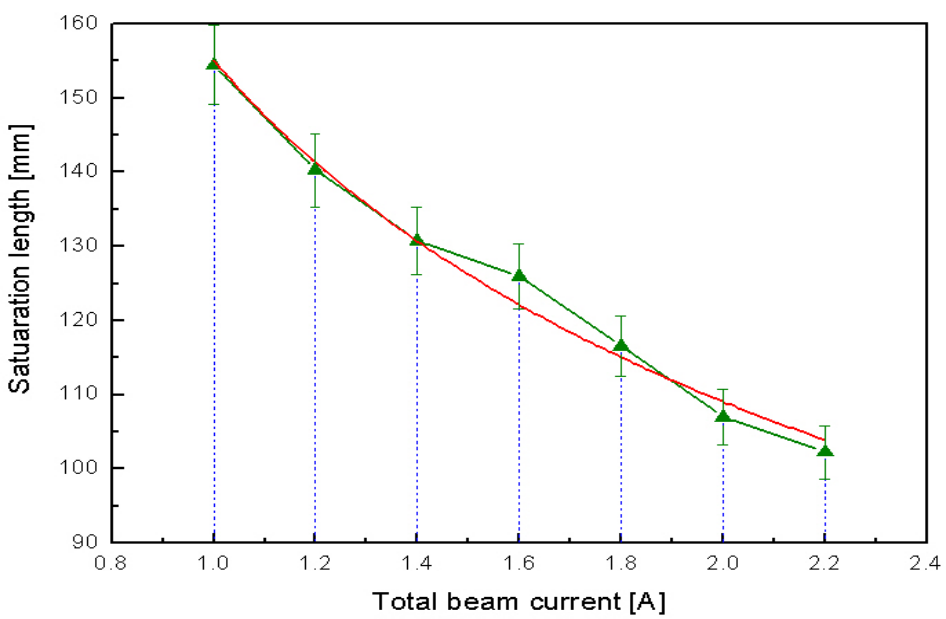

Figure 6.13: The variation of the saturation length of the 30-GHz mode from Figure 6.12 with beam current (green curve). The solid red curve is given by $y = Bx^n$.

Figure 6.13 is an estimate. For example, the value of the saturation length for 1.2 A was generated by averaging $z = 135.5$ mm and $z = 145$ mm for the red curve in Figure 6.12. Likewise, the saturation length for 2.2 A (cyan curve) was obtained by calculating the average of $z = 97.5$ mm and $z = 107$ mm in Figure 6.12.

To quantify the variation of the saturation length with total beam current, the green curve in Figure 6.12 is fitted with a power function given by

$$y = Bx^n. \tag{6.1}$$

The fitting parameters, B and n, determined from Figure 6.12 equal 155.1 ± 1.78 and -0.51 ± 0.025. Hence, as the beam current varies from 1.0 A to 2.2 A, the saturation length decreases from 155 mm to 103 mm. Therefore, the advantage of using two 1.1-A beams over, say, two 0.5-A beams is clear: not only does it reduce the length of the interaction region by 33%, but we also get a larger amplification (higher gain). The disadvantage of using high-current electron beams for amplification is that they require larger magnetic fields to counteract space-charge expansion. For instance, to focus 0.6-A and 0.7-mm beams, we would need a magnetic field of the order of 0.075 T. By contrast, 1.1-A and 0.7-mm beams would require 0.14 T, which is a fairly large value for a compact radiation source.

6.2 Studies of frequency dependence

In the previous section, we studied the interaction of two electron beams at 30 GHz. We start Section 6.2 by analyzing the magnitude of ac axial electric field at medium interaction frequencies, specifically, 110 GHz and 210 GHz. The second part of Section 6.2 is devoted to space-charge effects at low and medium interaction frequencies.

6.2.1 Axial electric field analysis

Figure 6.14 shows an FFT of $|E_z|$ for two 0.7-mm cold beams interacting at 110 GHz. For the red curve, the beam currents were 0.5 A and their energies 20 keV and

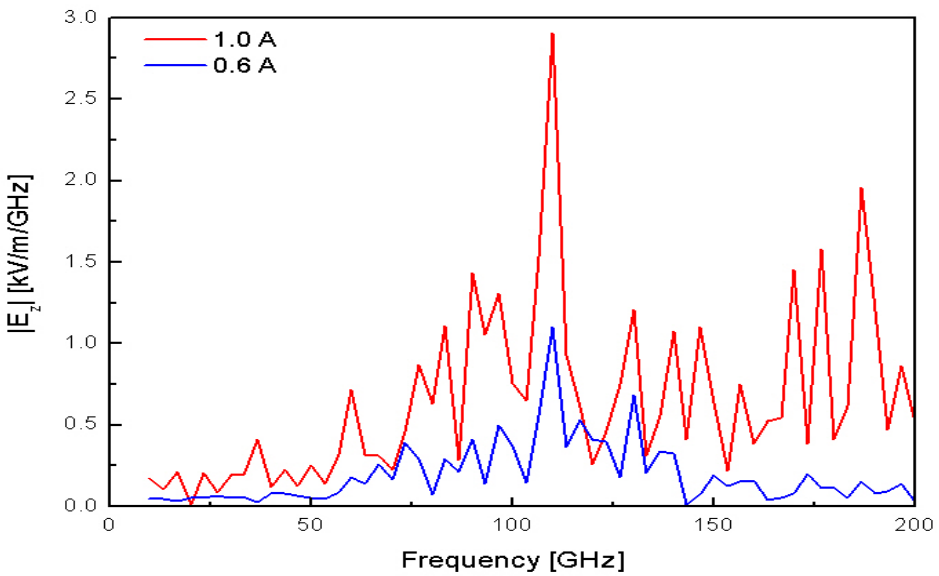

Figure 6.14: FFT of $|E_z|$ for the interaction of two 0.7-mm cold beams at 110 GHz. The blue and red curves correspond to $I = 0.6$ A and $I = 1.0$ A.

19.165 keV. For the blue curve, the beam currents were 0.3 A each and the corresponding energies equaled 20 keV and 19.350 keV. Both curves in Figure 6.14 were recorded at $z = 164$ mm, before the onset of nonlinearities. To resolve $|E_z|$ well (as explained in Section 5.3), the curves were obtained using a 0.3-ns time window, which was equivalent to 33 periods at 110 GHz. The FFT frequency window ranged from 10 GHz to 200 GHz, while the frequency resolution, corresponding to the 0.3-ns time window, was equal to 3.3 GHz.

As predicted by Equation 4.39, for both currents in Figure 6.14 the largest frequency component occurs at 110 GHz. As opposed to theory, however, the simulation

results exhibit a clear multi-mode behavior and the curves look much worse than for the interaction at 30 GHz in Figure 6.3. In Figure 6.14, a rough estimate of the FWHM frequency gives 80 GHz for $I = 1.0$ A and 50–60 GHz for $I = 0.6$ A. These values are about a factor of 10 greater than those in Figure 6.3. Hence, the number of competing modes in Figure 6.14 is significantly greater than for the interaction at 30 GHz (Figure 6.3).

As in Figure 6.3, the higher the total beam current in Figure 6.14, the larger the magnitude of competing modes in relation to $|E_z|$ of the 110 GHz mode. Indeed, a rough estimate of the average signal-to-noise ratio in Figure 6.14 yields 3.9 and 3.0 for $I = 0.6$ A and $I = 1.0$ A, respectively. Note that these values are about a factor three less than those for the interaction at 30 GHz in Figure 6.3. As will be shown in the next chapter, driven or modulated beams can be made to exhibit a single-mode behavior even at frequencies as high as 1 THz.

Our next task is to study the evolution of $|E_z|$ with longitudinal distance so we can eventually compare G_{sim} and G_{th} for interactions at medium frequencies. Figure 6.15 displays the variation of $|E_z|$ with longitudinal distance, z, for the interactions discussed in Figure 6.14.

For $I = 0.6$ A in Figure 6.15, the 110-GHz mode is initially smaller than both TM_{01} and TM_{02} waveguide modes. However, at about the same location as the 30-GHz mode in Figure 6.4, the 110-GHz mode overtakes the waveguide modes and grows without saturating. It will be shown later that its gain equals 0.289 dB/mm, which is within 0.4% (excluding error bars) of that of the 30-GHz mode in Figure 6.4. Although the TM_{01} waveguide mode (open squares) is the largest mode at the start of the simulation, it does not grow over the range of z values shown. By contrast, the TM_{02} mode (open circles) starts to grow around $z = 100$ mm at about the same rate as the 110-GHz mode. As a result, at the end of the simulation, the magnitude of the 110-GHz mode is merely a factor of 1.7 greater than that of the TM_{02} mode.

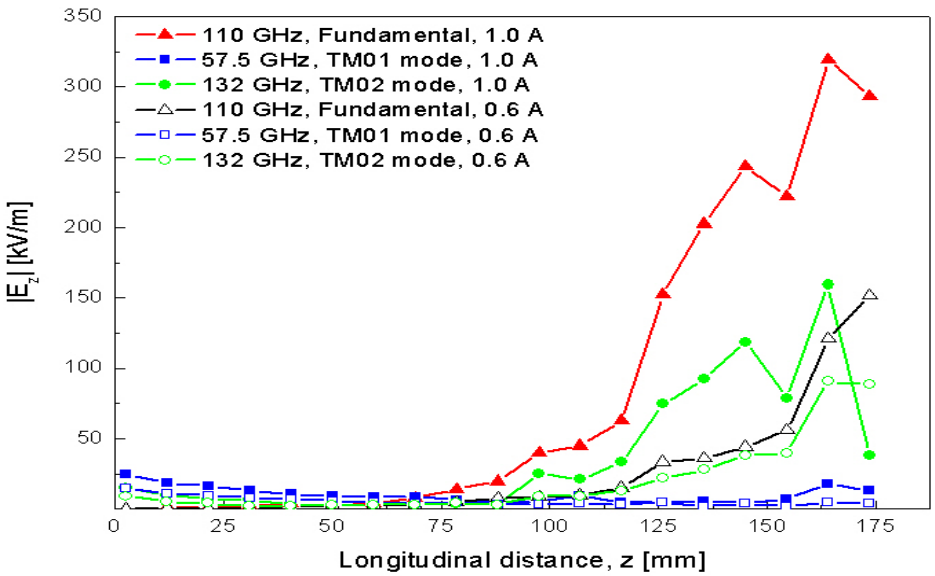

Figure 6.15: $|E_z|$ versus z for the interaction of two 0.7-mm cold beams at 110 GHz for $I = 0.6$ A and $I = 1.0$ A. The solid and open triangles represent a 110-GHz mode. The solid and open squares represent a TM_{01} waveguide mode, while the solid and open circles correspond to a TM_{02} waveguide mode.

Hence, the 110-GHz mode is not the most dominant mode, which is in contrast to what we observed for the interaction at 30 GHz in Figure 6.4.

For $I = 1.0$ A in Figure 6.15, the 110-GHz mode is again the smallest mode at the beginning of the simulation and overtakes the waveguide mode at about $z = 80$ mm. Note that the 110-GHz mode saturates at the same longitudinal location as the 30-GHz mode in Figure 6.5. In addition, the gain of the former equals 0.35 dB/mm and differs from that of the latter by 2.2% (excluding error bars). According to Figure 6.15, the TM_{01} waveguide mode (solid squares) first decreases and then increases towards the end of the simulation. Still, its magnitude there is less than at the start of the simulation. As opposed to the TM_{01} waveguide mode, the TM_{02} waveguide mode (solid circles) starts to grow at about $z = 90$ mm and follows the shape of the 110-GHz mode very closely (note the dip in both modes before saturation). At

the point of saturation, the magnitude of the 110-GHz mode is only twice as large as that of the TM_{02} waveguide mode. Hence, the 110-GHz mode is far from being dominant. This contradicts what we observed in Figure 6.5 for the interaction of 0.5-A beams at 30 GHz. It should be noted that no harmonics, if any, are shown in Figure 6.15 because of the frequency window used (10 GHz to 200 GHz) to record the data.

For $I = 1.0$ A in Figure 6.15, we studied the variation of $|E_z|$ for only three modes. Figure 6.16 depicts the evolution of $|E_z|$ for of all modes, within the range $10 \leq f \leq 200$ GHz, for the interaction of two 0.7-mm and 0.5-A cold beams with the same energies as the red curve in Figure 6.14. The left-hand vertical axis in

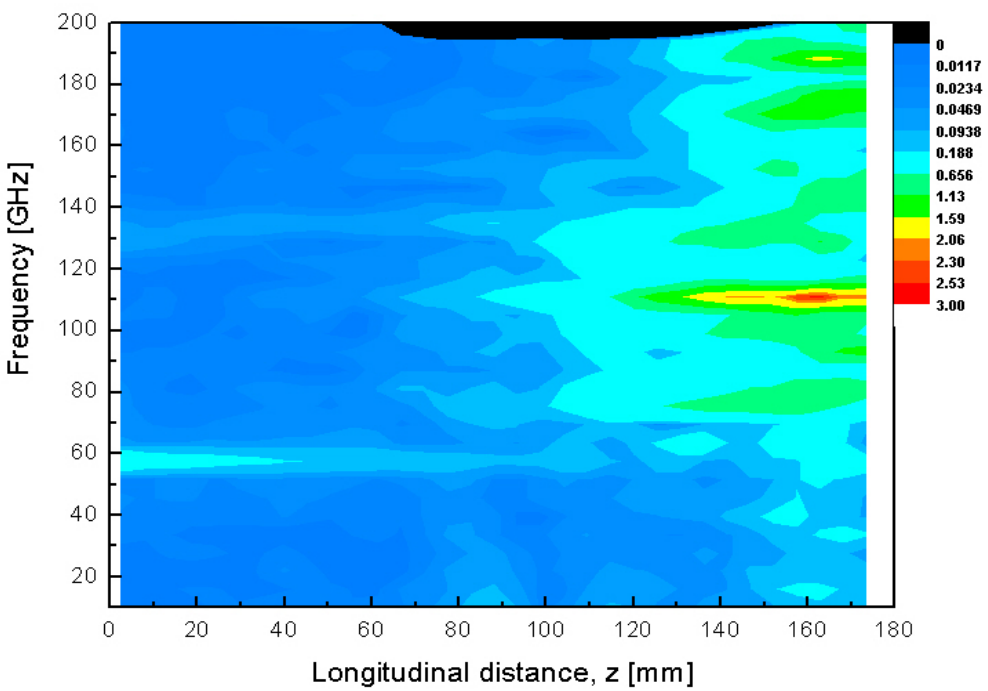

Figure 6.16: Contour plot of $|E_z|$ for the interaction of two 0.7-mm and 0.5-A cold beams at 110 GHz.

Figure 6.16 is frequency in units of GHz, the horizontal axis is longitudinal distance,

z, in units of mm. A color scale legend next to the right-hand vertical axis gives numerical values of $|E_z|$ in units of (kV/m)/GHz.

Equation 4.39 predicts that the interaction frequency of two 0.7-mm and 0.5-A beams with energies 20 keV and 19.165 keV will be 110 GHz. According to Figure 6.16, the 110-GHz mode does become the largest frequency component. However, note that the interaction at 110 GHz is markedly different from the interaction at 30 GHz depicted in Figure 6.6. Specifically, the interaction at 110 GHz exhibits a significantly stronger multi-mode behavior. As we saw in Figure 6.14, the FWHM frequency for the interaction in Figure 6.16 is about an order of magnitude greater than that in Figure 6.3. Despite a marked difference between the interactions at 30 GHz and 110 GHz, it will be shown that the gain of the 110-GHz mode (0.35 dB/mm) is within 2.2% (excluding error bars) of that of the 30-GHz mode (0.358 dB/mm) from Figure 6.6.

Comparing Figures 6.6 and 6.16, TM_{01} and TM_{02} waveguide modes at 57.5 GHz and 132 GHz can again be picked out initially, the TM_{01} mode being the more prominent of the two in both cases. The TM_{01} mode in Figure 6.16 varies in a similar fashion to that in Figure 6.6. The difference between the two is that in Figure 6.16 the magnitude of the TM_{01} at the end of the simulation is still less than at the start. As we can see in Figure 6.16, the TM_{02} waveguide mode grows markedly and its magnitude becomes half as large as that of the 110-GHz mode at about $z =$ 164 mm. This means that the 110-GHz mode is not dominant, which is in contrast to what we found for the interaction at 30 GHz in Figure 6.6. Last but not least, note that no harmonics are shown in Figure 6.16 owing to the frequency window used (10 GHz to 200 GHz) to record the data.

Having discussed the interaction of two electron beams at 30 GHz and 110 GHz, we will now look at the interaction of two electron beams at 210 GHz. An FFT plot shown in Figure 6.17 is similar to those in Figures 6.3 and 6.14 with the exception

that Figure 6.17 displays $|E_z|$ as a function of frequency for the interaction of two 0.7-mm cold beams at 210 GHz. As in Figures 6.3 and 6.14, the red and blue curves

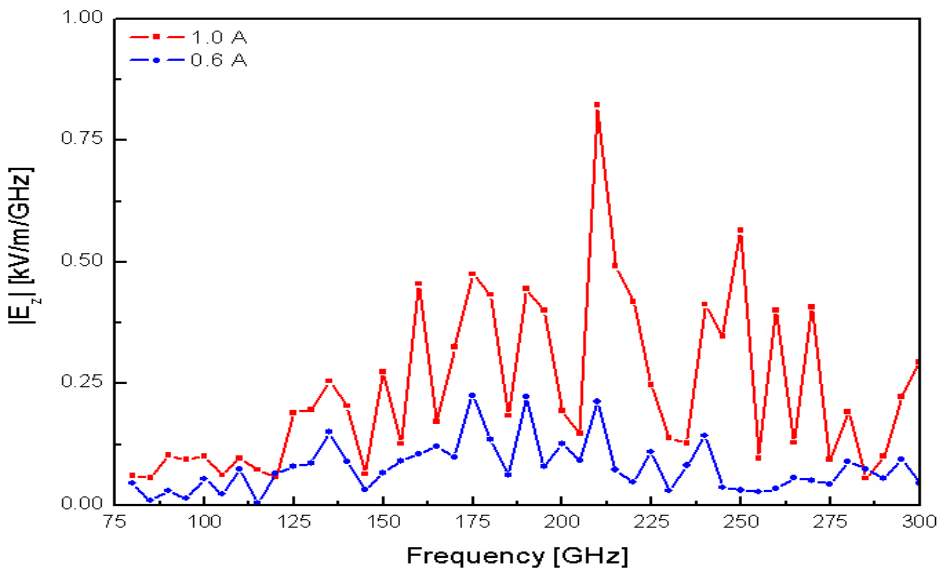

Figure 6.17: FFT of $|E_z|$ for the interaction of two 0.7-mm cold beams at 210 GHz. The blue and red curves correspond to $I = 0.6$ A and $I = 1.0$ A.

correspond to $I = 1.0$ A and $I = 0.6$ A, respectively. For $I = 1.0$ A, the beam energies were 20 keV and 19.549 keV. For $I = 0.6$ A, the beam energies used were 20 keV and 19.609 keV. The curves in Figure 6.17 were recorded at a longitudinal position of 164 mm. The FFT frequency window ranged from 80 GHz to 300 GHz. To resolve $|E_z|$ well (as explained in Section 5.3) over the frequency window used, the FFT curves were obtained using a 0.2-ns time window, which was equivalent to 42 periods at 210 GHz. The frequency resolution, corresponding to the 0.2-ns time window, was equal to 5 GHz.

When we explored the interactions at 30 GHz and 110 GHz in Figures 6.3 and 6.14, the 30- and 110-GHz modes were the largest frequency components for both 0.6 A and 1.0 A. Likewise, in Figure 6.17, the largest frequency component

for 1.0 A occurs at 210 GHz. However, as can be seen in Figure 6.17, the 210-GHz mode is no longer the largest component for 0.6 A, its magnitude being less than or comparable to that of the neighboring modes. This is most likely due to a combination of numerical noise and small ΔE (beam energy difference), which shrinks with increasing interaction frequency and decreasing beam current (Equation 4.39). For instance, ΔE for two 0.7-mm and 0.3-A beams interacting at 30 GHz is 2.4 keV and, thus, over a factor of 6 greater than that (391 eV) for the interaction of two 0.7-mm and 0.3-A beams at 210 GHz.

The interaction at 110 GHz in Figure 6.14 exhibited clear multi-mode behavior. As can be seen in Figure 6.17, the multi-mode behavior is even more pronounced for the interaction at 210 GHz. Considering the FFT curve for $I = 1.0$ A in Figure 6.17, a rough estimate of its FWHM frequency yields 125 GHz. This value is over a factor of 10 and 1.5 greater than that in Figures 6.3 and 6.14, respectively. The same holds true for $I = 0.6$ A. Hence, we are led to conclude that the FWHM frequency is affected by a given interaction frequency. Namely, the larger the interaction frequency is, the wider (worse) the FWHM frequency becomes.

As we did for 30 GHz and 110 GHz, we will next examine how $|E_z|$ varies with longitudinal distance, z, for the interaction at 210 GHz. In Figure 6.18, the variation of $|E_z|$ is displayed for the interaction of two 0.7-mm beams with the same energies as in Figure 6.17. The red and blue curves correspond to $I = 1.0$ A and $I = 0.6$ A, respectively.

For 0.6 A in Figure 6.18, the 210-GHz mode starts out as the smaller of the two modes and overtakes the TM_{02} waveguide mode around $z = 60$ mm. Like the 30- and 110-GHz modes in Figures 6.4 and 6.15, the 210-GHz mode does not reach saturation within the range $2.5 \leq z \leq 173.5$ mm. It will be shown later that the gain of the 210-GHz mode is 0.298 dB/mm and is within 3% (excluding error bars) of that of the 30- and 110-GHz modes. This suggests that G_{sim} is independent of interaction

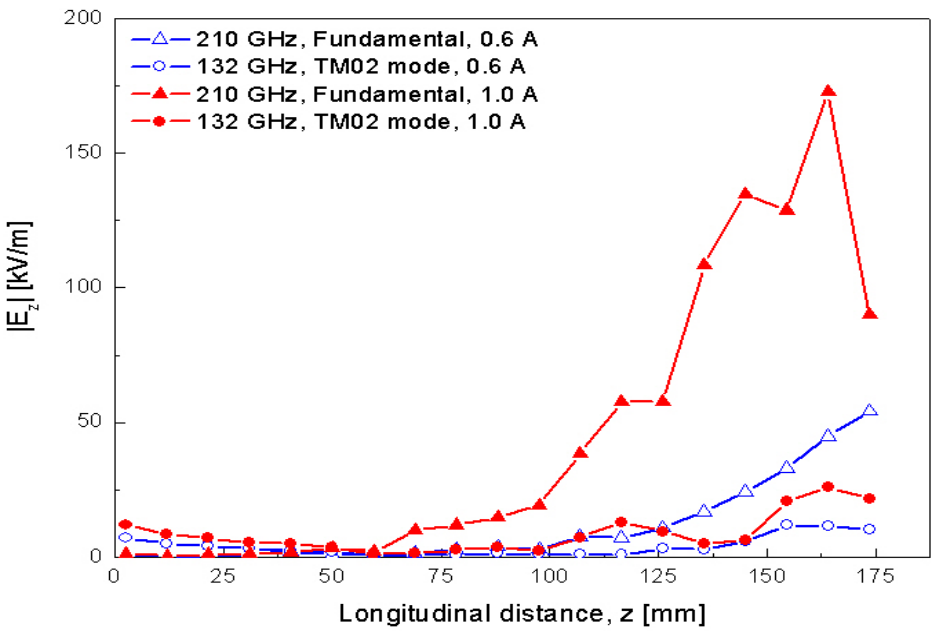

Figure 6.18: $|E_z|$ versus z for the interaction of two 0.7-mm cold beams at 210 GHz for $I = 0.6$ A and $I = 1.0$ A. The solid and open triangles represent a 210-GHz mode. The solid and open circles represent a TM_{02} waveguide mode.

frequency. According to Figure 6.18, the TM_{02} waveguide mode (open circles) grows towards the end of the simulation. However, its $|E_z|$ at the end of the simulation is merely a factor 1.4 greater than at the start. Hence, G_{sim} of the 210-GHz mode is much greater than that of the TM_{02} waveguide mode. Nevertheless, as we saw in Figure 6.17, the 210-GHz mode is far from being the most dominant mode. Note that Figure 6.18 shows neither harmonics nor the TM_{01} waveguide mode at 57.5 GHz. This was due to the frequency window (80 GHz to 300 GHz), which was dictated by the PIC code used (Section 5.2).

For 1.0 A in Figure 6.18, the 210-GHz mode overtakes the TM_{02} waveguide mode at about the same location as for 0.6 A. Even though the TM_{02} mode grows during the latter part of the simulation, it is clear from Figure 6.18 that G_{sim} of the 210-

GHz mode is much greater than that of the TM_{02} waveguide mode. Despite this, as can be seen in Figure 6.17, by no means is the 210-GHz mode most dominant. Comparing 30-, 110-, and 210-GHz modes in Figures 6.5, 6.15, and 6.18 for 1.0 A, we see that they saturate at the same longitudinal position of $z = 164$ mm. It will be shown later that G_{sim} of the 210-GHz mode equals 0.345 dB/mm and is within 3.5% of that of the 30-GHz mode and within 1.2% of that of the 110-GHz mode (excluding error bars in both cases). This again suggests that G_{sim} is independent of interaction frequency.

In Figure 6.18, we explored the variation of $|E_z|$ for two modes. Figure 6.19 depicts the evolution of $|E_z|$ for all modes, from 80 GHz to and including 300 GHz, for the interaction of two 0.7-mm and 0.5-A cold beams with the same energies as the red curve in Figure 6.17. Similar to Figures 6.6 and 6.16, the left-hand vertical axis in Figure 6.19 is frequency in units of GHz. The horizontal axis is longitudinal distance, z, in units of mm. Also, a color scale legend next to the right-hand vertical axis gives numerical values of $|E_z|$ in units of (kV/m)/GHz.

Over the range $150 \leq z \leq 165$ mm, according to Figure 6.19, the 210-GHz mode becomes the largest component. This is in agreement with Equation 4.39. However, the 210-GHz mode is by no means dominant and the interaction exhibits clear multi-mode behavior. In fact, comparing Figures 6.6, 6.16, and 6.19, the interaction at 210 GHz produces the largest number of competing modes. As we estimated in Figure 6.17, the average FWHM frequency is an order of magnitude greater than that for the interaction at 30 GHz and a factor of 1.5 greater than that for the interaction at 110 GHz. In spite of this marked difference between the interactions at 30 GHz, 110 GHz, and 210 GHz, it will be shown in the next subsection that the gain of the 210-GHz mode is within 3.5% of that of the 30-GHz and 110-GHz modes (error bars excluded). Also, note that the 30-, 110-, and 210-GHz modes shown in Figures 6.5, 6.15, and 6.18 reach saturation at a longitudinal position of z

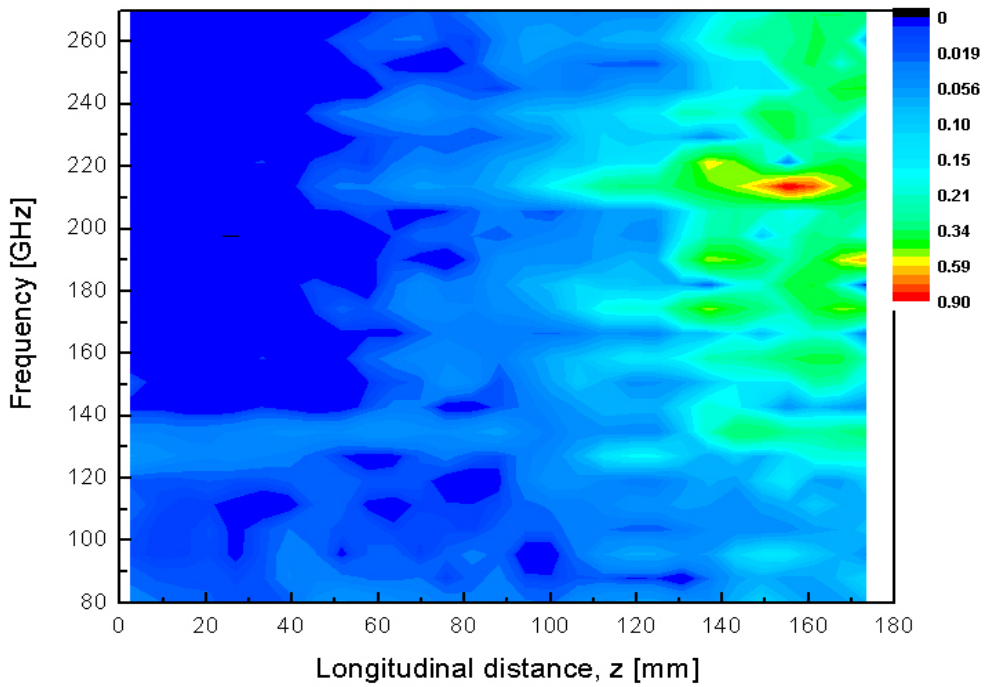

Figure 6.19: Contour plot of $|E_z|$ for the interaction of two 0.7-mm and 0.5-A cold beams at 210 GHz.

= 164 mm. This suggests that the saturation length for two 0.7-mm and 0.5-A cold beams interacting at 30 GHz, 110 GHz, and 210 GHz is independent of interaction frequency.

As we have already stated, the TM_{01} waveguide mode at 57.5 GHz and harmonics, if any, are absent in Figure 6.19 due to the frequency window used (80 GHz to 300 GHz). In Figure 6.19, at the start of the simulation, we can again identify the TM_{02} waveguide mode at 132 GHz. An unusual width of the TM_{02} waveguide mode can be attributed to a coarse resolution for the FFT analysis ($\Delta f = 5$ GHz). According to Figure 6.19, the TM_{02} waveguide mode grows towards the end of the interaction and at $z = 164$ mm its magnitude is about a factor of 7 less than that of the 210-GHz mode. As it will be shown in Chapter 7, waveguide modes are always

negligible in comparison with driven modes (modes at modulating frequencies) in the case of modulated beams.

6.2.2 Relationship between gain and space charge

The emphasis in this dissertation is on the gain of exponentially growing modes and our next task is to take a closer look at the 30-, 110-, and 210-GHz modes from Figures 6.4, 6.5, 6.15, and 6.18 so we can compare gain from simulations with that given by Equation 4.38.

Plotted in Figure 6.20 is the variation of $|E_z|$ with longitudinal distance, z, for

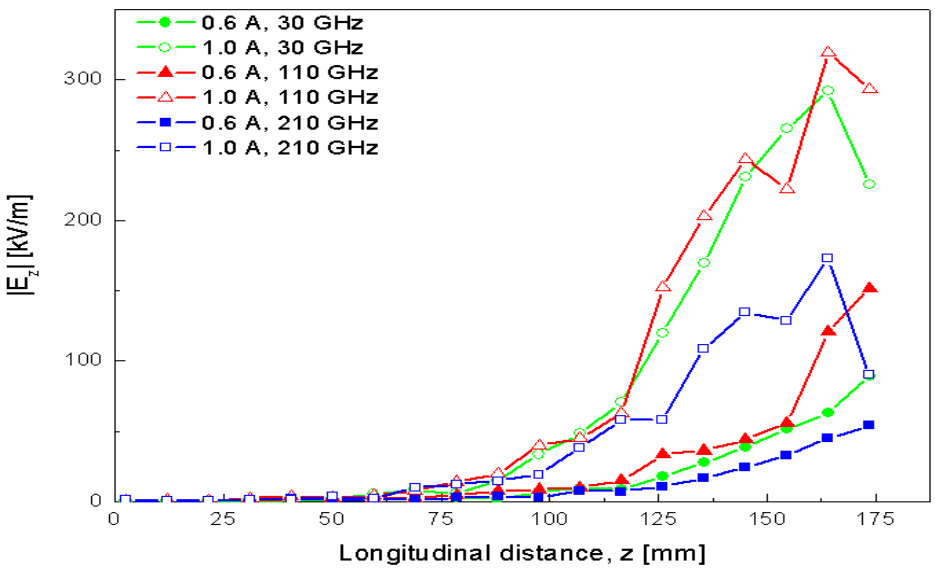

Figure 6.20: $|E_z|$ versus z for the interaction of two 0.7-mm cold beams for I = 0.6 A (solid symbols) and I = 1.0 A (open symbols). The green, red, and blue curves correspond to 30-, 110-, and 210-GHz modes.

the interaction of two 0.7-mm cold beams at 30 GHz (green curves), 110 GHz (red curves), and 210 GHz (blue curves). The solid and open symbols correspond to I =

0.6 A and $I = 1.0$ A, respectively.

As can be seen in Figure 6.20, the growth rate of 30-, 110-, and 210-GHz modes increases with increasing beam current. This is consistent with Equation 4.38, the theoretical gain formula. Note that $|E_z|$ of the 210-GHz mode is smaller than that of 30- and 110-GHz modes for both currents, which can be attributed to the fact that ΔE for the interaction at 210 GHz is less than that for the interaction at 30 GHz and 110 GHz. For $I = 1.0$ A in Figure 6.20, ΔE for the interaction at 210 GHz equals 451 eV and is approximately a factor of 1.8 and 6.7 less than that for the interaction at 110 GHz and 30 GHz, respectively. Hence, the beams interacting at 30 GHz and 110 GHz exchange energy and bunch more efficiently than those interacting at 210 GHz.

According to Figure 6.20, no mode saturation is observed for $I = 0.6$ A over the range of z values shown. For $I = 1.0$ A, however, all three modes, namely, the 30 GHz (open circles), 110 GHz (open triangles), and 210 GHz (open squares), reach saturation at the same longitudinal location of $z = 164$ mm. This leads us to conclude that the saturation length is independent of interaction frequency for two 0.7-mm cold beams interacting at 30 GHz, 110 GHz, and 210 GHz for $I = 0.6$ A and $I = 1.0$ A.

If we plot the modes in Figure 6.20 on a log-linear scale (discarding the nonlinear portions), fit them with Equation 5.9 and substitute the values of R into Equation 5.10, then we can compare G_{sim} of the 30-, 110-, and 210-GHz modes with G_{th} given by Equation 4.38.

Figure 6.21 shows gain as a function of total beam current, I, for the interaction of two 0.7-mm cold beams at 30 GHz (circles), 110 GHz (triangles), and 210 GHz (squares). The solid green, red, and blue curves represent G_{th} for the three modes.

Comparing G_{sim} and G_{th} at 30 GHz, the former and the latter are within 6.2%

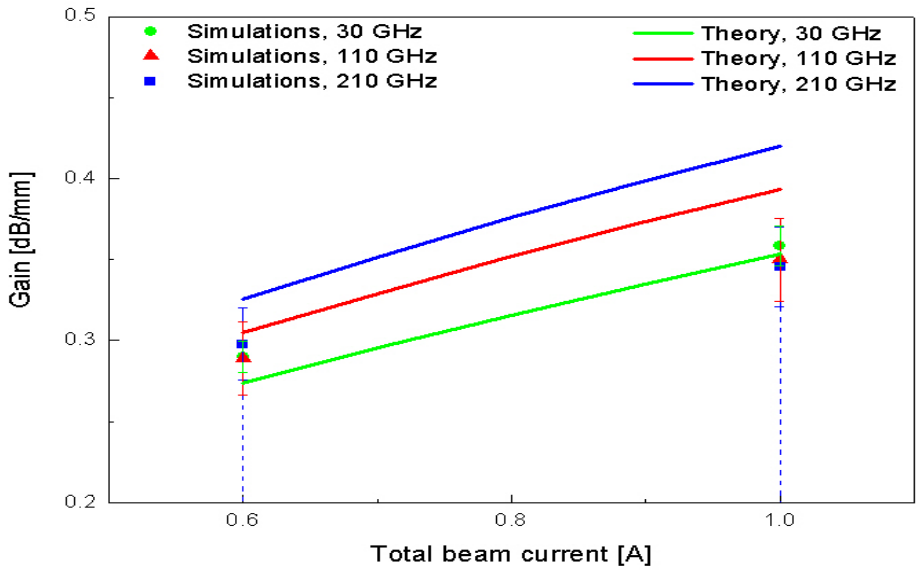

Figure 6.21: The variation of gain with total beam current for three modes: 30-GHz (circles), 110-GHz (triangles), and 210-GHz (squares). The solid green, red, and blue curves correspond to theory given by Equation 4.38.

and 2% of each other (excluding error bars) for 0.6 A and 1.0 A. At 110 GHz, the percent difference between G_{sim} and G_{th} increases from 4% to 9.9% (ignoring error bars) as the total beam current varies from 0.6 A to 1.0 A. Finally, at 210 GHz, G_{sim} differs from G_{th} by 9.7% for 0.6 A and by as much as 17.7% for 1.0 A, error bars being excluded. Hence, the discrepancy between G_{sim} and G_{th} increases with increasing interaction frequency. We will see this trend continue in the next chapter, which treats interaction frequencies from 30 GHz up to and including 1 THz.

The marked discrepancy between G_{sim} and G_{th}, especially for high frequencies, can be blamed in part on F (Figure 3.3), the plasma frequency reduction factor in Equation 4.38 for G_{th}. Figure 3.3 was plotted assuming a confined beam (zero scalloping, no variation of the beam envelope). However, as can be seen in Figure 6.2, scalloping was present in every simulation considered in this dissertation. In the

case of unfocused beams (nonzero scalloping), both $|E_z|$ and space charge are less in comparison with their counterparts for confined beams [12, 15]. As a consequence, F for unfocused beams is less than that for focused beams by 10–20% depending on the interaction frequency and the ratio of r_a to r_b, where r_a is the beam pipe radius. It is reasonable to assume that F in Figure 3.3 is overestimated and yields values of G_{th} that are larger than they should be. Hence, the large difference between G_{sim} and G_{th} seen in Figure 6.21.

Although the agreement between G_{sim} and G_{th} becomes poor as we increase the interaction frequency from 30 GHz to 210 GHz, the circles, triangles, and squares in Figure 6.21 appear to be on top of one another for both currents. According to Figure 6.21, the percent variation of G_{sim} is less than 3% and within 4% for 0.6 A and 1.0 A (ignoring error bars). Hence, G_{sim} for the interaction at 30 GHz agrees very well with that for the interaction at 110 GHz and also with that for the interaction at 210 GHz. Therefore, we can conclude that G_{sim} is independent of interaction frequency for two 0.7-mm cold beams interacting at 30 GHz, 110 GHz, and 210 GHz for both $I = 0.6$ A and $I = 1.0$ A.

Figure 6.22 combines the data in Figure 6.21 with some of the data in Figure 6.11 and displays the gain of 30-, 110-, and 210-GHz modes as a function of space charge density in units of A/mm^2. The green, red, and blue symbols in Figure 6.22 correspond to 30-, 110-, and 210-GHz modes.

For 30 GHz in Figure 6.22, the average deviation between G_{sim} and G_{th} is approximately 3.5% (ignoring error bars). For 110 GHz and 210 GHz, the average deviation increases to 9.2% and 13.2% (excluding error bars), respectively. Hence, the higher the interaction frequency, the larger the discrepancy between simulations and theory. As we argued earlier, this is partially due to the plasma frequency reduction factor (Figure 3.3) being overestimated in Equation 4.38. We will continue to see this trend in Chapter 7 for modulated beams.

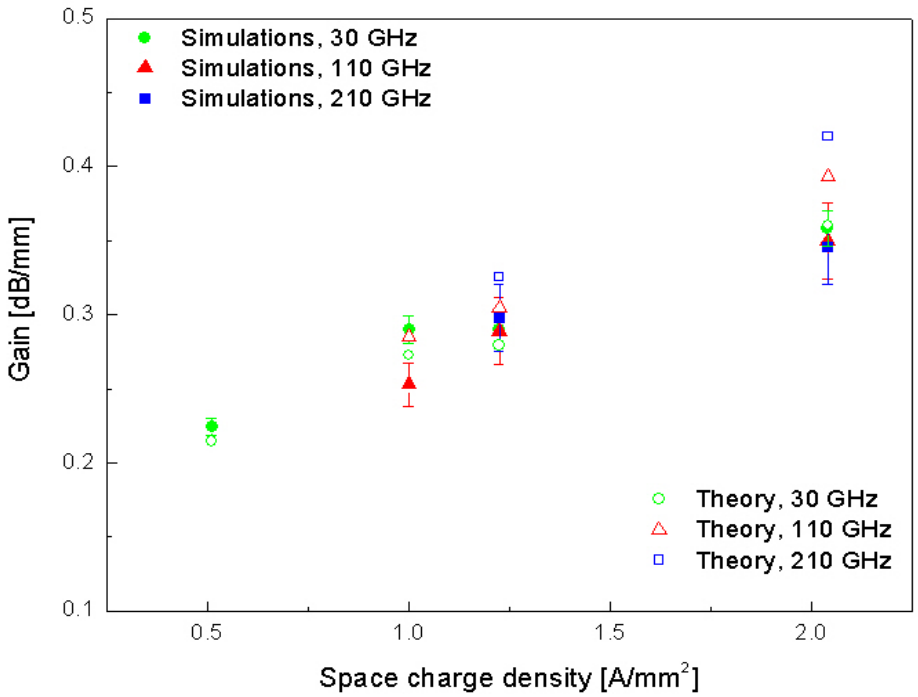

Figure 6.22: The variation of gain of 30-, 110-, and 210-GHz modes with space charge density. The solid and open symbols represent simulations and theory.

When studying the interaction at 30 GHz (Figure 6.11), we concluded that both G_{sim} and G_{th} vary as $\sqrt{I/r_b^2}$. As can be seen in Figure 6.22, the same does not hold true for the interaction at 110 GHz and 210 GHz. Note that for the interaction of 1.0-mm beams at 30 GHz and 110 GHz (where space charge is unity), G_{sim} for 30 GHz differs from that for 110 GHz by as much as 12.8% (excluding error bars). However, for the interaction of 0.7-mm beams at 30 GHz, 110 GHz, and 210 GHz, the data points from simulations are on top of one another (including error bars). Hence, based on the limited amount of data at our disposal, we can state that G_{sim} is not dependent on interaction frequency for the interaction of 0.7-mm cold beams at 30 GHz, 110 GHz, and 210 GHz. It will be shown in Chapter 7 that the foregoing conclusion also applies to the interaction of 0.7-mm cold and modulated beams at

frequencies up to and including 1 THz.

6.3 Energy-spread effects

The small-signal theory presented in Chapter 4 is not applicable to beams with a nonzero energy spread. Since beams in the laboratory are never monoenergetic, in this section we examine the impact of nonzero energy spread on the gain of growing modes for the interaction of warm beams at low and medium frequencies. The interaction of warm beams at higher frequencies will be treated in the next chapter.

According to Appendix D, warm beams (with average energies E_1 and E_2) considered in this dissertation have Gaussian (bell-shaped) energy profiles and a FWHM energy for each is defined as a percentage of the average energy, E_{avg}, of two beams. When discussing warm beams in this dissertation, we will refer to them as having a certain amount of percent spread or percent energy spread, the former and the latter being used interchangeably throughout.

Figure 6.23 shows energy profiles for two 0.7-mm and 0.5-A beams with energies 20 keV and 16.95 keV. The three curves correspond to 1%, 3%, and 5% spread, which, in the case of 20 keV and 16.95 keV, is equivalent to 184.75 eV, 554.25 eV, and 923.75 eV. The corresponding FWHM energy from Equation D.4 is 369.5 eV, 1108.5 eV, and 1847.5 eV, respectively.

According to Figure 6.23, for 1% spread the beam energies are well-defined and we can expect the interaction to be as strong as that for cold beams (this will be shown later). Despite a certain amount of overlap for 3% spread, the beams can still be viewed as two separate beams. However, for percent energy spread as large as 5%, as can be seen in Figure 6.23, the two beams start to merge into a single beam. Hence, it is reasonable to expect the resulting interaction to be much weaker than

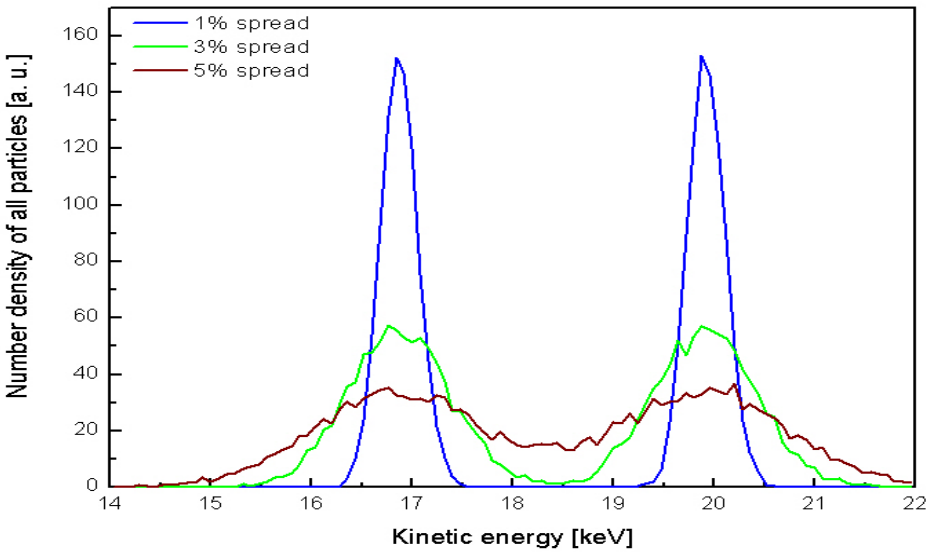

Figure 6.23: Gaussian energy profiles for warm 20- and 16.95-keV beams.

than that for 1% and 3% energy spread.

Equation 4.39 predicts that two 0.7-mm and 0.5-A cold beams with energies 20 keV and 16.95 keV will interact at 30 GHz and we saw in Figure 6.3 that the largest frequency component did occur at 30 GHz. In the case of two warm beams with the same parameters, the 30-GHz mode still grows exponentially. However, an FFT plot of $|E_z|$ shows that the peak frequency shifts from 30 GHz to 35 GHz and then to 22.5 GHz for beams with 3% and 5% energy spread, respectively. In addition, at the same longitudinal location of 145 mm as in Figure 6.3, the magnitude of the 30-GHz mode decreases by approximately 92% as energy spread increases from 0% to 5%, which is consistent with the energy profiles shown in Figure 6.23.

Figure 6.24 is similar to Figure 6.23 and depicts energy profiles for 0.5-A and 1.0-mm beams with energies 20 and 17.95 keV (solid curves) and 0.5-A and 1.4-mm beams with energies 20 and 18.5 keV (dashed curves). The red curves in Figure 6.24

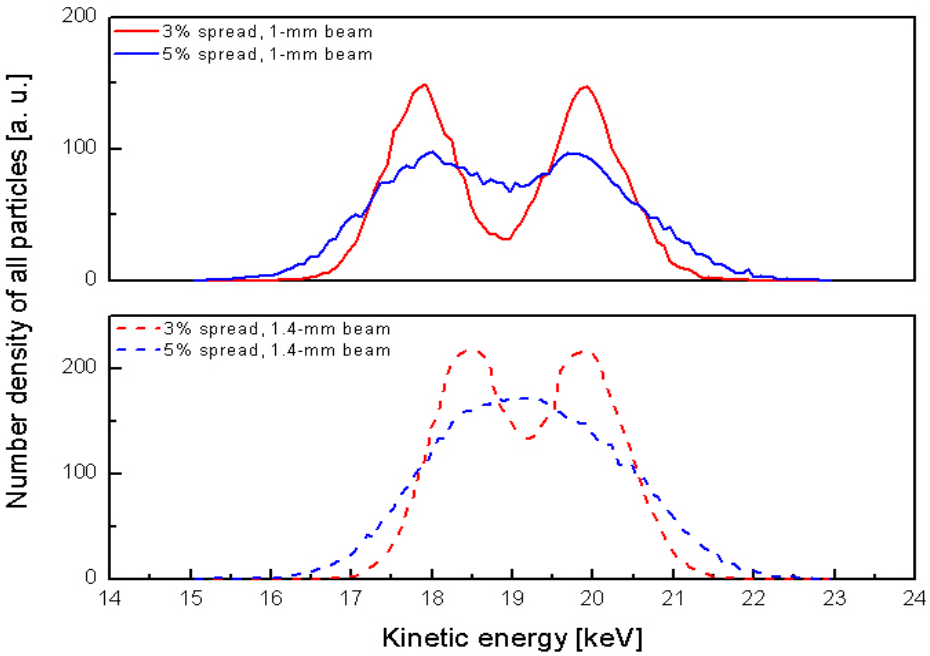

Figure 6.24: Gaussian energy profiles for warm beams with energies 20 keV and 17.95 keV (solid curves) and 20 keV and 18.5 keV (dashed curves).

correspond to 3% energy spread, while blue ones to 5% energy spread.

For the 1.0-mm beams, 3% energy spread is equivalent to 569.25 eV, while 5% energy spread equals 948.75 eV. The corresponding FWHM energy from Equation D.4 is 1138.5 eV and 1897.5 eV for 3% and 5% energy spread, respectively. For the 1.4-mm beams, due to a larger beam energy difference, 3% and 5% spread correspond to the FWHM energy of 1155 eV and 1925 eV, respectively.

According to Figure 6.24, the larger the beam radius and the warmer the beams are, the faster the beam energies overlap. For 5% energy spread, the beam energies for $r_b = 1.0$ mm are considerably overlapped but we are still able to identify two peaks belonging to the original energies. By contrast, as can be seen in Figure 6.24 for 5% energy spread, the beam energies corresponding to $r_b = 1.4$ mm merge to

yield a single beam and, thus, are indistinguishable. Hence, comparing Figures 6.23 and 6.24 for 5% energy spread, we can anticipate some interaction and nonzero gain for $r_b = 0.7$ mm and, possibly, $r_b = 1.0$ mm. However, we can be certain that no interaction and zero gain will result for the 1.4-mm warm beams with 5% energy spread.

We will next examine the variation of the magnitude of ac electric field, $|E_z|$, with longitudinal distance, z, for the interaction of 0.7-, 1.0-, and 1.4-mm warm beams at 30 GHz. This will be used later to study the effect of energy spread on numerical gain.

Figure 6.25 displays the variation of $|E_z|$ of a 30-GHz mode with z for the interaction of two 0.7-mm and 0.5-A beams with the same energies as in Figure 6.23. The four data sets correspond to 0% (magenta curve), 1% (blue curve), 3% (green curve), and 5% (burgundy curve) energy spread. The gray curves were obtained from Equation 5.9 and represent curve fits to the linear regions of the data.

In Figure 6.25, the warmer the beams are, the larger the initial value of $|E_z|$ is. As for the initial angles of $|E_z|$, they are positive for the magenta, green, and burgundy curves and negative for the blue curve. Note that the initial dip in $|E_z|$ shifts to lower values of z with increasing energy spread. According to Figure 6.25, the burgundy curve, corresponding to 5% spread, has the most number of dips. Moreover, it is the least linear among the curves shown.

According to Figure 6.25, the slope of the 30-GHz mode is unaffected provided percent energy spread is less than or equal to 1%. For percent spread greater than 1%, the slope of the 30-GHz mode, in relation to its value for cold beams, is reduced by approximately 19% and by as much as 66% for 3% and 5% spread, respectively. This is consistent with the energy profiles in Figure 6.23.

Figure 6.26 is similar to Figure 6.25 and again shows $|E_z|$ of a 30-GHz mode from

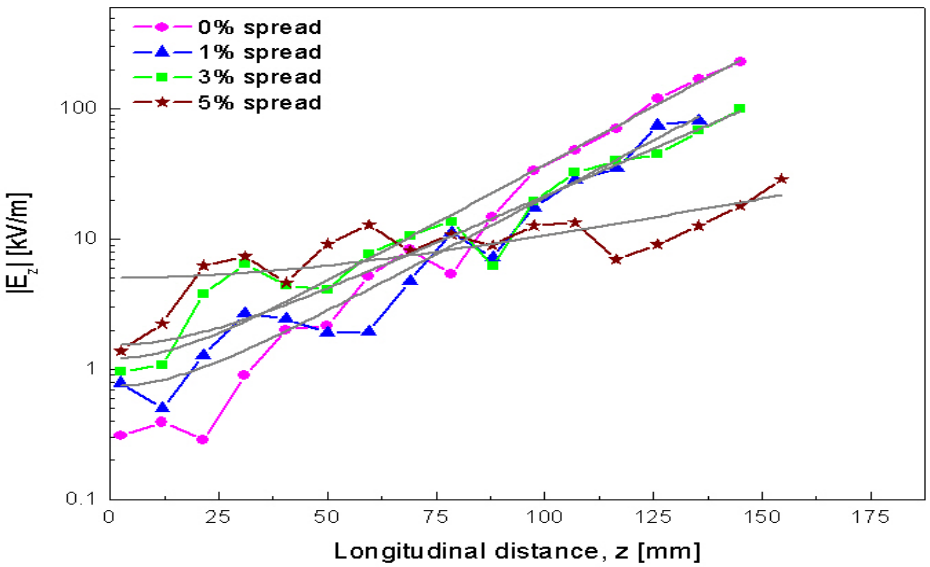

Figure 6.25: $|E_z|$ of a 30-GHz mode versus longitudinal distance, z, for 20- and 16.95-keV beams. The four curves correspond to 0% (magenta), 1% (blue), 3% (green), and 5% (burgundy) energy spread. Gray curves are curve fits given by Equation 5.9.

simulations involving 0.5-A beams with beam radii equal to 1.0 mm (top plot) and 1.4 mm (bottom plot). The beam energies used to generate the curves were 20 keV and 17.95 keV for two 1-mm beams and 20 keV and 18.5 keV for two 1.4-mm beams. The magenta, green, and burgundy curves in both plots correspond to 0%, 3%, and 5% spread, respectively. The gray curves (Equation 5.9) represent curve fits to the linear regions of the data.

For the 1-mm beams (top plot) in Figure 6.26, the initial value of $|E_z|$ appears to vary randomly. The initial angle of $|E_z|$ is positive for 3% and 5% spread, but negative for 0% spread. As in Figure 6.25, the burgundy curve (5% spread) is the least linear of the three data sets shown. In Figure 6.26, the slope of the 30-GHz mode is reduced by approximately 42% as percent energy spread ranges from 0% to 3%. In addition, as indicated by a horizontal gray curve in Figure 6.26, no growth

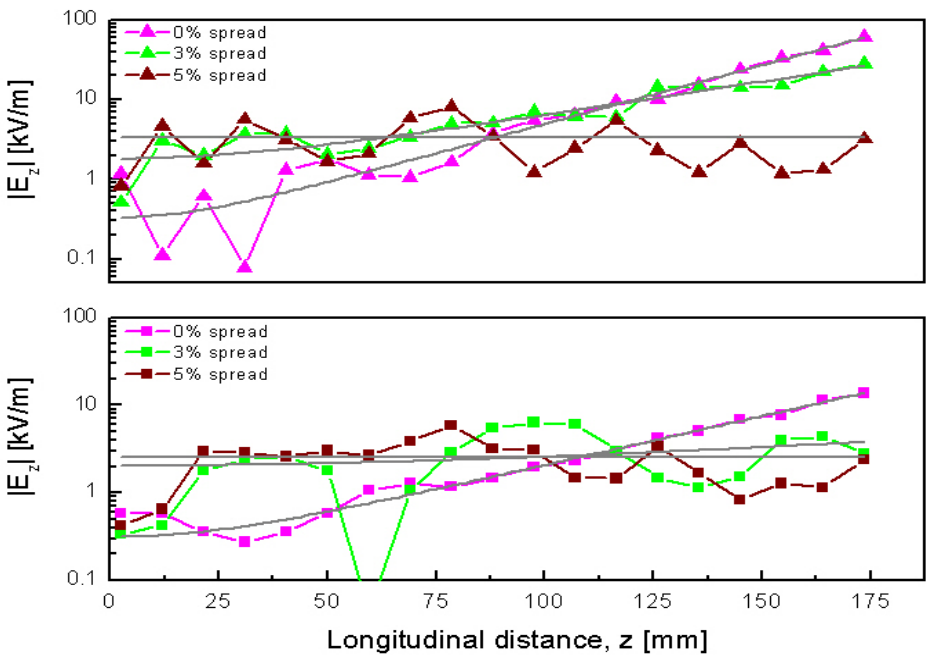

Figure 6.26: $|E_z|$ of a 30-GHz mode versus axial distance, z, for 20- and 17.95-keV (top plot) and 20- and 18.5-keV (bottom plot) beams. The three curves correspond to 0% (magenta), 3% (green), and 5% (burgundy) spread. Gray curves are curve fits given by Equation 5.9.

is observed for percent spread as large as 5%.

For the 1.4-mm beams (bottom plot) in Figure 6.26, the initial value of $|E_z|$ varies as randomly as it does for $r_b = 1.0$ mm. Note that the magenta curve (0% spread) in the bottom plot is markedly different from its counterpart in the top plot for values of z less than or equal to 40 mm. Also, the green curve (3% spread) is fairly linear in the top plot for values of z greater than or equal to 50 mm. By contrast, the green curve in the bottom plot oscillates over the same range. Due to a smaller energy difference for the 1.4-mm beams (Figure 6.24), the slope of the 30-GHz mode at 3% spread is as much as 72% less than that at 0% spread. Moreover, as is the case for the 1-mm beams, no growth results from the interaction of two 1.4-mm beams with 5%

spread, which is to be expected given the shape of the energy profile in Figure 6.24.

Having analyzed $|E_z|$ of a 30-GHz mode for warm beams with three different beam radii, we will now look at the variation of G_{sim} with energy spread. Figure 6.27 displays gain as a function of percent energy spread for the interactions considered

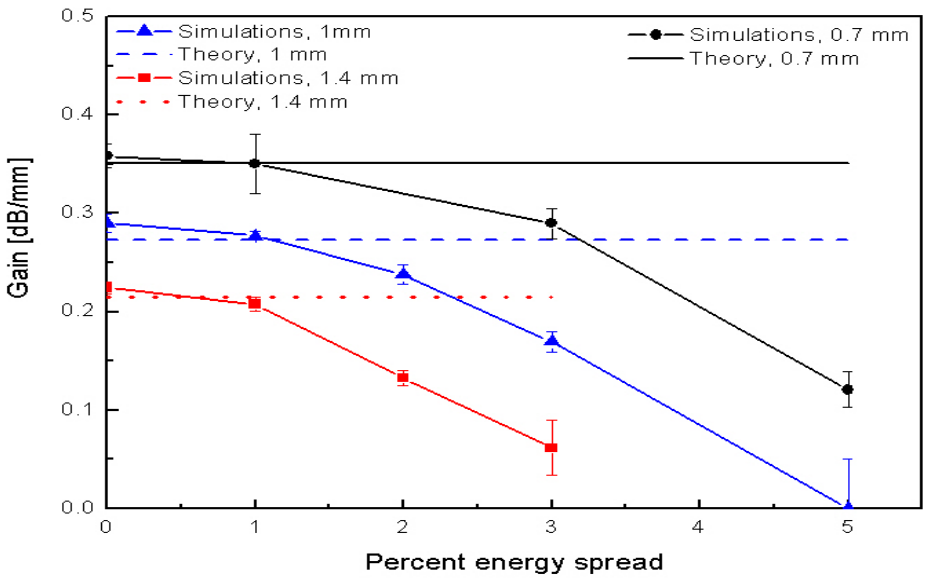

Figure 6.27: Gain of a 30-GHz mode versus percent energy spread for two 0.5-A beams with $r_b = 0.7$ mm (black curve), $r_b = 1.0$ mm (blue curve), and $r_b = 1.4$ mm (red curve). The dashed, dotted, and solid lines represent theoretical values for 0% spread (Equation 4.38).

in Figures 6.25 and 6.26. The solid, dashed, and dotted lines correspond to G_{th} (Equation 4.38) and are valid for cold beams.

For the blue curve in Figure 6.27, G_{th} is within 5.9% of G_{sim} for cold beams (ignoring error bars). Although Equation 4.38 is invalid for warm beams, the agreement between G_{th} and G_{sim} for beams with 1% spread is excellent, the two differing by as little as 1.5% (excluding error bars). However, already at 2% energy spread, as we can see in Figure 6.27, G_{sim} is 13% less than G_{th}. Also, in agreement with

Figure 6.26, no interaction is observed for beams with 5% spread due to the beam energies being markedly overlapped (Figure 6.24).

Examining the red curve in Figure 6.27, G_{th} is within 4.3% and 3.3% (ignoring error bars) of G_{sim} for 0% and 1% energy spread, respectively. Hence, the agreement is very good. However, the percent difference between G_{th} and G_{sim} increases from 38% to as much as 71% for beams with 2% and 3% energy spread. Moreover, comparing the energy profiles for 1.0- and 1.4-mm beams in Figure 6.24, we can predict no interaction and zero gain for the 1.4-mm beams with percent energy spread greater than 3% and less then 4%.

According to Figure 6.27, for percent energy spread greater than 1%, the percent difference between G_{th} and G_{sim} grows with increasing beam radius. Again, this is due to ΔE decreasing from 3.05 keV ($r_b = 0.7$ mm) to 2.05 keV and 1.5 keV for $r_b = 1.0$ mm and $r_b = 1.4$ mm, respectively. As a result, for the same amount of percent spread, the beam energies for $r_b = 1.4$ mm and $r_b = 1.0$ mm overlap and merge quicker than those for $r_b = 0.7$ mm.

Our analysis of the interaction of warm beams thus far has been at 30 GHz. Before closing this section, we will also look at the interaction of 0.5-A beams at a medium frequency, specifically, 110 GHz. According to Equation 4.39, the higher the interaction frequency, the smaller ΔE (beam energy difference) is. Hence, for the same amount of energy spread, it is reasonable to expect that beams interacting at 110 GHz will overlap/merge faster than those interacting at 30 GHz.

Figure 6.28 shows energy profiles for 0.5-A and 0.7-mm warm beams with energies 20 keV and 19.165 keV. The red, blue, and black curves correspond to 0.4%, 1%, and 2% energy spread, where, as was discussed earlier, energy refers to the average energy of two beams. Hence, 0.4%, 1%, and 2% energy spread are equivalent to 78.33 eV, 195.82 eV, and 391.65 eV. The corresponding values of FWHM energy

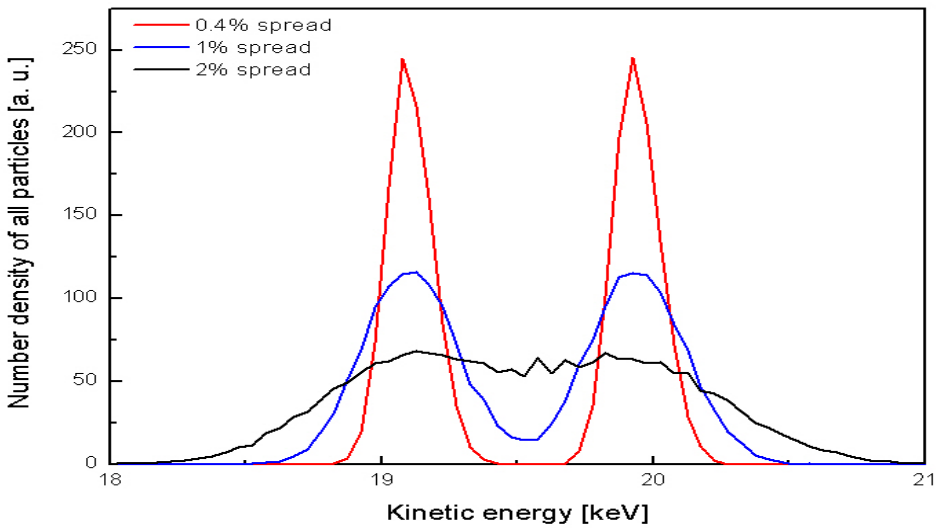

Figure 6.28: Gaussian energy profiles for warm 20- and 19.165-keV beams.

(Equation D.4) are 156.66 eV, 391.64 eV, and 783.3 eV, respectively.

For 0.4% energy spread in Figure 6.28, the energy profile has a well-defined FWHM energy and it is reasonable to expect that the interaction will be as efficient as that for cold beams. However, due to a smaller ΔE (835 eV as compared with 3.05 keV for beams in Figure 6.23), we should expect a weak interaction for 2% spread as 20- and 19.165-keV beams virtually merge to form a single beam.

Although the interaction of 0.5-A and 0.7-mm cold beams, with the same energies as those in Figure 6.28, gives rise to multiple modes (Figure 6.14), the largest frequency component, as predicted by Equation 4.39, occurs at 110 GHz. For the warm beams in Figure 6.28, an FFT of $|E_z|$ shows the peak frequency shifting from 110 GHz to 103.3 GHz and subsequently to 76.6 GHz for 0.4% and 1% energy spread, respectively. Moreover, as percent energy spread varies from 0% to 1%, the magnitude of the 110-GHz component shown in Figure 6.14 is reduced by more than a factor of 10. As we pointed out above, ΔE in Figure 6.28 is about a factor of

3.6 smaller than that in Figure 6.23. As a result, as can be seen in Figure 6.28, the interaction of 0.5-A and 0.7-mm warm beams at 110 GHz will most likely yield negligible gain for energy spread as small as 2%.

Figure 6.29 depicts the variation of $|E_z|$ of a 110-GHz mode with longitudinal distance, z, for the interaction of 0.7-mm and 0.5-A beams with the same energies as in Figure 6.28. The three data sets correspond to 0% (red curve), 0.4% (blue curve),

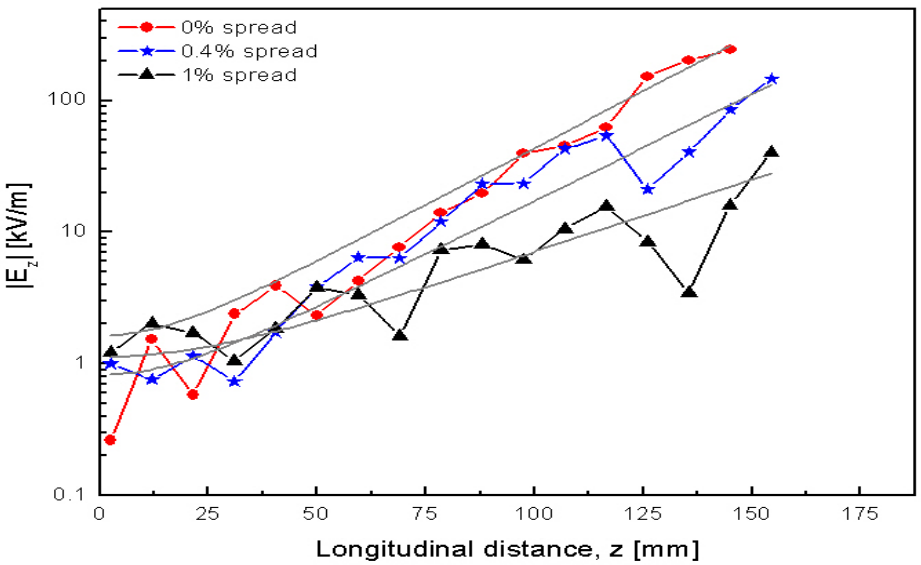

Figure 6.29: $|E_z|$ of a 110-GHz mode versus longitudinal distance, z, for two 0.7-mm and 0.5-A beams with energies 20 keV and 19.165 keV. The red, blue, and black curves correspond to 0%, 0.4%, and 1% spread. Gray curves are curve fits given by Equation 5.9.

and 1% spread (black curve). The gray curves are again given by Equation 5.9 and represent curve fits to the linear regions of the data in Figure 6.29.

The initial value of $|E_z|$ in Figure 6.29 increases with percent energy spread, which is what we also observed for interactions at 30 GHz in Figure 6.25. While the initial angle of $|E_z|$ is positive for 0% and 1.0% spread, it is negative for 0.4%.

The dips in the black curve appear to be more pronounced than those in the red and blue curves. In addition, the black curve is the least linear of the three curves shown. Note in Figure 6.29 that the slope for cold beams is approximately 7.2% more (ignoring error bars) than that for warm beams with 0.4% spread.

Comparing Figures 6.25 and 6.29, the slope of the 30-GHz mode is unchanged as long as energy spread is within 1%. By contrast, the slope of the 110-GHz mode for 1% spread is already less than half as big as that for cold beams. As stated above, this is due to ΔE for the interaction of 0.5-A and 0.7-mm beams (with energies 20 keV and 19.165 keV) at 110 GHz being over three times smaller than that for the interaction of 0.5-A and 0.7-mm beams (with energies 20 keV and 16.95 keV) at 30 GHz. Even though Figure 6.29 displays no data for beams with 2% spread, Figures 6.23 and 6.28 lead us to conclude that the interaction and growth will be negligible in this case.

Figure 6.30 compares the gain of 30-GHz and 110-GHz modes as a function of percent energy spread. In Figure 6.30, the solid black curve is from a simulation involving the interaction of 0.7-mm and 0.3-A beams with energies 20 keV and 17.6 keV, while the solid red curve is from Figure 6.27. The solid squares are from simulations with 0.7-mm and 0.5-A beams with the same energies as in Figures 6.28 and 6.29. The theoretical curves were generated using Equation 4.38.

Examining the dashed and solid red curves, G_{th} agrees well with G_{sim} for cold beams, the two being within 2.2% (ignoring error bars) of one another. Even though Equation 4.38 (theoretical gain) is invalid for warm beams, G_{th} is in excellent agreement with G_{sim} for warm beams with 1% spread, the latter being within 1% (excluding error bars) of the former. As percent spread increases and warm beams become less and less distinguishable, G_{sim} for cold beams is reduced by 17% and as much as 66% for beams with 3% and 5% spread, respectively. Moreover, we can anticipate negligible interaction for beams with percent spread in excess of 5% (Figure 6.23),

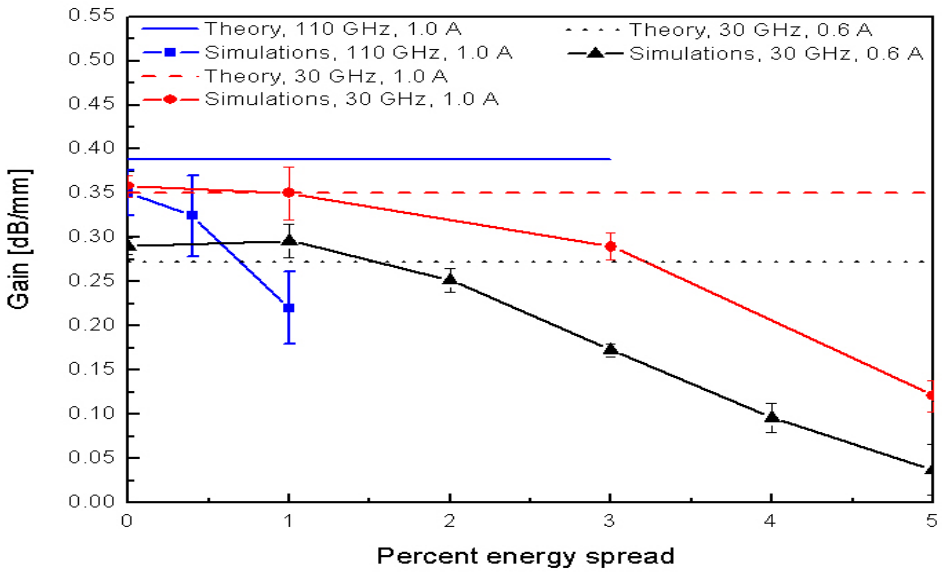

Figure 6.30: The variation of gain of a 30-GHz (solid red and black curves) and 110-GHz (solid blue curve with squares) modes with percent energy spread. The dotted (theory 30 GHz, 0.6 A), dashed (theory 30 GHz, 1.0 A), and solid blue (theory 110 GHz, 1.0 A) lines are given by Equation 4.38.

the beam energies (20 keV and 16.95 keV) virtually merging into a single beam.

According to Figure 6.30, G_{sim} for cold beams at 110 GHz is within 2.3% (without error bars) of that for cold beams at 30 GHz (solid circles). Thus, the agreement is very good. Due to a smaller energy difference, G_{sim} at 110 GHz decreases by as much as 53% as energy spread varies from 0% to 1%. By contrast, G_{sim} for cold beams at 30 GHz is approximately the same as that for beams with 1% spread, the former and the latter being within 2.2% of one another (ignoring error bars). Moreover, G_{sim} at 110 GHz drops off rather quickly, approaching zero somewhere between 1% and 2% spread (Figure 6.28). G_{sim} at 30 GHz, however, is nonzero even for percent spread as large as 5%. Last but not least, the agreement between G_{th} and G_{sim} for cold beams at 110 GHz is not good, namely, 9.9%, as compared to 2.2% at 30 GHz (excluding error bars).

Finally, for the black curve (30 GHz, 0.6 A) in Figure 6.30, G_{th} is within 7% (ignoring error bars) of G_{sim} for percent energy spread less than or equal to 3%. Hence, the agreement is fairly good. For percent energy spread exceeding 3%, however, G_{sim} starts to decrease quickly, being approximately 37% and 65% less than G_{th} for 4% and 5% spread, respectively. Moreover, for percent energy spread over 5% (energy measured at FWHM is greater than 1880 eV), 20- and 17.6-keV beams begin to merge to form a single beam and, thus, we should expect negligible interaction and growth.

6.4 Chapter summary

Chapter 6 presents simulation results for the interaction of two unmodulated (without initial energy modulation) cold (monoenergetic) and warm (Gaussian) electron beams at low (30 GHz) and medium (110 GHz and 210 GHz) frequencies. The primary emphasis is on exploring exponentially growing modes and comparing their gain from simulations, G_{sim}, with that from theory, G_{th}, in order to validate the 1-D theory discussed in Chapter 4.

For the interaction of cold beams at a low interaction frequency it is found that G_{sim} agrees well with G_{th} and both vary as $\sqrt{I/r_b^2}$, where I and r_b are the total beam current and beam radius, respectively. The agreement between G_{sim} and G_{th} worsens for medium interaction frequencies. Namely, it is found that the higher the interaction frequency, the larger the discrepancy. This is partially attributed to F, the plasma frequency reduction factor, being overestimated for G_{th} (Equation 4.38).

Although G_{sim} and G_{th} disagree at higher frequencies, for the interaction of two 0.7-mm cold beams at 30 GHz, 110 GHz, and 210 GHz it is determined that G_{sim} is independent of interaction frequency for $I = 0.6$ A and $I = 1.0$ A. In addition, it is found that the saturation length for 30-, 110-, and 210-GHz modes is also independent

of interaction frequency. The variation of the saturation length of a 30-GHz mode with total beam current reveals that the saturation length can be reduced by as much as 33% by varying I from 1.0 A to 2.2 A. This finding is useful in that it enables us to make the potential source of mm and sub-mm wave radiation (Chapter 1) even more compact.

The 1-D theory discussed in Chapter 4 is not applicable to warm beams. However, since electron beams in the laboratory are not monoenergetic, Chapter 6 also explores the variation of G_{sim} for the interaction of Gaussian beams at 30 GHz and 110 GHz. It is found that reducing the space charge (decreasing I or increasing r_b) leads to lower values of G_{sim} regardless of interaction frequency. According to Equation 4.39, the energy difference of two interacting electron beams shrinks with increasing interaction frequency. Hence, it is found that G_{sim} drops off faster for 110 GHz than it does for 30 GHz. Specifically, for the interaction of two 0.7-mm and 0.5-A electron beams, G_{sim} at 30 GHz is still found to be nonzero for energy spread as large as 5%. By contrast, G_{sim} at 110 GHz is already zero (negligible at best) for energy spread equal to 2%.

The next chapter will present simulation results for the interaction of modulated (with initial energy modulation at a given frequency) cold and warm electron beams at frequencies ranging from 30 GHz up to and including 1 THz.

Chapter 7

Interaction of modulated electron beams

In Chapter 6, we presented simulation results for the interaction of unmodulated electron beams. Chapter 7 discusses simulation results for the interaction of modulated electron beams. As in Chapter 6, the primary emphasis is on the variation of the gain of exponentially growing modes as a function of total beam current, beam radius, and percent energy spread. Section 7.1 analyzes the magnitude of axial electric field at low, medium, and high interaction frequencies. In Section 7.2, we discuss the variation of gain with space charge and frequency. Section 7.3 explores gain bandwidth for the interaction of cold beams. In Section 7.4, we analyze the effect of nonzero energy spread on gain and gain bandwidth. Finally, a summary of the chapter is presented in Section 7.5.

7.1 Frequency-dependent analysis

According to Equation D.2, modulated (seeded) electron beams in this dissertation are generated by modifying their dc energies, E_1 and E_2, as

$$E_{1,2}(t) = E_{1,2} + \delta E \times \sin(2\pi f t), \tag{7.1}$$

where f is the modulation frequency and δE is the modulation amplitude. δE is always given as some percentage of the beam energy difference, $\Delta E = E_1$ - E_2.

7.1.1 Axial electric field at low frequency

As it was done in Chapter 6, we start this section by looking at the magnitude of the ac component of axial electric field, $|E_z(z,t)|$. This will enable us to analyze G_{sim} and to compare it with G_{th}, the theoretical gain from Equation 4.38.

Figure 7.1 shows an FFT of $|E_z|$ for the interaction of two 0.7-mm cold and modulated beams for $I = 0.6$ A (blue curve) and $I = 1.0$ A (red curve). The modulation amplitude, δE, was 1% at 30 GHz. The red and blue curves in Figure 7.1 were recorded at $z = 116.5$ mm and $z = 145$ mm to exclude nonlinear regions. Also, the beam energies and FFT parameters used were exactly the same as those in Figure 6.3.

According to Figure 7.1, a frequency component at 30 GHz is clearly dominant for both $I = 0.6$ A and $I = 1.0$ A. This is in agreement with Equation 4.39, which predicts that two beams with the same parameters as those in Figure 7.1 will interact at 30 GHz. The curves in Figure 7.1 were recorded with a frequency resolution of 2.5 GHz. Hence, the FWHM frequency for both curves is at most 2.5 GHz. By contrast, the FWHM frequency for unmodulated beams in Figure 6.3 is about 8 GHz.

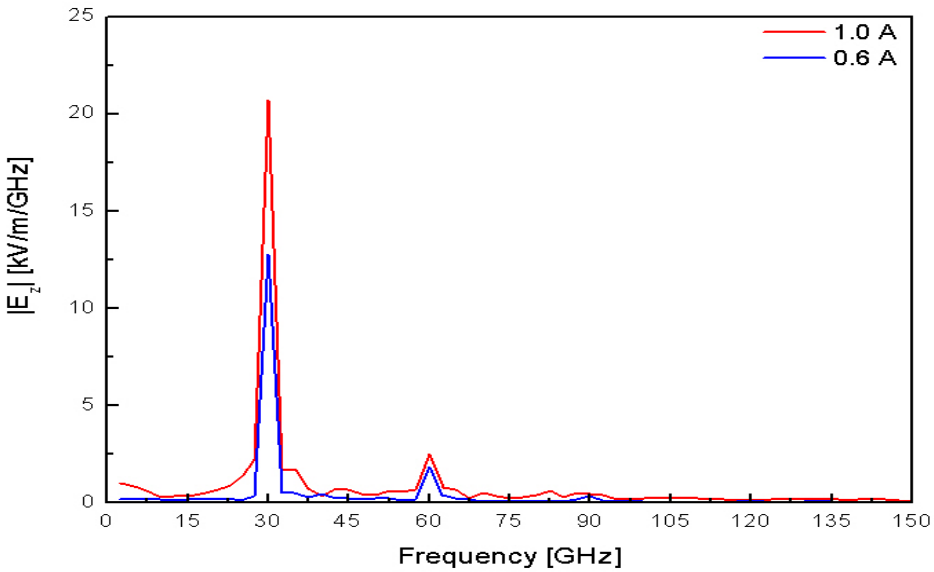

Figure 7.1: FFT of $|E_z|$ for the interaction of two 0.7-mm cold and modulated beams at 30 GHz. The blue and red curves correspond to $I = 0.6$ A and $I = 1.0$ A.

The average signal-to-noise ratio in Figure 7.1 can be estimated by dividing $|E_z|$ at 30-GHz by the average value of $|E_z|$ for the remaining frequencies shown. The average signal-to-noise ratio for $I = 0.6$ A yields 76.1. For $I = 1.0$ A the average signal-to-noise ratio approximately equals 33.5. These values are a factor 5.5 and 3.5 greater than those in Figure 6.3 for unmodulated beams. Therefore, it is clear that the interaction of modulated beams produces a superior signal-to-noise ratio.

Figure 7.2 displays the variation of $|E_z|$ with longitudinal distance, z, for the 0.6-A case (blue curve) in Figure 7.1. Note that in Figure 7.2 $|E_z|$ is given in units of kV/m, while in Figure 7.1 $|E_z|$ has units of (kV/m)/GHz. The solid circles in Figure 7.2 show a 30-GHz mode and its two harmonics, while the open circles represent TM_{01} and TM_{02} waveguide modes.

Comparing the 30-GHz mode in Figure 7.2 with that in Figure 6.4, they both have the smallest magnitude at the start of the interaction. However, the 30-GHz

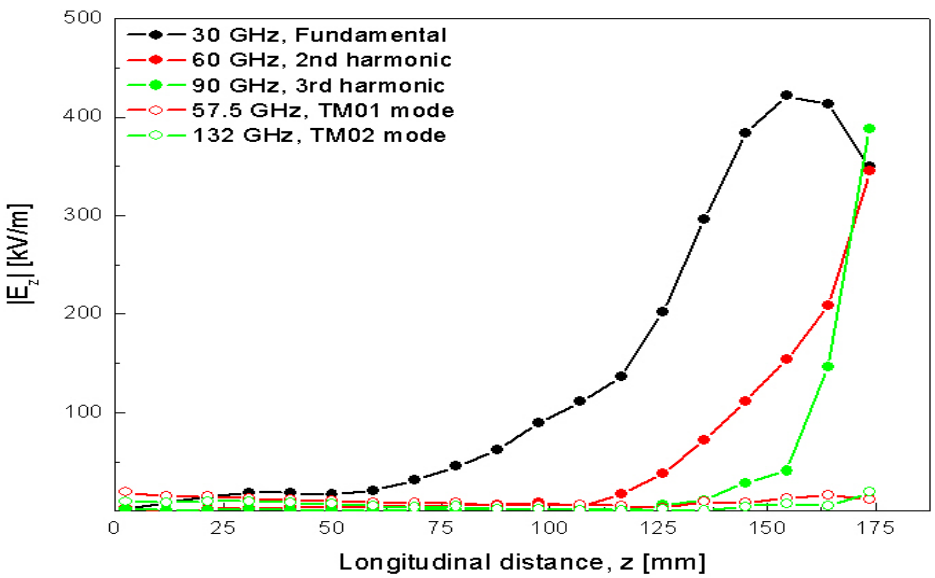

Figure 7.2: $|E_z|$ versus z for the interaction of two 0.7-mm cold and modulated electron beams at 30 GHz for $I = 0.6$ A. The solid black, red, and green circles represent 30-, 60-, and 90-GHz modes. The open red and green circles are TM_{01} and TM_{02} waveguide modes.

mode in Figure 7.2 overtakes the other modes shown faster and saturates sooner. Still, the gain of the 30-GHz mode for modulated beams equals 0.289 dB/mm and is within 0.1% (excluding error bars) of the 30-GHz mode for unmodulated beams. Note that the gain of the fundamental mode in Figure 7.2 is much greater than that of the rest of the modes in the linear region, which is what we observed in Figure 6.4.

Of the 5 modes shown in Figure 7.2, the TM_{01} and TM_{02} waveguide modes have the largest initial magnitudes. However, the waveguide modes exhibit negligible growth over the rest of the interaction region and the gain of each is much smaller than that of the fundamental mode.

Past the saturation point, as can be seen in Figure 7.2, the magnitude of the 30-GHz mode becomes comparable to that of the 60-GHz and 90-GHz modes. This is in

contrast to what we observed for the interaction of umodulated beams in Figure 6.4. Hence, according to Figure 7.2, in the linear region the interaction predominantly occurs at 30 GHz. However, past the saturation point electromagnetic radiation can also be generated at two and three times the fundamental frequency via some frequency selection mechanism.

Figure 7.3 is similar to Figure 7.2 and displays the variation of $|E_z|$ with longitudinal distance for the 1.0-A case (red curve) in Figure 7.1. The solid circles show a

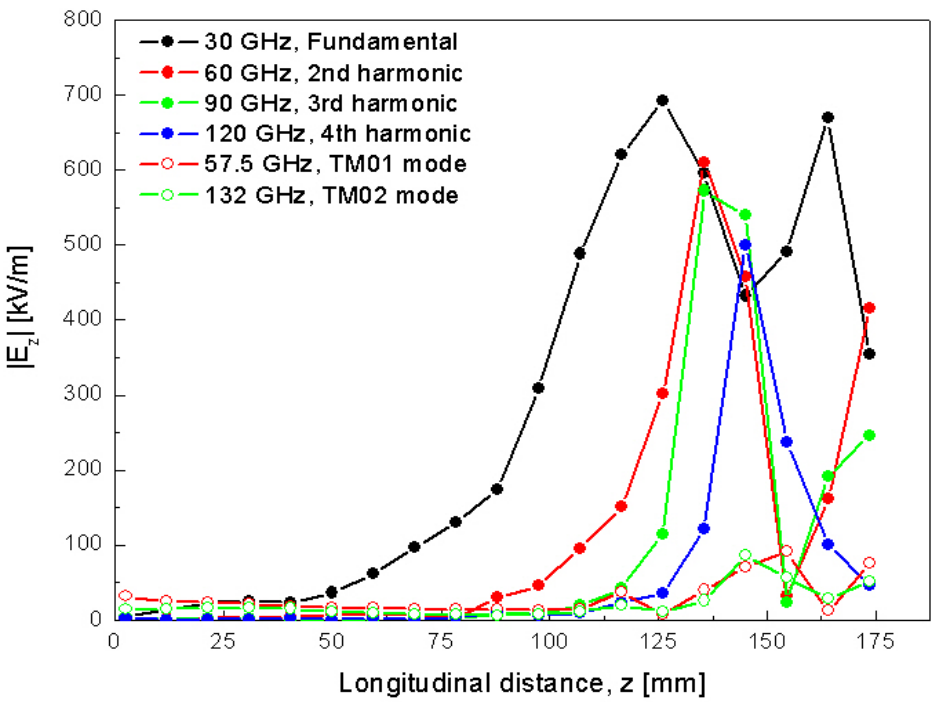

Figure 7.3: $|E_z|$ versus z for the interaction of two 0.7-mm cold and modulated electron beams at 30 GHz for $I = 1.0$ A. The solid black, red, green, and blue circles represent 30-, 60-, 90-, and 120-GHz modes. The open red and green circles are TM_{01} and TM_{02} waveguide modes.

30-GHz mode and its three harmonics. The open circles represent TM_{01} and TM_{02} waveguide modes.

As for $I = 0.6$ A in Figure 7.2, the 30-GHz mode in Figure 7.3 starts to grow sooner and saturates faster than the 30-GHz mode for unmodulated beams (Figure 6.5). Nevertheless, the gain of the 30-GHz mode for modulated beams equals 0.351 dB/mm and is within 1.9% (ignoring error bars) of that of the 30-GHz mode for unmodulated beams. Note that the gain of the fundamental mode in Figure 7.3 is much greater than that of the rest of the modes in the linear region, which extends to about $z = 116$ mm.

In Figure 7.3, the TM_{01} and TM_{02} waveguide modes again possess the largest magnitudes at the beginning of the interaction. Although they grow for large values of z, the gain of both waveguide modes is much smaller than that of the 30-GHz mode in the linear region.

The variation of $|E_z|$ for the 30-GHz mode in Figure 7.3 is markedly different from that in Figure 6.5. Namely, $|E_z|$ has two saturation points with comparable magnitudes. As can be seen in Figure 7.3, the second and third harmonics become comparable to that of the fundamental mode between the first saturation point and local minimum of the 30-GHz mode. By contrast, the fourth harmonic peaks about halfway between the two saturation points of the fundamental mode. Note that the second and third harmonics reach a local minimum at about the same longitudinal position as the second saturation point of the 30-GHz mode. From the foregoing discussion we can conclude that the signal at 30 GHz can be extracted before and after the first saturation point. In addition, beyond the first maximum of the fundamental mode, electromagnetic radiation can also be generated at 60 GHz, 90 GHz, and even 120 GHz.

The red curve in Figure 7.1 is a snapshot of $|E_z|$ at $z = 116.5$ mm and Figure 7.3 shows $|E_z|$ for only 5 modes. Figure 7.4 depicts all modes within a frequency window from 2 GHz to 150 GHz for the interaction of two 0.7-mm cold and modulated beams at 30 GHz for $I = 1.0$ A. As in Figure 6.6, the left-hand vertical axis in Figure 7.4 is

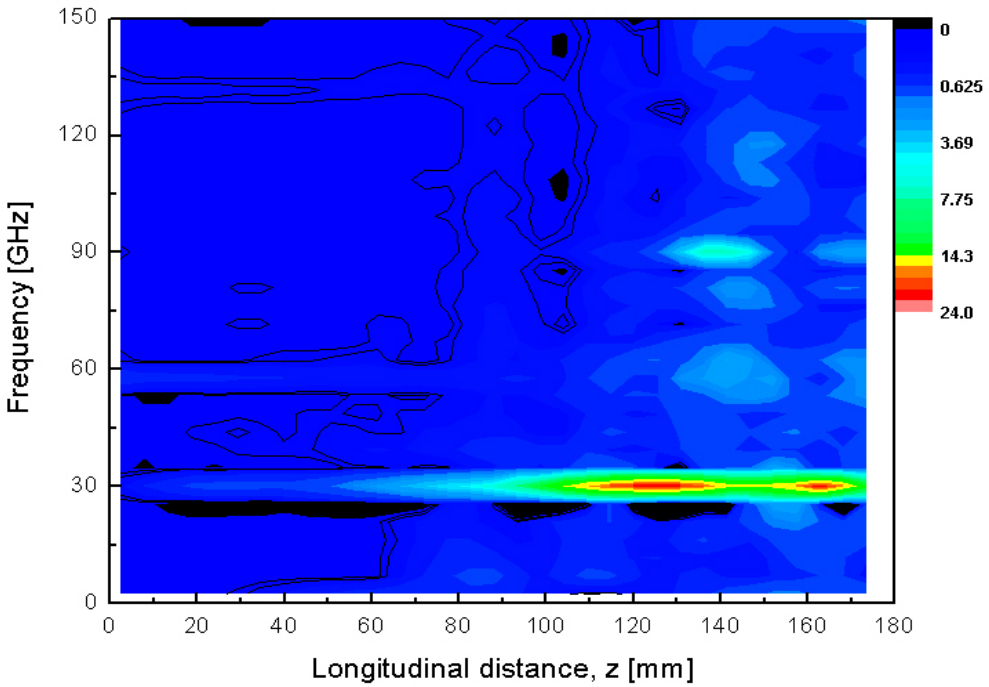

Figure 7.4: Contour plot of $|E_z|$ for the interaction of two 0.7-mm cold and modulated beams at 30 GHz for $I = 1.0$ A. The modulation amplitude is 1% at 30 GHz.

frequency in units of GHz and the numerical values of $|E_z|$ in units of (kV/m)/GHz are given by a color scale legend located next to the right-hand axis.

According to Figure 7.4, a frequency component at 30 GHz dominates over most of the interaction region. This is in agreement with Equation 4.39 from the 1-D theory. Beyond the first peak of the 30-GHz mode, in the highly nonlinear region, we can see the second (60 GHz), third (90 GHz), and fourth (120 GHz) harmonics growing in magnitude. As we saw in Figure 7.3, the magnitudes of the second and third harmonics become comparable to that of the 30-GHz mode for large values of z. Note that in the linear region, which is important to us in this dissertation, the beams interact at a single frequency of 30 GHz.

As in Figure 6.6, we can observe TM_{01} and TM_{02} waveguide modes at 57.5 GHz and 132 GHz at the start of the interaction. Note that the 30-GHz mode in Figure 7.4 overtakes the waveguide modes considerably faster. Comparing the dominant peak in Figure 6.6 with that in Figure 7.4, the former has a FWHM frequency of about 8.8 GHz. The FWHM frequency of at most 2.5 GHz for the latter is due solely to the frequency resolution used, which was 2.5 GHz. Hence, the modulated beams can interact at a single frequency given a sufficiently high modulation amplitude. Another advantage of the modulated beams in Figure 7.4 is that their interaction yields a better signal-to-noise ratio. Moreover, as we saw in Figure 7.3, the interaction of modulated beams at 30 GHz can be used to generate electromagnetic radiation at 60 GHz, 90 GHz, and 120 GHz.

Figure 7.5 displays beam current (left-hand vertical axis) and radial distance (right-hand vertical axis), r, versus longitudinal distance, z, for the simulation discussed in Figure 7.2. Note that for the sake of clarity, Figure 7.5 shows the beam current and radial distance for the 20-keV beam only.

The simulation used approximately 1.22×10^6 particles (610,000 particles or about 6.1×10^{10} electrons for each beam) and every single particle was used for post-processing and analysis. However, to make the data file small and manageable (less than 500 MB) for plotting purposes, only 5% of the particles (30,500 particles) were used for the 20-keV beam to generate Figure 7.5. Hence we obtain the nonuniform distribution of particles within the range $50 \leq z \leq 112.5$ mm.

For $I = 0.6$ A and $r_b = 0.7$ mm, Equation 4.39 predicts that two beams with energies 20 keV and 17.6 keV will interact at 30 GHz regardless of the modulation amplitude. As we saw in Figure 7.2, a frequency component at 30 GHz is the largest mode in the linear region. In Figure 7.5, at the saturation point of the 30-GHz mode, the current amplitude is approximately 20% more than the dc value of 0.3 A. Note that the beam expands markedly for large values of z, its radius at $z = 154.5$ mm

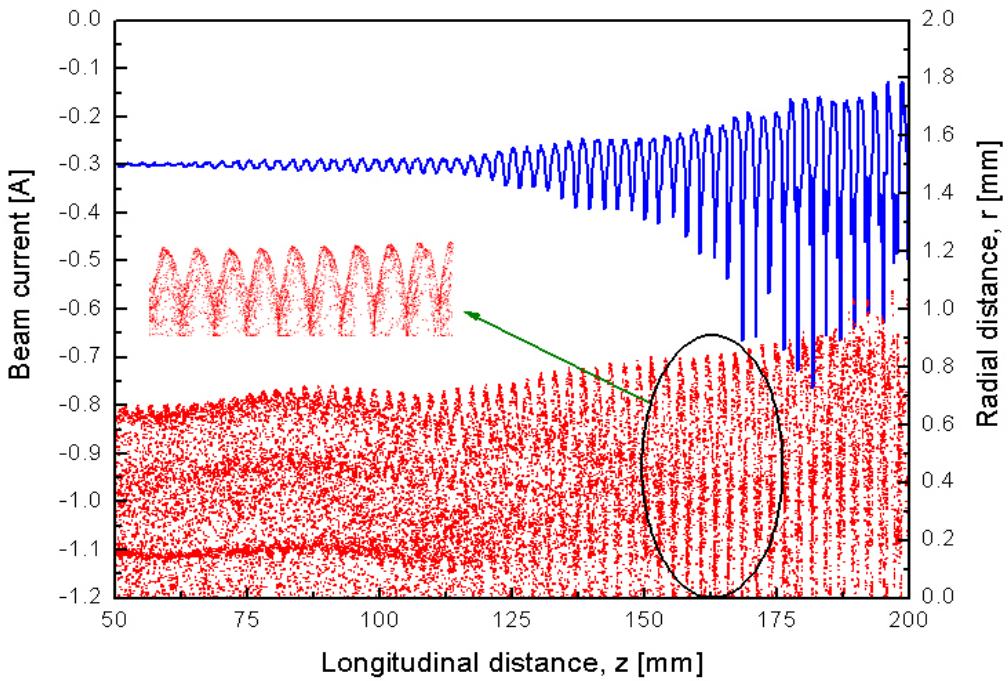

Figure 7.5: Beam current (blue curve) and radial distance, r, (red dots) as a function of longitudinal distance, z, for a 20-keV beam. Data taken from the interaction of two 0.7-mm cold and modulated beams at 30 GHz for $I = 0.6$ A.

increasing by about 15% from 0.7 mm to 0.82 mm.

The inset in Figure 7.5 shows a portion of the beam from 150 mm to 175 mm. As can be seen in the enlarged region of the beam, the bunches are sharply defined and evenly spaced. This is in contrast to what we observed in Figure 6.2 for unmodulated beams. Owing to the shape of the bunches, we can expect the current (or $|E_z|$) to be rich in harmonics. As we can see in Figure 7.2, the magnitudes of the second and third harmonics become comparable to that of the fundamental mode past the saturation point. Hence, by modulating two cold beams at 30 GHz for $I = 0.6$ A and $r_b = 0.7$ mm, not only can we extract radiation at 30 GHz, but also at two and three times the fundamental frequency.

7.1.2 Axial electric field at medium frequencies

The previous subsection analyzed $|E_z|$ for the interaction of modulated beams at 30 GHz. In this subsection, we continue to study $|E_z|$ at medium interaction frequencies, specifically, 110 GHz and 210 GHz.

Figure 7.6 displays an FFT of $|E_z|$ for two 0.7-mm cold and modulated beams interacting at 110 GHz for $I = 0.6$ A (blue curve) and $I = 1.0$ A (red curve). The

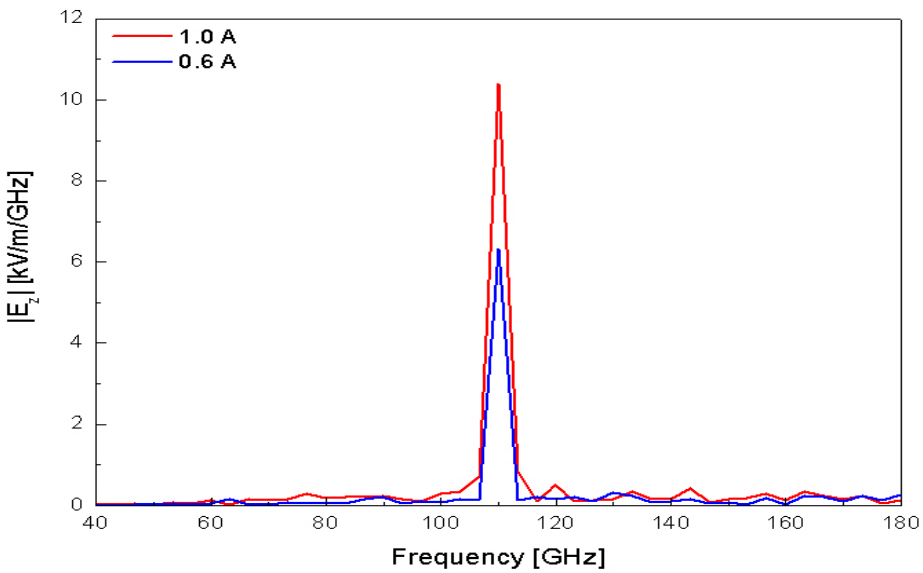

Figure 7.6: FFT of $|E_z|$ for the interaction of two 0.7-mm cold and modulated beams at 110 GHz. The blue and red curves correspond to $I = 0.6$ A and $I = 1.0$ A.

modulation amplitude was 1% at 110 GHz. The blue and red curves were recorded at $z = 154.5$ mm and at $z = 116.5$ mm, respectively. The beam energies and FFT parameters used were exactly the same as those in Figure 6.14.

Due to the FFT frequency resolution used, which was 3.3 GHz, the curves in Figure 7.6 have a FWHM frequency of about 3.3 GHz or less. A frequency component at 110 GHz is clearly dominant over the range shown. Hence, the interaction for both

currents occurs at a single frequency and this is in agreement with Equation 4.39. When we looked at the FFT plots in Figure 7.1 (for the interaction of modulated beams at 30 GHz), we noted that there were several harmonics present. It is very likely that the same holds true for the interaction of modulated beams at 110 GHz. However, due to the frequency window used ($10 \leq f \leq 200$ GHz), those harmonics, if any, were not recorded.

Figure 7.6 is noticeably different from Figure 6.14, which depicts FFT plots for the interaction of unmodulated beams at 110 GHz. Although the 110-GHz mode in Figure 6.14 is the largest frequency component for both currents, the FWHM frequency is much greater than in Figure 7.6 for both $I = 0.6$ A and $I = 1.0$ A. As a result, the interaction of unmodulated beams produces a significant number of competing modes. In addition, the number of modes increases with total beam current. By contrast, as can be seen in Figure 7.6, the interaction of modulated beams occurs at a single frequency (at least in the linear regime). Moreover, the signal-to-noise ratio in Figure 7.6 is markedly superior to that in Figure 6.14.

Figure 7.7 displays the variation of $|E_z|$ with longitudinal distance, z, for the interactions discussed in Figure 7.6. The open and solid symbols correspond to $I = 0.6$ A and $I = 1.0$ A, respectively. The blue and green curves show TM_{01} and TM_{02} waveguide modes.

For a total beam current of 0.6 A in Figure 7.7, the 110-GHz mode overtakes the waveguide modes faster than its counterpart (unmodulated case) in Figure 6.15. In addition, the 110-GHz mode for modulated beams saturates, while the 110-GHz mode in Figure 6.15 fails to reach saturation over the length of the beam pipe. Still, the gain of the 110-GHz mode in Figure 7.7 equals 0.29 dB/mm and is within 0.3% (ignoring error bars) of that of the 110-GHz mode for unmodulated beams. As can be seen in Figure 7.7, the gain of the fundamental mode is much greater than that of the waveguide modes.

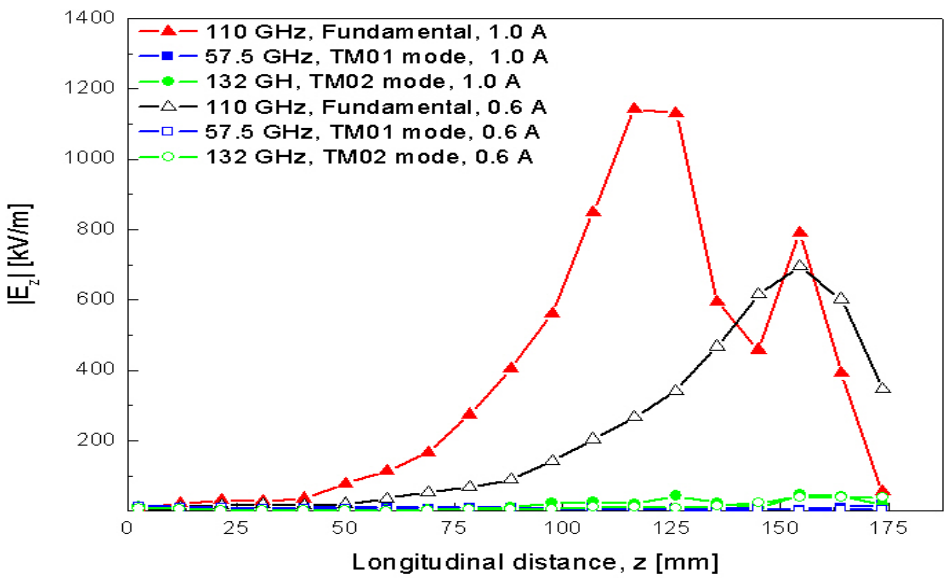

Figure 7.7: $|E_z|$ versus z for the interaction of two 0.7-mm cold and modulated beams at 110 GHz for $I = 0.6$ A and $I = 1.0$ A. The solid and open triangles represent a 110-GHz mode. The solid and open squares represent a TM_{01} waveguide mode, while the solid and open circles correspond to a TM_{02} waveguide mode.

Comparing the 110-GHz modes for modulated and unmodulated beams for $I = 1.0$ A, the former overtakes the waveguide modes markedly faster and reaches saturation sooner than the latter. Note that the shape of the 110-GHz mode in Figure 7.7 is different from that in Figure 6.15. Specifically, the 110-GHz mode in Figure 7.7 has a second maximum beyond the saturation point, where its $|E_z|$ is a factor of 1.8 less than at the location of the first peak. The gain of the 110-GHz mode in Figure 7.7 equals 0.363 dB/mm and differs from that of the 110-GHz mode in Figure 6.15 by about 3.6% (excluding error bars). Last but not least, that gain of the 110-GHz mode in Figure 7.7 is again much greater than that of the TM_{01} and TM_{02} waveguide modes.

Figure 7.8 shows the evolution of $|E_z|$ for all modes from 10 GHz to 200 GHz for the interaction discussed in Figure 7.6 (red curve). In Figure 7.8, the right-hand

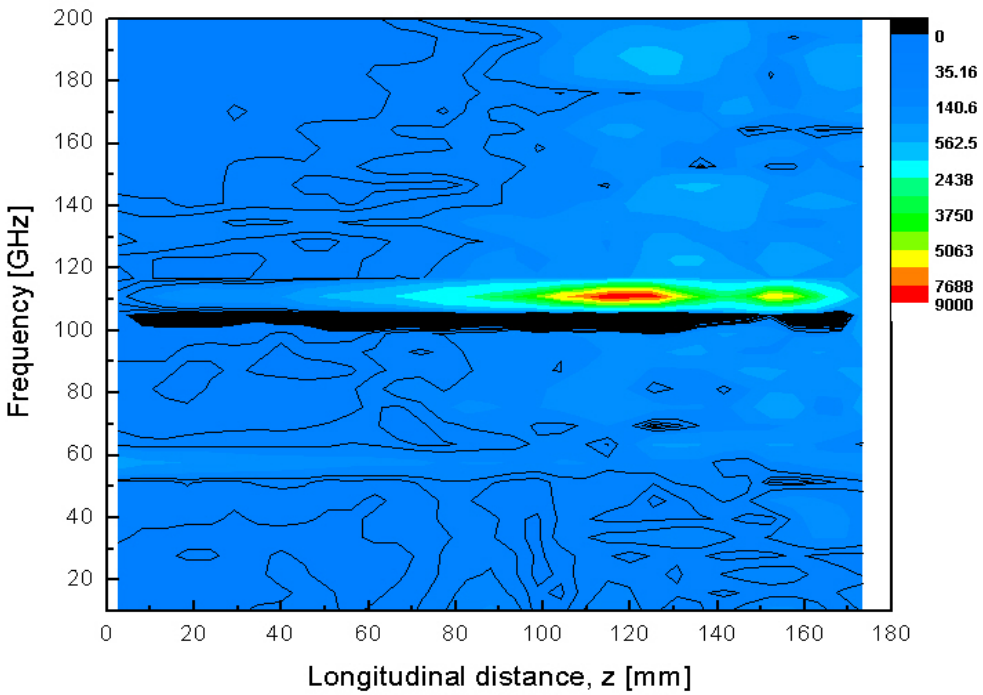

Figure 7.8: Contour plot of $|E_z|$ for the interaction of two 0.7-mm cold and modulated beams at 110 GHz for $I = 1.0$ A.

vertical axis is frequency in units of GHz and the magnitude of $|E_z|$ is given by the color scale legend in units of (kV/m)/GHz.

As we can see in Figure 7.8, the 110-GHz mode is dominant over most of the interaction region. This is consistent with Equation 4.39, which predicts that two 0.7-mm and 0.5-A beams with energies 20 keV and 19.165 keV will interact at 110 GHz regardless of the modulation amplitude. The interaction in Figure 7.8 is markedly different from the interaction of unmodulated beams shown in Figure 6.16. The FWHM frequency for the latter is over an order of magnitude greater and exhibits strong multi-mode behavior. By contrast, as can be seen in Figure 7.8, modulated beams interact at a single frequency. In addition, the interaction of modulated beams yields a significantly better signal-to-noise ratio. According to Figure 7.8, the gain

of the 110-GHz mode is much greater than that of the rest of the modes shown.

Similar to Figure 6.16, TM_{01} and TM_{02} waveguide modes at 57.5 GHz and 132 GHz can be seen in Figure 7.8. It is clear in Figure 7.8 that the magnitude (also gain) of the waveguide modes is negligible in comparison with that of the 110-GHz mode. This contradicts our observations for the interaction of unmodulated beams. As we saw in Figure 6.16, the TM_{02} waveguide mode grows substantially and its magnitude is a factor two less than that of the 110-GHz mode towards the end of the interaction. Note that due to the frequency window used ($10 \leq f \leq 200$ GHz), no harmonics, if any, can be observed in Figure 7.8.

Figure 7.9 looks identical to Figure 7.5; however it was generated from a simula-

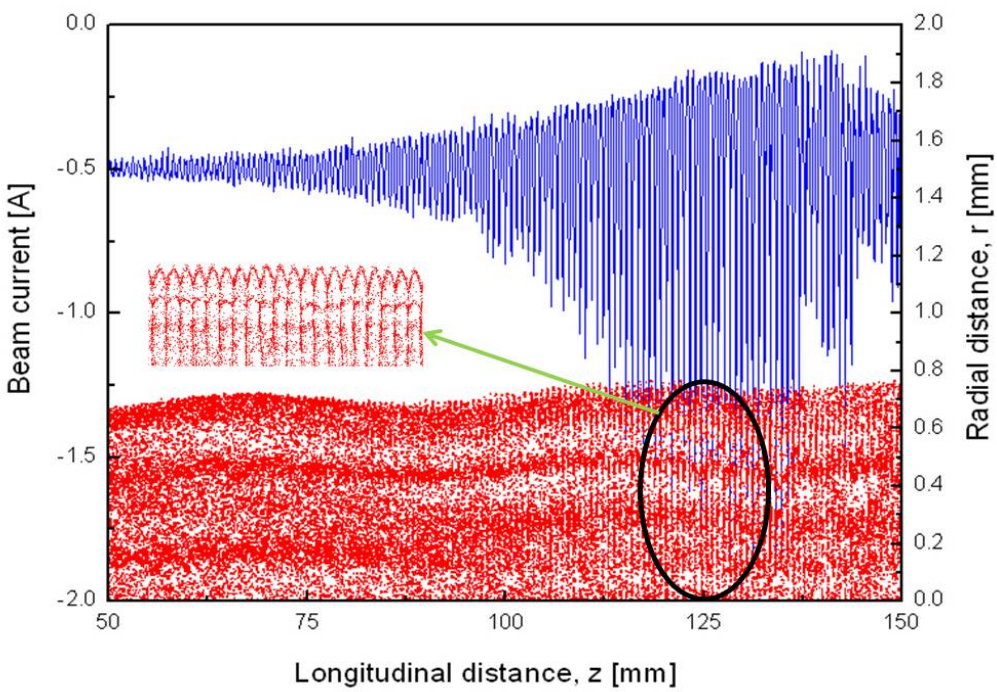

Figure 7.9: Beam current (blue curve) and radial distance, r, (red dots) as a function of longitudinal distance, z, for a 20-keV beam. Data taken from the interaction of two 0.7-mm cold and modulated beams at 110 GHz for $I = 1.0$ A.

tion involving the interaction of two 0.7-mm cold and modulated beams at 110 GHz discussed in Figure 7.6 (red curve). As in Figure 7.5, Figure 7.9 only shows the 20-keV data to keep the graph from becoming crowded.

For the simulation, the beam emission duration, t_{emiss}, was 0.9 ns (Section 5.2). At 1200 particles per bunch (Appendix A), this was equivalent to a total of 1.7×10^6 particles (about 1.7×10^{11} electrons). Hence, each beam consisted of 850,000 particles. Even though all particles were used to analyze the data, only 5% of 850,000 particles (42,500) were used for the 20-keV beam to generate Figure 7.9. This was done to limit the particle data file size to 500 MB or less and to keep the analysis software (Origin by OriginLab, Inc.) from crashing.

According to Figures 7.6 and 7.7, the interaction shown in Figure 7.9 occurs at a single frequency of 110 GHz, at least in the linear region. Due to a higher interaction frequency, the bunches in Figure 7.9 are closer than those in Figure 7.5. In addition, owing to a larger current, the 110-GHz mode (shown in Figure 7.7) starts to grow earlier and saturates faster than the 30-GHz mode in Figure 7.2. The inset in Figure 7.9 displays a portion of the beam indicated by the oval. We can see that the bunches are sharply defined and evenly spaced, which is not the case for the interaction of unmodulated beams in Figure 6.2. As can be seen in Figure 7.9, the current has a significant ac component at and past the saturation point.

Note that both beams in Figures 7.5 and 7.9 exhibit a certain amount of scalloping (sinusoidal variation of the beam envelope), which we also pointed out when describing Figure 6.2. As was discussed at the beginning of Chapter 6, scalloping was present in every simulation considered in this dissertation and could not be eliminated. However, the scalloping amplitude was kept within 6% of the beam radius, r_b, and, according to Appendix C, the impact of scalloping on numerical gain is negligible.

The last part of this subsection is devoted to the analysis of $|E_z|$ for the interaction of modulated beams at 210 GHz. Figure 7.10 looks similar to Figures 7.1 and 7.6 and depicts an FFT of $|E_z|$ for the interaction of two 0.7-mm cold and modulated beams at 210 GHz for $I = 0.6$ A (blue curve) and $I = 1.0$ A (red curve). The modulation

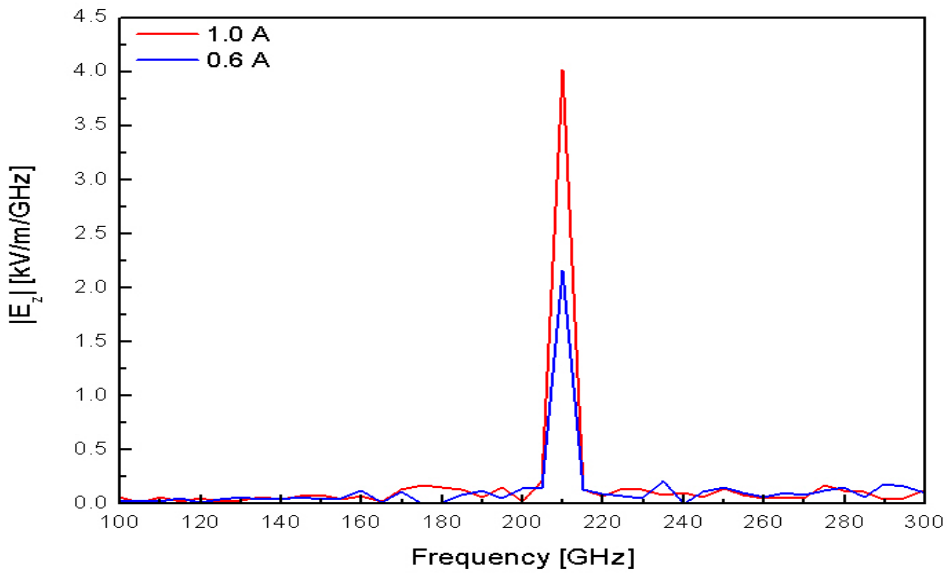

Figure 7.10: FFT of $|E_z|$ for the interaction of two 0.7-mm cold and modulated beams at 210 GHz. The blue and red curves correspond to $I = 0.6$ A and $I = 1.0$ A.

amplitude was 1% at 210 GHz. The blue and red curves in Figure 7.10 were recorded at $z = 164$ mm and $z = 116.5$ mm, respectively. Also, the FFT parameters and beam energies used were the same as those in Figure 6.17.

According to Figure 6.17, the interaction of unmodulated beams at 210 GHz exhibits a pronounced multi-mode behavior. By contrast, as we can see in Figure 7.10, the multi-mode behavior in Figure 6.17 gives way to a clear single-mode behavior for both 0.6 A and 1.0 A. Note that the curves in Figure 7.10 have a FWHM frequency of 5.0 GHz or less, which is due to the frequency resolution used (5 GHz) to record the curves. In any case, the FWHM frequency for unmodulated beams is well over an

order of magnitude greater than that for modulated beams in Figure 7.10. In addition, the interaction of modulated beams offers a significantly better signal-to-noise ratio.

It is very likely that the interaction of modulated beams in Figure 7.10 becomes nonlinear at some point and harmonics should be present (we observed this for the interaction at 30 GHz in Figures 7.2 and 7.3). However, owing to the frequency window used to record the FFT curves (80 GHz to 300 GHz), these harmonics, if any, are absent in Figure 7.10.

The variation of the 210-GHz mode with longitudinal distance is explored in more detail in Figure 7.11, which shows $|E_z|$ of the 210-GHz mode for the interactions discussed in Figure 7.10. The solid and open triangles correspond to a 210-GHz

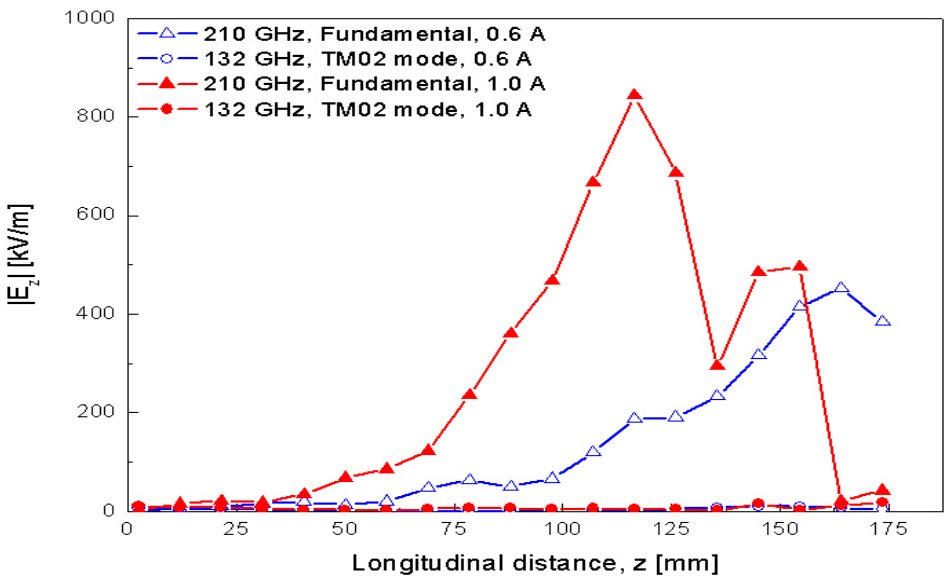

Figure 7.11: $|E_z|$ versus z for the interaction of two 0.7-mm cold and modulated beams at 210 GHz for $I = 0.6$ A and $I = 1.0$ A. The solid and open triangles represent a 210-GHz mode. The solid and open circles represent a TM_{02} waveguide mode.

mode, while the solid and open circles are TM_{02} waveguide modes.

For $I = 0.6$ A in Figure 7.11, the 210-GHz mode saturates at about the same longitudinal position as the 30- and 110-GHz modes in Figures 7.2 and 7.7. Comparing the 210-GHz mode in Figure 7.11 with that in Figure 6.18 (unmodulated case), the former starts to grow earlier and saturates sooner. This is consistent with what we have seen so far for the interaction at 30 GHz and 110 GHz. The gain of the 210-GHz mode in Figure 7.11 is within 10% (excluding error bars) of that of the 210-GHz mode for unmodulated beams. Note that no TM_{01} waveguide mode and harmonics, if any, are shown due to the frequency window used (80 GHz to 300 GHz) to record the data. As can be seen in Figure 7.7, the gain of the 210-GHz mode is much greater than that of the TM_{02} waveguide mode for $I = 0.6$ A.

For $I = 1.0$ A in Figure 7.11, the 210-GHz mode has a shape very similar to that of the 30- and 110-GHz modes in Figures 7.3 and 7.7. The gain of the 210-GHz is within 1% of that of the 30-GHz mode and within 4% of that of the 110-GHz mode, which suggests that numerical gain, G_{sim}, is independent of interaction frequency and modulation amplitude. Comparing the 210-GHz mode for unmodulated beams in Figure 6.18 with that in Figure 7.11, the latter begins to grow earlier and saturates faster than the former. Nevertheless, the gain of the 210-GHz mode for modulated beams differs from that of the 210-GHz mode for unmodulated beams by approximately 1% (ignoring error bars). Note again that the gain of the 210-GHz mode in Figure 7.11 is much greater than that of the TM_{02} waveguide mode for $I = 1.0$ A.

Figure 7.12 is identical to Figures 7.4 and 7.8, except that it shows the variation of $|E_z|$ for all modes (from 80 GHz to 300 GHz) for the interaction of two 0.7-mm cold and modulated beams at 210 GHz (the red curve in Figure 7.10). As in the previous contour plots, the right-hand vertical axis is frequency in units of GHz and the magnitude of $|E_z|$ is given by the color scale legend in units of (kV/m)/GHz.

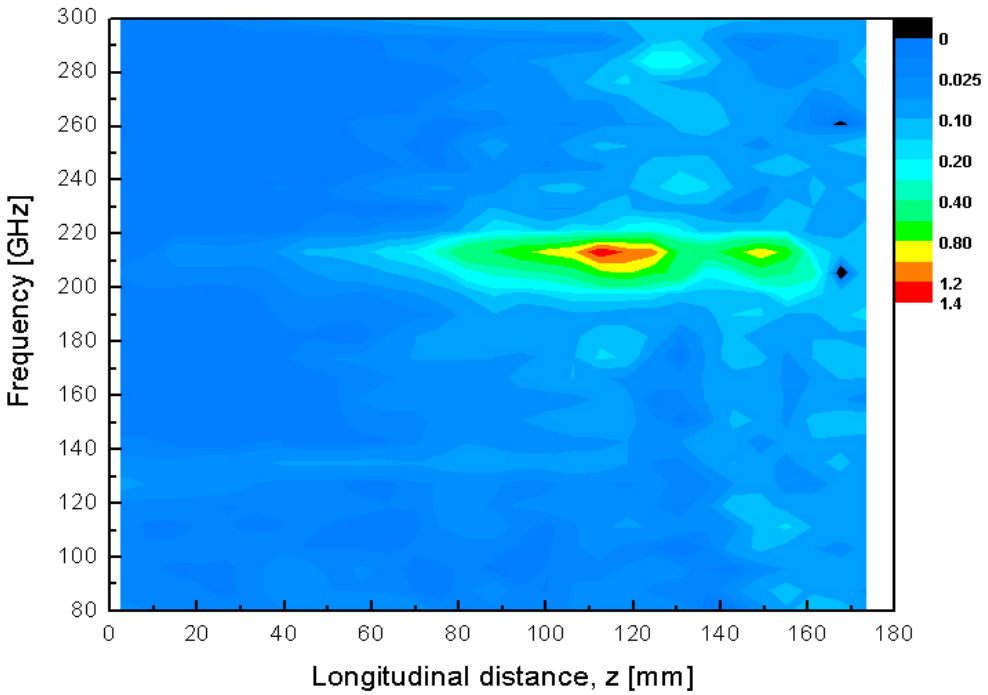

Figure 7.12: Contour plot of $|E_z|$ for the interaction of two 0.7-mm cold and modulated beams at 210 GHz for $I = 1.0$ A.

Equation 4.39 predicts that two 0.7-mm and 0.5-A beam with energies 20 keV and 19.549 keV will interact at 210 GHz regardless of their modulation amplitude. As we can see in Figure 7.12, a frequency component at 210 GHz is clearly the largest mode observed. A fairly large FWHM frequency of 5 GHz or less in Figure 7.12 is due to the coarse FFT resolution used (5 GHz). According to Figure 6.19, the interaction of unmodulated beams at 210 GHz gives rise to a significant number of competing modes. This is in contrast with the interaction of modulated beams depicted in Figure 7.12. Note that the interaction of modulated beams at 210 GHz produces a markedly better signal-to-noise ratio, which is what we also observed for the interaction of modulated beams at 30 GHz and 110 GHz.

As was the case in Figures 7.4 and 7.8, we can identify a TM_{02} waveguide mode

(132 GHz) at the beginning of Figure 7.12. No TM_{01} at 57.5 GHz can be seen due to the frequency window used (from 80 GHz to 300 GHz). Also, no harmonics, if any, are observed for the same reason. $|E_z|$ of the 210-GHz mode is greater than that of the TM_{02} for all values z with the exception of $z = 2.5$ mm, where the magnitude of the latter is over 70% greater than that of the former.

7.1.3 Axial electric field at high frequencies

Subsections 7.1.1 and 7.1.2 examined the magnitude of the ac component of axial electric field at low and medium interaction frequencies. In this subsection, we examine $|E_z|$ at high interaction frequencies, namely, 400 GHz, 800 GHz, and 1 THz.

Figure 7.13 shows the variation of $|E_z|$ with longitudinal distance and frequency for two 0.7-mm and 0.5-A cold and modulated beams with energies 20 keV and 19.767 keV. The modulation amplitude was 1% at 400 GHz. The numerical values of $|E_z|$ are given by the vertical axis in units of (V/m)/GHz.

The contour plot in Figure 7.13 was recorded using a frequency resolution of 10 GHz in order to keep the total number of particles under 5 million (Chapter 5). Therefore, the growing mode shown has a FWHM frequency of 10 GHz or less. No waveguide modes (for instance, TM_{04} at 281.5 GHz or TM_{05} at 356.4 GHz) can be seen in Figure 7.13 over the frequency range plotted. Still, as we observed in Figures 7.4 and 7.8, it is highly likely that TM_{01} and TM_{02} at 57.5 GHz and 132 GHz are present, the former being more prominent than the latter. Note also that harmonics, if any, are absent because of the frequency window chosen (250 GHz to 500 GHz).

According to Equation 4.39, two 0.7-mm and 0.5-A beams with the same energies as in Figure 7.13 will interact at 400 GHz regardless of the modulation amplitude. As we can see in Figure 7.13, the interaction of modulated beams ($\delta E = 2.33$ eV)

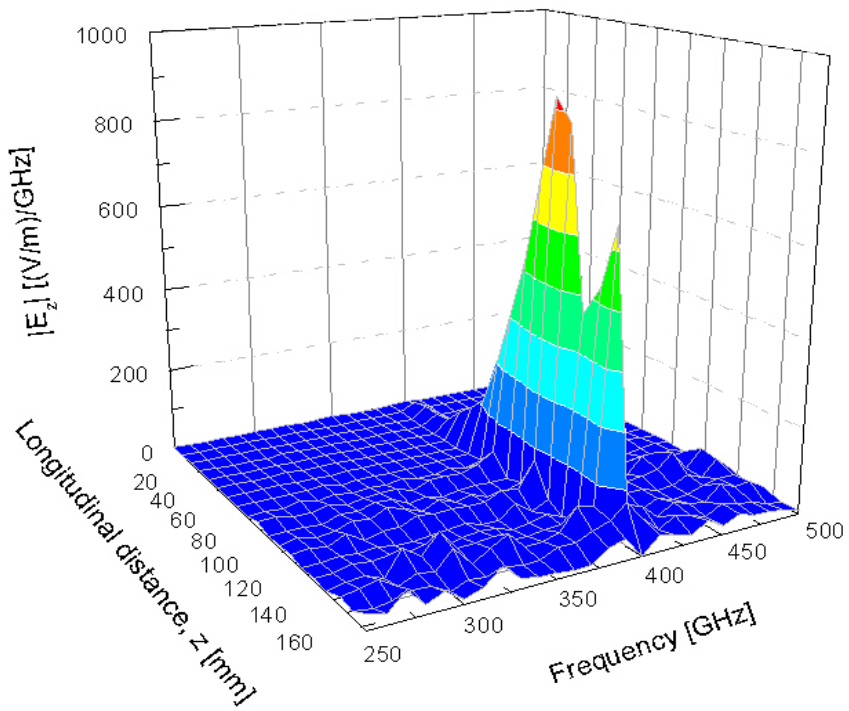

Figure 7.13: Three-dimensional contour plot of $|E_z|$ for the interaction of two 0.7-mm cold and modulated beams at 400 GHz for $I = 1.0$ A.

resulted in the exponential growth of a 400-GHz mode, which is clearly dominant over most of the interaction region. The 400-GHz mode has a two-peak structure similar to that of the 30-, 110-, and 210-GHz modes for $I = 1$ A. Note that the saturation length of the 400-GHz mode is the same as that for the interaction of two 0.7-mm and 0.5-A cold and modulated beams at 30 GHz, 110 GHz, and 210 GHz displayed in Figures 7.3, 7.7, and 7.11. This suggests that the saturation length of all fundamental modes considered so far is independent of interaction frequency and modulation amplitude.

Figure 7.14 is similar to Figure 7.13 and shows $|E_z|$ for the interaction of 0.7-mm and 0.5-A cold and modulated beams at 800 GHz. The beam energies were 20 keV and 19.884 keV. The modulation amplitude was 1.5% at 800 GHz. As in Figure 7.13,

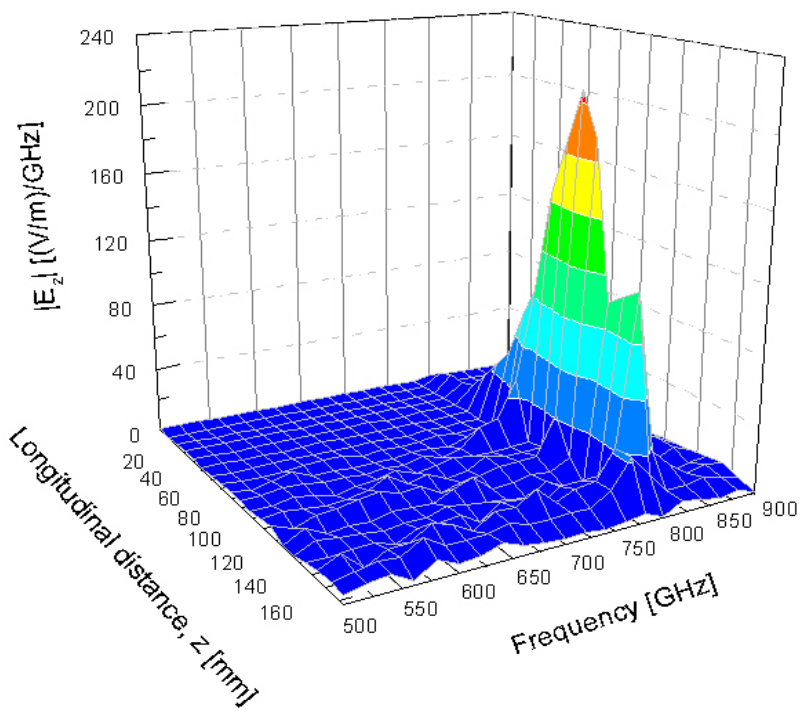

Figure 7.14: Three-dimensional contour plot of $|E_z|$ for the interaction of two 0.7-mm cold and modulated beams at 800 GHz for $I = 1.0$ A.

the vertical axis of Figure 7.15 is the magnitude of $|E_z|$ in units of (V/m)/GHz.

According to Figure 7.14, a frequency component at 800 GHz grows and saturates at the same longitudinal position as the 400-GHz mode in Figure 7.13. In addition, the location of the second peak in Figure 7.14 coincides with that in Figure 7.13. Note that the gain of the 800-GHz mode is within 3% (excluding error bars) of that of the 30-, 110-, 210-, and 400-GHz modes shown in Figures 7.3, 7.7, 7.11, and 7.13. Hence, we can argue that the gain is not a function of interaction frequency and modulation amplitude.

As we can see in Figure 7.14, the 800 GHz mode is dominant over the length of the interaction region. This is in agreement with Equation 4.39, which predicts that

the interaction frequency of two 0.7-mm and 0.5-A beams with energies 20 keV and 19.884 keV will be 800 GHz. Note that due to the frequency window used (500 GHz to 900 GHz) to generate the contour plot, harmonics, if any, are absent in Figure 7.14. In addition, no TM_{01}, TM_{02}, and higher waveguide modes can be observed for the same reason as above.

The next three-dimensional contour plot shown in Figure 7.15 depicts $|E_z|$ for

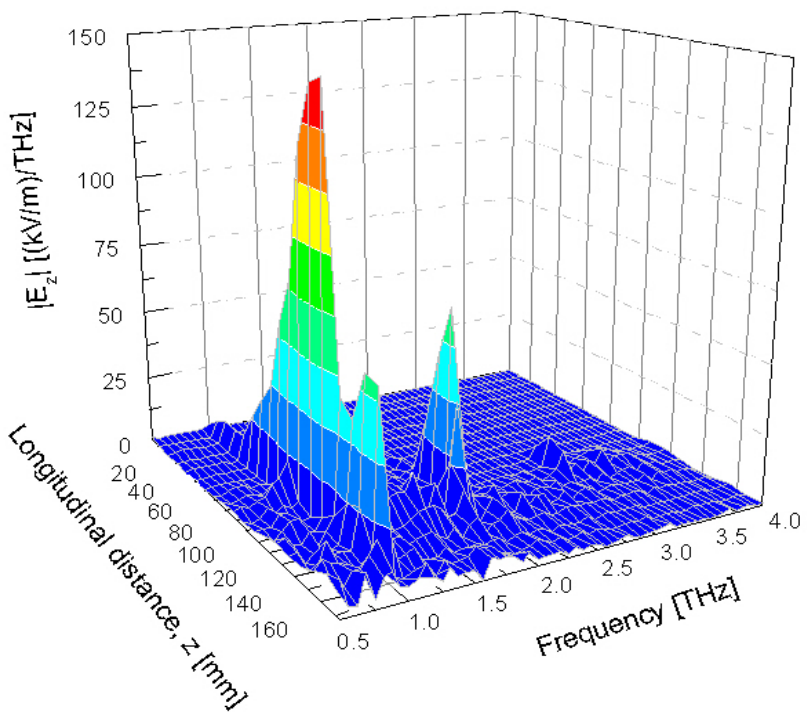

Figure 7.15: Three-dimensional contour plot of $|E_z|$ for the interaction of two 0.7-mm cold and modulated beams at 1 THz for $I = 1.0$ A.

two 0.7-mm and 0.5-A cold and modulated beams interacting at 1 THz. The beam energies used were 20 keV and 19.907 keV, while the modulation amplitude was 1.5% at 1 THz. The vertical axis of Figure 7.15 represents the magnitude of $|E_z|$ in units of (kV/m)/THz.

Figure 7.15 was obtained using a 0.05-ns time window, which equaled 50 periods at 1 THz and, thus, was more than adequate to resolve $|E_z|$ within the range $0.5 \leq f \leq 4$ THz. The frequency resolution, corresponding to the 0.05-ns time window, was 20 GHz.

According to Equation 4.39, two 0.7-mm and 0.5-A beams with energies 20 keV and 19.907 keV will interact at 1 THz. As can be seen in Figure 7.15, a frequency component at 1 THz is dominant in the linear region, which extends to about $z =$ 98 mm. Besides the 1-THz mode, harmonics at 2 THz and 3 THz can clearly be seen in Figure 7.15. Even though the second harmonic is negligible in the linear region, its magnitude becomes comparable (within 6%) to that of the fundamental mode where the 1-THz mode saturates. A frequency component at 3 THz peaks slightly before the saturation point, where its magnitude is less than half that of the 1-THz mode. Note that the saturation length of the 1-THz mode is the same as that for the interaction of two 0.7-mm and 0.5-A cold and modulated beams at 30 GHz, 110 GHz, 210 GHz, 400 GHz, and 800 GHz in Figures 7.3, 7.7, 7.11, 7.13, and 7.14, respectively. This again suggests that the saturation length of all fundamental modes considered so far is independent of interaction frequency and modulation amplitude.

7.2 Space-charge effects and the relationship between gain and interaction frequency

In this section, we turn our attention to the variation of G_{sim} with total beam current and interaction frequency. As in Chapter 6, G_{sim} will be compared with G_{th} to validate the 1-D theory presented in Chapter 4.

Plotted in Figure 7.16 is the variation of $|E_z|$ of a 30-GHz mode with longitudinal distance, z, for different beam currents and beam radii. The top plot in Figure 7.16

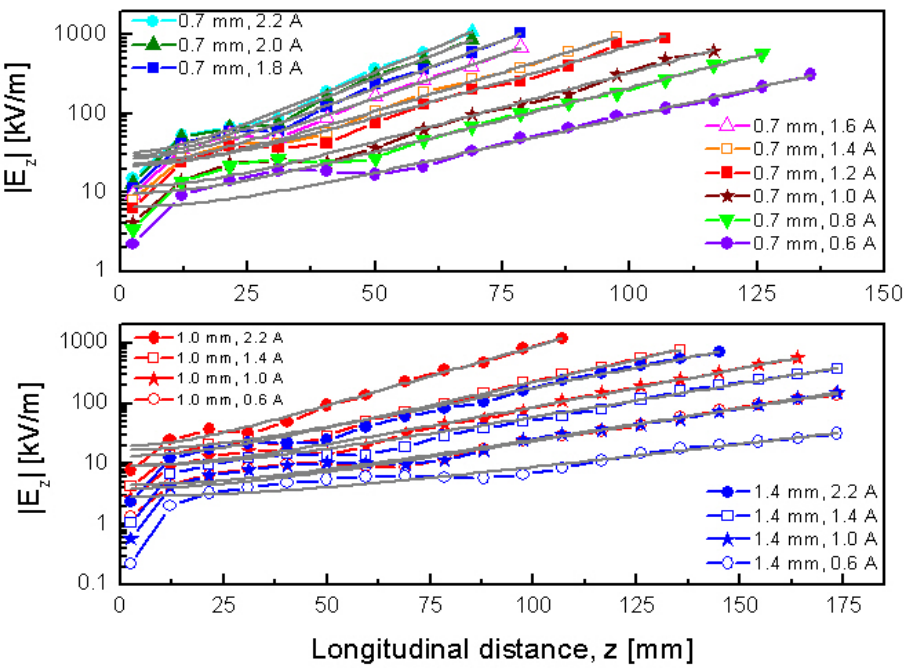

Figure 7.16: $|E_z|$ of a 30-GHz mode versus z for $r_b = 0.7$ mm (top plot), $r_b = 1.0$ mm (bottom plot, red curves), and $r_b = 1.4$ mm (bottom plot, blue curves). Total beam current varies from $I = 0.6$ A to $I = 2.2$ A. Solid gray lines are curve fits given by Equation 5.9.

was generated from 9 simulations involving the interaction of two 0.7-mm cold and modulated beams. The red curves in the bottom plot were obtained by simulating the interaction of two 1.0-mm cold and modulated beams. Finally, the blue curves in the bottom plot were generated from 4 simulations involving the interaction of two 1.4-mm cold and modulated beams. For every single simulation listed, the energy of the faster beam was fixed at 20 keV. The energies of slower beams were determined from Equation 4.39, where $f_{\text{bunching}} = 30$ GHz. In addition, the modulation amplitude was 1% at 30 GHz.

As in Figure 6.7 for unmodulated beams, the datasets in Figure 7.16 are shown

up to and including the linear region. Hence, the curves corresponding to larger currents have fewer data points. The variation of the saturation length of the 30-GHz mode with total beam current is examined at the end of the section for different beam radii. Also, the saturation length for $r_b = 0.7$ mm in Figure 7.16 (top lot) is compared with that for unmodulated beams shown in Figure 6.13.

Due to a better signal-to-noise ratio, the curves in Figure 7.16 are markedly less noisy than those in Figure 6.7. As can be seen in Figure 7.16, the curves oscillate regardless of the values of I and r_b. In addition, the oscillation amplitude is pronounced for low values of z and decreases noticeably in the linear region. The initial values of $|E_z|$ increase with space charge, which is what we observed for unmodulated beams in Figure 6.7. Note that the initial angle, which is a function of modulation amplitude, is always positive for the interaction of modulated beams in Figure 7.16. By contrast, the initial angle of $|E_z|$ in Figure 6.7 is both positive and negative. According to Figure 7.16, the larger the space charge is, the more acute the slope of the linear region becomes and, therefore, the higher G_{sim} is.

Figure 7.17 displays the variation of G_{sim} (open symbols) from Figure 7.16 with total beam current. The solid, dashed, and dotted red curves represent G_{th} (Equation 4.38) for $r_b = 0.7$ mm, $r_b = 1.0$ mm, and $r_b = 1.4$ mm, respectively. The solid symbols correspond to unmodulated beams and are from Figures 6.8 and 6.10.

As can be seen in Figure 7.17, G_{sim} for modulated beams is always less than G_{th} for $r_b = 1.0$ mm. However, the same does not hold true for either $r_b = 1.4$ mm or $r_b = 0.7$-mm. For $r_b = 0.7$-mm, the average deviation between G_{th} and G_{sim} for modulated beams is about 4.4% (excluding error bars). In the case of modulated 1.0- and 1.4-mm beams, the average deviation (excluding error bars) between G_{th} and G_{sim} reduces to 4% and 2.4%, respectively. Considering the fact that G_{sim} was obtained from 2-D simulations and G_{th} was derived using the 1-D theory, the agreement between theory and simulations is very good. Hence, we can conclude

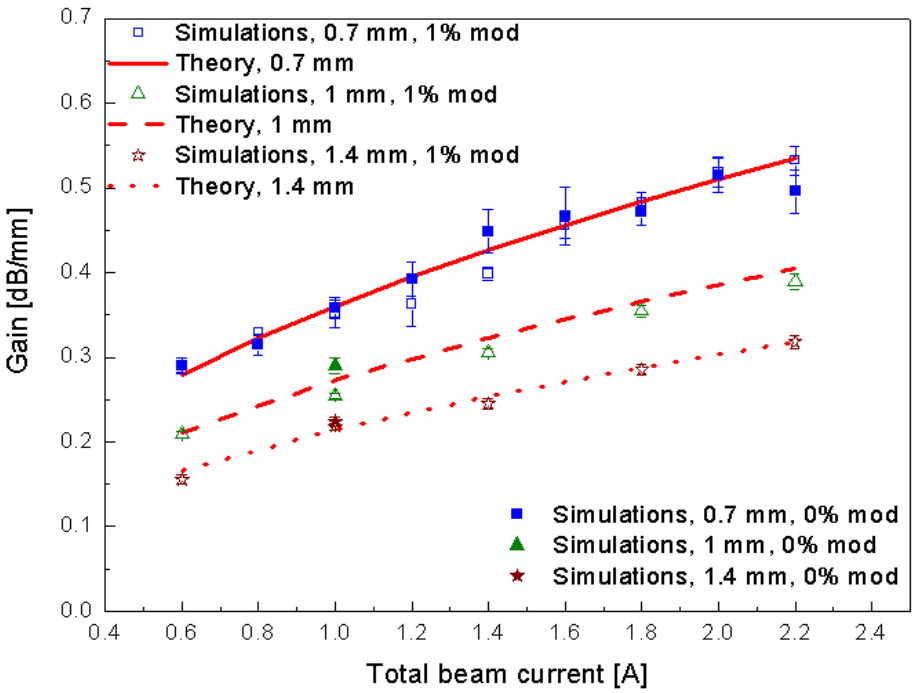

Figure 7.17: Gain of a 30-GHz mode as a function of total beam current for three different beam radii. The open and solid symbols represent modulated and umodulated cases, respectively. The three red curves corresponding to $G_{\rm th}$ from Equation 4.38.

that $G_{\rm sim}$ for modulated beams varies as $\sqrt{I/r_b^2}$, which is what we found for the interaction of unmodulated beams at 30 GHz.

For $r_b = 1.4$ mm in Figure 7.17, $G_{\rm sim}$ for unmodulated beams differs from $G_{\rm sim}$ for modulated beams by less than 3% (ignoring error bars). For $r_b = 1.0$ mm, however, the discrepancy is as large as 12.2% (excluding error bars). For $r_b = 0.7$ mm in Figure 7.17, which has more data points than the other two cases, the average deviation between $G_{\rm sim}$ for unmodulated beams and $G_{\rm sim}$ for modulated beams is less than 3% (excluding error bars). Therefore, not only does $G_{\rm sim}$ vary as $\sqrt{I/r_b^2}$, it also appears to be independent of modulation amplitude.

The 30-, 110-, and 210-GHz modes discussed in Figures 7.2, 7.3, 7.7, and 7.11 are

combined and shown together in Figure 7.18. Note that the curves represented by

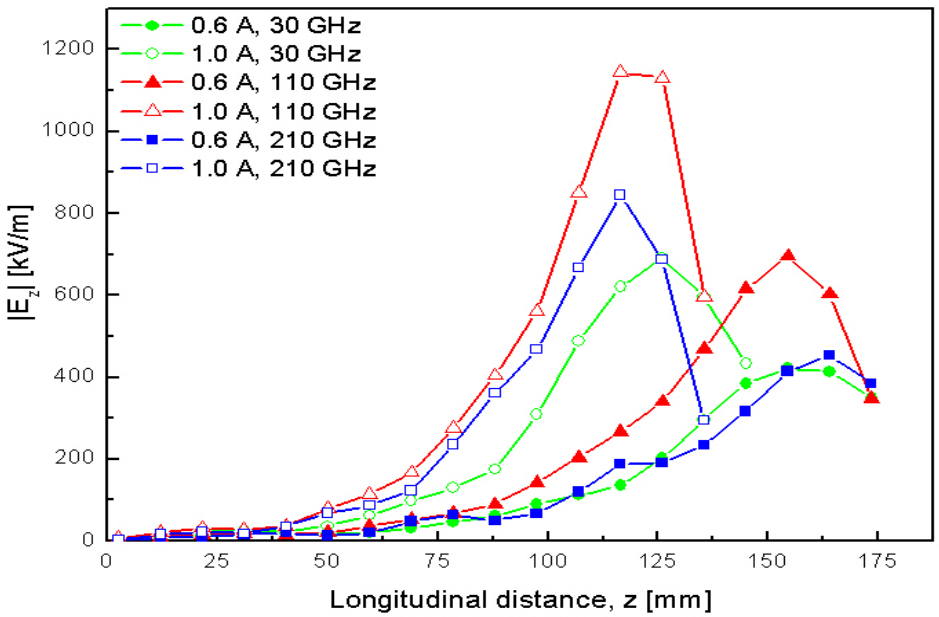

Figure 7.18: $|E_z|$ versus z for the interaction of two 0.7-mm cold and modulated beams for $I = 0.6$ A (solid symbols) and $I = 1.0$ A (open symbols). The green, red, and blue curves correspond to 30-, 110-, and 210-GHz modes.

the open symbols were truncated (second peaks were omitted) for the sake of clarity.

Comparing Figure 7.18 to Figure 6.20, we see that the larger current results in faster mode growth for all three modes regardless of the modulation level used. In Figure 6.20, no mode saturation is observed for $I = 0.6$ A. By contrast, all three modes in Figure 7.18 saturate at about the same longitudinal position, slightly before the end of the simulation box. Therefore, to first order, we may conclude that the saturation length is independent of interaction frequency and dependent on modulation amplitude.

For $I = 1.0$ A, as we can see in Figures 6.20 and 7.18, the three modes for modulated beams start to grow earlier and reach saturation faster than those for

unmodulated beams. For $I = 1.0$ A in Figure 7.18, the modes again saturate at about the same longitudinal position. Comparing the three modes in Figures 6.20 and 7.18 for $I = 1.0$ A, the larger the modulation amplitude, the shorter the saturation length is. Hence, as in the case for $I = 0.6$ A, we are led to conclude that the saturation length is a function modulation amplitude, δE. Moreover, the saturation length is independent of interaction frequency.

In Figure 7.19, G_{sim} of the 30- (circles), 110- (triangles), and 210-GHz (squares) modes from Figures 6.20 and 7.18 is plotted as a function of total beam current. Note that the unmodulated and modulated cases are shown by the solid and open

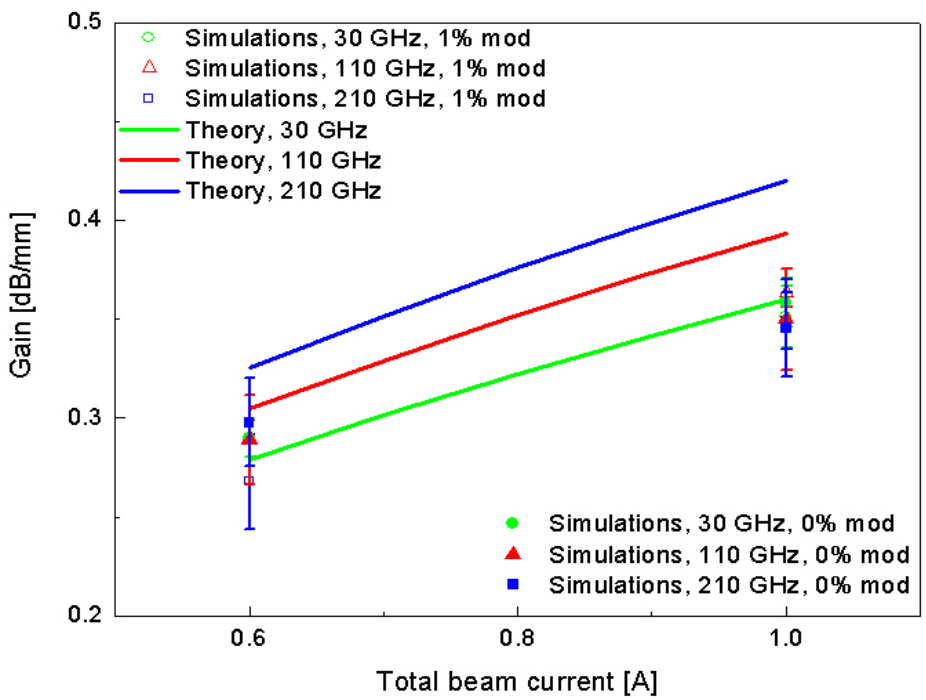

Figure 7.19: The variation of gain with total beam current for three modes: 30-GHz (circles), 110-GHz (triangles), and 210-GHz (squares). The open and solid symbols correspond to modulated and unmodulated cases. The solid green, red, and blue curves represent G_{th} given by Equation 4.38.

symbols, respectively. The solid green, red, and blue curves are theoretical curves at 30 GHz, 110 GHz, and 210 GHz.

According to Figure 7.19, the discrepancy between G_{sim} and G_{th} increases with interaction frequency for both $I = 0.6$ A and $I = 1.0$ A. For $I = 0.6$ A, G_{sim} and G_{th} are within 6.1% and 18.8% (excluding error bars) at 30 GHz and 210 GHz, respectively. For $I = 1.0$ A, G_{sim} and G_{th} differ by 0.1% and 16.9% (ignoring error bars) at 30 GHz and 210 GHz, respectively. This is similar to what we observed when discussing the interaction of unmodulated beams in Figure 6.21. As we argued in Chapter 6, the discrepancy could be partially due to F (Figure 3.3) being overestimated in Equation 4.38 for G_{th}.

Comparing G_{sim} for modulated and unmodulated beams at $I = 0.6$ A (excluding error bars), the two differ by 0.1%, 0.2%, and 10% at 30 GHz, 110 GHz, and 210 GHz, respectively. For $I = 1.0$ A in Figure 7.19, G_{sim} for modulated and unmodulated beams are within 1.8%, 3.7%, and 1% (excluding error bars) at 30 GHz, 110 GHz, and 210 GHz, respectively. Note that if we do not ignore the error bars in Figure 7.19, then the agreement between the data points is very good for both 0.6 A and 1.0 A. Hence, for the interaction of two 0.7-mm cold beams at 30 GHz, 110 GHz, and 210 GHz, we may conclude that G_{sim} is independent of modulation frequency and amplitude for both $I = 0.6$ A and $I = 1.0$ A.

Figure 7.20 shows the variation of $|E_z|$ with longitudinal distance, z, for the 30-, 110-, 210-, 400-, 800-, and 1-THz modes discussed in Figures 7.3, 7.7, 7.11, 7.13, 7.14, and 7.15, respectively. Note that the modes displayed in Figure 7.20 were generated from simulations involving two 0.7-mm cold and modulated beams for $I = 1.0$ A.

Examining Figure 7.20, we notice a large discrepancy in $|E_z|$ for the low/medium and high interaction frequencies. For instance, the magnitude of the 30-GHz mode is approximately a factor of 4.23 greater than that of the 1-THz mode at $z = 116.5$ mm.

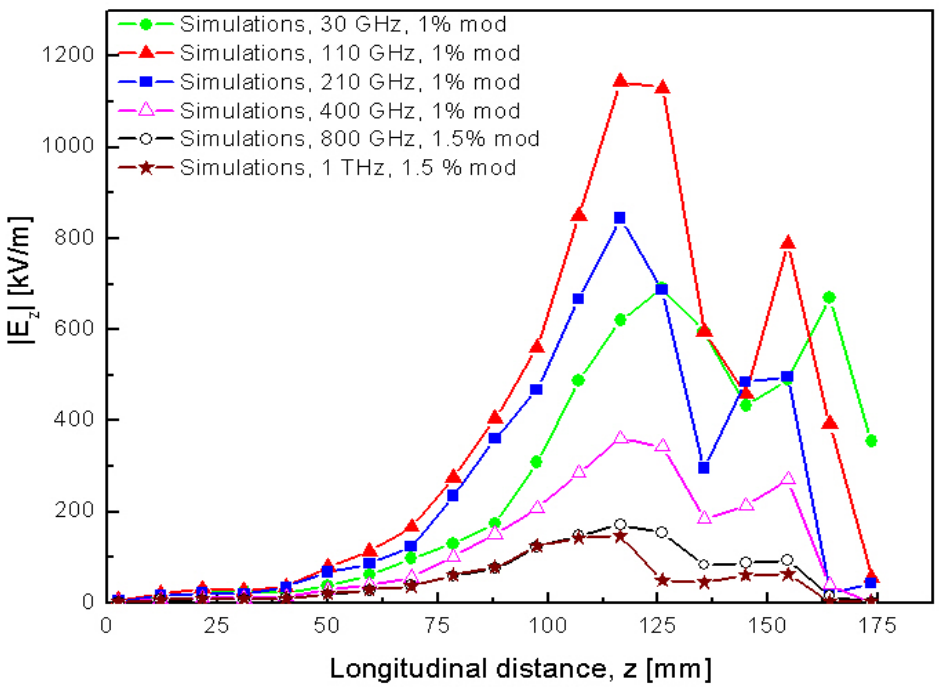

Figure 7.20: $|E_z|$ versus longitudinal distance, z, for 30- (green), 110- (red), 210- (blue), 400- (magenta), 800- (black), and 1-THz (burgundy) modes. $I = 1.0$ A and $r_b = 0.7$ mm.

This difference in magnitudes can be partially explained by recalling that numerical noise is inversely proportional to $\sqrt{N}$, where N is the total number of particles used in a simulation. Hence, the more particles we have, the smaller the initial and all subsequent values of $|E_z|$ will be. Since simulations at 30 GHz require fewer particles than those at 1 THz (Appendix A), we should expect $|E_z|$ obtained from the former to be larger than that obtained from the latter. The green curve (30 GHz) in Figure 7.20 was generated using 718,200 particles, while the burgundy curve (1 THz) was obtained with 5,000,000 particles. The ratio of these numbers approximately equals 6.96, whose square root is about 2.64. If we were to multiply $|E_z|$ for the 1-THz mode by 2.64, this would push up the burgundy curve in Figure 7.20 towards

the green curve and bring the two datasets to within a factor of 1.6 of one another. Note that the foregoing argument fails to explain why $|E_z|$ of the 110-GHz mode (N = 2,562,000) and 210-GHz mode (N = 3,210,480) is greater than that of the 30-GHz mode (N = 718,200) in Figure 7.20.

In Figure 7.20, all modes saturate at about the same longitudinal position. Hence, to first order, we can conclude that the saturation length in Figure 7.20 is not a function of interaction frequency. According to Appendix D, the smaller the interaction frequency, the larger the modulation amplitude, δE. The modulation amplitude used for the green curve (30 GHz) was 30.5 eV and, thus, over a factor of 6 greater than that (4.51 eV) for the blue curve (210 GHz) and over a factor of 20 greater than that (1.39 eV) for the burgundy curve (1 THz). In spite of this, to first order, the modes shown in Figure 7.20 peak and saturate at the same longitudinal position. This leads us to conclude that the saturation length is also independent of δE. Note that for the interaction frequencies greater than or equal to 110 GHz, the second peaks in Figure 7.20 occur at the same longitudinal position. The second peak for the 30-GHz mode is shifted with respect to the others by a mere 9.5 mm.

If we fit the linear portions of the curves in Figure 7.20 with Equation 5.9 and substitute the values of R obtained into Equation 5.10, we can plot G_{sim} as a function of interaction frequency. G_{sim} of the 6 modes in Figure 7.20 is displayed in Figure 7.21. The solid symbols in Figure 7.21 correspond to theoretical values for I = 1.0 A. Note that G_{th} has the same value for interactions at 400 GHz, 800 GHz, and 1 THz (stars).

According to Figure 7.21, G_{th} increases with interaction frequency and saturates at 400 GHz. At 30 GHz, 110 GHz, and 210 GHz, as can be shown, G_{sim} and G_{th} differ by 0.1%, 6.5%, and 16.9%, respectively. For interaction frequencies greater than or equal to 400 GHz, however, the former and the latter differ by as much as 26%. This marked discrepancy between G_{sim} and G_{th}, especially for high frequencies, was

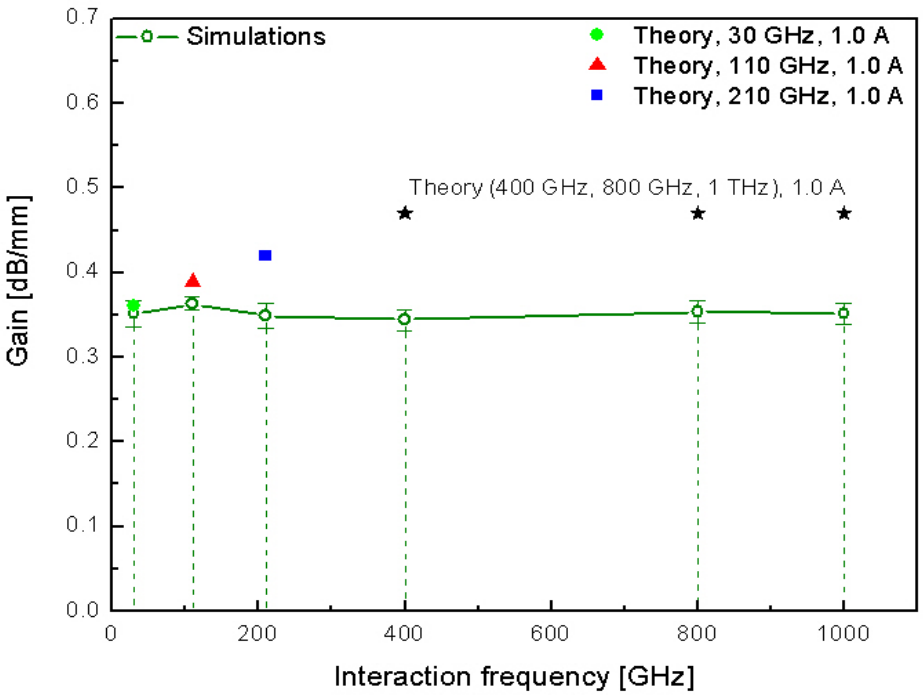

Figure 7.21: The variation of gain with interaction frequency for two 0.7-mm cold and modulated beams for $I = 1.0$ A. The solid symbols represent G_{th} (Equation 4.38).

partly explained earlier (Figure 7.19). It is interesting to note that G_{th} at 30 GHz (solid circle) is in good agreement with G_{sim} over the entire frequency range shown in Figure 7.21.

Examining the simulation data in Figure 7.21, the largest percent deviation in numerical gain is 5.2% (disregarding error bars) and occurs between G_{sim} at 110 GHz and that at 400 GHz. If the error bars are taken into account, however, we can confidently say that the variation of G_{sim} is negligible. This leads us to conclude that G_{sim} is independent of both interaction frequency and modulation amplitude for the interaction of two 0.7-mm and 0.5-A cold and modulated beams at frequencies ranging from 30 GHz up to and including 1 THz.

In Figure 7.22, we combine the data in Figures 6.22, 7.17, 7.19, and 7.21 to plot G_{sim} as a function of space charge density in units of A/mm^2. The solid symbols

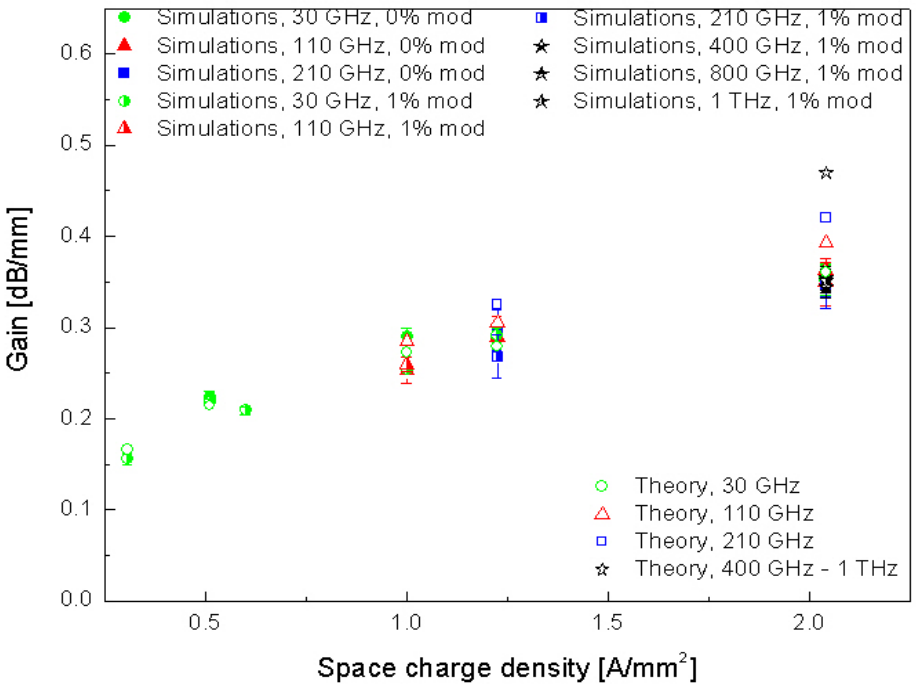

Figure 7.22: The variation of gain of 30-, 110-,210-, 400-, 800-, and 1-THz modes with space charge density. The solid symbols correspond to 0% modulation. The open symbols represent G_{th} from Equation 4.38.

in Figure 7.22 correspond to unmodulated beams, while the open symbols represent theory. The rest of the data points represent modulated beams.

According to Figure 7.22, the smallest average deviation (less than 4%, excluding error bars) between G_{sim} and G_{th} occurs at 30 GHz over the entire range shown. This applies to both unmodulated and modulated beams. Hence, we can conclude that G_{sim} at 30 GHz varies as $\sqrt{I/r_b^2}$, which is consistent with theory. As can be seen in Figure 7.22, the agreement between simulations and theory deteriorates for higher interaction frequencies. For instance, when the space charge density is approximately

equal to 2 A/mm^2, the deviation between G_{sim} and G_{th} increases from 0.1% at 30 GHz to as much as 26% at 400 GHz and above. The reason accounting for part of this discrepancy was discussed earlier.

Although G_{sim} and G_{th} disagree at medium and high interaction frequencies, the same is not true of G_{sim} for modulated and unmodulated cases. Namely, for 1.2 A/mm^2 and 2 A/mm^2, the agreement between G_{sim} for modulated beams and G_{sim} for unmodulated beams is very good (error bars included). Hence, G_{sim} is independent of interaction frequency and modulation amplitude. In addition, as can be seen in Figure 7.22 for 2 A/mm^2, G_{sim} is independent of interaction frequency and modulation amplitude over a wide frequency range, specifically, $0.3 \leq f \leq 1$ THz.

Before closing this subsection, we will compare the saturation length of a 30-GHz mode for the interaction of modulated and unmodulated beams. Our goal is to determine whether or not the saturation length is affected by a nonzero modulation amplitude.

Figure 7.23 is $|E_z|$ of a 30-GHz mode for the interaction of two 0.7-mm cold and modulated beams. The curves depicted are exactly the same as those in the top plot of Figure 7.16. As opposed to Figure 7.16, Figure 7.23 shows data points before and after saturation.

As can be seen in Figure 7.23, the 30-GHz mode saturates for all currents shown. By contrast, no saturation is observed in Figure 6.12 for values of I less than 1.0 A. Comparing the 30-GHz mode for modulated beams in Figures 7.23 with that for unmodulated beams in Figure 6.12, the former starts to grow earlier and saturates faster. Based on the foregoing discussion, we can conclude that the greater the modulation amplitude is, the shorter is the saturation length.

An estimate of the saturation length of the 30-GHz mode in Figure 7.23 is shown by the blue curve in Figure 7.24. The green curve corresponds to unmodulated beams

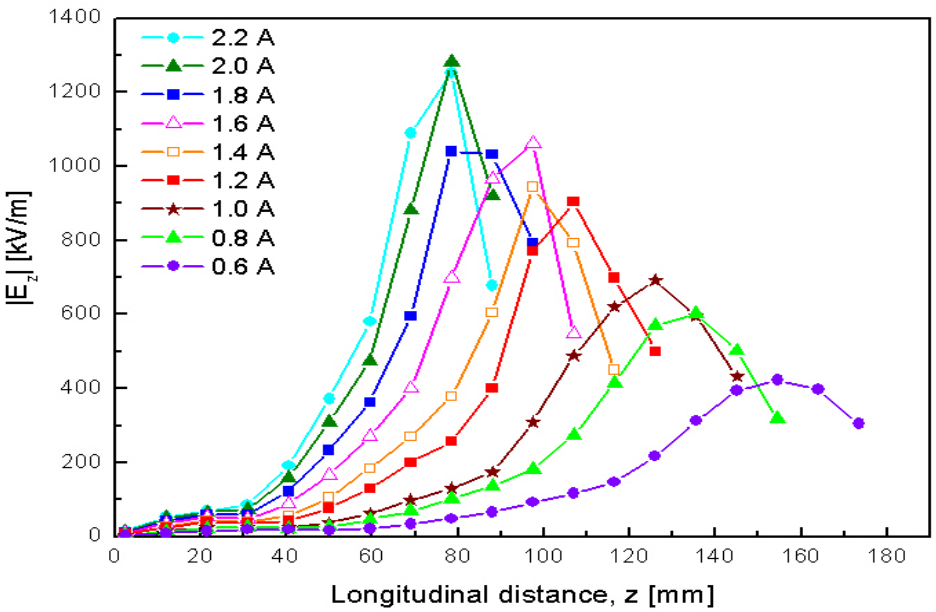

Figure 7.23: The variation of $|E_z|$ of a 30-GHz mode for I ranging from 0.6 A to 2.2 A.

and is the same curve as that in Figure 6.13.

To relate the saturation length and total beam current, the blue curve is fitted with $y = Bx^n$ (Equation 6.1). The values of B and n extracted from the curve fit are given by 118.2 ± 0.92 and -0.58 ± 0.016. Hence, on average, the saturation length for the modulated case is about 26% less. Note that as I varies from 1.0 A to 2.2 A, the difference between the green and blue curves decreases from approximately 37 mm to 29 mm. Even though the interaction of modulated and unmodulated beams at 30 GHz yields the same gain (within 3%), the use of modulated beams is advantageous because it reduces the interaction length by about 26%.

If we analyze the curves in the bottom plot of Figure 7.16, it can be shown that the 30-GHz mode saturates for values of I greater than or equal to 1.2 A when r_b = 1 mm. For r_b = 1.4 mm, the 30-GHz mode does not saturate for values of I less

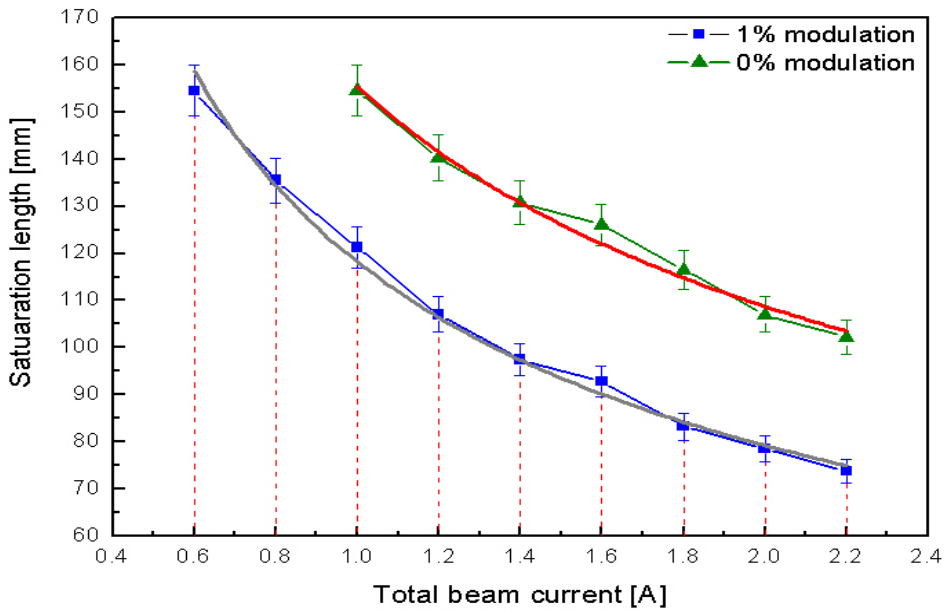

Figure 7.24: Saturation length of a 30-GHz mode as a function of total beam current. The blue and green curves correspond to modulated and unmodulated cases, respectively. The solid gray and red curves are given by $y = Bx^n$.

than 2 A. In addition, the saturation length for $r_b = 1$ mm is approximately 32% more than that for $r_b = 0.7$ mm. Moreover, the saturation length for $r_b = 1.4$ mm is over twice as long as that for $r_b = 0.7$ mm. Hence, not only does the interaction of two 0.7-mm and 0.5-A beams yield a higher gain, it makes the interaction region shorter.

7.3 Frequency bandwidth for amplification

Depending on their energies, currents, and radii, two beams will interact at the bunching frequency, f_{bunching}, predicted by Equation 4.39. To generate a gain bandwidth plot, two electron beams with given energies, currents, and beam radii are

made to interact while they are modulated at f_{bunching} and neighboring frequencies (both greater than and less than f_{bunching}). We continue to scan frequencies as long as the resulting gain, G_{sim}, is nonzero. The modulation frequencies, on either side of f_{bunching}, at which G_{sim} becomes negligible mark the endpoints of the gain curve. In this section, we explore gain bandwidth curves for the interaction of two cold electron beams. The effect of nonzero energy spread on gain bandwidth is treated in Subsection 7.4.2.

Figure 7.25 displays gain as a function of driving/modulation frequency for simulations involving the interaction of two 0.7-mm modulated beams at 30 GHz. For the blue and red curves, beam energies and currents were the same as those in Figure 7.1. In the case of the burgundy curve, $I = 1.5$ A and beam energies were 20 keV and 16.532 keV. The modulation amplitude was 1% and the modulation frequency

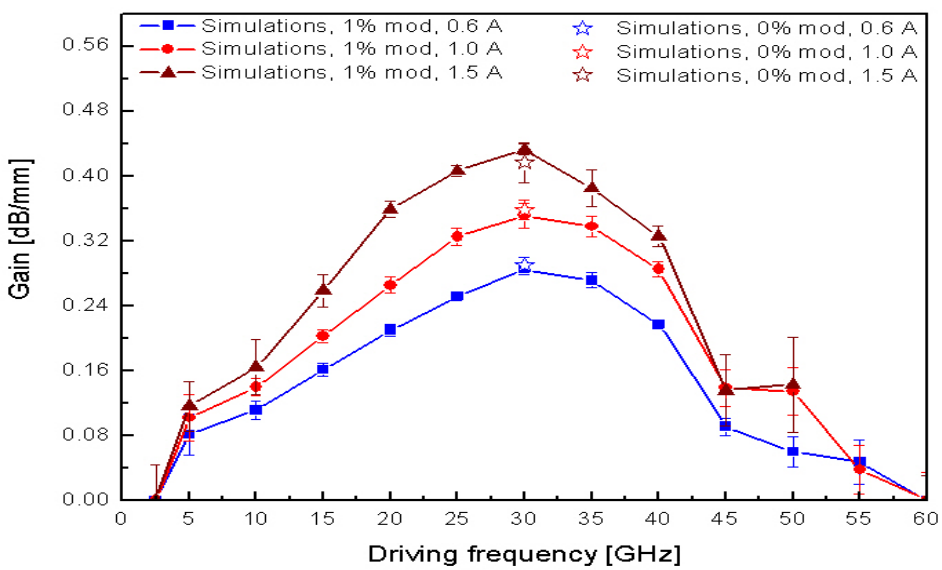

Figure 7.25: Gain bandwidth for two 0.7-mm modulated beams interacting at 30 GHz. The blue, red, and burgundy curves correspond to $I = 0.6$ A, $I = 1.0$ A, and $I = 1.5$ A, respectively. The open stars are G_{sim} for cold and unmodulated beams.

ranged from 2.5 GHz to 60 GHz, amounting to a total of 39 runs (13 per curve). The open stars in Figure 7.25 represent G_{sim} for unmodulated beams at 30 GHz.

In Figure 7.25, the gain bandwidth measured at FWHM for $I = 0.6$ A, $I = 1.0$ A, and $I = 1.5$ A is approximately 30 GHz (from 13 GHz to 43 GHz), 31 GHz (12.8 GHz to 43.8 GHz), and 30.1 GHz (12.7 GHz to 42.8 GHz), respectively. To first order, then, the FWHM bandwidth is the same for all three curves and equals the central frequency, 30 GHz. In addition, the ratio of the endpoints at half maximum is more than an octave. Moreover, as we can see in Figure 7.25, the ratio between the endpoints of the curves is more than a decade. From the foregoing discussion it is clear that the interaction of two 0.7-mm cold beams at 30 GHz possesses a significant gain bandwidth.

As can be seen in Figure 7.25, all three curves are centered around 30 GHz, where G_{sim} has a maximum. This is in agreement with Equation 4.39 from the 1-D theory. In Figure 7.25, over the range $5 \leq f \leq 40$ GHz, the average ratio of G_{sim} for $I = 1.5$ A to that for $I = 1.0$ A is about 1.2. Over the same range, the average ratio of G_{sim} for $I = 1.0$ A to that for $I = 0.6$ A approximately equals 1.33. The ratios of G_{sim} are within 3% of the corresponding ratios for G_{th}. Hence, the agreement is very good. However, the agreement deteriorates near the edges of the bandwidth curves, which can be attributed to noisy data from simulations (not shown), as indicated by large error bars in Figure 7.25. Note that for all three currents in Figure 7.25, G_{sim} for modulated beams differs from that for unmodulated beams by 3% (ignoring error bars). Therefore, G_{sim} is not a function of modulation amplitude for $I = 0.6$ A, $I = 1.0$ A, and $I = 1.5$ A, respectively.

Figure 7.26 is similar to Figure 7.25 and depicts bandwidth curves for the interaction of two 0.5-A modulated beams at 30 GHz. The red curve is the same as that in Figure 7.25. For the blue and green curves the beam radii were 1.0 mm and 1.4 mm and beam energies were the same as those in Figure 7.16. For each dataset shown the

modulation amplitude and frequencies were the same as those in the previous plot. As in Figure 7.25, the open stars in Figure 7.26 represent G_{sim} for unmodulated

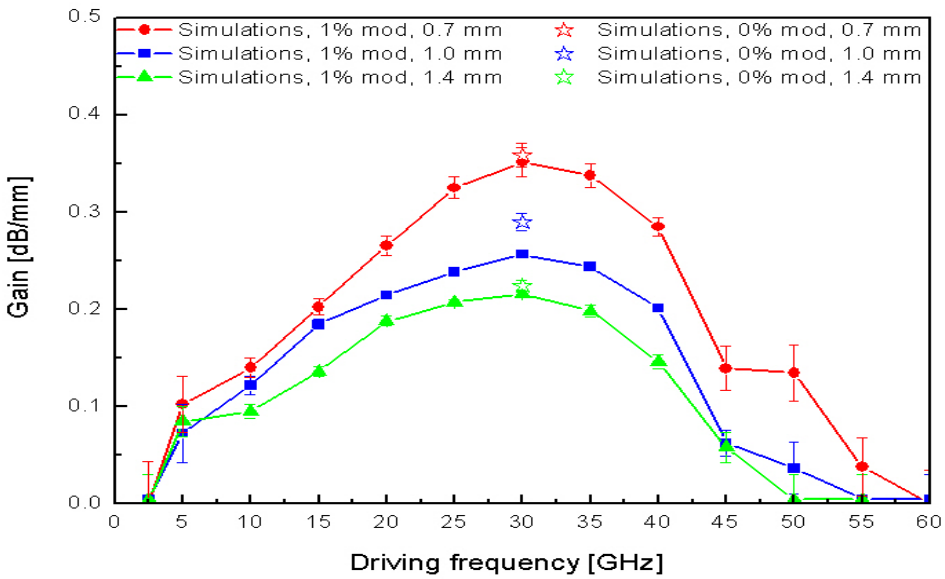

Figure 7.26: Bandwidth curves for two 0.5-A modulated beams interacting at 30 GHz. The red, blue, and green curves correspond to $r_b = 0.7$ mm, $r_b = 1.0$ mm, and $r_b = 1.4$ mm, respectively. The open stars are G_{sim} for cold and unmodulated beams.

beams at 30 GHz.

According to Figure 7.26, G_{sim} peaks at 30 GHz, which is consistent with Equation 4.39. The gain bandwidth of the blue and green curves, estimated at FWHM in Figure 7.26, yields 30.5 GHz and 32.1 GHz. To first order, the FWHM bandwidth for $r_b = 1.4$ mm and $r_b = 1.0$ mm is approximately the same as that for $r_b = 0.7$ mm, which is equal to 31 GHz. Hence, as in Figure 7.25, the ratio of the endpoints corresponding to 50% of G_{sim} is more than an octave. Also, the ratio between the endpoints of the blue and green curves is more than a decade. Comparing Figures 7.26 and 7.25, we can conclude that the FWHM bandwidth is independent of total beam current and beam radius (space charge) for the interaction of two cold

electron beams at 30 GHz.

Examining the curves in Figure 7.26, the smaller the beam radius, the faster G_{sim} becomes negligible for large modulation frequencies. Note that G_{sim} for modulated beams is in good agreement with that for unmodulated beams for $r_b = 0.7$ mm and $r_b = 1.4$ mm. However, the former and the latter differ by as much as 11.5% (ignoring error bars) for $r_b = 1.0$ mm. As r_b ranges from 0.7 mm to 1.4 mm, G_{sim} at 30 GHz increases by as much as 38.5%. Although the red curve ($r_b = 0.7$ mm) has no advantage over the other two curves in terms of the bandwidth, the interaction of two 0.7-mm beams yields a higher gain over the entire frequency range shown. In addition, as was discussed earlier (Figure 7.24), the interaction of two 0.7-mm beams enables us to makes the interaction region shorter.

Having explored bandwidth plots at 30 GHz, we will now examine gain bandwidth at a medium interaction frequency. Figure 7.27 displays gain bandwidth curves for the interaction of two 0.7-mm modulated beams at 110 GHz. For the blue and red curves in Figure 7.27, the beam currents and energies were the same as those in Figure 7.6. The modulation amplitude was 1% and the modulation frequency ranged from 10 GHz to 170 GHz (15 frequencies in total, as indicated by the data points). As in the previous two figures, the open stars in Figure 7.27 represent G_{sim} for unmodulated beams at 110 GHz.

According to Figure 7.27, for $I = 0.6$ A the FWHM bandwidth is about 128 GHz (from 34.4 GHz to 162.4 GHz), while that for $I = 1.0$ A approximately equals 134 GHz (28.5 GHz to 162.5 GHz). The ratio of the endpoints corresponding to 50% of G_{sim} is about 4.7 and 5.7 for the blue and red curves, respectively. These values are a factor of 1.4 and 1.7 greater than those in Figure 7.25. This suggests that the gain bandwidth increases with increasing interaction frequency. Note that the ratio between the endpoints of the blue and red curves is more than a decade, which is what we observed for the interaction at 30 GHz in Figure 7.25. The values of the

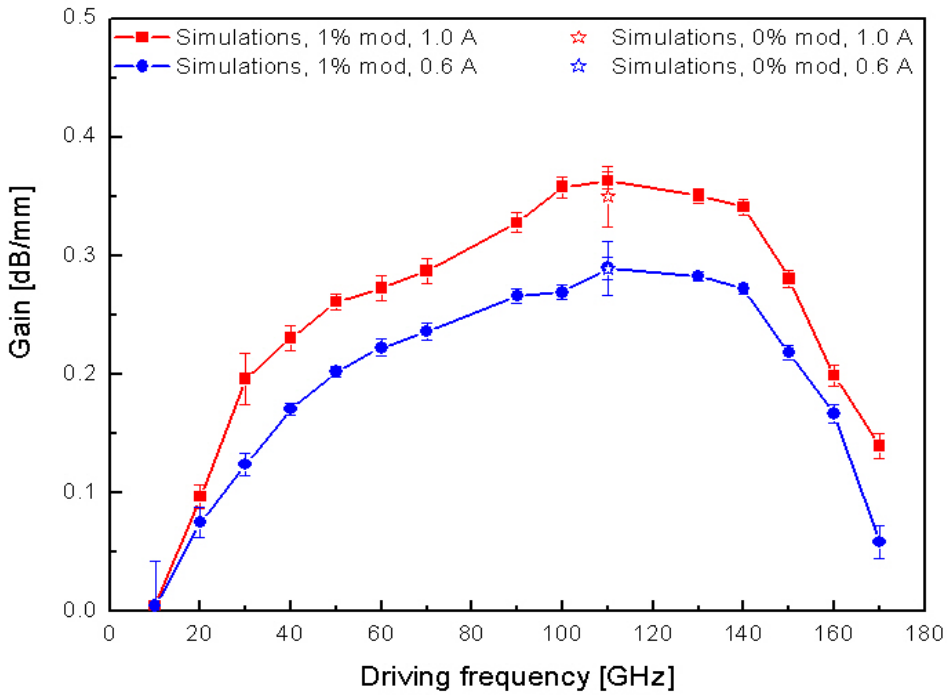

Figure 7.27: Gain bandwidth for two 0.7-mm modulated beams interacting at 110 GHz. The blue and red curves correspond to $I = 0.6$ A and $I = 1.0$ A. The open stars are G_{sim} for cold and unmodulated beams.

bandwidth given above are estimates and are within a factor of 1.05 of one another. Hence, we can conclude that the interaction of two cold electron beams at 110 GHz has an impressive gain bandwidth, which, to first order, is independent of total beam current.

As can be seen in Figure 7.27, the largest gain occurs at 110 GHz. This agrees with Equation 4.39, which predicts that two 0.7-mm beams, with the same beam currents and energies as in Figure 7.27, will interact at 110 GHz. Over the range $20 \leq f \leq 160$ GHz, the average ratio of G_{sim} for $I = 1.0$ A to that for $I = 0.6$ A is within 3% of the corresponding ratios for G_{th}. The discrepancy between the numerical and theoretical ratios becomes significant at the bandwidth curve edges,

being as much as 22% and 46% at 10 GHz and 170 GHz, respectively. Note that G_{sim} for modulated and unmodulated beams are in good agreement (including error bars) for both currents. Hence, G_{sim} is independent of modulation amplitude.

Figure 7.28 combines bandwidth plots from Figures 7.25 and 7.27 with those for the interaction of two 0.7-mm and 0.5-A modulated beams at 400 GHz (green curve) and 800 GHz (burgundy curve). For the green and burgundy curves in Figure 7.28,

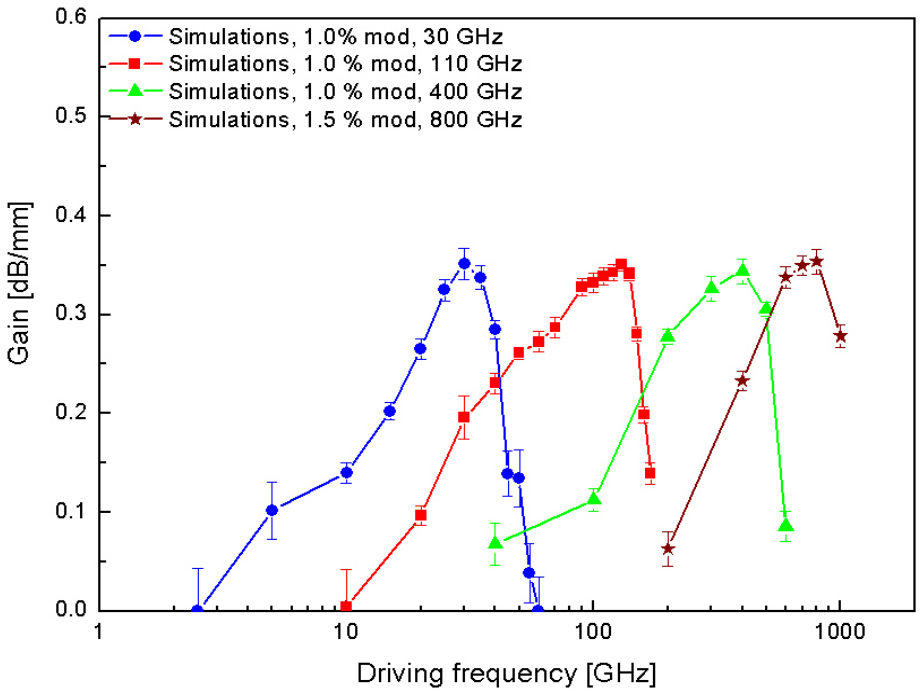

Figure 7.28: Gain bandwidth for two 0.7-mm and 0.5-A modulated beams interacting at 30 GHz, 110 GHz, 400 GHz, and 800 GHz.

the beam energies were the same as those in Figures 7.13 and 7.14. Also, for the green curve the modulation amplitude was 1% and the modulation frequency ranged from 40 GHz to 600 GHz. For the burgundy curve the modulation amplitude was 1.5% and the modulation frequency ranged from 200 GHz to 1 THz.

According to Figure 7.28, the green curve peaks at 400 GHz, while the burgundy curve has a maximum at 800 GHz. This agrees with Equation 4.39, which predicts that the beams with the same currents and energies as those (green and burgundy curves) in Figure 7.28 will interact at 400 GHz and 800 GHz, respectively. Note that the agreement between the peak values of G_{sim} at 30 GHz, 110 GHz, 400 GHz, and 800 GHz is very good (including error bars). Hence, as we saw earlier, G_{sim} is independent of interaction frequency and modulation amplitude.

The gain bandwidth of the green curve estimated at FWHM approximately equals 378 GHz (163 GHz to 541 GHz). For the burgundy curve, if we use a rough estimate, the FWHM bandwidth is approximately 780 GHz. Using these estimates, the ratio between the endpoints corresponding to 50% of G_{sim} is about 3.3 for both 400 GHz and 800 GHz. This value is about the same as that for 30 GHz and a factor 1.7 smaller than that for 110 GHz. Hence, to first order, the gain bandwidth measured at FWHM is independent of interaction frequency and modulation amplitude for the interactions from 30 GHz to 800 GHz. According to Figure 7.28, a radiation source based on the interaction of two 0.7-mm and 0.5-A modulated beams will have an impressively wide gain bandwidth from the microwave to the far infrared region of the spectrum. We should keep in mind, however, that the curves in Figure 7.28 correspond to cold beams. As will be shown in Section 7.4, for the interaction of warm beams the actual gain obtained is lower than that in Figure 7.28.

7.4 Consequences of energy spread

All simulation results up to this point in this chapter have been for the interaction of two cold electron beams. Section 7.4 explores the interaction of two warm beams. In addition, we examine the effect of nonzero energy spread on gain and gain bandwidth.

7.4.1 Degradation of gain

In this subsection, we will look at the interaction of two warm and modulated beams at low (30 GHz), medium (110 GHz, 210 GHz), and high (400 GHz, 800 GHz) interaction frequencies. We will also study the influence of nonzero energy spread on G_{sim}.

7.4.1.1 Low interaction frequency

Figure 7.29 depicts the magnitude of the ac component of electric field, $|E_z|$, as a function of frequency for the interaction of two 0.7-mm and 0.5-A modulated beams with three different values of percent energy spread, namely, 0% spread (red curve), 3% spread (burgundy curve), and 5% spread (green curve). The beam energies, mod-

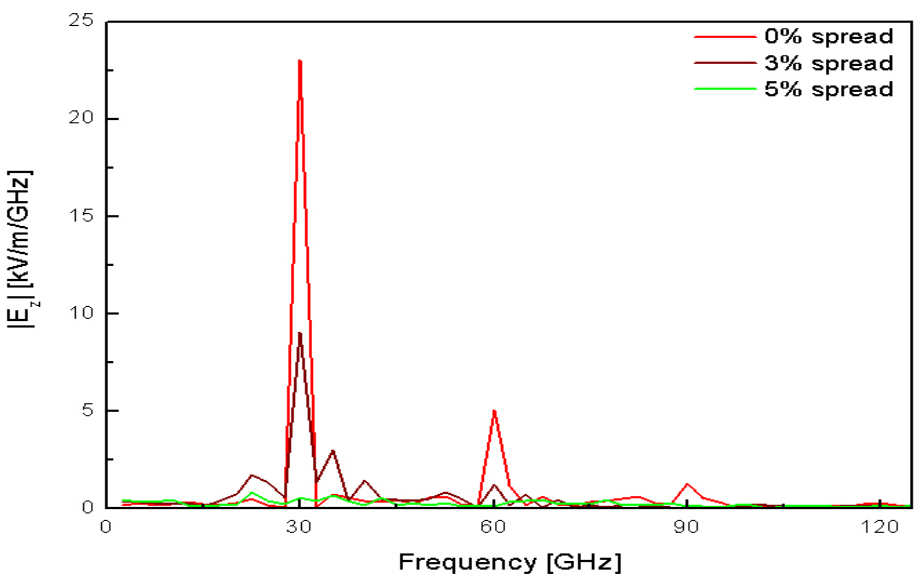

Figure 7.29: FFT of $|E_z|$ for the interaction of two 0.7-mm modulated beams at 30 GHz for $I = 1.0$ A. The red, burgundy, and green curves correspond to 0%, 3%, and 5% energy spread.

ulation frequency, and modulation amplitude were the same as those in Figure 7.1. The curves in Figure 7.29 were recorded at a longitudinal position equal to $z =$ 126 mm. Also, the FFT parameters used were the same as those in Figure 7.1.

According to Appendix D, 3% and 5% energy spread for 20- and 16.95-keV beams is equivalent to 1108 eV and 1847 eV at FWHM. As can be seen in Figure 7.29, a frequency component at 30 GHz is dominant for 0% and 3% energy spread. This agrees with Equation 4.39, which states that two 0.7-mm and 0.5-A beams with the same energies as those in Figure 7.29 will interact at 30 GHz regardless of the modulation amplitude and the amount of energy spread.

For 5% energy spread in Figure 7.29, the interaction is very weak due to a significant overlap of the beam energies (1847 eV at FWHM). It can be shown that as percent energy spread ranges from 0% to 5%, the average signal-noise-ratio is reduced by about a factor of 34. Even though the 30-GHz mode has the largest magnitude for 3% spread, it is not the only mode present as we can see in Figure 7.29. Three modes stand out, specifically, those at 22.5 GHz, 35 GHz, and 40 GHz. The magnitude of the largest of the three, 35 GHz, is approximately a factor three less than that of the 30-GHz mode. Note that the interaction for 0% energy spread is already nonlinear at $z = 126$ mm, Figure 7.29 showing as many as three harmonics at 60 GHz, 90 GHz, and 120 GHz, respectively.

Figure 7.30 shows $|E_z|$ of a 30-GHz mode for the interaction of two 0.7-mm and 0.5-A modulated beams with the same beam energies as in Figure 7.29. The datasets in Figure 7.30 were obtained from 6 different simulations involving the beams with 0% (red), 1% (blue), 2% (black), 3% (burgundy), 4% (magenta), and 5% spread (green). The gray curves in Figure 7.30 are given by Equation 5.9 and represent curve fits to the linear regions of the data.

In Figure 7.30, the slope of the linear portion is unchanged for percent energy

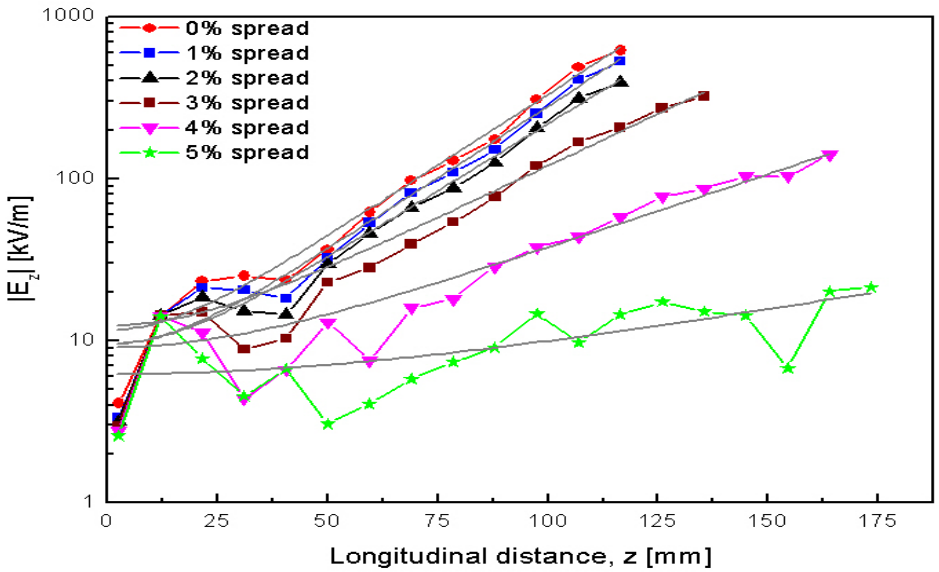

Figure 7.30: $|E_z|$ of a 30-GHz mode versus longitudinal distance, z, for two 0.7-mm modulated beams interacting at 30 GHz for $I = 1.0$ A. The datasets correspond to 6 different values of percent energy spread. The solid gray curves are curve fits given by Equation 5.9.

spread less than or equal to 1%. This agrees with what we observed for unmodulated beams in Figure 6.25. For values of percent spread exceeding 1%, the slope starts to decrease steadily, its magnitude for 3% and 5% spread being approximately 27% and as much as 74% less than that for 0% spread. This is consistent with the energy profiles shown in in Figure 6.23.

According to Figure 7.30, the initial value of $|E_z|$ increases with decreasing energy spread. By contrast, as can be seen in Figure 6.25, the initial value of $|E_z|$ decreases with decreasing energy spread. Also, the initial angle of $|E_z|$ for modulated beams is always positive, which is not the case for unmodulated beams in Figure 6.25. In Figure 7.30, the warmer the beams are, the noisier $|E_z|$ becomes. The green curve (5% spread) has at least four pronounced dips and it is the least linear of those displayed. Note that the initial dip in $|E_z|$ shifts from right to left with increasing

energy spread, which is what we saw in Figure 6.25.

Figure 7.30 depicted the variation of $|E_z|$ for 0.7-mm beams. Figure 7.31 is similar to the previous figure and shows the variation of $|E_z|$ of a 30-GHz mode for

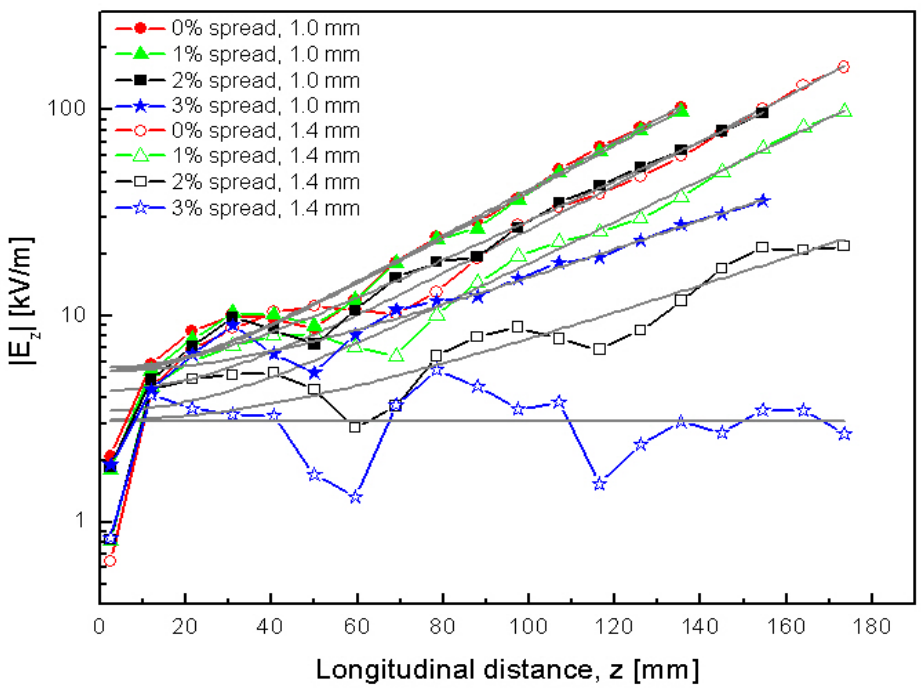

Figure 7.31: $|E_z|$ of a 30-GHz mode versus axial distance, z, for $r_b = 1.0$ mm (solid symbols) and $r_b = 1.4$ mm (open symbols). The data are shown for four different values of percent energy spread and $I = 1.0$ A. Gray curves represent curve fits given by Equation 5.9.

the interaction of two 0.5-A modulated beams with $r_b = 1.0$ mm (solid symbols) and $r_b = 1.4$ mm (open symbols). The beam energies, modulation frequency, and modulation amplitude were the same as those in Figure 6.26. The red, green, black, and blue curves correspond to 0%, 1%, 2%, and 3% energy spread for both sets of data. Also, the gray curves (given by Equation 5.9) are curve fits to the linear portions of the two sets of data.

The slope of the linear portion in Figure 7.31 behaves the same way as in Figure 7.30. Namely, it decreases with increasing percent energy spread. However, due to a larger ΔE and a smaller FWHM energy, the slope for $r_b = 0.7$ mm in Figure 7.30 decreases by approximately 27% as percent energy spread varies from 0% to 3%. By contrast, as can be seen in Figure 7.31, the slopes for $r_b = 1.0$ mm and $r_b = 1.4$ mm decrease by approximately 38% and by as much as 98% over the same range of percent energy spread.

In Figure 7.31, the larger the beams radius (less space charge), the smaller the initial value of $|E_z|$. For 0.7-mm beams in Figure 7.30, the initial value of $|E_z|$ increases with decreasing energy spread. As we can see in Figure 7.31, the same does not hold true for either dataset. For $r_b = 1.0$ mm, the red curve (0% spread) has the largest initial magnitude. However, the green, black, and blue curves have identical initial values. Likewise, for $r_b = 1.4$ mm, the initial values of $|E_z|$ are on top one another for 1%, 2%, and 3% spread. However, as opposed to $r_b = 1.0$ mm, the red curve (0% spread) for $r_b = 1.4$ mm has the lowest initial magnitude. It is interesting to note in Figure 7.31 that $|E_z|$ for $r_b = 1.4$ mm is markedly less linear than for $r_b = 1.0$ mm.

Figure 7.32 displays the gain of a 30-GHz mode as a function of percent energy spread. The solid symbols in Figure 7.32 correspond to G_{sim} for modulated beams and were obtained by substituting the values of R from Figures 7.30 and 7.31 into Equation 5.10. The open symbols represent G_{sim} for unmodulated beams. In the top plot, G_{sim} curves for unmodulated beams were taken from Figure 6.30. In the bottom plot, G_{sim} curves for unmodulated beams are the same as those in Figure 6.27. The dashed red and blue lines represent G_{th} from Equation 4.38.

For $I = 0.6$ A in the top plot of Figure 7.32, G_{sim} for modulated and unmodulated beams is unchanged for percent energy spread less than or equal to 1%, the former and the latter being within 5% and 6.2% of G_{th} (ignoring error bars). As percent

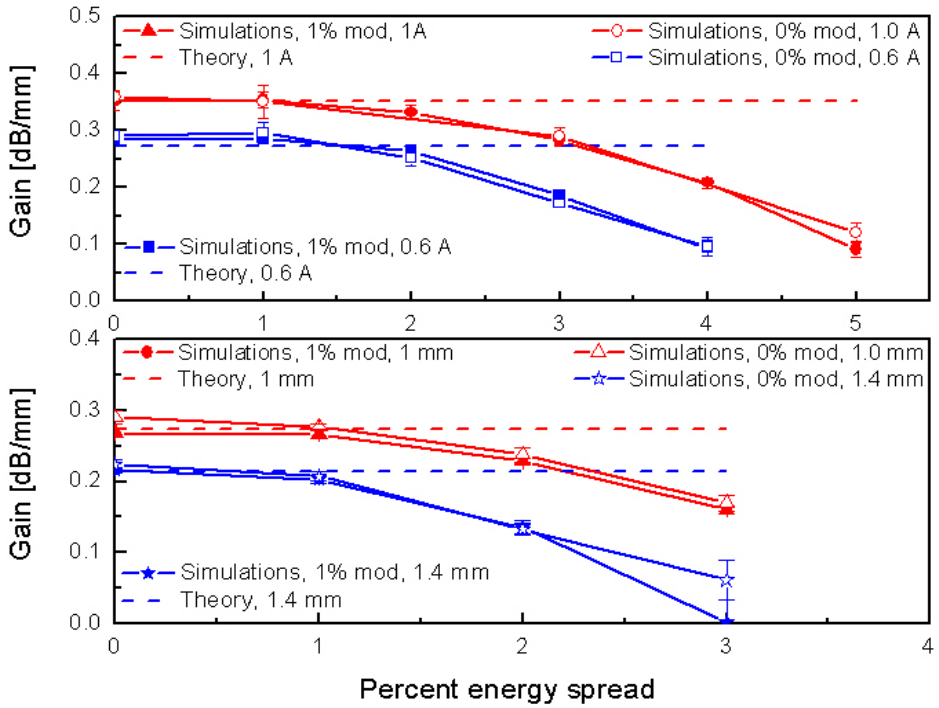

Figure 7.32: Gain of a 30-GHz mode as a function of percent energy spread. In the top plot, all data are for $r_b = 0.7$ mm. In the bottom pot, red curves correspond to $r_b = 1.0$ mm and blue curves are for $r_b = 1.4$ mm. The dashed red and blue lines represent theoretical gain. The solid and open symbols show $G_{\rm sim}$ for modulated and unmodulated cases.

spread increases from 1% to 4%, both decrease by as much as 67% as compared to their values for 0% spread. The average deviation between the former and the latter is within 4% (error bars excluded) and we can conclude that $G_{\rm sim}$ is independent of modulation amplitude for $I = 0.6$ A and $r_b = 0.7$ mm.

For $I = 1.0$ A in the top plot of Figure 7.32, $G_{\rm sim}$ for modulated and unmodulated beams are in good agreement (within 2%) for 0% and 1% energy spread. Also, they agree very well with $G_{\rm th}$ for energy spread less than or equal to 1%, $G_{\rm sim}$ for modulated beams being within 0.8% of $G_{\rm th}$ and $G_{\rm sim}$ for unmodulated beams being witin 2% of $G_{\rm th}$ (error bars excluded). As percent energy spread varies from 0% to

5%, the overlap between 20- and 16.95-keV becomes significant. As a result, G_{sim} for modulated beams and that for unmodulated ones decrease by as much as 74% and 66%, respectively. As can be seen in Figure 7.32, the average deviation between the former and the latter is within 3% (ignoring error bars) for percent spread less than or equal to 4%. However, the two differ by as much as 24% (excluding error bars) when percent energy spread equals 5%. Still, we can again state that G_{sim} is independent of modulation amplitude for $I = 1.0$ A and $r_b = 0.7$ mm.

For $r_b = 1.0$ mm in Figure 7.32, the average difference between G_{sim} for modulated and unmodulated beams is about 5% (ignoring error bars). In addition, the former and the latter are within 1.5% and 5.9% (excluding error bars) of G_{th} for 0% energy spread. Hence, the agreement with theory (Equation 4.38) is very good and fairly good for modulated and unmodulated beams, respectively. As percent energy spread increases from 0% to 3%, G_{sim} for the modulated and unmodulated cases decrease by approximately 40%. For $r_b = 1.4$ mm in Figure 7.32, G_{sim} for modulated and unmodulated beams are within 3.6% (ignoring error bars) with the exception of 3% energy spread, where the two differ by as much as 96% (excluding error bars). This is most likely due to a considerable amount of noise for the $|E_z|$ data in Figure 7.31. According to Figure 7.32, G_{sim} for modulated and unmodulated beams are within 4% (ignoring error bars) of G_{th}. Hence, the agreement is very good. Based on the foregoing discussion, if error bars are taken into account, we can conclude G_{sim} is independent of modulation amplitude for both $r_b = 1.0$ mm and $r_b = 1.4$ mm.

According to Figure 7.32, G_{sim} for 0% spread decreases with increasing beam radius. This is consistent with Equation 4.38 (theoretical gain), which is inversely proportional to r_b. Moreover, even though Equation 4.38 is invalid for warm beams, G_{sim} for $r_b = 0.7$ mm (red curve) is consistently larger than that for $r_b = 1.0$ mm and $r_b = 1.4$ mm over the entire range of percent energy spread in Figure 7.32.

7.4.1.2 Medium interaction frequencies

Figure 7.33 shows an FFT of $|E_z|$ for the interaction of two 0.7-mm and 0.5-A beams

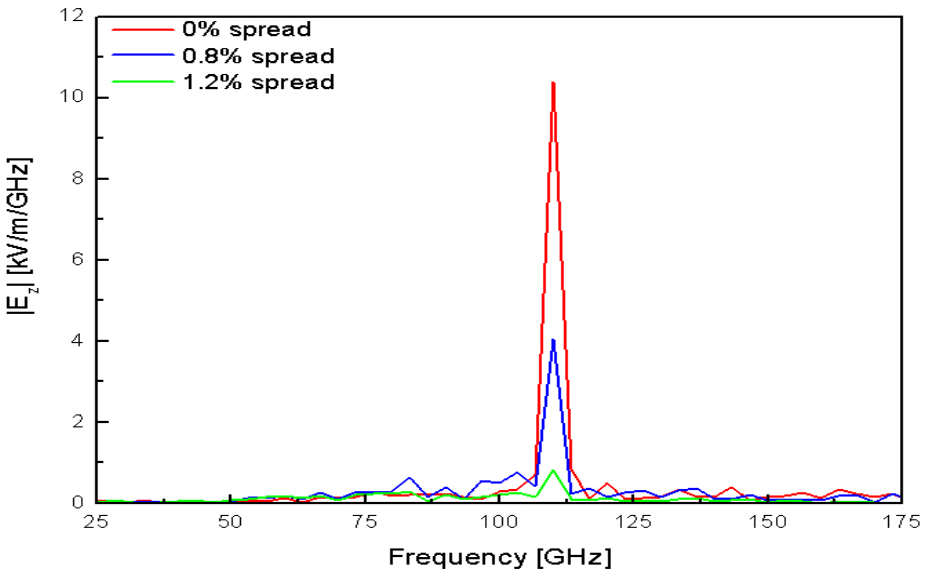

Figure 7.33: FFT of $|E_z|$ for the interaction of two 0.7-mm modulated beams at 110 GHz for $I = 1.0$ A. The red, blue, and green curves correspond to 0%, 0.8%, and 1.2% energy spread.

with three different values of percent energy spread, specifically, 0% (red curve), 0.8% (blue curve), and 1.2% spread (green curve). The modulation amplitude, modulation frequency, time window, and frequency window were the same as those in Figure 7.6. Also, the curves were recorded at a longitudinal position equal to $z = 116.5$ mm.

For the beams used to generate Figure 7.33, 0.8% spread is equivalent to 156.66 eV and 1.2% spread corresponds to 234.98 eV. According to Figure 7.33, a mode at 110 GHz is clearly dominant for 0% and 0.8% spread over the frequency range shown. As we can see, the 110-GHz mode appears to be the largest frequency component even for percent spread as big as 1.2%. However, the average signal-to-noise ratio is reduced by about a factor of 5 as percent spread varies from 0% to 1.2%.

Comparing the FFT curves in Figure 7.33 with those in Figure 7.29, we can see that $|E_z|$ for the 30-GHz mode is reduced by approximately 61% as percent energy spread increases from 0% to 3%. By contrast, $|E_z|$ of the 110-GHz mode for 1.2% spread is already 92% less compared to its value for 0% energy spread. This is due to ΔE for interactions at 110 GHz being approximately a factor of 3.6 less than that for beams interacting at 30 GHz. Note that no harmonics, if any, are shown in Figure 7.33 because of the frequency window used (10 GHz to 200 GHz) to record the FFT curves.

Figure 7.34 shows the variation of $|E_z|$ of a 110-GHz mode with longitudinal distance, z, for the interaction of two 0.7-mm and 0.5-A modulated beams with 6 different values of percent energy spread, namely, 0% (red), 0.4% (burgundy), 0.8% (blue), 1% (black), 1.2% (green), and 1.5% spread (orange). The modulation frequency and amplitude were the same as those in the previous figure. The gray curves in Figure 7.34 are given by Equation 5.9 and represent curve fits to the linear regions of the datasets.

According to Figure 7.34, the larger the percent spread, the smaller the slope of the linear region. This is consistent with what we have observed so far for the interaction of warm beams regardless of their interaction frequency, radii, and modulation level.

As we can see in Figure 7.34, the slope is already zero for 1.5% spread due to the beam energies being significantly overlapped. By contrast, owing to a larger ΔE, the slope in Figure 7.30 is nonzero even for percent energy spread as large as 5%. Note that the distribution of the initial values of $|E_z|$ in Figure 7.34 is random, which is different from that in Figure 7.30, where the initial values of $|E_z|$ increase with decreasing energy spread.

Figure 7.35 shows $|E_z|$ of a 110-GHz mode as a function of longitudinal distance,

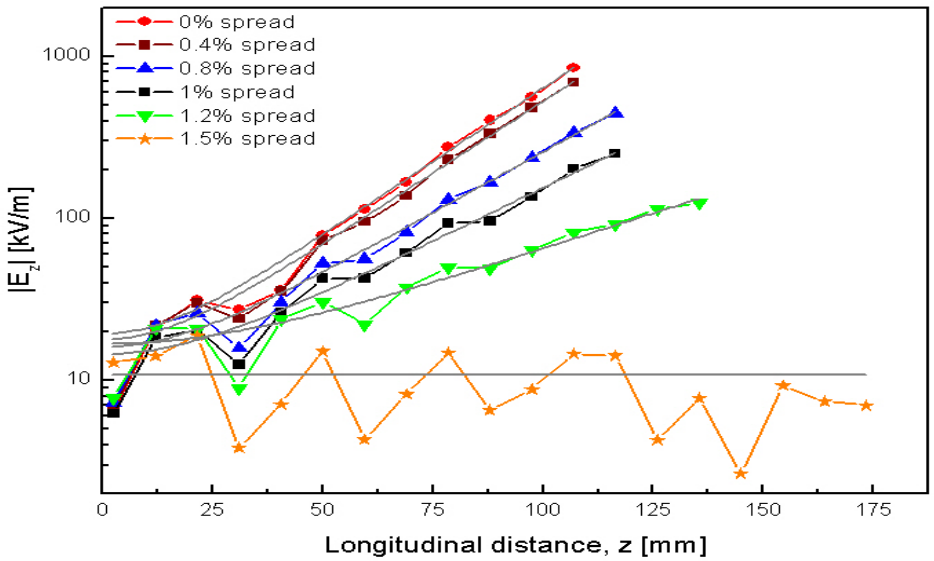

Figure 7.34: $|E_z|$ of a 110-GHz mode versus longitudinal distance, z, for the interaction of two 0.7-mm modulated beams at 110 GHz for $I = 1.0$ A. The datasets correspond to 6 different values of percent energy spread. The solid gray curves are curve fits given by Equation 5.9.

z, for the interaction of two 1.0-mm and 0.5-A modulated beams with three different values of percent energy spread, namely, 0% (red), 0.4% (burgundy), and 1% spread (black). The modulation amplitude was 1% at 110 GHz. The beam energies used were 20 keV and 19.413 keV. The gray curves in Figure 7.35 are given by Equation 5.9 and represent curve fits to the linear regions of the datasets.

In Figure 7.35, 0.4% and 1% percent energy spread correspond to 78.82 eV and 197.06 eV. The curves in Figure 7.35 exhibit an oscillatory behavior, which is most prominent for the black curve (1.0% spread). Note that the initial value of $|E_z|$ has the smallest magnitude for 0% spread. This is to contrast to what we saw in Figure 7.31 for the interaction of 1.0-mm beams at 30 GHz.

Comparing Figures 7.35 and 7.34, the slope of the linear region decreases with

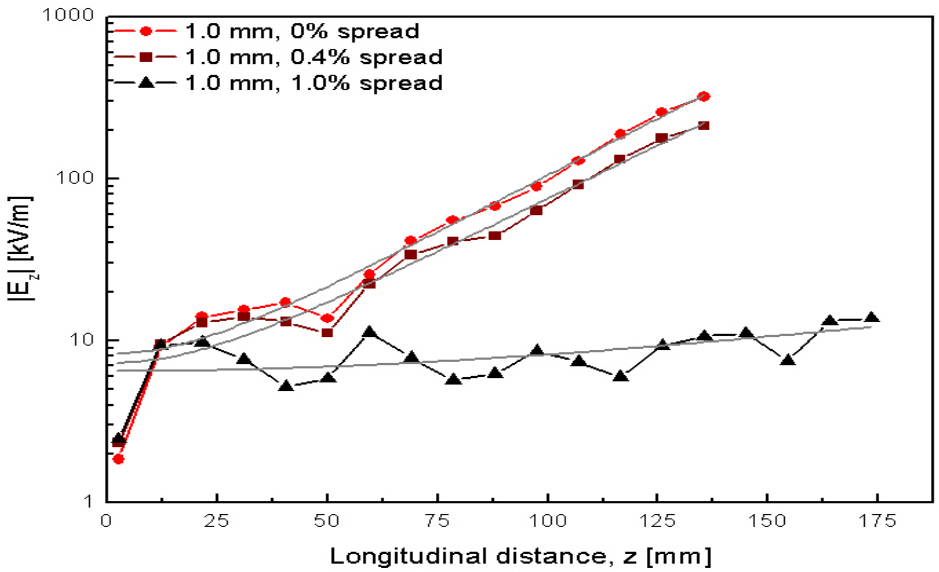

Figure 7.35: $|E_z|$ of a 110-GHz mode versus axial distance, z, for the interaction of two 1.0-mm modulated beams at 110 GHz for $I = 1.0$ A. The data are shown for three different values of percent energy spread. Gray curves represent curve fits given by Equation 5.9.

increasing energy spread for both $r_b = 0.7$ mm $r_b = 1.0$ mm. As percent energy spread varies from 0% to 1%, the slope in Figure 7.35 is reduced by as much as 78%. In contrast, owing to a larger ΔE, the slope in Figure 7.34 decreases by approximately 27%. Hence, G_{sim} for $r_b = 1.0$ mm is less than that for $r_b = 0.7$ mm, which agrees with theory.

The next plot is that of the gain of a 110-GHz mode as a function of percent energy spread in Figure 7.36. The solid symbols correspond to G_{sim} for modulated beams and were obtained by substituting the values of R from Figures 7.34 and 7.35 into Equation 5.10. The open symbols represent G_{sim} for unmodulated beams (Figure 6.30). G_{th} from Equation 4.38 is shown by the dashed lines.

For $I = 1.0$ A in the top plot, G_{th} is within 6.5% and 3.7% (excluding error bars)

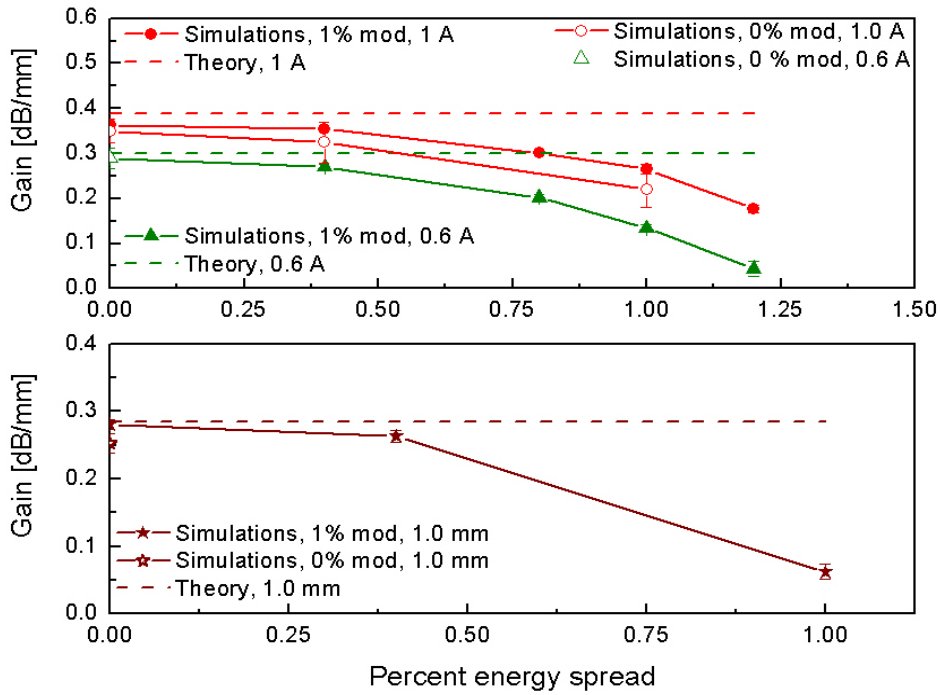

Figure 7.36: Gain of a 110-GHz mode as a function of percent energy spread. In the top and bottom plots, the data are for $r_b = 0.7$ mm and $r_b = 1.0$ mm, respectively. The dashed lines represent theoretical gain. The solid and open symbols show $G_{\rm sim}$ for modulated and unmodulated cases.

of $G_{\rm sim}$ for unmodulated and modulated beams with 0% energy spread. As can be seen in Figure 7.36, the agreement between theory and simulations is slightly better for $I = 0.6$ A and $G_{\rm th}$ is within 4% (excluding error bars) of $G_{\rm sim}$ for modulated and unmodulated beams with 0% energy spread. As percent spread ranges from 0% to 1.2%, $G_{\rm sim}$ for $I = 1.0$ A decreases by about 51%. By contrast, due to a smaller ΔE, $G_{\rm sim}$ for $I = 0.6$ A is reduced by as much as 85%. For $I = 1.0$ A in the top plot, the average deviation between $G_{\rm sim}$ for modulated and unmodulated beams is approximately 10% (excluding error bars). However, with the error bars taken into account, the two red curves are very close and we can conclude that $G_{\rm sim}$ is independent of modulation amplitude for $r_b = 0.7$ mm and $I = 1.0$ A.

For $r_b = 1.0$ mm and 0% energy spread in the bottom plot, G_{sim} for modulated beams and G_{th} are within 1.5% (ignoring error bars) of one another. Hence, the agreement is very good. G_{sim} for unmodulated and modulated beams are within 9.9%, the former differing from G_{th} by approximately 11.3% (excluding error bars). As percent spread varies from 0% to 1.0%, G_{sim} for modulated beams decreases by as much as 78%. In contrast, owing to a larger ΔE, G_{sim} of the 30-GHz mode in Figure 7.32 remains unaffected for percent energy spread less than or equal to 1.0%. Note that G_{sim} for $r_b = 0.7$ mm (red curve) is consistently larger than that for $r_b = 1.0$ mm (burgundy curve) over the range of percent energy spread shown, which agrees with theory.

Next, we examine the interaction of warm beams at 210 GHz. Figure 7.37 shows an FFT of $|E_z|$ for the interaction of two 0.7-mm and 0.5-A modulated beams with 0%

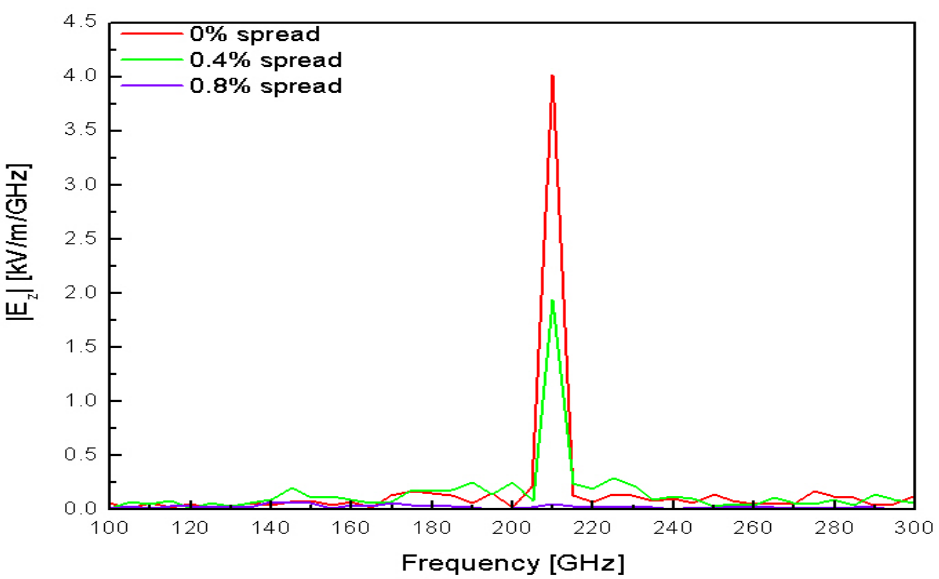

Figure 7.37: FFT of $|E_z|$ for the interaction of two 0.7-mm modulated beams at 210 GHz for $I = 1.0$ A. The red, green, and violet curves correspond to 0%, 0.4%, and 0.8% energy spread.

(red), 0.4% (green), and 0.8% (violet) energy spread. The beam energies, modulation amplitude, modulation frequency, time window, and frequency window in all three cases were the same as those in Figure 7.10. The curves were recorded at $z =$ 116.5 mm.

In Figure 7.37, 0.4% energy spread is equivalent to 79.1 eV and 0.8% spread corresponds to 158.2 eV. Hence, we can expect negligible interaction for beams with 0.8% energy spread. Equation 4.39 predicts the interaction frequency in Figure 7.37 to be 210 GHz. As we can see in Figure 7.37, not only is a frequency component at 210 GHz dominant for 0% spread, it is the largest mode even for 0.4% spread.

According to Figure 7.37, the magnitude of the 210-GHz mode for 0.8% spread is negligible in comparison with that for 0% energy spread. By contrast, as can be seen in Figure 7.33, $|E_z|$ of the 110-GHz mode for 0.8% energy spread is only a factor 2.6 less than that for 0% spread. This is due to ΔE for interactions at 210 GHz being approximately a factor of 1.8 smaller than that for beams interacting at 110 GHz. As in Figure 7.29, it would be reasonable to assume that the interaction depicted in Figure 7.37 becomes nonlinear at some point. However, since the curves in Figure 7.37 were recorded over a frequency window ranging from 80 GHz to 300 GHz, harmonics, if any, were excluded from the data.

Figure 7.38 shows $|E_z|$ of a 210-GHz mode as a function of longitudinal distance, z, for the interaction of two 0.7-mm and 0.5-A modulated beams with 5 different values of percent energy spread, namely, 0% (red), 0.2% (blue), 0.4% (green), 0.6% spread (black), and 0.8% spread (violet). The modulation frequency, modulation amplitude, and beam energies were the same as in Figure 7.37. The gray curves in Figure 7.38 are given by Equation 5.9 and represent curve fits to the linear regions of the datasets.

According to Figure 7.38, the general shape of the curves is very similar to that

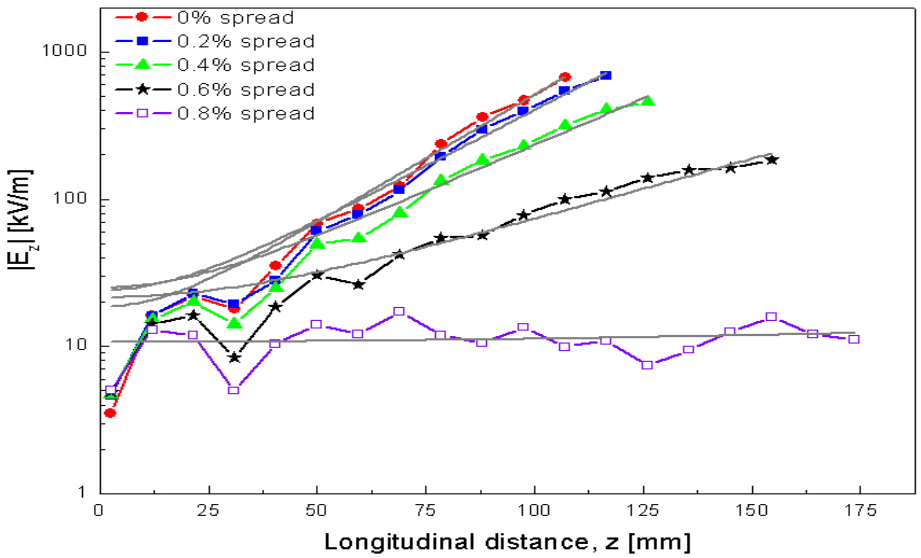

Figure 7.38: $|E_z|$ of a 210-GHz mode for the interaction of two 0.7-mm modulated beams at 210 GHz for $I = 1.0$ A. The red, blue, green, black, and violet curves correspond to 0%, 0.2%, 0.4%, 0.6%, and 0.8% spread. The gray curves are curve fits given by Equation 5.9.

in Figures 7.30 and 7.34. Note that the violet curve, which corresponds to the largest energy spread, is the least linear of the curves shown. This was observed in Figures 7.30 and 7.34 as well. In Figure 7.38, the initial values of $|E_z|$ increase with increasing energy spread, which is in contrast to what we observed in Figure 7.30, where the initial values of $|E_z|$ increase with decreasing energy spread.

As we can see in Figure 7.38, the warmer the beams are, the smaller the slope of the linear region. Owing to a smaller ΔE, the slope of the 210-GHz mode is negligible for 0.8% energy spread. In contrast, the slope of the 30-GHz mode in Figure 7.30 is the same as that for 0% spread. In addition, the slope of the 110-GHz mode in Figure 7.34 is within 17% of that for 0% energy spread. Note that for 0% spread, the slopes in Figures 7.30, 7.34, and 7.38 differ by less than 4% (excluding error bars). This suggests that G_{sim} is independent of interaction frequency and modulation

amplitude for the interaction of two 0.7-mm and 0.5-A beams at 30 GHz, 110 GHz, and 210 GHz.

Figure 7.39 displays the variation of the gain of a 210-GHz mode with percent energy spread. The blue curve in Figure 7.39 was obtained by substituting the values

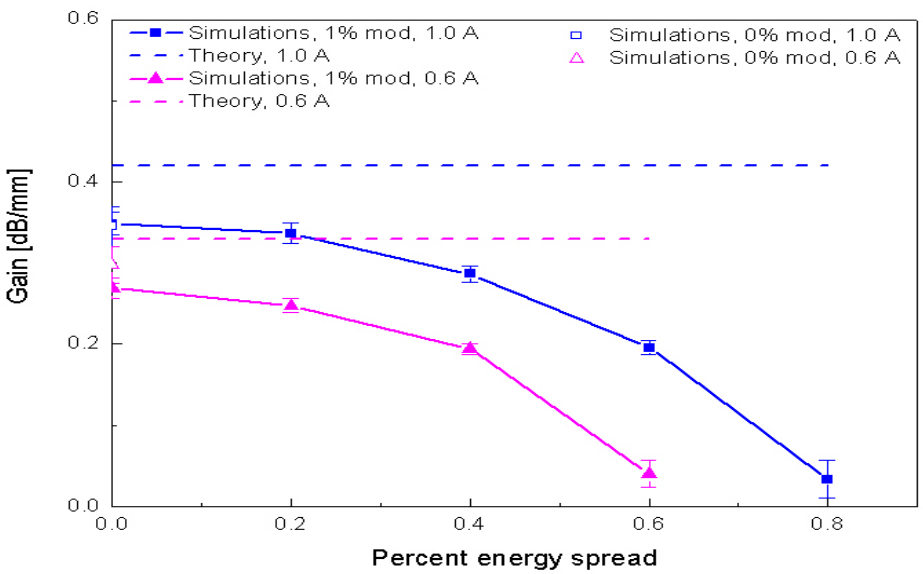

Figure 7.39: Gain of a 210-GHz mode as a function of percent energy spread for $I = 0.6$ A (magenta) and $I = 1.0$ A (blue). The solid and open symbols correspond to modulated and unmodulated cases. The dashed lines represent theoretical gain.

of R from Figure 7.38 into Equation 5.10. The magenta curve was generated from simulations involving the interaction of two 0.7-mm and 0.3-A modulated beams with energies 20 keV and 19.609 keV. The open triangle and open square correspond to unmodulated beams and are taken from Figure 7.19. Finally, the dashed blue and magenta lines represent G_{th} from Equation 4.38.

For $I = 0.6$ A and 0% spread in Figure 7.39, G_{th} is within 9.7% and 18.8% (ignoring error bars) of G_{sim} for unmodulated and modulated beams, respectively. G_{sim} for modulated beams differs from that for unmodulated beams by approximately

9.6% (excluding error bars). Thus, at first sight, the agreement is poor. However, if we take into account large error bars for both sets of data, then the discrepancy is negligible. As percent energy spread varies from 0% to 0.6%, G_{sim} for modulated beams decreases by as much as 85%. Note that due to a larger ΔE, G_{sim} (green curve) in Figure 7.36 reduces by 85% for only 1.2% spread, which is twice as large as that in Figure 7.39.

For $I = 1.0$ A and 0% spread in Figure 7.39, G_{th} is within 17.7% and 16.9% (ignoring error bars) of G_{sim} for unmodulated and modulated beams, respectively. Hence, the agreement is again poor. However, G_{sim} for modulated beams differs from that for unmodulated beams by approximately 1% (excluding error bars), and the agreement is very good. As percent energy spread varies from 0% to 0.8%, G_{sim} decreases by as much as 90%. Note that the values of G_{sim} for $I = 1.0$ A are greater than those for $I = 0.6$ A over the entire range of percent spread shown, which agrees with theory.

7.4.1.3 High interaction frequencies

Figure 7.40 shows an FFT of $|E_z|$ for the interaction of two 0.7-mm and 0.5-A modulated (red and blue curves) and unmodulated (green curve) beams at 400 GHz. For the red and green curves, the beams were cold. For the blue curve, on the other hand, the beams were warm with 0.2% energy spread. The modulation amplitude, modulation frequency, and beam energies were the same as those in Figure 7.13. Also, the FFT parameters were exactly the same as those used for Figure 7.13.

In Figure 7.40, a frequency component at 400 GHz for the green curve is negligible and does not rise above the noise floor. We believe that this is most likely due to a small ΔE (only 233 eV and over a factor of 10 less than that for interactions at 30 GHz) and a poor signal-to-noise ratio associated with simulations involving

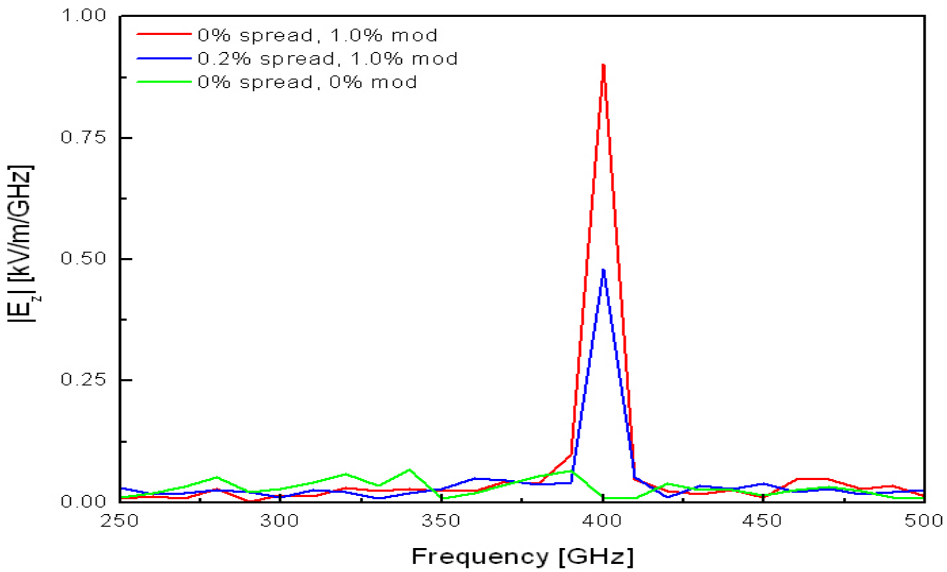

Figure 7.40: FFT of $|E_z|$ for the interaction of two 0.7-mm beams at 400 GHz for $I = 1.0$ A. The red and blue curves correspond to modulated beams. The green curve represents 0% modulation.

unmodulated beams. By contrast, both the red and blue curves in Figure 7.40 show a dominant mode at 400 GHz, which agrees with Equation 4.39. As percent spread increases from 0% to 0.2%, $|E_z|$ of the 400-GHz mode is reduced by approximately a factor of 1.9. Also, the magnitude of the 400-GHz mode for the green curve is merely 1% of that for the red curve in Figure 7.40.

A coarse resolution of the curves in Figure 7.40 can be blamed on the time window used (0.1 ns), which was equivalent to a frequency resolution of 10 GHz. This was necessary to keep the number of total particles in the simulation under 5,000,000 (Chapter 5). Note the red curve in Figure 7.40 is a slice of Figure 7.13 at $z = 116.5$ mm. As we saw in Figure 7.13, the 400-GHz mode saturates and peaks at this exact longitudinal position. Although no harmonics, if any, can be seen in Figure 7.40 owing to the frequency window used, it is very likely that the interaction

for modulated beams becomes nonlinear in the neighborhood of $z = 116.5$ mm.

Figure 7.41 is similar to Figure 7.40 and displays $|E_z|$ as a function of frequency

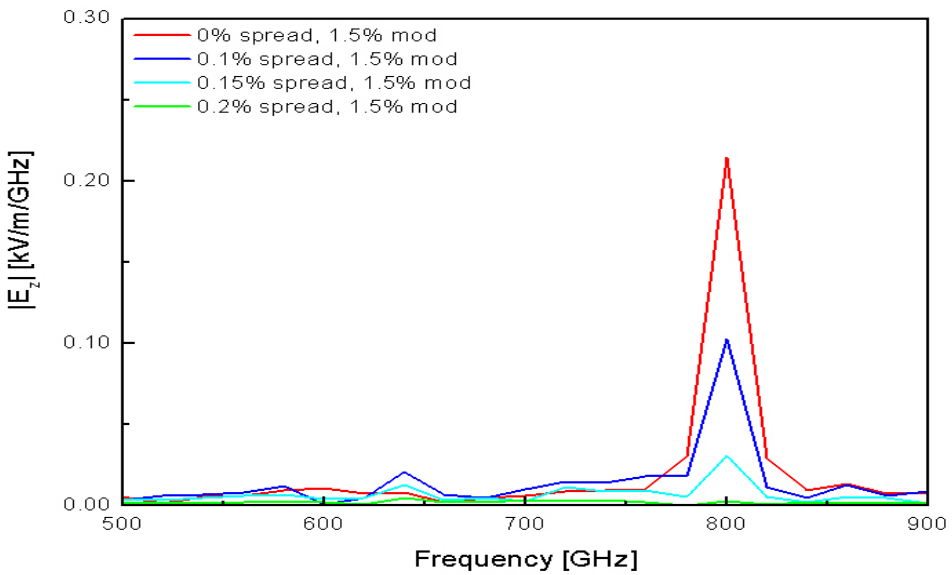

Figure 7.41: FFT of $|E_z|$ for the interaction of two 0.7-mm modulated beams at 800 GHz for $I = 1.0$ A. The red, blue, cyan, and green curves correspond to 0%, 0.1%, 0.15%, and 0.2% energy spread, respectively.

for the interaction of two 0.7-mm and 0.5-A modulated beams with 0% (red), 0.1% (blues), 0.15% (cyan), and 0.2% (green) energy spread. The beam energies, modulation amplitude, and modulation frequency were the same as those in Figure 7.14. Also, the frequency and time windows were identical to those in Figure 7.14. The curves in Figure 7.41 were recorded at $z = 116.5$ mm

In Figure 7.41, 0.1%, 0.15%, and 0.2% energy spread correspond to 39.88 eV, 59.82 eV, and 79.76 eV at FWHM. Equation 4.39 predicts that two 0.7-mm and 0.5-A beams with energies 20 keV and 19.884 keV will interact at 800 GHz. As can be seen in Figure 7.41, a frequency component at 800 GHz is dominant with the exception of 0.2% spread. For 0.2% spread, the beam energies overlap significantly

and negligible or no interaction is the result. Consequently, $|E_z|$ for 0% energy spread is approximately two orders of magnitude greater than that for 0.2% energy spread.

As in Figure 7.40, a low frequency resolution ($\Delta f = 20$ GHz) in Figure 7.41 can be attributed to a short time window (0.05 ns), which was dictated by MAGIC due to an upper limit on the total number of particles (Chapter 5). Note that the red curve in Figure 7.41 represents a 2-D image of Figure 7.14 at $z = 116.5$ mm, where, according to Figure 7.14, the 800-GHz mode has the largest amplitude. Owing to the frequency window used (500 GHz to 900 GHz), no harmonics, if any, can be seen in Figure 7.41. However, judging by Figure 7.15, the likelihood of the interaction at 800 GHz becoming nonlinear is quite high.

Figure 7.42 displays the variation of $|E_z|$ with longitudinal distance, z, for the

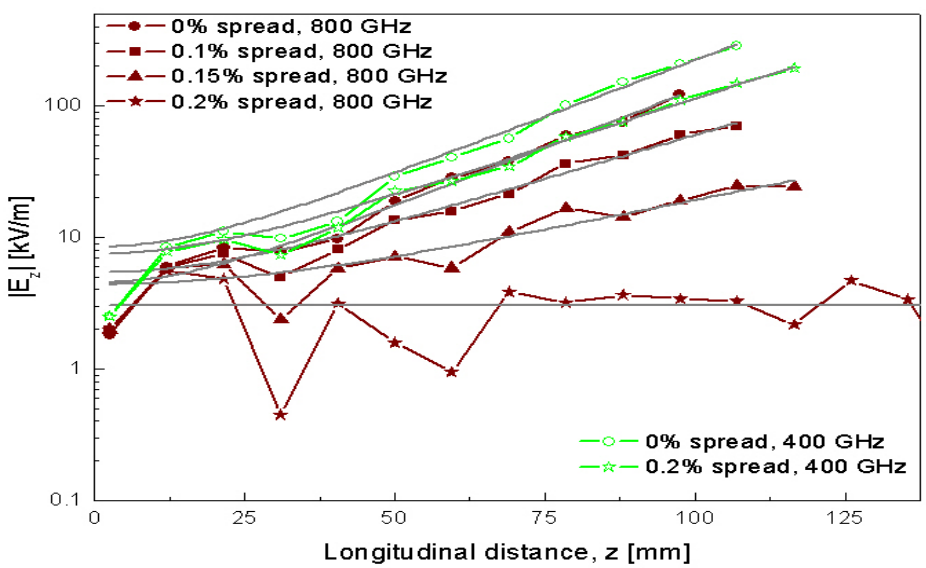

Figure 7.42: $|E_z|$ versus z for the interaction of two 0.7-mm modulated beams at 400 GHz (green) and 800 GHz (burgundy) for $I = 1.0$ A. The gray curves are curve fits given by Equation 5.9.

interactions discussed in Figures 7.40 (green curves) and 7.41 (burgundy curves).

The gray curves, given by Equation 5.9, represent curve fits to the linear portions of the datasets.

In Figure 7.42, all curves exhibit an oscillatory behavior, which becomes more pronounced with increasing energy spread. The overall shape of $|E_z|$ in Figure 7.42 resembles that in Figures 7.30, 7.34, and 7.38 for the interaction at 30 GHz, 110 GHz, and 210 GHz. Note that the effect of percent energy spread on the initial angle of $|E_z|$ is negligible for both sets of curves in Figure 7.42. In addition, the initial values of $|E_z|$ line up and appear to be independent of modulation amplitude. This is in contrast to what we observed in Figures 7.30, 7.34, and 7.38.

According to Figure 7.42, the slope of the linear portion decreases with increasing percent energy spread in both cases. This is consistent with what we have observed so far for the interaction of warm beams at 30 GHz, 110 GHz, and 210 GHz. As percent energy spread varies from 0% to 0.2% in Figure 7.42, the slope for 400 GHz is reduced by approximately 14%. Owing to a smaller ΔE, the slope for 800 GHz tends to zero as percent energy spread ranges from 0% to 0.2%. This is due to the beam energies overlapping and forming a single beam. Note that for 0% spread the slope at 400 GHz is within 3% (excluding error bars) of that at 800 GHz, which means that G_{sim} is independent of modulation amplitude and interaction frequency.

Figure 7.43 displays gain as a function of percent energy spread for the interaction of two 0.7-mm and 0.5-A modulated beams at 30 GHz (blue), 110 GHz (black), 210 GHz (magenta), 400 GHz (green), and 800 GHz (burgundy). The green and burgundy curves were obtained by substituting the values of R from Figure 7.42 into Equation 5.10. The blue, black, and magenta curves are from Figures 7.32, 7.36, and 7.39. The dashed lines represent G_{th} from Equation 4.38.

According to Figure 7.43, the discrepancy between G_{th} and G_{sim} for 0% spread is as much as 26% (ignoring error bars) for both 400 GHz and 800 GHz. Thus,

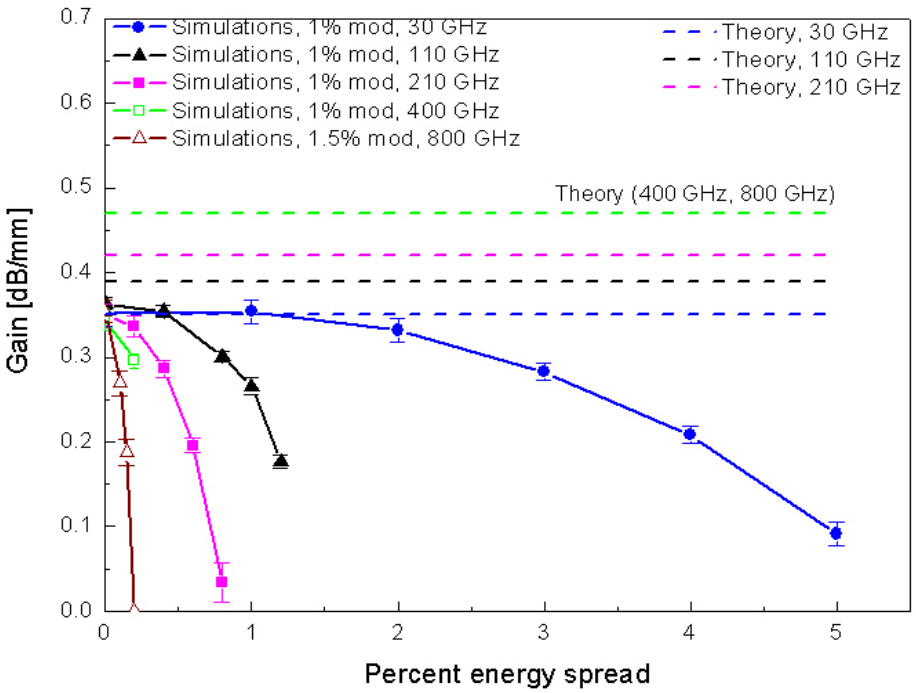

Figure 7.43: Gain as a function of percent spread for 5 modes from 30 GHz (blue) to 800 GHz (burgundy). The dashed lines correspond to G_{th}.

the agreement is poor. Between 0% and 0.15% spread, G_{sim} for 800 GHz decreases by 35.4% and tends to zero for 0.2% energy spread, which is what we observed in Figure 7.42. G_{sim} for 400 GHz is reduced by approximately 14% as percent energy spread increases from 0% to 0.2%. Even though there are only two data points for 400 GHz in Figure 7.43, we should expect negligible growth and gain for percent energy spread greater than or equal to 0.6%. Indeed, 0.6% spread is equivalent to 238 eV at FWHM, which means that 20- and 19.767-keV beams become indistinguishable.

In Figure 7.43, G_{sim} at 30 GHz is still nonzero for 5% spread (albeit about 74% less than for 0% spread). By contrast, as can be seen in Figure 7.43, G_{sim} at 110 GHz goes to zero between 1.5% and 2% spread, while G_{sim} at 210 GHz tends to zero for

percent spread less than 1%. Moreover, G_{sim} at 400 GHz is certainly zero for percent energy spread greater than or equal to 0.6% (20- and 19.767-keV beams merge into a single beam), whereas G_{sim} at 800 GHz is already zero for percent energy spread as little as 0.2%. Hence, to build a two-beam amplifier involving 0.7-mm and 0.5-A beams interacting at 30 GHz (blue curve), we would need electron guns with energy spread less than 4.3% to obtain gain half as big as that for 0% spread. In contrast, the two-beam amplifier with comparable gain and operating at 800 GHz (burgundy curve) would require guns with percent energy spread as little as 0.15%.

7.4.2 Effects on bandwidth capability

In Section 7.3, we discussed gain bandwidth plots for simulations involving the interaction of cold beams. In this subsection, we will consider the effect on nonzero energy spread on gain bandwidth for the interaction of warm and modulated beams at 30 GHz and 110 GHz.

Figure 7.44 shows gain bandwidth plots for the interaction of two 0.7-mm and 0.3-A modulated beams at 30 GHz. The blue curve is the same as that in Figure 7.25. For the green and burgundy curves in Figure 7.44, the beams were warm with 3% and 5% energy spread, respectively. The modulation amplitude in each case was 1% and the bandwidth curves were generated by driving the beams at frequencies ranging from 2.5 GHz to 60 GHz.

According to Figure 7.44, the ratio between the endpoints of the green curve (3% spread) is the same as that for the blue curve. In addition, the gain bandwidth of the green curve estimated at FWHM equals 39 GHz (11 GHz to 50 GHz), which is about 23% larger than for the blue curve (30 GHz). Hence, we can conclude that the gain bandwidth for the cold beams in Figure 7.44 is not reduced for energy spread even as large as 3%. By contrast, due to a significant overlap (1880 eV) of the beam

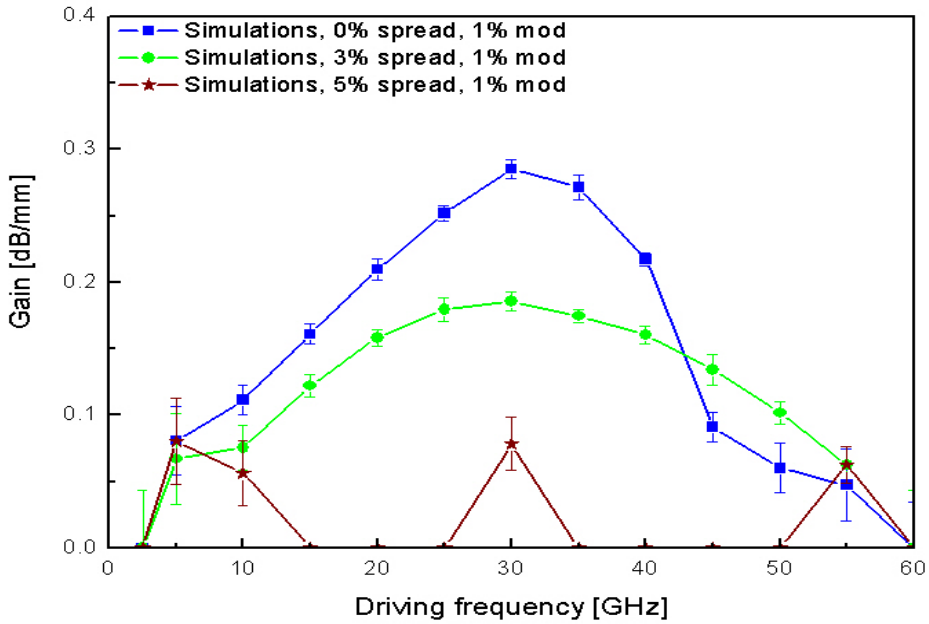

Figure 7.44: Gain bandwidth for two 0.7-mm and 0.3-A modulated beams interacting at 30 GHz. The blue, green, and burgundy curves correspond to 0%, 3%, and 5% energy spread.

energies, the bandwidth curve for 5% spread collapses and becomes discontinuous. Hence, the gain bandwidth for the cold beams is severely affected for energy spread as large as 5%.

In Figure 7.44, the blue and green curves peak at 30 GHz. This is in agreement with Equation 4.39, which predicts that two 0.7-mm and 0.3-A beams with energies 20 keV and 17.6 keV will interact at 30 GHz. Although the FWHM bandwidth of the green curve is comparable to or greater than that of the blue curve, G_{sim} for the cold beams is larger than that for the warm beams with 3% spread over most of the frequency range shown. Note that as percent energy spread increases from 0% to 5%, G_{sim} at 30 GHz decreases by more than 72%. Therefore, we should expect negligible interaction and growth for the interaction of two 0.7-mm warm beams with

5% energy spread.

Figure 7.45 is similar to Figure 7.44 and depicts gain bandwidth plots for the interaction of 0.7-mm and 0.5-A modulated beams at 30 GHz. The red curve is

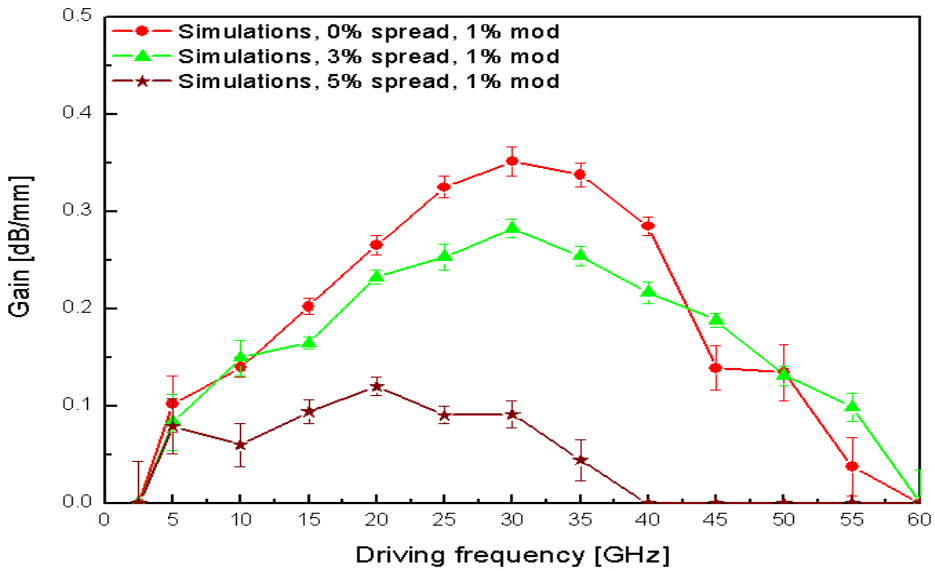

Figure 7.45: Gain bandwidth for two 0.7-mm and 0.5-A modulated beams interacting at 30 GHz. The three datasets correspond to 0%, 3%, and 5% energy spread.

the same as that in Figure 7.25. As in Figure 7.44, the green and burgundy curves correspond to 3% and 5% energy spread, respectively.

In Figure 7.45, the FWHM bandwidth of the green curve (3% spread) is roughly the same as that of the green curve in Figure 7.44. Thus, as was the case for $I =$ 0.6 A in Figure 7.44, the bandwidth for 3% in Figure 7.45 is greater than for 0% spread, which is approximately equal to 31 GHz. Comparing Figures 7.44 and 7.45, to first order we may conclude that the FWHM bandwidth for 0% spread and that for 3% are independent of total beam current. Note that the burgundy curve (5% spread) in Figure 7.45 is markedly different from that in Figure 7.44. Specifically, the former is no longer discontinuous due to a larger ΔE and has a nonzero gain

bandwidth. The gain bandwidth of the burgundy curve in Figure 7.45, estimated at FWHM, yields 31.0 GHz (4 GHz to 35 GHz), which is surprisingly as large as that for 0% spread.

According to Figure 7.45, the red and green curves are centered at 30 GHz, which agrees with Equation 4.39. By contrast, the burgundy curve peaks and is centered at 20 GHz. Even though the green curve (3% spread) in Figure 7.45 possesses the same bandwidth as that in Figure 7.44, the former yields a larger amplification due to a larger ΔE and beam current. In Figure 7.45, the interaction of warm beams with 5% spread will yield a fairly low amplification within the range $5 \leq f \leq 35$ GHz. As can be seen in Figure 7.45, we should expect no interaction and growth for 5% when the driving frequency is greater than or equal to 40 GHz.

We close this section by exploring gain bandwidth plots for the interaction of two 0.7-mm and 0.5-A beams at 110 GHz. In Figure 7.46, the red curve is the same as that in Figure 7.27. The black curve corresponds to 1% energy spread.

In Figure 7.46, the gain bandwidth of the black curve (1% spread) estimated at FWHM equals 139 GHz (38 GHz to 177 GHz) and is larger than that (134 GHz) for the red curve representing cold beams. This is similar to what we observed in Figure 7.45 for the interaction at 30 GHz. Based on the limited amount of data in Figure 7.46, to first order we can conclude that the gain bandwidth is unaffected for energy spread less than or equal to 1%. Hence, the interaction of two 0.7-mm and 0.5-A warm beams with 1% has a gain bandwidth as impressive as that for the interaction of two 0.7-mm and 0.5-A cold beams at 110 GHz.

Although the red and black curves have comparable gain bandwidths, over most of the frequency range of interest shown the black curve yields G_{sim} that is approximately 32% less than that for the red curve (0% spread). Last but not least, Equation 4.39 predicts that two 0.7-mm and 0.5-A beams with energies 20 keV and

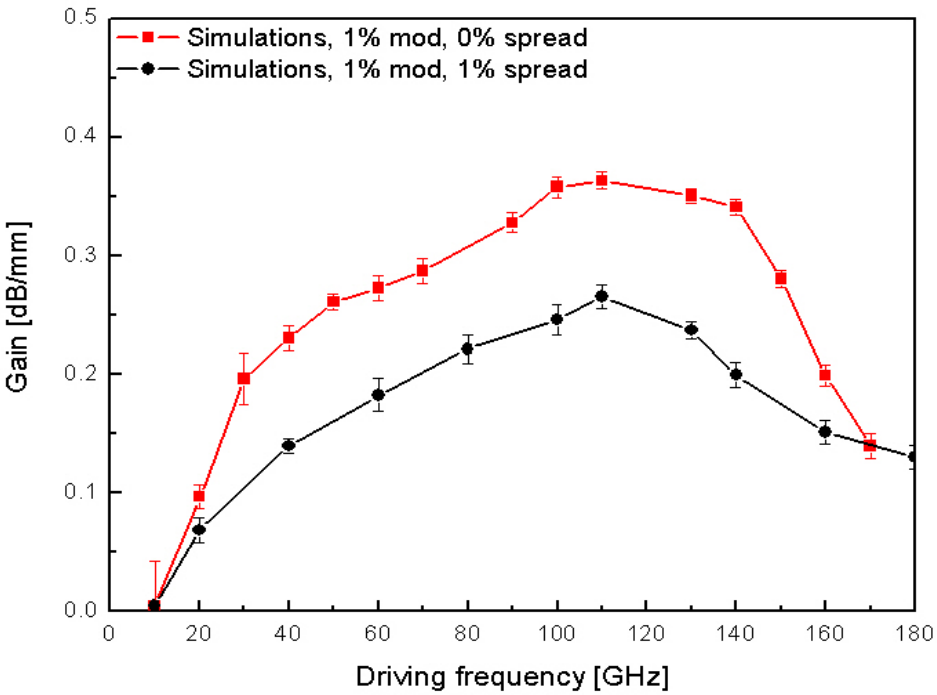

Figure 7.46: Gain bandwidth for two 0.7-mm and 0.5-A modulated beams interacting at 110 GHz. The two datasets correspond to 0% and 1% energy spread.

19.165 keV (the same as those in Figure 7.46) will interact at 110 GHz. As we can see in Figure 7.46, the largest gain for both curves does occur at 110 GHz.

7.5 Chapter summary

In Chapter 7, we discuss simulation results for the interaction of two modulated (with initial energy modulation) cold and warm electron beams at frequencies ranging from low (30 GHz) to high (1 THz). As in Chapter 6, the emphasis is placed on the variation of numerical gain, G_{sim}, with space charge, frequency, and percent energy spread.

The analysis of axial electric field reveals that $|E_z|$ exhibits strong exponential growth regardless of interaction frequency. In addition, before saturation, $|E_z|$ is shown to have a single dominant frequency component. By contrast, $|E_z|$ for unmodulated beams has a fairly large FWHM frequency which increases from low to medium interaction frequencies. Besides a single-mode operation, after the onset of nonlinearities, the interaction of modulated beams can generate multiple harmonics whose magnitudes are comparable to or greater than that of the fundamental mode. For example, the interaction of two 0.5-A beams at 30 GHz produces three harmonics at 60 GHz, 90 GHz, and 120 GHz. This means that the interaction at 30 GHz can be used to generate radiation at, say, 120 GHz via some frequency selection technique.

The variation of the gain of growing modes with space charge density shows that the agreement between the 1-D theory and simulations is very good at low interaction frequencies. As in the case of unmodualted beams, a discrepancy remains between G_{sim} and G_{th} for medium and high frequencies. One of the causes of this discrepancy is thought to be the plasma reduction factor, F, which overestimates G_{th}. The analysis of numerical gain shows that G_{sim} is independent of interaction frequency and modulation amplitude over a wide frequency range, specifically, $0.03 \leq f \leq 1$ THz. The values of G_{sim} obtained are impressive. For instance, the interaction of two 0.7-mm and 0.5-A beams (typical in this dissertation) yields G_{sim} of 0.35 dB/mm, which is an order of magnitude greater than that (0.03 dB/mm) reported in the literature for a proposed two-stream relativistic klystron amplifier involving 1.0- and 5.0-kA annular relativistic electron beams [23].

In addition to possessing a large G_{sim}, the potential two-beam amplifier has an impressive gain bandwidth over a wide range of frequencies. Namely, it is found that the ratios between end frequencies exceed a decade. Also, the ratios between 0.707 G_{sim} points (at FWHM) are greater than an octave. Hence, the interaction of two electron beams at 30 GHz can amplify frequencies ranging from 5 GHz to

55 GHz. Moreover, the interaction of two beams at 800 GHz is capable of amplifying frequencies from 200 GHz to 1 THz and beyond.

For two electron beams with given energies, currents, and beam radii the gain bandwidth at FWHM is found to be greater than or equal to f_{bunching} predicted by Equation 4.39. Also, a comparison of gain bandwidth curves for low, medium, and high interaction frequencies shows that the FWHM bandwidth (to first order) is independent of interaction frequency. Hence, based on the data in this dissertation, the two-beam source possesses an incredibly wide gain bandwidth from the microwave to the far infrared region of the electromagnetic spectrum.

For the interaction of two warm beams, the gain bandwidth is comparable to that for cold beams provided the beam energies do not significantly overlap. For example, for two 0.3-A warm beams interacting at 30 GHz, the gain bandwidth is the same as that for cold beams as long as energy spread is less than or equal to 3%. The gain bandwidth becomes severely deteriorated for energy spread as large as 5%. For the interaction at 110 GHz, cold beams and warm beams with 1% spread have similar gain bandwidths. However, negligible amplification is observed for energy spread greater than or equal to 1.5%. Even though cold and warm beams can have comparable gain bandwidths, the magnitude of G_{sim} is in general smaller for nonzero energy spread. Specifically, the warmer the beams are, the smaller G_{sim} becomes.

The analysis of exponentially growing modes, for a given beam current and beam radius, shows that they saturate at the same longitudinal position regardless of interaction frequency. Hence, without modifying the interaction region, the potential two-beam amplifier is capable of amplifying signals form 30 GHz to 1 THz and, possibly, beyond. For the interaction of two 0.7-mm beams at 30 GHz it is found that the saturation length for modulated beams is on average 26% less than that for unmodulated beams. In addition, for $I = 1.0$ A, it is determined that the interaction of two 0.7-mm beams minimizes the saturation (interaction) length and maximizes

gain, which makes is superior to the interaction of either two 1.0-mm or two 1.4-mm beams.

Chapter 8

Conclusions and future work

This dissertation presents the results of 2-D particle-in-cell simulations of the interaction region of the potential mm and sub-mm radiation source based on the two-stream instability. The interaction region consists of a beam pipe with radius r_a and two co-propagating and interacting electron beams of radius r_b. The simulations performed involve the interaction of unmodulated (no initial energy modulation) and modulated (energy-modulated, seeded at a given frequency) electron beams. In addition, both cold (monoenergetic) and warm (Gaussian) beams are treated. Moreover, the interaction frequencies considered range from 30 GHz up to and including 1 THz.

The primary emphasis in this dissertation is on exploring exponentially growing modes and comparing their gain from simulations, $G_{\rm sim}$, with that from theory, $G_{\rm th}$, in order to validate the 1-D theory discussed in Chapter 4. At low interaction frequencies it is found that $G_{\rm sim}$ and $G_{\rm th}$ are in very good agreement. Also, both vary as $\sqrt{I/r_b^2}$, where I and r_b are the total beam current and beam radius, respectively. A discrepancy arises between $G_{\rm sim}$ and $G_{\rm th}$ for medium and high frequencies. Namely, the higher the interaction frequency, the farther apart $G_{\rm sim}$ and $G_{\rm th}$ are. One of the reasons for this discrepancy is believed to be the plasma reduction factor, F, which

overestimates G_{th} (Equation 4.38).

Besides comparing numerical and theoretical gain, we also make a comparison between G_{sim} for modulated beams and G_{sim} for unmodulated beams. Simulations show that G_{sim} is independent of interaction frequency and modulation amplitude for all interaction frequencies considered. Specifically, G_{sim} is found to be independent of frequency and modulation amplitude within the frequency range $0.03 \leq f \leq 1$ THz.

The values of G_{sim} obtained are impressive for both unmodulated and modulated cases. For instance, the interaction of two 0.7-mm and 0.5-A beams with energies 20 keV and 16.95 keV yields G_{sim} of 0.35 dB/mm, which is an order of magnitude greater than that (0.03 dB/mm) reported in the literature for a proposed two-stream relativistic klystron amplifier involving 1.0- and 5.0-kA annular relativistic electron beams [23]. Note the difference of about four orders of magnitude between the beam currents. Hence, the two-beam amplifier promises to be a reliable and inexpensive source of millimeter and sub-millimeter wave radiation and has the potential to generate watts of power at THz frequencies.

A large portion of this dissertation is devoted to a detailed analysis of the magnitude of axial electric field, $|E_z|$, which is used throughout to evaluate numerical gain, G_{sim}. For unmodulated beams $|E_z|$ is shown to exhibit a strong exponential growth at all interaction frequencies considered. However, simulations also show a multimode behavior and a fairly large FWHM frequency. For example, as the interaction frequency ranges from 30 GHz to 210 GHz, the FWHM frequency of $|E_z|$ increases by more than a factor of 10 from about 9 GHz to 125 GHz. This is in contrast to theory (Equation 4.39), which states that two electron beams will interact at a single frequency in accordance with their energies, currents, and beam radii.

As opposed to unmodulated beams, $|E_z|$ for modulated beams is shown to have

a single dominant frequency component (before saturation) regardless of interaction frequency. In addition, after the onset of nonlinearities, $|E_z|$ shows a significant harmonic content. It is determined that the interaction of modulated beams can generate multiple harmonics whose magnitudes are comparable to or greater than that of the fundamental mode. For example, the interaction of two 0.5-A beams at 30 GHz produces three harmonics at 60 GHz, 90 GHz, and 120 GHz. Hence, the potential two-beam source operating at 30 GHz could be used to generate radiation at four times the fundamental frequency, 120 GHz, via some frequency selection technique.

The study of gain bandwidth for cold and modulated beams reveals that the two-beam amplifier has an impressive gain bandwidth over a wide range of frequencies. Namely, it is found that the ratios between end frequencies exceed a decade. Also, the ratios between 0.707 G_{sim} points (at FWHM) are greater than an octave and the FWHM bandwidth is comparable to or greater than f_{bunching} predicted by Equation 4.39. Moreover, it is determined that the gain bandwidth at FWHM is, to first order, independent of interaction frequency. According to simulation results, the interaction of two electron beams at 30 GHz can amplify frequencies ranging from 5 GHz to 55 GHz, while the interaction of two beams at 800 GHz is capable of amplifying frequencies from 200 GHz to 1 THz and beyond. Hence, the potential two-beam source possesses an astonishingly wide gain bandwidth from the microwave to the far infrared region of the electromagnetic spectrum.

Since in the laboratory electron beams are not monoenergetic, we examine the variation of G_{sim} as a function energy spread for the interaction of both unmodulated and modulated warm beams at low through high frequencies. According to the small-signal theory presented in Chapter 4, ΔE (energy difference of two interacting beams) increases with decreasing interaction frequency and increasing space charge. Hence, the warmer the beams are and the higher the interaction frequency is, the

faster G_{sim} drops off. For example, if we take $r_b = 0.7$ mm and $I = 1.0$ A, G_{sim} at 30 GHz is still nonzero for energy spread as large as 5%, while G_{sim} at 210 GHz is already negligible for energy spread approximately equal to 0.85%. By contrast, G_{sim} at 800 GHz becomes negligible for energy spread as little as 0.2%. Hence, to build the two-beam source involving 0.7-mm and 0.5-A warm beams interacting at 30 GHz, we would need electron guns with energy spread less than 4.3% to obtain gain half as large as that for cold beams. In contrast, a device with comparable gain and operating at 800 GHz would require guns with percent energy spread as little as 0.15%.

The analysis of gain bandwidth for nonzero energy spread shows that bandwidth curves for warm beams are comparable to those for cold beams provided the beam energies do not significantly overlap. It is also determined that the higher the interaction frequency is and the warmer the beams are, the faster the gain bandwidth deteriorates. For instance, for two 0.3-A warm beams interacting at 30 GHz, the gain bandwidth is the same as that for cold beams as long as energy spread is less than or equal to 3%. The gain bandwidth becomes severely deteriorated for energy spread as large as 5%. For the interaction at 110 GHz, cold beams and warm beams with 1% spread have similar gain bandwidths. However, negligible amplification is observed for energy spread greater than or equal to 1.5%.

Note that despite running hundreds of simulations, only a limited number of beam currents, beam radii, and modulation amplitudes have been covered in this dissertation. Hence, future simulations should involve more extensive parameter scans. In addition, future investigations may include studies of the two-beam amplifier in the nonlinear regime. For instance, a detailed analysis of the onset of nonlinearities for different modulation levels and that of the relationship between fundamental modes and various harmonics. Moreover, since the simulations presented are in two dimensions only, future work should include 3-D simulations for a better understanding

of the underlying physics involved, especially in the nonlinear regime. Last but not least, it is believed that the PIC simulations presented in this dissertation will provide a solid foundation for successful experiments involving the sub-mm and mm radiation source based on the two-stream instability.

In conclusion, the simulation results presented in this dissertation demonstrate that the two-beam amplifier, which relies on low-energy and low-current electron beams for operation, can be a compact, simple, and inexpensive alternative to conventional sources of mm and sub-mm wave radiation. In addition, due to its large gain and impressive gain bandwidth, it has the potential to generate watts of power at frequencies ranging from the microwave to the far infrared region of the electromagnetic spectrum. Moreover, the two-beam source would be an invaluable tool to a wide variety of research fields such as cancer research, terahertz imaging, agriculture, homeland security, environmental monitoring, and satellite communications.

Appendix A

Convergence considerations

A.1 Introduction

This appendix is devoted to a quantitative discussion of convergence with regard to dz, dr, and the number particles emitted per cell and per time step (PPC). dz and dr are responsible for accuracy and stability of electromagnetic solutions and represent the cell size in axial and radial directions, respectively. PPC is crucial to successful electron bunching and we will attempt to determine the minimum amount of PPC necessary to properly resolve electron bunches at 30 GHz and different beam modulation amplitudes.

A.2 Convergence for dz

Consider two electron beams (0.7-mm and 0.3-A each) with energies $E_1 = 20$ keV and $E_2 = 17.6$ keV propagating in a 2-mm beam pipe. According to Equation 4.39 (Section 4.3), the expected frequency of bunching is 30 GHz. The beams are thus

modulated at the bunching frequency and the modulation amplitude, δE, is 1%. Using the average velocity of the beams, $\bar{v} \approx 8.13 \times 10^7$ m/s, the bunching wavelength at 30 GHz is given by

$$\lambda = \frac{8.13 \times 10^7}{30 \times 10^9} \approx 2.71 \text{ mm}. \tag{A.1}$$

Figure A.1 shows gain as a function of dz for 7 different runs. For each of the 7

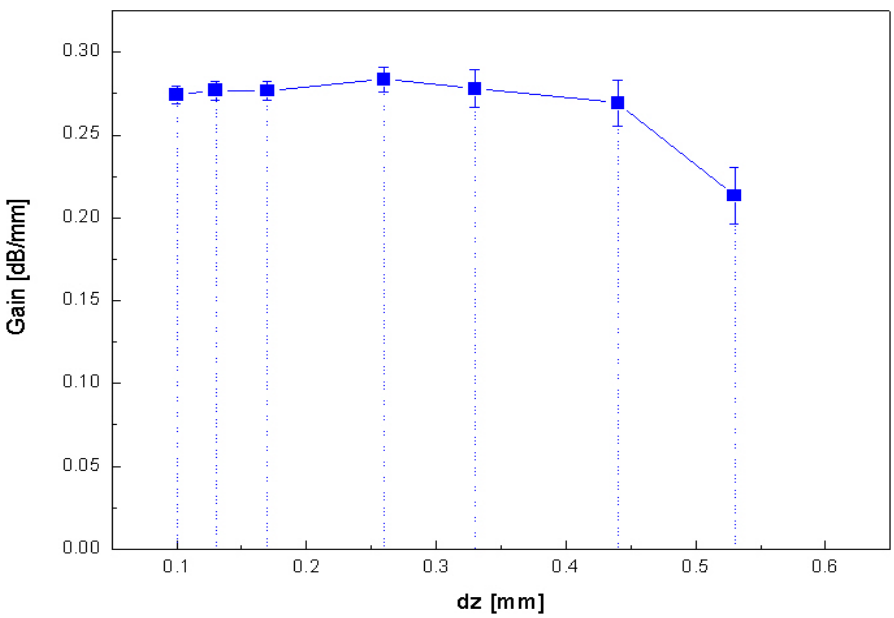

Figure A.1: Gain versus dz for two 0.7-mm and 0.3-A modulated beams with energies 20 keV and 17.6 keV interacting at 30 GHz.

runs dr was held fixed at 0.1 mm, while dz values ranged from 0.542 mm ($\lambda = 5\,dz$) to 0.1 mm ($\lambda = 27.1\,dz$). According to Figure A.1, when $6\,dz \leq \lambda \leq 27.1\,dz$, the percent variation in gain is within 3.3%. For $\lambda \leq 5\,dz$, however, the value of gain is reduced by as much as 22%. The conclusion we can draw from this short analysis is as follows:

- Convergence with regard to dz is achieved for $\lambda \geq 6\,dz$

- $\lambda = 6\,dz$ is a threshold value and all solutions corresponding to $\lambda < 6\,dz$ cannot not be properly resolved.

It should be noted that the ratio of dz to dr is greater than 5 for $\lambda = 5\,dz$ and, thus, an additional source of errors [13].

A.3 Convergence for dr

To study convergence for dr, 6 cases were run, the beam and beam pipe parameters

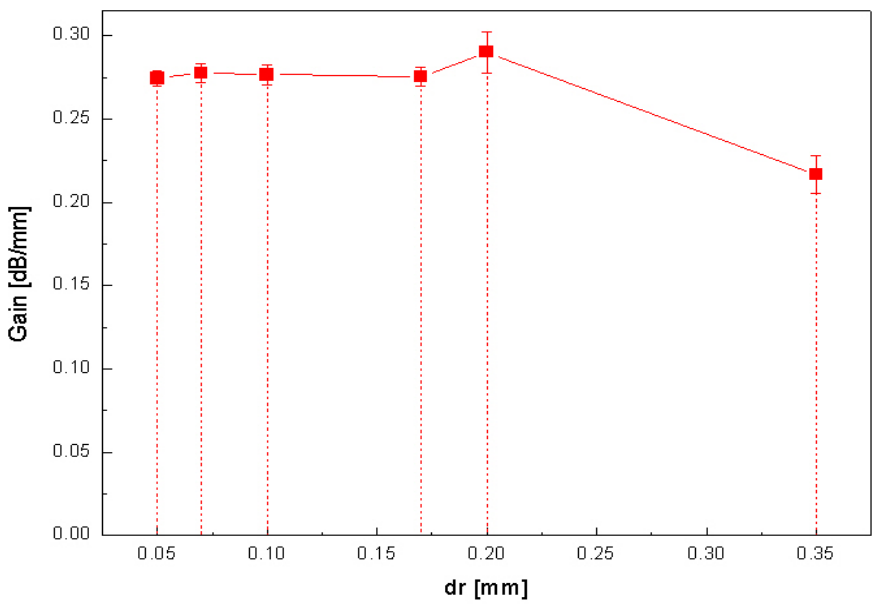

Figure A.2: Gain versus dr for two 0.7-mm and 0.3-A modulated beams with energies 20 keV and 17.6 keV interacting at 30 GHz.

being identical to those in Section A.2. Plotted in Figure A.2 is again gain as a function of dr for 6 different runs. Here dz was fixed at 0.17 mm and dr varied from

0.05 mm to 0.35 mm. For the 0.7-mm cathode, $dr = 0.05\,\text{mm}$ and $dr = 0.35\,\text{mm}$ correspond to more than 10 and merely two emission cells, respectively.

From Figure A.2, the percent variation in gain is within 1.2% when $0.5 \leq \lambda \leq 0.17\,\text{mm}$. Therefore, in terms of the number of emission cells in the cathode, convergence is achieved providing there are at least four emission cells. In the range $dr \geq 0.2\,\text{mm}$ (three emission cells and less) gain is markedly different, deviating from its converged value by as much as 21% for $dr = 0.35\,\text{mm}$ (merely two emission cells). The large error cannot be attributed to the apect ratio (dr/dz), which is two for $dr = 0.35\,\text{mm}$ and, thus, acceptable [13]. Hence, we can conclude that beam emission processes in MAGIC are properly represented if and only if the number of emission cells is greater than or equal to four.

A.4 Convergence with respect to the number of particles emitted per cell and per time step (PPC)

For this convergence test, two sets of simulations were performed. The beam dimensions, energies, currents, and modulation frequency were identical to those in Section A.2. However, the modulation amplitudes used were 1% and 0.1% (Appendix D) for the first and second sets, respectively. Also, dz and dr were kept fixed at 0.1 mm for both sets of simulations.

Gain as a function PPC shown in Figures A.3 and A.4 was generated by varying PPC from 6 to 12. For modulation amplitudes as high as 1% and as low as 0.1%, as can be seen in Figures A.3 and A.3, convergence is achieved for PPC = 6. Indeed, the percent variation in gain between PPC = 6 and PPC = 12 is within 1%. This leads us to conclude that at modulation amplitudes equal to or greater than 0.1% of

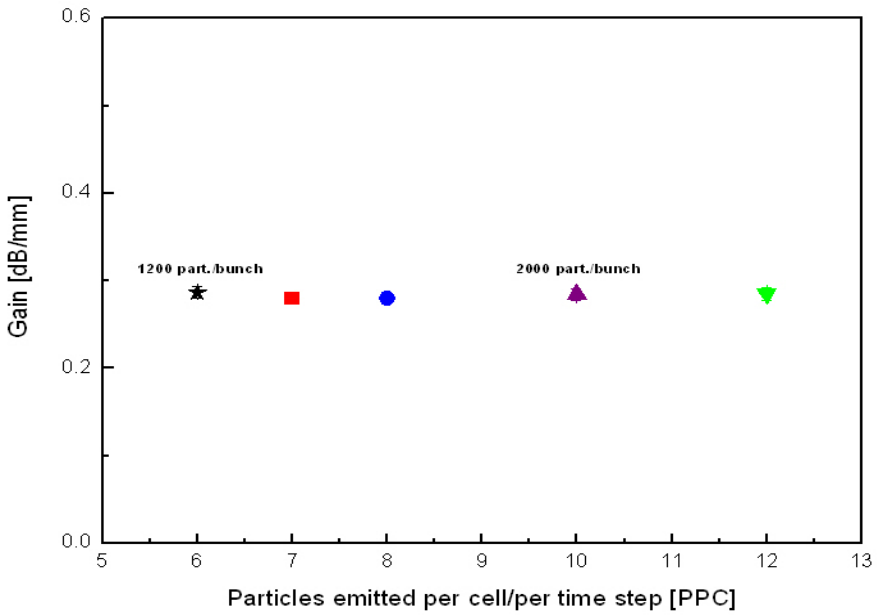

Figure A.3: Gain versus PPC for two 0.7-mm and 0.3-A modulated beams with energies 20 keV and 17.6 keV interacting at 30 GHz. Modulation amplitude, δE, is 1%.

ΔE, bunches are properly resolved for PPC ≥ 6. To estimate the number of particles per bunch corresponding to PPC $= 6$, we can use the following simple formula

$$\#\text{ of particles/bunch} = \text{PPC} \times \frac{T}{\delta t}, \tag{A.2}$$

where T is the inverse of bunching frequency, 30 GHz, and δt is the electromagnetic time step used. Substituting the values for T, δt, and PPC, it is straightforward to show that PPC $= 6$ is equivalent to approximately 1200 particles per bunch.

It is interesting to note that convergence tests with regard to PPC for unmodulated beams were unsuccessful. Despite the fact that we exhausted the entire amount of particle allocation space (5,000,000 particles for the current version of MAGIC), no convergence was observed. It looks as though this issue will not be resolved until

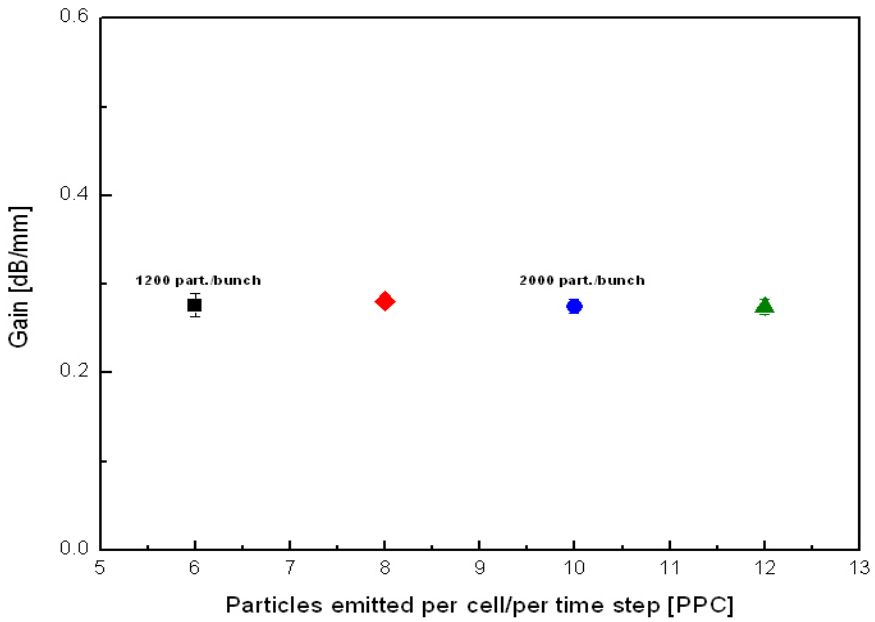

Figure A.4: Gain versus PPC for two 0.7-mm and 0.3-A modulated beams with energies 20 keV and 17.6 keV interacting at 30 GHz. Modulation amplitude, δE, is 0.1%.

after a new version of MAGIC, capable of supporting 10 times as many particles, is released.

Appendix B

A theoretical curve fit to $|E_z(z,t)|$

B.1 Introduction

This appendix describes our attempt to derive a theoretical curve-fit formula to the magnitude of the ac component of axial electric field, $|E_z(z,t)|$, using the small-signal theory presented in Chapter 4. This is accomplished by imposing the appropriate boundary conditions on the magnitudes of the ac components of electric field, velocity, and current density at $z = 0$ mm. Derived curve-fit expressions (for modulated and unmodulated beams) are fitted to $|E_z(z,t)|$-versus-z data obtained from simulations.

B.2 Derivation of curve fit formulas

A general expressions for total electric field may be written as follows:

$$E_{\mathrm{TOT}}(z,t) = E_0 + E_z(z,t) = E_0 + \sum_{i=1}^{n} E_{\mathrm{AC}i} e^{j(\omega t - k_i z)}. \tag{B.1}$$

With the help of Equations 4.11 and 4.12, total velocity and current density read:

$$v_{\text{TOT}}(z,t) = v_0 + v_z(z,t) = v_0 + j\frac{\eta}{\bar{v}}\sum_{i=1}^{n}\frac{E_{\text{AC}i}}{k_e - k_i}e^{j(\omega t - k_i z)}, \tag{B.2}$$

$$J_{\text{TOT}}(z,t) = J_0 + J_z(z,t) = J_0 + j\omega\epsilon_0\frac{\omega_p^2}{\bar{v}^2}\sum_{i=1}^{n}\frac{E_{\text{AC}i}}{(k_e - k_i)^2}e^{j(\omega t - k_i z)}, \tag{B.3}$$

where, as before, the dc and ac quantities are denoted by the subscripts 0 and z, respectively. Also, the summation is included to account for all roots of a given dispersion relation. It should be emphasized that E_{TOT}, v_{TOT}, J_{TOT}, E_0, v_0, J_0, $E_{\text{AC}i}$ are all real quantities. Even though the ac quantities, namely, E_z, v_z, and J_z, are written in terms of complex expressions, it is implied in Equations B.1 through B.3 that $\text{Im}(E_z) = \text{Im}(v_z) = \text{Im}(J_z) = 0$. According to Equation 4.20, a dispersion relation for two co-propagating electron streams reads

$$(k^2 - k_0^2)\left\{1 - \frac{\omega_{p1}^2}{(\omega - kv_1)^2} - \frac{\omega_{p2}^2}{(\omega - kv_2)^2}\right\} = 0, \tag{B.4}$$

where v_1 and v_2 are the beam velocities, whereas ω_{p1}^2 and ω_{p2}^2 are the electron plasma frequencies. Taking $\omega_{p1}^2 = \omega_{p2}^2 = \omega_p^2$, Equation B.4 admits 6 solutions and it can be shown that four of those roots are real, while the remaining two are complex conjugates of one another. To simplify the analysis, we will assume that of the 6 roots only four, namely, $\pm k_0$ and complex conjugate solutions, are dominant. Hence, the roots to be included in the ac parts of Equations B.1 through B.3 will be

$$k_{1,2} = k_e \pm j\alpha \text{ and } k_{3,4} = \pm k_0, \tag{B.5}$$

where $k_{1,2}$ represent growing and decaying waves, whereas $k_{3,4}$ correspond to forward and backward traveling waves, respectively. $k_e = \omega/\bar{v}$, where $\bar{v}$ is the average velocity of two beams, and α in Equation B.5 are real and positive. Substituting $k_{1,2}$ and

$k_{3,4}$ into Equations B.1 through B.3, the ac component of electric field, velocity, and current density become

$$E_z(z,t) = (Ae^{\alpha z}e^{-jk_e z} + Be^{-\alpha z}e^{-jk_e z} + Ce^{-jk_0 z} + De^{jk_0 z})e^{j\omega t}, \tag{B.6}$$

$$v_z(z,t) = j\frac{\eta}{\bar{v}}\left\{j\frac{1}{\alpha}(Ae^{\alpha z} - Be^{-\alpha z})e^{-jk_e z} + \frac{Ce^{-jk_0 z}}{k_e - k_0} + \frac{De^{jk_0 z}}{k_e + k_0}\right\}e^{j\omega t}, \tag{B.7}$$

$$\begin{aligned} J_z(z,t) &= j\omega\epsilon_0\frac{\omega_p^2}{\bar{v}^2}\left\{-\frac{1}{\alpha^2}(Ae^{\alpha z} + Be^{-\alpha z})e^{-jk_e z} + \right. \\ &\quad \left. + \frac{Ce^{-jk_0 z}}{(k_e - k_0)^2} + \frac{De^{jk_0 z}}{(k_e + k_0)^2}\right\}e^{j\omega t}, \end{aligned} \tag{B.8}$$

where $A \equiv E_{\text{AC1}}$, $B \equiv E_{\text{AC2}}$, $C \equiv E_{\text{AC3}}$, and $D \equiv E_{\text{AC4}}$ are real quantities. To determine A, B, C, and D, we will impose boundary conditions on $|E_z(z,t)|$, $|E_z(z,t)|'$, $|v_z(z,t)|$, and $|J_z(z,t)|$ at $z = 0$, where $|E_z(z,t)|'$ stands for the derivative of $|E_z(z,t)|$ with respect to z. Taking the absolute value of Equation B.6 and doing some algebra, we get

$$\begin{aligned} |E_z(z,t)| &= \left\{[(Ae^{\alpha z} + Be^{-\alpha z})\cos(k_e z) + (C + D)\cos(k_0 z)]^2 + \right. \\ &\quad \left. + [(Ae^{\alpha z} + Be^{-\alpha z})\sin(k_e z) + (C - D)\sin(k_0 z)]^2\right\}^{1/2}. \end{aligned} \tag{B.9}$$

Differentiating Equation B.9 with respect to z and evaluating the result at $z = 0$, the slope of $|E_z(z,t)|$ becomes

$$|E_z(0,t)|' = \alpha(A - B), \tag{B.10}$$

provided $|E_z(0,t)| = A + B + C + D \neq 0$. The magnitude of $v_z(z,t)$ at $z = 0$ is

$$|v_z(0,t)| = \frac{\eta}{\bar{v}}\sqrt{\frac{1}{\alpha^2}(A - B)^2 + \left[\frac{C}{k_e - k_0} + \frac{D}{k_e + k_0}\right]^2}, \tag{B.11}$$

while that of $|J_z(z,t)|$ reads

$$|J_z(0,t)| = \omega\epsilon\frac{\omega_p^2}{\bar{v}^2}\left\{-\frac{1}{\alpha^2}(A+B) + \frac{C}{(k_e-k_0)^2} + \frac{D}{(k_e+k_0)^2}\right\}. \tag{B.12}$$

The boundary conditions for two modulated beams, with energies E_1 and E_2, co-propagating and interacting in a beam pipe read

$$|E_z(0,t)| = E_0, \quad |E_z(0,t)|' = l, \quad |v_z(0,t)| = v_0, \quad \text{and} \quad |J_z(0,t)| = J_0, \tag{B.13}$$

where E_0 and J_0 are related via Maxwell's equations and represent the values of $|E_z(z,t)|$ and $|J_z(z,t)|$ at $z = 0$. Moreover, l, the slope of $|E_z(z,t)|$ at $z = 0$, is positive and is a function of v_0, where v_0 is related to the modulation amplitude, $\delta E = x(E_1 - E_2)$, as follows

$$v_0 = \sqrt{2\eta\delta E}, \tag{B.14}$$

where $x = 0$ amounts to 0% modulation. With the boundary conditions thus defined, Equations B.9 through B.12 become

$$A + B + C + D = E_0, \tag{B.15}$$

$$\alpha(A - B) = l, \tag{B.16}$$

$$\frac{1}{\alpha^2}(A-B)^2 + \left[\frac{C}{k_e-k_0} + \frac{D}{k_e+k_0}\right]^2 = \left(\frac{v_0\bar{v}}{\eta}\right)^2, \tag{B.17}$$

$$-\frac{1}{\alpha^2}(A+B) + \frac{C}{(k_e-k_0)^2} + \frac{D}{(k_e+k_0)^2} = J_0\left(\frac{\bar{v}^2}{\omega\epsilon_0\omega_p^2}\right). \tag{B.18}$$

Appendix B. A theoretical curve fit to $|E_z(z,t)|$

The curve fit to $|E_z(z,t)|$ is given by Equation B.9, where A, B, C, D, k_e, k_0, and α are related via the constraint Equations B.15 through B.18. Hence, the curve-fitting formula for modulated beams reads

$$|E_z(z,t)| = \left\{ \left[\left(B(e^{\alpha z} + e^{-\alpha z}) + \frac{l}{\alpha} e^{\alpha z} \right) \cos(k_e z) + (C+D)\cos(k_0 z) \right]^2 + \right.$$

$$\left. + \left[\left(B(e^{\alpha z} + e^{-\alpha z}) + \frac{l}{\alpha} e^{\alpha z} \right) \sin(k_e z) + (C-D)\sin(k_0 z) \right]^2 \right\}^{1/2}, \tag{B.19}$$

where A has been eliminated with the help of Equation B.16 and $C+D$ and $C-D$ are given by the following expressions

$$C + D = \Gamma - \frac{\alpha^2(\Gamma - 2\psi k_e)}{\alpha^2 + k_0^2 - k_e^2}, \tag{B.20}$$

$$C - D = -\frac{\psi k_0^4 + k_e^2(\alpha^2\psi - \Gamma k_e + \psi k_e^2) + k_0^2(\alpha^2\psi + \Gamma k_e - 2\psi k_e^2)}{k_0(\alpha^2 + k_0^2 - k_e^2)}, \tag{B.21}$$

where $\psi \equiv \pm\sqrt{(v_0\bar{v}/\eta)^2 - l^2/\alpha^4}$ and $\Gamma \equiv E_0 + J_0\left(\frac{\bar{v}^2\alpha^2}{\omega\epsilon_0\omega_p^2}\right)$.

The curve fit to $|E_z(z,t)|$ for unmodulated beams is obtained from Equation B.19 by setting v_0 and l equal to zero to yield

$$|E_z(z,t)| = \left\{ [2B\cosh(\alpha z)\cos(k_e z) + (C+D)\cos(k_0 z)]^2 + \right.$$

$$\left. + [2B\cosh(\alpha z)\sin(k_e z) + (C-D)\sin(k_0 z)]^2 \right\}^{1/2}, \tag{B.22}$$

where $C + D = E_0 - 2B$, $C - D = -k_e/k_0(E_0 - 2B)$, and k_e, k_0, and α are related via

$$k_e = \sqrt{k_0^2 + \alpha^2\left\{1 - \frac{E_0}{2B}\right\}}. \tag{B.23}$$

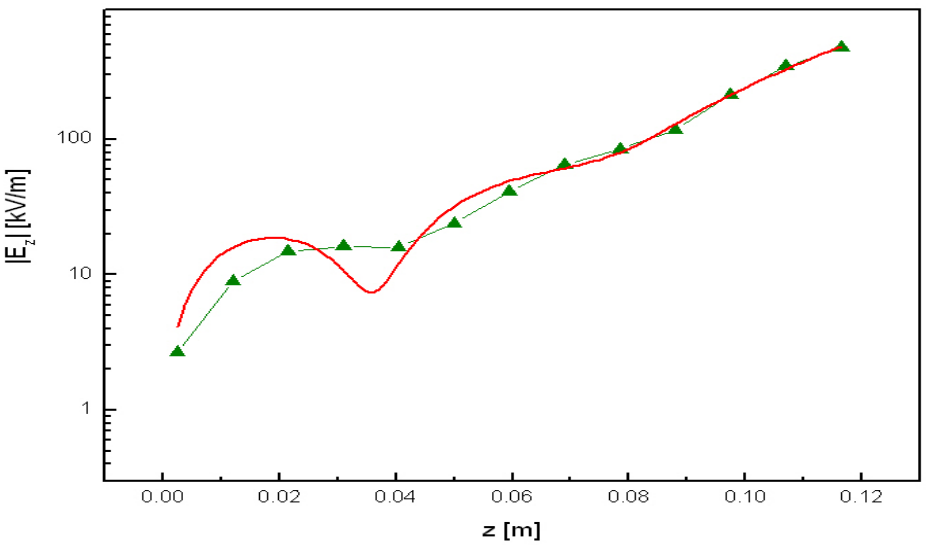

Figure B.1: $|E_z(z,t)|$ versus z for two 0.5-A modulated beams interacting at 30 GHz (green curve) and Equation B.19 (red curve).

Let us now fit Equations B.19 and B.22 to $|E_z(z,t)|$-versus-z data from simulations. Figure B.1 shows $|E_z(z,t)|$ as a function of z for two 0.5-A modulated beams interacting at 30 GHz. Plotted on top of the data in Figure B.1 is Equation B.19 (red curve). A plot of $|E_z(z,t)|$ as a function of z for unmodulated beams, 0.5 A each, also interacting at 30 GHz is displayed in Figure B.2. The curve fit to the data, Equation B.22, is again represented by the red curve.

According to Figures B.1 and B.2, the slope of $|E_z(z,t)|$ at $z = 0$ mm is clearly nonzero/positive and nearly zero for the modulated and unmodulated beams, respectively. Even though Equations B.19 and B.22 model the shape of the data well, in both cases the fit is poor for small values of z. Only for large values of z, in the linear region, which is due to exponenetial growth, do Equations B.19 and B.22 and the corresponding data from simulations converge. Gain calculated from the slope of the linear regions in Figure B.1 and Figure B.2 is 0.351 $\pm$ 0.016 dB/mm and 0.358 $\pm$ 0.012 dB/mm, while that from the 1-D theory is 0.36 dB/mm. Hence, the values

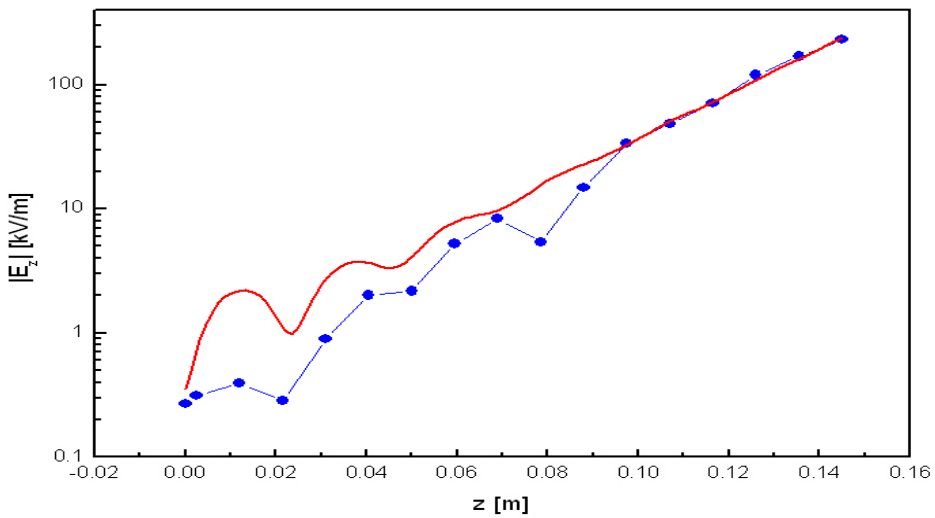

Figure B.2: $|E_z(z,t)|$ versus z for two 0.5-A unmodulated beams interacting at 30 GHz (blue curve) and Equation B.22 (red curve).

of gain are within 2.5% and the agreement is very good. The discrepancy (for low values of z) between Equations B.19 and B.22 and the data in Figures B.1 and B.2 should be attributed to the fact that we ignored two roots of the dispersion relation (Equation B.4) in deriving Equations B.19 and B.22. The two disregarded solutions to Equation B.4 span multiple lines when written in analytical form and do not lend themselves to any reasonable simplification. Therefore, the derivation of curve-fitting expressions to $|E_z(z,t)|$ with all 6 roots included can only be accomplished numerically.

Appendix C

The impact of scalloping on gain

C.1 introduction

In this appendix our goal is to determine whether or not gain is affected by scalloping, which is a sinusoidal variation of the beam envelope. We will examine the interaction of two modulated beams at 30 GHz for three different values of the focusing magnetic field, B_z. The corresponding scalloping amplitudes range from small to large, approximately 6% and 30% of the beam radius, respectively.

C.2 Two-beam interaction for different scalloping amplitudes

Figure C.1 shows the magnitude of the ac component of axial electric field, $|E_z|$ (left-hand vertical axis), and r (right-hand vertical axis) versus axial distance, z, for two 0.7-mm and 0.5-A beams with energies 20 keV and 16.950 keV interacting at 30 GHz. The beams are cold and modulated. The modulation amplitude, δE, is 1% at

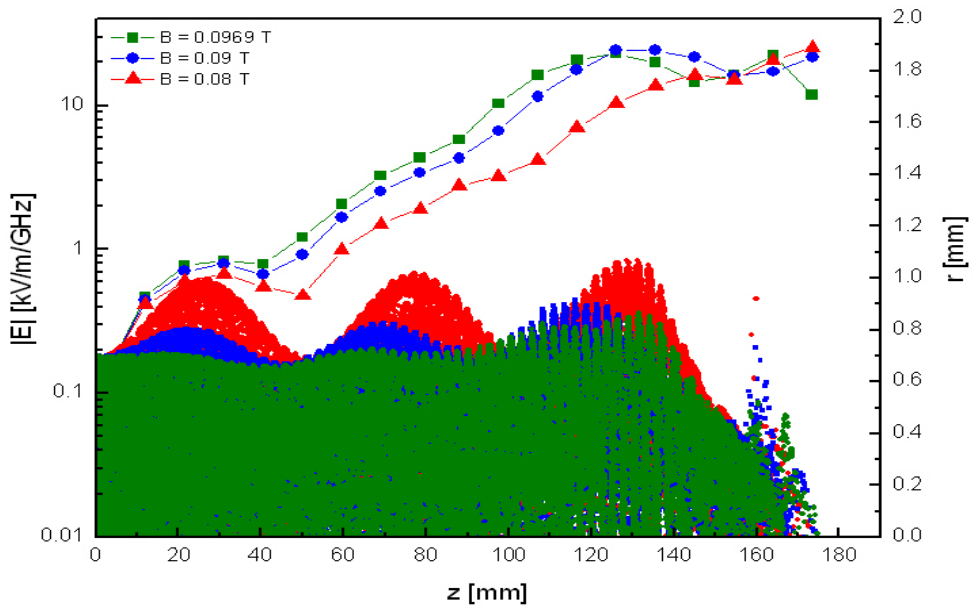

Figure C.1: $|E_z|$ and r as a function of z for the interaction of two 0.7-mm and 0.5-A beams at 30 GHz. B_z is 0.0969 T (green), 0.09 T (blue), and 0.08 T (red).

30 GHz. The curves and particle plots in Figure C.1 correspond to three different values of the focusing magnetic field, B_z, namely, 0.0969 T (green), 0.09 T (blue), and 0.08 T (red).

According to the particle plots in Figure C.1, the smaller B_z is, the larger the departure from the initial beam radius, r_b, which is equal to 0.7 mm. The scalloping amplitude is as little as 5.7% and as much as 30% of r_b for 0.0969 T and 0.08 T magnetic fields, respectively. For large values of z, $z > 90$ mm, we can observe the expansion of the beams due to a significant amount of bunching at 30 GHz. The scalloping wavelength, λ_{scallop}, is inversely proportional to B_z and is given by [12]

$$\lambda_{\text{scallop}} = \frac{4\pi\bar{v}}{\sqrt{2}\eta B_z}, \tag{C.1}$$

where $\bar{v}$ is the average beam velocity and η is the electron charge-to-mass ratio. Sub-

stituting $\bar{v} \approx 7.84 \times 10^7$ m/s into Equation C.1, λ_{scallop} corresponding to 0.0969 T, 0.09 T, and 0.08 T is approximately 41 mm, 44 mm, and 49.5 mm, respectively. These values are fairly close to those in Figure C.1. Note that the dips in the curves line up (with the exception of $B_z = 0.09$ T around $z = 44$ mm) with those in the particle plots. Also, the larger the scalloping amplitude is, the more pronounced the dips become. The dips for $B_z = 0.09$ T (blue curve) are misaligned around $z = 44$ mm due to the absence of an FFT probe there (see Section 5.3), the closest probes being at z = 40.5 mm and z = 50 mm, respectively.

Figure C.2 shows $|E_z|$-versus-z curves from Figure C.1 along with curve fits to

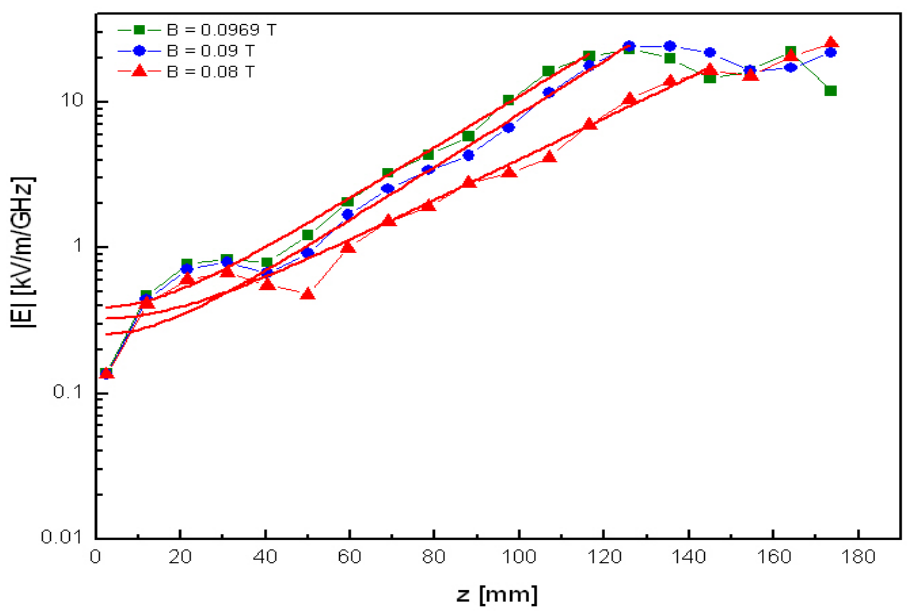

Figure C.2: The variation of $|E_z|$ with z for the same beams as in Figure C.1. B_z is 0.0969 T (squares), 0.09 T (circles), and 0.08 T (triangles). Red curves are curve fits given by Equation 5.9.

the linear regions of the data. The curve fits are given by Equation 5.9,

$$y = A(e^{Rz} + e^{-Rz}),$$

where A and R are fitting parameters. The values of R extracted from the curve fits in Figure C.2 are 0.0405 ± 0.0018, 0.0419 ± 0.0013, and 0.0322 ± 0.0014 for 0.0969 T (squares), 0.09 T (circles), and 0.08 T (triangles), respectively.

Plotted in Figure C.3 is gain versus scalloping amplitude for the three datasets

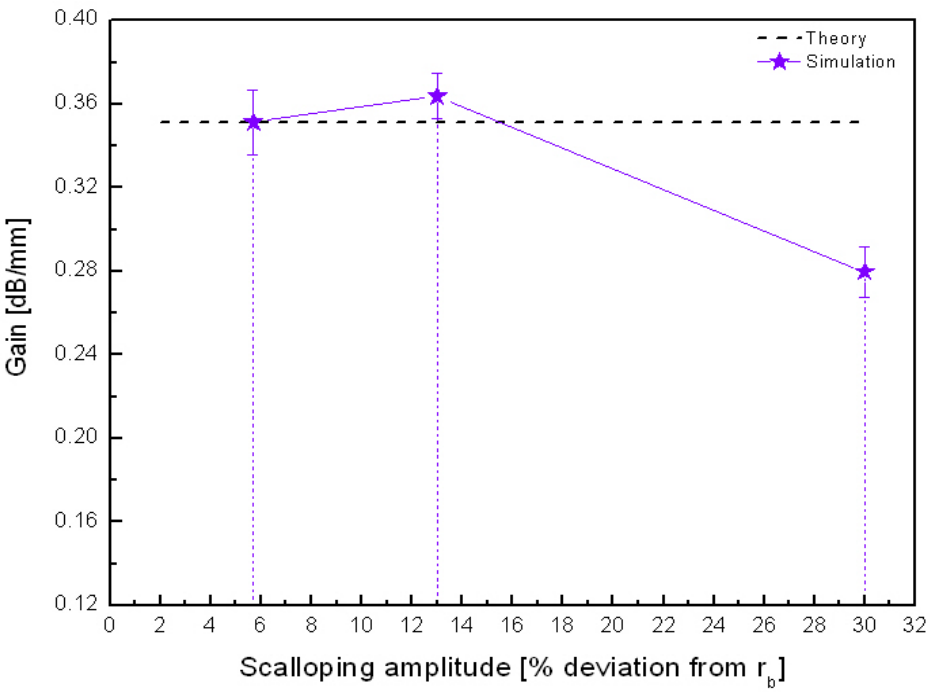

Figure C.3: Gain versus scalloping amplitude for the same beams as in Figure C.1. Dashed line represents a theoretical value given by Equation 4.38.

shown in Figure C.2. The plot was generated by substituting the values of R obtained from Figure C.2 into Equation 5.10 (numerical gain formula). The dashed line is a theoretical value of gain given by Equation 4.38.

As we can see in Figure C.3, the variation of numerical gain is negligible (including error bars) as long as the scalloping amplitude is kept within 13% of the beam radius. The average deviation (excluding error bars) between the numerical and theoretical

gain is less than 4% when the scalloping amplitude is less than or equal to 13% of r_b. For scalloping amplitudes as large as 30% of r_b, as can be seen in Figure C.3, the value of numerical gain is reduced by as much as 21%.

On the basis of the foregoing quantitative analysis we may conclude that simulation results will be valid provided the scalloping amplitude is less than or equal to 13% of the beam radius, r_b. Note that for all simulation considered in this thesis the scalloping amplitude never exceeds 6% of r_b.

Appendix D

Beam emission in MAGIC and various beam types

D.1 Introduction

In this appendix, we briefly discuss the beam emission process used in simulations (MAGIC [13]) and the generation of cold, energy-modulated, and warm electron beams.

D.2 Beam emission and cold, energy-modulated, and warm beams

All simulations presented in this thesis use an "emission beam" process in MAGIC to generate co-propagating electron streams. The process takes a number of optional and mandatory parameters, the latter being beam current densities, beam energies, the number of particles emitted per emission cell and per time step (PPC), and the

particle emission interval. By default, the particle emission interval is equal to the electromagnetic time step, δt, which is given by Equation F.15

$$\delta t = \frac{\chi}{c} \frac{dz \times dr}{\sqrt{dz^2 + dr^2}}, \tag{D.1}$$

where $\chi = 0.8$ is the Courant ratio, c is the speed of light, dz and dr are grid dimensions in axial and radial directions, respectively. The values of dz and dr in Equation D.1 are dependent upon convergence (Appendix A) and aspect ratio requirements. The latter states that the ratio of dz to dr (or vice versa) must not exceed 5. In choosing the number of particles emitted per emission cell and per time step (PPC), we must take into account convergence with regard to PPC (Appendix A) and the total number of particles available to us (5×10^6 particles in the current version of MAGIC).

Having determined the electromagnetic time step and PPC, the "emission beam" process requires that we also specify beam current densities, J_1 and J_2, and energies, E_1 and E_2. For simulations involving cold electron beams, both current densities and energies are specified as constants, equal to their dc values. In the case of energy-modulated beams, J_1 and J_2 are again input as constants, while E_1 and E_2 are modified as follows

$$E_{1,2} + x\% \times \Delta E \times \sin(2\pi f t) = E_{1,2} + \delta E \times \sin(2\pi f t), \tag{D.2}$$

where $\Delta E = E_1$ - E_2, f is the modulation frequency, and x is greater than or equal to 0 (for unmodulated beams $x = 0$). The modulation amplitude, denoted in this thesis by δE, is always specified as some percentage of the beam energy difference, ΔE. Hence, by stating that two beams are modulated at one percent level (or, that, the modulation amplitude is one percent), we mean that $\delta E = 0.01 \times \Delta E$. Warm beams in this thesis have a Gaussian (bell-shaped) energy profile. The transition

from cold to warm beams is accomplished by modifying E_1 and E_2 as follows

$$E_{1,2} + w\% \times E_{\text{avg}} \times \exp\left\{-\frac{(r-1)^2}{2\sigma^2}\right\}, \tag{D.3}$$

where $E_{1,2}$ represents the mean of the bell-shaped distribution, w is greater than or equal to 0, E_{avg} is the average energy of two interacting beams, r is a random number between 0 and 1, and σ (the variance) affects the full width at half maximum (FWHM). The value of σ, namely, 0.18, is chosen such that the FWHM energy is

$$\text{FWHM energy} = 2 \times w\% \times E_{\text{avg}} \tag{D.4}$$

for any given Gaussian profile. J_1 and J_2 for warm beams are input as constants and are the same as those for cold and energy-modulated beams. Figure D.1 shows a Gaussian energy profile for a warm 20-keV electron beam. The peak is slightly shifted

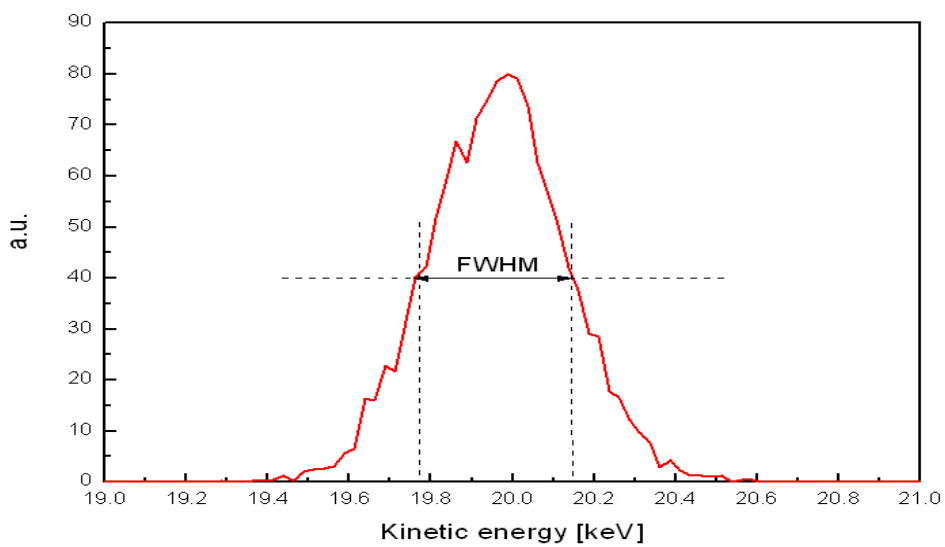

Figure D.1: Gaussian profile of a warm 0.3-A beam with $r_b = 0.7$ mm and $E_1 = 20$ keV. w is 0.01 and FWHM energy from Equation D.4 is 376 eV.

from 20 keV due to potential depression (Section 3.1). The data in Figure D.1 are

taken from a simulation involving the interaction of two 0.7-mm and 0.3-A warm beams ($w = 0.01$) with energies $E_1 = 20$ keV and $E_1 = 17.6$ keV. Substituting the average energy of the beams, $E_{\text{avg}} = 18.8$ keV, into Equation D.4, the FWHM energy can be calculated to yield

$$\text{FWHM} = 2 \times 0.01 \times 18.8 = 376\,\text{eV},$$

which is seen to be in good agreement with that shown in Figure D.1.

If two beams under consideration are both warm and modulated, beam energies are expressed via a combination of Equations D.2 and D.3 and read

$$E_{1,2} + \delta E \times \sin(2\pi f t) + w\% \times E_{\text{avg}} \times \exp\left\{-\frac{(r-1)^2}{2\sigma^2}\right\}. \tag{D.5}$$

As in the case of cold, energy-modulated, and warm beams, current densities, J_1 and J_2, for both warm and modulated beams are input as constants (dc values).

Appendix E

Waveguide modes coexisting with exponentially growing modes

E.1 The impact of TM_{01} waveguide modes on the frequency and gain of exponentially growing modes

In this appendix we analyze the influence of TM_{01} waveguide modes of a circular beam pipe on the frequency and gain of an exponentially growing mode. The results presented here are from four simulations involving two 0.3-A electron beams with energies 20 keV and 17.6 keV propagating and interacting in the setup shown in Figure 5.1. The simulations are performed with four different beam pipe radii, namely, $r_a = 3.825$ mm, $r_a = 3.275$ mm, $r_a = 2.875$ mm, and $r_a = 1.275$ mm. The cutoff frequencies of TM_{01} modes corresponding to the four beam pipe radii are 30 GHz, 35 GHz, 40 GHz, and 90 GHz, respectively. The cutoff frequencies of these four TM_{01} modes along with several TM_{02} modes are displayed in Figure E.1.

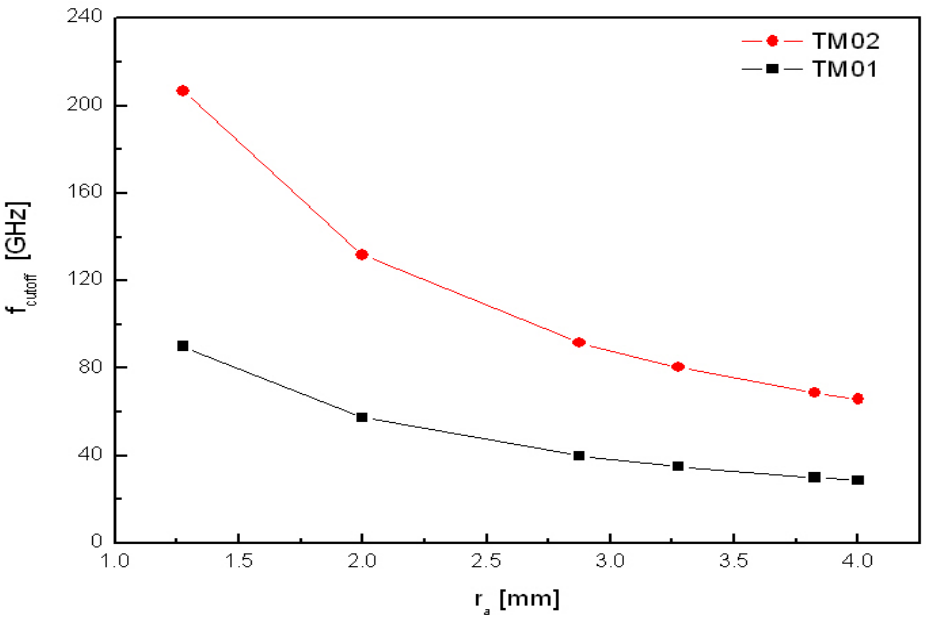

Figure E.1: Cutoff frequency for TM_{01} and TM_{02} waveguide modes as a function beam pipe radius, r_a.

According to Section 4.3, the beams will interact at 30 GHz, henceforth called the exponential mode, regardless of the beam pipe radius. Our goal is to determine the following: 1) does the frequency of the exponential mode shift as we vary the beam pipe radius? and 2) is the growth rate of the exponential mode affected by the proximity of the four TM_{01} modes?

Figure E.2 shows an FFT of the magnitude of the ac component of axial electric filed as a function frequency. The FFT plots are recorded at the same axial location of 173.5 mm.

According to Figure E.2, the largest magnitude occurs at 30 GHz, which is in agreement with that predicted by the 1-D theory in Section 4.3. In addition, the frequency of interaction is always 30 GHz irrespective of the beam pipe radius. Moreover, except for minor differences in the magnitude, the FFT curves are on top of

each other.

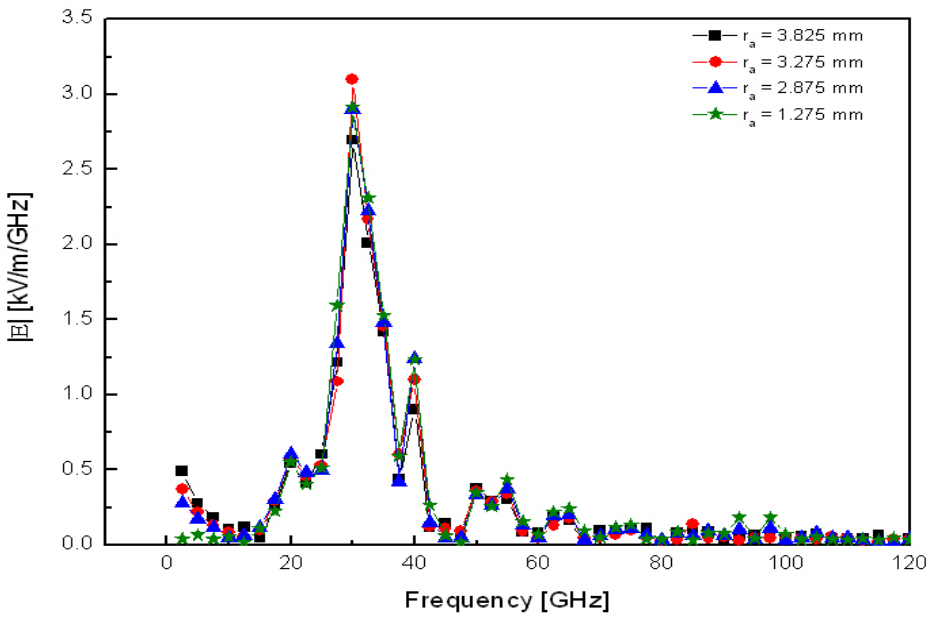

Figure E.2: $|E_z|$ of the exponential mode versus frequency for the four beam pipe radii: $r_a = 3.825$ mm, $r_a = 3.275$ mm, $r_a = 2.875$ mm, and $r_a = 1.275$ mm.

Let us now examine to what extent the growth rate of the exponential mode is affected by the four TM_{01} modes. By the growth rate we mean gain in units of dB/mm.

Figure E.2 shows a snapshot of $|E_z|$ at a given longitudinal distance. Plotted in Figure E.3 is the variation of $|E_z|$ of the exponential mode with longitudinal distance, z, for the four beam pipe radii. According to Figure E.3, the closer the frequencies of the exponential and TM_{01} modes are, the larger the magnitude of the latter for small values of z. Indeed, for $r_a = 3.825$ mm ($\mathrm{f}_{\mathrm{cutoff}} = 30$ GHz), the TM_{01} mode is clearly dominant up to approximately $z = 80$ mm, at which point it is overtaken by the exponential mode. The dominance of the TM_{01} mode for small values of z diminishes quickly, however, as indicated by a 10-fold decrease in its initial magnitude

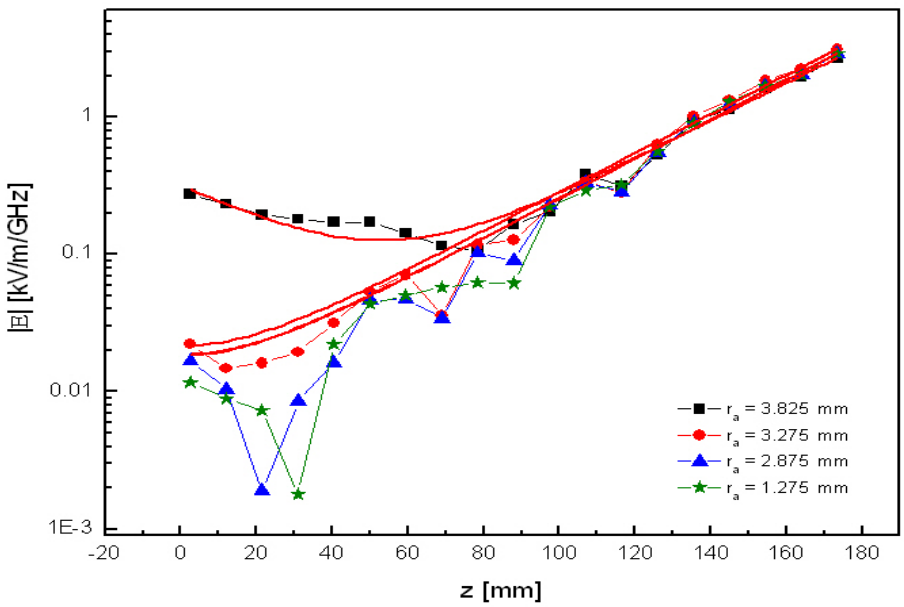

Figure E.3: $|E_z|$ of the exponential mode versus z for the four beam pipe radii. Solid red lines (given by $y = Ae^{Rz} + Be^{-Rz}$) represent curve fits to data.

for $r_a = 3.275$ mm ($f_{cutoff} = 35$ GHz). Despite the difference in the shape of the data curves for small values of z, they all converge in the linear region (for large values of z), where the exponential mode is always dominant regardless of the beam pipe radius.

Shown in Figure E.4 is the gain of the exponential mode as a function of the cutoff frequency of TM_{01} modes. Figure E.4 is generated by fitting each of the curves in Figure E.3 with $y = Ae^{Rz} + Be^{-Rz}$ function (solid red lines in Figure E.3) and substituting the value of R thus obtained into Equation 5.10 (numerical gain)

$$G = 20 \log_{10}\{e^{RL}\}.$$

According to Figure E.4, the gain starts at 0.275 dB/mm and asymptotically approaches 0.289 dB/mm as the beam pipe radius is decreased from $r_a = 3.825$ mm

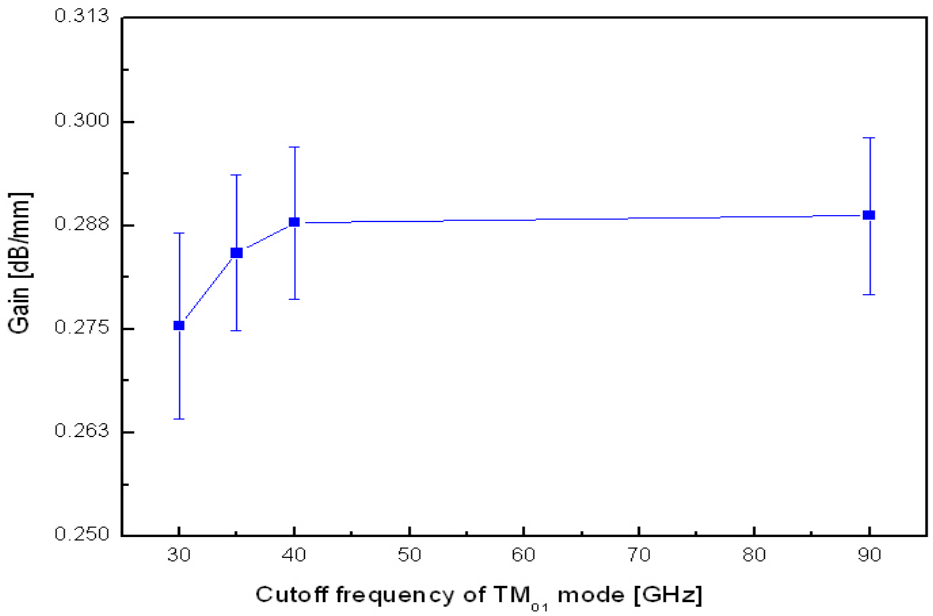

Figure E.4: Gain of the exponential mode versus cutoff frequency of TM_{01} modes for four beam pipe radii: $r_a = 3.825$ mm ($f_{cutoff} = 30$ GHz), $r_a = 3.275$ mm ($f_{cutoff} = 35$ GHz), $r_a = 2.875$ mm ($f_{cutoff} = 40$ GHz), and $r_a = 1.275$ mm ($f_{cutoff} = 90$ GHz).

($f_{cutoff} = 30$ GHz) to $r_a = 1.275$ mm ($f_{cutoff} = 90$ GHz). Hence, the gain varies by less than 5% if we were to exclude the error bars. With the error bars included, as can be seen in Figure E.4, the variation is negligible.

The foregoing analysis leads us to make the following conclusions:

- TM_{01} waveguide modes do not affect the frequency of the exponential mode
- The impact of TM_{01} modes on the gain of the exponential mode is negligible.

Appendix F

Numerical techniques in electromagnetics and MAGIC

F.1 Introduction

Up until the 1940s, scientists relied on analytical techniques, such as the separation of variables, integral transforms, conformal mapping, and perturbation methods, to solve fairly difficult electromagnetic (EM) problems [18]. As EM problems grew in complexity, however, it became apparent that the said analytical methods were no longer adequate to solve EM problems involving inhomogeneous/anisotropic media with complex shapes, time-dependent/mixed boundary conditions, etc. The availability of digital computers around the mid-1960s enabled researchers to start investigating involved EM problems using numerical techniques that provided sufficient accuracy and were much less time-consuming than their analytical counterparts. Some of the most common numerical techniques in use today are as follows [18]:

- Finite difference method

- Finite element method
- Monte Carlo method
- Moment method.

These techniques are not confined to electromagnetics and find application in such problems as heat transfer, acoustics, etc. [18].

EM problems are formulated in terms of partial differential equations (PDEs), the general form (in 2-D) of which in Cartesian coordinates reads [18]

$$A\frac{\partial^2\Psi}{\partial x^2} + B\frac{\partial^2\Psi}{\partial x\partial y} + C\frac{\partial^2\Psi}{\partial y^2} + D\frac{\partial\Psi}{\partial x} + E\frac{\partial\Psi}{\partial y} + F\Psi = f, \tag{F.1}$$

where Ψ is an unknown field quantity, A through F are given coefficients, and f is a known forcing function. Equation F.1 is linear provided A, B, and C are not functions of Ψ. Depending on the sign of $B^2 - 4AC$, Equation F.1 is classified as elliptic, hyperbolic, or parabolic. If $B^2 - 4AC < 0$, Equation F.1 is elliptic (good examples being Poisson and Laplace's equations) and is applicable to EM problems with closed boundaries. When $B^2 - 4AC > 0$, Equation F.1 is hyperbolic and arises in propagation problems. Thus, hyperbolic PDEs have associated with them both initial and boundary values (e.g. a one-dimensional scalar wave equation). Finally, if $B^2 - 4AC = 0$, Equation F.1 is called parabolic, the most common example being a one-dimensional diffusion equation. It should be noted that EM problems are also classified in terms of the solution region in question (closed/open), boundary conditions (homogeneous/inhomogeneous Dirichlet/Neumann conditions or the mixture of the two), and constitutive parameters (σ, ϵ, μ) of the region being considered [18].

F.2 Finite difference method

Developed by A. Thom in the 1920s, the finite difference (FD) technique is a widely used tool for solving PDEs. The FD method consists of the following three steps [18]:

- Division of the solution region into a grid
- Conversion of the underlaying PDEs to finite-difference equations, which are algebraic in nature
- Solution of the finite-difference equations over the gridded region subject to appropriate boundary conditions.

As an example, let us solve a one-dimensional scalar wave equation,

$$\frac{\partial^2 u}{\partial x^2} = \frac{1}{c^2}\frac{\partial^2 u}{\partial t^2}, \tag{F.2}$$

in free space by deriving second-order accurate, central-difference expressions for the first and second partial derivatives of the function u, which is a continuous, single-valued function of x and t and has continuous partial derivatives with respect to x and t. c in Equation F.2 is the speed of light. Suppose $x_i - \Delta x$, x_i, and $x_i + \Delta x$ are neighboring grid points. Using a Taylor series, we can express $u(x_i + \Delta x, t)$ and $u(x_i - \Delta x, t)$ in terms of $u(x_i, t)$ (keeping t fixed at t_n) to give [18]

$$u(x_i + \Delta x, t_n) = u + u_x \Delta x + u_{xx}\frac{\Delta x^2}{2!} + u_{xxx}\frac{\Delta x^3}{3!} + O_1[\Delta x^4], \tag{F.3}$$

$$u(x_i - \Delta x, t_n) = u - u_x \Delta x + u_{xx}\frac{\Delta x^2}{2!} - u_{xxx}\frac{\Delta x^3}{3!} + O_2[\Delta x^4], \tag{F.4}$$

where u_x, u_{xx}, and u_{xxx} are the first, second, and third partial derivatives of u with respect to x and O_1 and O_2 represent the error incurred due to truncating the series

and are of the order Δx^4. Some algebraic manipulation of Equations F.3 and F.4 yields the following expressions for $u_x(x_i, t_n)$ and $u_{xx}(x_i, t_n)$:

$$u_x = \frac{u(x_i + \Delta x, t_n) - u(x_i - \Delta x, t_n)}{2\Delta x} + O[\Delta x^2], \tag{F.5}$$

$$u_{xx} = \frac{u(x_i + \Delta x, t_n) - 2u(x_i, t) + u(x_i - \Delta x, t_n)}{\Delta x^2} + O[\Delta x^2]. \tag{F.6}$$

Keeping x_i constant and retracing the steps, one can obtain similar expressions for $u_t(x_i, t_n)$ and $u_{tt}(x_i, t_n)$, the first and second partial derivatives of u with respect to t

$$u_t = \frac{u(x_i, t_n + \Delta t) - u(x_i, t_n - \Delta t)}{2\Delta t} + O[\Delta t^2], \tag{F.7}$$

$$u_{tt} = \frac{u(x_i, t_n + \Delta t) - 2u(x_i, t) + u(x_i, t_n - \Delta t)}{\Delta t^2} + O[\Delta t^2]. \tag{F.8}$$

Equations F.5 through F.8 are second-order accurate, central-difference approximations to the first and second partial derivatives of u with respect to x and t, respectively. If we denote a spatial position by a subscript i and a temporal one by a superscript n (i and n being integers), Equations F.5 through F.8 may be rewritten as follows [18]:

$$u_x|_{(x_i,t_n)} = \frac{u_{i+1}^n - u_{i-1}^n}{2\Delta x} + O[\Delta x^2], \tag{F.9}$$

$$u_{xx}|_{(x_i,t_n)} = \frac{u_{i+1}^n - 2u_i^n + u_{i-1}^n}{\Delta x^2} + O[\Delta x^2], \tag{F.10}$$

$$u_t|_{(x_i,t_n)} = \frac{u_i^{n+1} - u_i^{n-1}}{2\Delta t} + O[\Delta t^2], \tag{F.11}$$

$$u_{tt}|_{(x_i,t_n)} = \frac{u_i^{n+1} - 2u_i^n + u_i^{n-1}}{\Delta t^2} + O[\Delta t^2]. \tag{F.12}$$

With this notation, u_{i+1}^n, for instance, represents the value of the function at a spatial position $(i+1)\Delta x$ and a time point $n\Delta t$. Substituting Equations F.10 and F.12 into Equation F.2 and solving for u_i^{n+1}, we get [18]:

$$u_i^{n+1} = (c\Delta t)^2 \left\{ \frac{u_{i+1}^n - 2u_i^n + u_{i-1}^n}{\Delta x^2} \right\} + 2u_i^n - u_i^{n-1} + O[\Delta x^2] + O[\Delta t^2]. \quad \text{(F.13)}$$

Note that the right-hand side of Equation F.13 contains known quantities since all the values of the function u are from the previous time steps $n\Delta t$ and $(n-1)\Delta t$. Therefore, u_i^{n+1}, the latest value of u, can be calculated explicitly over the entire grid of the solution region. Solution of Equation F.13 for every subsequent time step, until the time-stepping is completed, constitutes the numerical finite-difference time-domain (FDTD) solution of the one-dimensional scalar wave equation [18]. Owing to its robustness, versatility, ease of implementation, and efficiency, the FDTD method has become the most popular technique in computational electromagnetics [18].

Numerical methods are useful so long as produced numerical solutions approximate exact ones (provided they exist) with a desirable/acceptable degree of accuracy [18]. Because of their inherently approximate nature, every single numerical method is a source of truncation and roundoff errors. Using the FDTD solution of Equation F.2 as an example, we introduced truncation errors by retaining four terms in the Taylor series representation of $u(x_i + \Delta x, t_n)$ and $u(x_i - \Delta x, t_n)$ (Equations F.3 and F.4). Roundoff errors arise because computers can carry only a finite number of significant digits, after which they rounds off, and the accumulation of rounded values over many iterations degrades accuracy. Although the finer mesh (smaller Δx and Δt) or more terms kept in the Taylor series will reduce truncation error, this approach will eventually become impractical in terms of computation time and expense [14]. Also, the finer grid amounts to more calculations per time step (increased roundoff error), thereby diminishing accuracy. Therefore, one can anticipate the existence of an optimal mesh (Δx and Δt) for which the combined numerical error (truncation

plus roundoff) is minimized [14]. Another factor that imposes further restrictions on the size of the time step is the numerical stability of computed solutions. Numerical instability results in computed values increasing spuriously with time. Referring to the FDTD solution of Equation F.2, it can be shown that Equation F.13 is stable providing

$$\Delta t \leq \frac{\Delta x}{c}. \tag{F.14}$$

Should Equation F.14 be violated, u_i^{n+1} from Equation F.13 will grow unboundedly, by approximately a common factor on each time step, yielding unphysical results [18].

F.3 MAGIC

MAGIC is a 2- and 3-D particle-in-cell (PIC) code developed by ATK Mission Research. It is based on the FDTD method, which divides space and time into grids. Having created a spatial grid, MAGIC calculates an electromagnetic time step, δt, and uses it to advance interacting charged particles and electromagnetic fields in time in a self-consistent manner as follows [13]:

- For each δt, Maxwell's coupled curl equations are solved for electric and magnetic fields
- The Lorentz force equation is solved next to determine the charged particle momenta and coordinates
- The continuity equation is solved and the charge and current densities obtained are input to Maxwell's equations on the following time step.

This procedure is schematically shown in Figure F.1. As with any other numerical

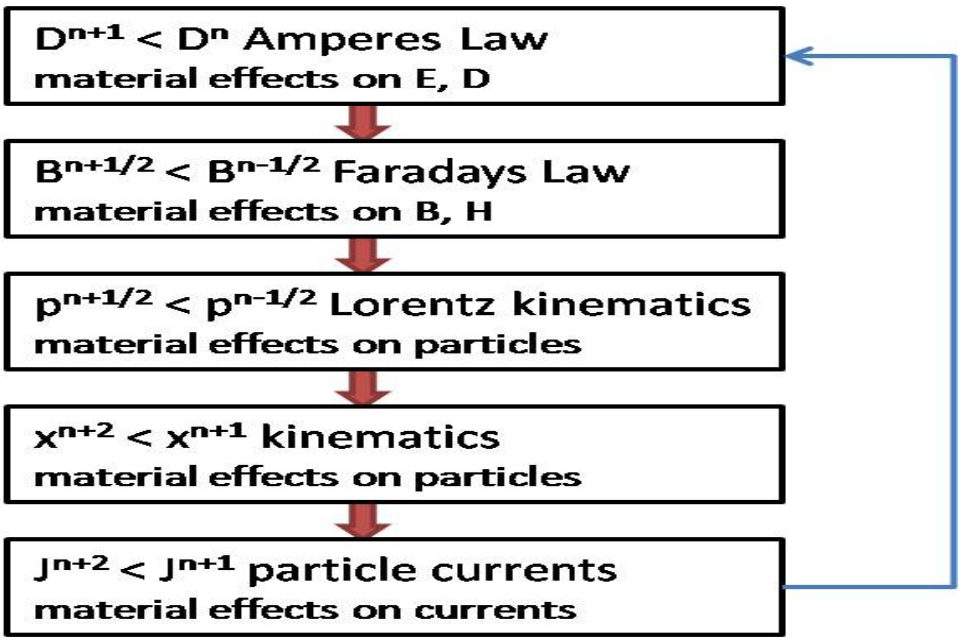

Figure F.1: Self-consistent interaction of particles and fields [13].

package, one must take into account various accuracy and stability considerations when running MAGIC in order to obtain valid results. Accuracy and stability in the electromagnetic solution is determined by spatial resolution (the cell size relative to wavelength) and time step. Any wavelength shorter than about 6 cells will degenerate into noise and be lost from the solution. The size of the time step, δt, is limited by a Courant stability criterion and particle dynamics: one must ensure that no particle is able to move more than one cell in a particle time step. Rapid, catastrophic failure results from exceeding this limit [13]. The centered-difference Courant stability criterion is given by $\chi < 1$, where

$$\chi^2 = c^2 \delta t^2 \sum_{i=1}^{N} \frac{1}{(dx_i)^2} \tag{F.15}$$

is the Courant ratio squared, dx_i is the cell size in meters, c is the speed of light, and N is the number of dimensions (2 or 3). Once the spatial grid is completed, it is automatically searched to find the most restrictive cell. Then the default time

step is calculated using $\chi = 0.8$. Other important stability constraints that may be encountered include the cyclotron frequency resolution, $\omega_c \delta t < 1$, an orbit resolution problem associated with high applied magnetic fields, and the plasma resolution, $\omega_p \delta t \ < 2$, a problem associated with high-density plasmas that can result in catastrophic instability [13].

Appendix G

Sector magnet with a field gradient

G.1 Equations of motion and the transfer matrix of a sector magnet with a field gradient n

In this appendix we shall derive the horizontal and vertical equations of motion and transfer matrix for a sector magnet shown in Figure G.1 [10]. The magnetic field, B_{Z}, at the central ray ($r = R$) and at $r = R + y$ is given as

$$B_{\mathrm{Z}}(r = R) = B_0, \tag{G.1}$$

$$B_{\mathrm{Z}}(r = R + y) = B_0 \left\{ \frac{r}{R} \right\}^{-n}. \tag{G.2}$$

The derivation is based on the following assumptions [10]:

- The boundaries of the magnet are perpendicular to the central ray (orbit) located at $r = R$
- $r \approx R$ or $y < R$. Therefore, we shall only retain first-order terms in y/R as if the motion were about the central orbit

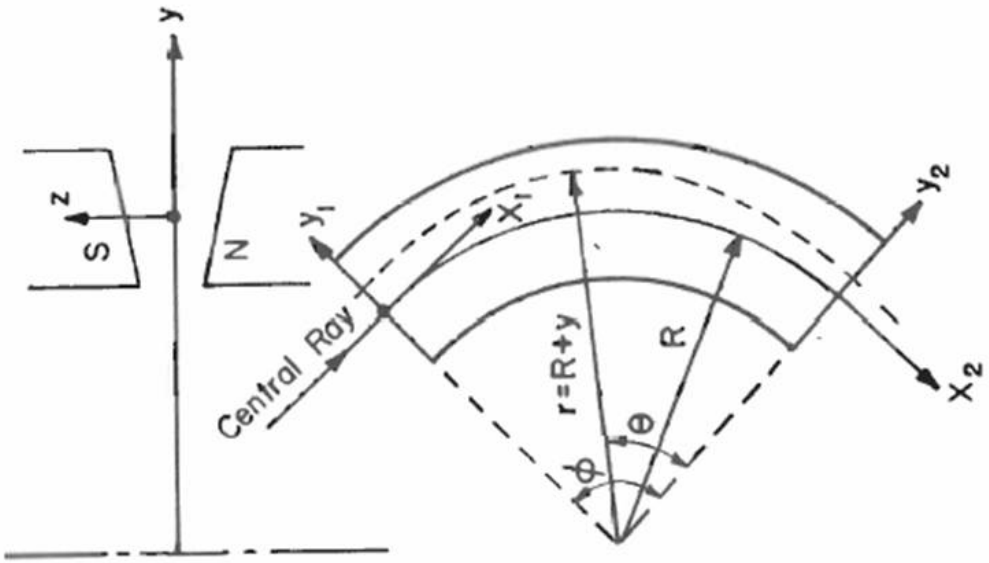

Figure G.1: Side (left) and top views of the tapered sector magnet [10].

- The magnetic field is static ($\vec{\nabla} \times \vec{B} = \vec{0}$) and γ is a constant
- The gap width is smaller than the particle gyroradius: edge focusing is neglected.

Using Equations 2.7 and 2.8, the horizontal (r), azimuthal (ϕ), and vertical (z) componenets of the equation of motion take the form [10]

$$\frac{d^2r}{dt^2} = r\left(\frac{d\phi}{dt}\right)^2 + \frac{q}{m}r\frac{d\phi}{dt}B_{\mathrm{z}}, \tag{G.3}$$

$$\frac{d}{dt}\left(r^2\frac{d\phi}{dt}\right) = -\frac{q}{m}r\frac{dr}{dt}B_{\mathrm{z}}, \tag{G.4}$$

$$\frac{d^2z}{dt^2} = -\frac{q}{m}r\frac{d\phi}{dt}B_r. \tag{G.5}$$

Substituting Equation G.2 into Equations G.3 and G.4, the latter become

$$\frac{d^2r}{dt^2} = r\left(\frac{d\phi}{dt}\right)^2 + \omega\frac{d\phi}{dt}r^{1-n}R^n, \tag{G.6}$$

$$\frac{d}{dt}\left(r^2\frac{d\phi}{dt}\right) = -\omega\frac{dr}{dt}r^{1-n}R^n, \tag{G.7}$$

where $\omega = qB_0/m$. Integrating Equation G.7 and using a binomial expansion (keeping only y/R terms), we have [10]

$$r^2\frac{d\phi}{dt} = -\omega R^n\int_R^{R+y} r^{1-n}\frac{dr}{dt}dt \Longrightarrow$$

$$\frac{d\phi}{dt} = -\omega\frac{R^2}{r^2}\frac{y}{R}. \tag{G.8}$$

When $r \approx R$, Equation G.8 reduces to

$$\frac{d\phi}{dt} = -\omega\frac{y}{R}. \tag{G.9}$$

Using the fact that $d\phi/dt = -\omega$ when $r = R$, to first order in y/R we can write

$$\frac{d\phi}{dt} = -\omega\left(1 - \frac{y}{R}\right). \tag{G.10}$$

Upon substitution of Equation G.10 into Equation G.6 (again keeping only y/R terms), the radial equation of motion becomes [10]

$$\frac{d^2(R+y)}{dt^2} = (R+y)\omega^2\left(1-\frac{y}{R}\right)^2 - R^n\omega^2(R+y)^{1-n}\left(1-\frac{y}{R}\right) \Longrightarrow$$

$$\frac{d^2y}{dt^2} + (1-n)\omega^2 y = 0. \tag{G.11}$$

In component form $\vec{\nabla} \times \vec{B} = \vec{0}$ reads

$$\vec{\nabla} \times \vec{B} = \hat{r}\left(\frac{\partial B_z}{\partial \phi} - \frac{\partial B_\phi}{\partial z}\right) + \hat{\phi}\left(\frac{\partial B_r}{\partial z} - \frac{\partial B_z}{\partial r}\right) + \hat{z}\left(\frac{\partial B_\phi}{\partial r} - \frac{\partial B_r}{\partial \phi}\right) = \vec{0}. \quad \text{(G.12)}$$

Since the unit vectors are linearly independent, Equation G.12 will hold if and only if the components of $\vec{\nabla} \times \vec{B}$ vanish. Setting the azimuthal component equal to zero, we get

$$\frac{\partial B_r}{\partial z} = \frac{\partial B_z}{\partial r}. \quad \text{(G.13)}$$

If we take $B_r = 0$ at $z = 0$ (azimuthal symmetry), to first order ($r \approx R$) we obtain

$$B_r = \int \frac{\partial}{\partial r}\left(B_0 \left\{\frac{r}{R}\right\}^{-n}\right)_{r \approx R} \partial z = -\frac{nB_0}{R} z. \quad \text{(G.14)}$$

Substitution of Equation G.14 into Equation G.5 reduces the latter to

$$\frac{d^2 z}{dt^2} + n\omega^2 z = 0. \quad \text{(G.15)}$$

Equations G.11 and G.15 are called the Kerst-Serber equations [10]. When $0 < n < 1$, the solutions to these equations are sinusoidal functions, which means that the sector magnet may act as a focusing lens in both horizontal and vertical directions [11].

To construct a transfer matrix, we need entrance and exit positions and inclination angles with respect to the central orbit. If x is a variable along the central orbit, then with a change of variables $x = R\omega t$ time derivatives can be converted to x derivatives to give

$$\frac{d}{dt} = R\omega \frac{d}{dx} \quad \text{and} \quad \frac{d^2}{dt^2} = R^2\omega^2 \frac{d^2}{dx^2}. \quad \text{(G.16)}$$

Substitution of Equation G.16 into Equations G.11 and G.15 yields [10]

$$\frac{d^2 y}{dx^2} + k_h^2 y = 0, \quad \text{(G.17)}$$

$$\frac{d^2z}{dx^2} + k_v^2 z = 0, \tag{G.18}$$

where $k_h^2 = (1-n)/R^2$ and $k_\nu^2 = n/R^2$. Solving Equation G.17, we have for the dispplacement (y) and angle ($\acute{y}$) in the horizontal direction

$$y(x) = A\cos(k_h x) + B\sin(k_h x) = C\sin(k_h x + \gamma_h), \tag{G.19}$$

$$\acute{y}(x) = Ck_h\cos(k_h x + \gamma_h). \tag{G.20}$$

The entrance position and angle ($y_i, \acute{y_i}$) anf the exit position and angle ($y_f, \acute{y_f}$) can be determined by setting x equal to 0 and $R\Phi$, respectively, in Equations G.19 and G.20

$$\begin{cases} y_i &= C\sin\gamma_h, \\ \acute{y_i} &= Ck_h\cos\gamma_h, \end{cases} \tag{G.21}$$

$$\begin{cases} y_f &= \cos(k_h\Phi R)y_i + \frac{\sin(k_h\Phi R)}{k_h}\acute{y_i}, \\ \acute{y_f} &= -k_h\sin(k_h\Phi R)y_i + \cos(k_h\Phi R)\acute{y_i}, \end{cases} \tag{G.22}$$

where Φ is the angle subtended by the magnet. The exit position and angle in the vertical direction (solution to Equation G.18) are identical to those given in Equation G.22 with k_h replaced by k_v. In matrix form the exit position and angle in the horizontal and vertical directions are given as [10]

$$\begin{pmatrix} y_f \\ \acute{y_f} \end{pmatrix} = \begin{pmatrix} \cos(k_h\Phi R) & \frac{\sin(k_h\Phi R)}{k_h} \\ -k_h\sin(k_h\Phi R) & \cos(k_h\Phi R) \end{pmatrix} \begin{pmatrix} y_i \\ \acute{y_i} \end{pmatrix}, \tag{G.23}$$

$$\begin{pmatrix} z_f \\ \acute{z_f} \end{pmatrix} = \begin{pmatrix} \cos(k_v\Phi R) & \frac{\sin(k_v\Phi R)}{k_v} \\ -k_v\sin(k_v\Phi R) & \cos(k_v\Phi R) \end{pmatrix} \begin{pmatrix} z_i \\ \acute{z_i} \end{pmatrix}. \tag{G.24}$$

In view of Equations G.23 and G.24, the focal planes in horizontal and vertical directions are located at [11]

$$F_h = -\frac{a_{11}}{a_{21}} = \frac{R}{\sqrt{1-n}}\cot(k_h \Phi R) = \frac{R}{\sqrt{1-n}}\cot(\Psi_1), \tag{G.25}$$

$$F_v = -\frac{a_{11}}{a_{21}} = \frac{R}{\sqrt{n}}\cot(k_v \Phi R) = \frac{R}{\sqrt{n}}\cot(\Psi_2), \tag{G.26}$$

where $\Psi_1 = k_h \Phi R$ and $\Psi_2 = k_v \Phi R$. When $0 < n < 1$ and $\Psi_{1,2} < 90^\circ$, F_h and F_v are positive (located outside the lens), which means that the sector magnet is focusing in both transverse directions. When n = 0.5, F_h and F_v are equal. Therefore, the magnet can produce a 2-D image. If the magnetic field is uniform ($n = 0$), the magnetic lens is focusing in the horizontal direction only, the focusing distance in the vertical direction tending to infinity [11].

References

[1] B. Carlsten, K. Bishofberger, R. Faehl, "Compact two-stream generator of millimeter- and submillimeter-wave radiation," *Phys. Plasmas*, vol. 15, 073101, 2008.

[2] P. Siegel, "Terahertz Technology," *IEEE Trans. Microwave Theory Tech.*, vol. 50, no. 3, pp. 910 – 928, March 2002.

[3] M. Tonouchi, "Prospect of Terahertz Technology," *19th International Conference on Applied Electromagnetics and Communications*, pp. 1 – 4, September 2007.

[4] E. Hecht, "Optics, 4th edition," *Addison Wesley, San Francisco, CA*, 2002.

[5] M. Sherwin, "Terahertz power," *Nature.*, vol. 420, pp. 131 – 133, November 2002.

[6] M. Shur, "Terahertz technology: devices and applications," *Proceedings of ESSCIRC*, Grenoble, France, pp. 13 – 22, 2005.

[7] S. Gold, G. Nusinovich, "Review of high-power microwave source research," *Rev. Sci. Instrum.*, vol. 68, no. 11, pp. 3945 – 3974, November 1997.

[8] V. Bratman, M. Glyavin, T. Idehara, Y. Kalynov, A. Luchinin, V. Manuilov, S. Mitsudo, I. Ogawa, T. Saito, Y. Tatematsu, V. Zapevalov, "Review of Subterahertz and Terahertz Gyrodevices at IAP RAS and FIR FU," *IEEE Trans. Plasma Sci.*, vol. 37, no. 1, pp. 36 – 43, January 2009.

[9] M. Reiser, "Theory and Design of Charged Particle Beams," *Wiley-VCH, New York*, 1994.

[10] A. Septier, "Focusing of charged particles," *Academic Press, New York*, vol. 1, 1967.

[11] S. Humphries, "Principles of Charged Particle Acceleration," *John Wiley and Sons, New York*, 1986.

[12] A. Gilmour, "Principles of traveling wave tubes," *Artech House, Inc., Norwood, MA*, 1994.

[13] L. Ludeking, "Magic Help Manual 2007," *ATK Mission Systems*, 2007.

[14] M. Greenberg, "Advanced Engineering Mathematics," *Prentice Hall, Englewood Cliffs, NJ*, 1998.

[15] R. Collin, "Foundations for Microwave Engineering," *McGraw-Hill, New York*, 1966.

[16] M. Chodorow, C. Susskind, "Fundamentals of Microwave Electronics," *McGraw-Hill, New York*, 1964.

[17] M. Abramowitz, I. Stegun, "Handbook of Mathematical Functions: with Formulas, Graphs, and Mathematical Tables," *Dover Publications, New York*, 1965.

[18] M. Sadiku, "Numerical Techniques in Electromagnetics, Second Edition," *CRC, Boca Raton, Florida*, 2000.

[19] A. Taflove, "Computational Electrodynamics: The Finite-Difference Time-Domain Method," *Artech House Publishers, Norwood, MA*, 2000.

[20] J. Pierce, W. Hebenstreit "A New Type of High-Frequency Amplifier," *Bell Syst. Tech. J.*, vol. 28, pp. 33 – 51, 1949.

[21] A. Haeff, "The Electron-Wave Tube - A Novel Generation and Amplification of Microwave Energy," *Proc. I.R.E.*, vol. 37, pp. 4 – 10, January 1949.

[22] J. Hollenberg, "Experimental Observation of Amplification by Interaction Between Two Electron Streams," *Bell Syst. Tech. J.*, vol. 28, pp. 52 – 58, 1949.

[23] C. Chen, P. Catravas, and G. Bekefi,"Growth and saturation of stimulated beam modulation in a two-cavity klystron amplifier," *Appl. Phys. Lett.*, vol. 62, pp. 1579 – 1581, April 1993.

[24] B. Carlsten, "USPAS course on microwave sources."

[25] S. Humphries, "Charged Particle Beams," *John Wiley and Sons, New York*, 1990.

[26] R. Briggs, "Electron-stream interaction with plasmas," *MIT Press*, chap. 2, pp. 8–46, 1964.